

NATIONAL INSTITUTE FOR FUSION SCIENCE

Nonlinear Physics of Plasmas:
Spatiotemporal Structures in Strong Turbulence
- Lecture Notes -

Miloš M. Škorić

(Received - Apr. 3, 2008 -)

NIFS-PROC-74

May 2008

RESEARCH REPORT
NIFS-PROC Series

This report was prepared as a preprint of work performed as a collaboration research of the National Institute for Fusion Science (NIFS) of Japan. The views presented here are solely those of the authors. This document is intended for information only and may be published in a journal after some rearrangement of its contents in the future.

Inquiries about copyright should be addressed to the Research Information Office, National Institute for Fusion Science, Oroshi-cho, Toki-shi, Gifu-ken 509-5292 Japan.

E-mail: bunken@nifs.ac.jp

<Notice about photocopying>

In order to photocopy any work from this publication, you or your organization must obtain permission from the following organization which has been delegated for copyright for clearance by the copyright owner of this publication.

Except in the USA

Japan Academic Association for Copyright Clearance (JAACC)
6-41 Akasaka 9-chome, Minato-ku, Tokyo 107-0052 Japan
Phone: 81-3-3475-5618 FAX: 81-3-3475-5619 E-mail: jaacc@mtd.biglobe.ne.jp

In the USA

Copyright Clearance Center, Inc.
222 Rosewood Drive, Danvers, MA 01923 USA
Phone: 1-978-750-8400 FAX: 1-978-646-8600

Nonlinear Physics of Plasmas:
Spatiotemporal Structures in Strong Turbulence
-Lecture Notes-

Miloš M. Škorić

April, 2008

Preface

This material has been prepared and partly delivered in a series of lectures given at NIFS to Doctor course students of the SOKENDAI (Graduate University of Advanced Studies, Japan) in academic 2007/08 year.

Special gratitude is due to colleagues for fruitful collaboration: Profs. K. Mima, Lj. Hadžievski, S. Ishiguro, A. Maluckov, M. Rajković and Dr Li Baiwen and Dr Lj. Nikolić, in particular, and to Prof. Mitsuo Kono for motivating the work on this text. I wish to pay unique tribute to close friends and longtime collaborators, Prof. Dik ter Haar and Prof. Moma Jovanović who are no longer with us.

Continuing support and encouragement by Prof. S. Sudo, Prof. N. Nakajima, and Prof. O. Motojima of NIFS, are gratefully acknowledged.

Toki-shi, 30th April, 2008.

Contents

1	Strong Langmuir Turbulence	5
1.1	Introduction	5
1.2	Derivation of the generalized Zakharov equations	6
1.3	Adiabatic Scaling and Spherical Collapse	12
1.4	Qualitative discussion of the collapse	15
2	Wave Collapse in Plasmas	17
2.1	Langmuir Soliton Stability and Collapse	17
2.1.1	Introduction	17
2.1.2	Basic Equations	19
2.1.3	Variational Treatment of Soliton Stability	21
2.1.4	Numerical Treatment	22
2.1.5	Nonlinear Stage of Soliton Instability	26
2.1.6	Self-similarity and collapse regimes	30
2.2	Virial Theory of Wave Collapse	32
2.3	Hierarchy of Collapse Regimes in a Magnetized Plasma	34
2.3.1	Introduction	35
2.3.2	Model Equation	35
2.3.3	Nonexistence of Three-Dimensional Solitons	37
2.3.4	Necessary Condition for Wave Collapse	39
2.3.5	Classification of Wave Collapse Regimes	40
2.4	Weak and Strong Langmuir Collapse	42
3	Spatiotemporal Complexity in Plasmas	49
3.1	Spatiotemporal Effects in Three-Wave Interaction	49
3.1.1	Time-Only Problem in Three Wave Interaction	50
3.1.2	Space-Only Problem in Three Wave Interaction	54
3.1.3	Spatiotemporal Evolution in Three-Wave Interaction	57
3.1.4	Convective and Absolute Instability	59
3.2	Complexity in Laser Plasma Instabilities	61
3.2.1	Introduction	61
3.2.2	Nonlinear 3WI Paradigm for SRS	63
3.2.3	Bifurcations and Low-Dimensional Chaos	66

3.2.4	Spatiotemporal Wave Patterns	69
3.2.5	Quantitative Signatures of Spatiotemporal Regimes	72
3.2.6	Transition from Spatiotemporal Intermittency to Spatiotemporal Chaos	75
3.2.7	Conclusions	77
3.3	Self-Organization in a Dissipative Three-Wave Interaction- Saturated SRS Paradigm	78
3.3.1	Introduction	79
3.3.2	Physical Preliminaries on Nonlinear Kinetic SRS	79
3.3.3	A Three-Wave Dissipative Interaction Model	81
3.3.4	Kinetic-Hybrid Scheme	82
3.3.5	Open Boundary Model	84
3.3.6	Micro-Scale and Macro-Scale Self-Organization	86
3.3.7	Dissipative Structures and Entropy Rate	90
3.3.8	Summary	93
4	Relativistic Plasma Interactions	95
4.1	Electronic Parametric Wave Coupling	95
4.1.1	Stimulated Raman Scattering	96
4.1.2	Relativistic Dispersion Relation for Cold Plasma	97
4.1.3	Summary	103
4.2	Computer simulations	105
4.2.1	Particle-in-cell simulations	105
4.3	Weakly Relativistic Electromagnetic Solitons	107
4.3.1	Dynamical Equations	108
4.3.2	Relativistic Soliton Stability	110
4.3.3	Numerical Results	111
4.3.4	Ultra-Relativistic Solitons	112
4.4	Stimulated Raman Scattering Cascade into Photon Condensation	116
4.4.1	Introduction	116
4.4.2	Relativistic Fluid-Maxwell Simulation	118
4.4.3	Particle Simulations	121
4.5	Ultra Relativistic EM Solitons in Intense Laser Interaction with a Low Density Plasma	131
4.5.1	Introduction	131
4.5.2	Ultra Relativistic EM Solitons	132
4.6	Stimulated Electron Acoustic Scattering in High Intensity Laser Plasma Interaction	137
4.6.1	On the Electron Acoustic Waves	137
4.6.2	Stimulated Raman and Acoustic Wave Scattering	138
4.6.3	SEAS Model	140
4.6.4	Simulations	141
4.7	Stimulated Trapped Electron Acoustic Wave Scattering, EM Soliton and Ion-Vortices in Subcritical Plasmas	143
4.7.1	Introduction	143

4.7.2	Simulation Model	144
4.7.3	Stimulated Trapped Electron Acoustic Wave Scattering	145
4.7.4	Electromagnetic Soliton and Ion-Vortices	147
5	Ponderomotive Potential and Magnetization	153
5.1	Hamiltonian formulation of ponderomotive interactions in a Vlasov plasma	153
5.2	The hydrodynamics of ponderomotive interactions in a collisionless plasma	159
5.3	Spontaneous generation of magnetostatic fields	163
5.3.1	Coupled mode equations	164
5.3.2	Instability analysis	165

Chapter 1

Strong Langmuir Turbulence

A set of generalized Zakharov equations for nonlinear Langmuir waves is derived which is valid for both electrostatic and electromagnetic, that is, potential and transverse, perturbations which include corrections due to higher electron nonlinearities and allowing for a breakdown of slow-time scale quasi-neutrality. Further, we show how these correction terms may possibly affect the Langmuir collapse in two or three dimensions.

1.1 Introduction

An important question in contemporary plasma physics is the problem of strong Langmuir turbulence [1, 2, 3, 4, 5, 6]. The simplest case is that of Langmuir turbulence in an unmagnetized plasma which has been studied extensively, especially the transition from weak to strong turbulence in which the parametric modulational instability (MI), first suggested by Vedenov and Rudakov [7] and by Gailitis [8], plays a major role. A set of two equations for Langmuir wave coupled to ion-sound was formulated and dispersion relation solved for MI growth rate, predicting spatial localization of long-wavelength unstable perturbations of initially homogenous weak turbulence state [2, 3]. It is currently well established both through numerical work [9, 10, 11] and through experiments [11, 12] that if sufficient energy is put into a plasma, Langmuir solitons will be formed, that is, localized structures which are both density depressions and electric field maxima [4]. The numerical work is often concerned with one-dimensional models, although Nicholson and Goldman [13] deal with a two-dimensional plasma, and it is normally based on the so-called Zakharov equations which were derived by Zakharov [2] to describe the development of the modulational instability in an unmagnetized plasma. From these equations it follows that in two or three dimensions collapse will occur, and much numerical work has been devoted to a study of the existence and dynamics of the so-called Langmuir collapse (for a review of this type see, e.g., Rudakov and Tsytovich [14], Thornhill and ter Haar [3, 15], Goldman [11]) it is necessary to use numerical methods as the only known analytical solution of the two- or three-dimensional Zakharov equations is the planar Langmuir soliton. Unfortunately, the numerical procedure can only be applied to the early stages of the collapse, since the Zakharov equations lose their validity when the field intensities become too large. It is the aim of this section to consider a generalization of the Zakharov equations which will be valid at higher amplitudes in order to show consistent derivation

and possibly answer the question of whether the collapse will continue until the size of the Langmuir cavitons become of the order of the Debye length so that Landau damping can play a role. In this context it is interesting to note that the experiments by Antipov and collaborators [12] indicated structures which are smaller than the Langmuir solitons, but large enough for Landau damping still to be negligible. There has been relatively little work on the limitation of the Zakharov equations. Khakimov and Tsytovich [16](see also Tsytovich [17]) used their non-linear dielectric formalism to investigate the limit of applicability of the Zakharov equations. They claim to have taken all non-linearities up to the fifth order in the electric field into account and they derived a generalized set of equations. Using an approach similar to the original approach of Zakharov's and to the approach to be used here [18], Kuznetsov [19] examined the effect of higher electrostatic non-linearities and came to the conclusion that they become important at large field amplitudes. It is our purpose to clarify the effect of electron nonlinearities upon the collapse, including both electrostatic and electromagnetic perturbations. It is important to include both potential and non-potential modes, as the frequently used electrostatic (potential) approximation is normally violated in the case of developed (strong) Langmuir turbulence of hot plasmas (see, e.g., Thornhill and ter Haar [3] ; Nicholson and Goldman [13]). We shall follow original work of Zakharov [2] by separating "fast" and "slow" time scales and applying a hydrodynamic approach, but in addition we shall include higher electron nonlinearities describing the scattering by stimulated fluctuations in the low frequency electron velocity and in the $2\omega_p$ -components of the electron density and velocity (ω_p - electron plasma frequency). We thus allow the possibility of the breakdown of the quasi-neutrality for slow motions (compare also [20]). We also shall apply the adiabatic scaling approach [18, 21] to examine the collapse and the possibility of the existence of quasi-stationary structures in two or three dimensions. Although we find that in the spherically symmetric case the correction terms introduced by us halt the collapse, that is, prevent the appearance of a mathematical singularity, we have not yet investigated whether the collapse is halted before Landau damping becomes effective, that is, before the caviton reaches a size of the order of the Debye length. This means that the question whether the higher hydrodynamic non-linearities studied by us can fully stabilize the physical collapse still needs to be answered.

1.2 Derivation of the generalized Zakharov equations

We consider an isotropic, unmagnetized plasma in which the electron temperature T_e , is much higher than the ion temperature T_i and we restrict ourselves to considering long-wavelength electrostatic and electromagnetic modes so that

$$(k^l r_{De})^2 \ll 1 \quad (k^t c/\omega_p)^2 \ll 1, \quad (1.1)$$

where k^l and k^t are, respectively, the wavenumber of the electrostatic and electromagnetic waves, c is the velocity of light, and r_{De} is the electron Debye radius.

We consider Langmuir turbulence when the dominant plasma mode is that of the Langmuir waves with frequencies close to the electron plasmas frequency (ω_p). We follow the original idea of well separated "slow" (ion) and "fast" electron time scales [2] and

split the electron density n_e , electron velocity \mathbf{v}_e , electric field strength \mathbf{E} , and current density \mathbf{j} in terms corresponding to different time scales [18] :

$$n_e = n_0 + n_s + n_1 + n_2 + \dots, \quad (1.2)$$

$$\mathbf{v}_e = \mathbf{v}_s + \mathbf{v}_1 + \mathbf{v}_2 + \dots, \quad (1.3)$$

$$\mathbf{E} = \mathbf{E}_s + \mathbf{E}_1 + \mathbf{E}_2 + \dots, \quad (1.4)$$

$$\mathbf{j}_e = \mathbf{j}_s + \mathbf{j}_1 + \mathbf{j}_2 + \dots \quad (1.5)$$

Here, n_0 is the initial uniform electron density corresponding to the situation where there are no waves present, the quantities with index s vary on the slow time scale, those with index 1 on the fast, $(2\pi/\omega_p)$ time scale, those with index 2 on the fast, $2(2\pi/\omega_p)$ time scale (2^{nd} harmonic), and so on. It is convenient to write

$$n_l = \tilde{n}_l \exp(-i\omega_p t) + \tilde{n}_l^* \exp(i\omega_p t), n_2 = \tilde{n}_2 \exp(-2i\omega_p t) + c.c., \quad (1.6)$$

$$\mathbf{v}_l = \tilde{\mathbf{v}}_l \exp(-i\omega_p t) + \tilde{\mathbf{v}}_l^* \exp(i\omega_p t), \mathbf{v}_2 = \tilde{\mathbf{v}}_2 \exp(-2i\omega_p t) + c.c., \quad (1.7)$$

and so on, where the quantities with tildes are slowly varying and where the asterisk sign indicates the complex conjugate quantity.

We assume that the density perturbation is not too strong, that is,

$$n_0 \gg n_s, n_1, n_2, \quad (1.8)$$

where, however, n_s may sometimes be taken to be comparable with, though still well below, n_0 , while the basic assumption of the predominance of the Langmuir mode leads to the inequalities

$$|\mathbf{v}_1| \gg |\mathbf{v}_s|, |\mathbf{v}_2| \dots, \quad |\mathbf{E}_1| \gg |\mathbf{E}_s|, |\mathbf{E}_2| \dots, \quad (1.9)$$

Our basic equations are the Maxwell equations

$$\nabla \cdot \mathbf{E} = 4\pi\rho, \nabla \times \mathbf{E} = -\frac{1}{c} \frac{\partial \mathbf{H}}{\partial t}, \nabla \times \mathbf{H} = \frac{1}{c} \left(4\pi\mathbf{j} + \frac{\partial \mathbf{E}}{\partial t} \right), \quad (1.10)$$

where ρ is the charge density; the quantities ρ and \mathbf{j} satisfy the relations

$$\rho = -e(n_e - n_i), \mathbf{j} = -e(n_e \mathbf{v}_e - n_i \mathbf{v}_i), \quad (1.11)$$

where n_i and \mathbf{v}_i are the ion density and the ion velocity, and $-e$ is the electron charge.

We shall split the ion density as follows:

$$n_i = n_0 + \delta n_i, \quad (1.12)$$

where δn_i changes on the slow time scale and where δn_i is not necessarily equal to n_s : we are not, as in Zakharov's original treatment [2], *a priori* assuming the quasi-neutrality on the slow time scale.

The Maxwell equations (1.10) lead to the wave equation,

$$\frac{\partial^2 \mathbf{E}}{\partial t^2} + c^2 \nabla \times \nabla \times \mathbf{E} = -4\pi \frac{\partial \mathbf{j}}{\partial t}, \quad (1.13)$$

which is linear in both, \mathbf{E} and \mathbf{j} and convenient for further calculations. We can readily split up above equation corresponding to various time scales. The equation corresponding to the ω_p -time scale is

$$\frac{\partial^2 \mathbf{E}_1}{\partial t^2} + c^2 \nabla \times \nabla \times \mathbf{E}_1 = -4\pi \frac{\partial \mathbf{j}_1}{\partial t}. \quad (1.14)$$

We must draw attention to the fact that the representation (1.7), (1.8) in the case of \mathbf{E} differs by a factor 2 from the one normally used. The quantity \mathbf{j}_1 follows from Eq. (1.11) and satisfies the relation

$$\mathbf{j}_1 = -e (n_0 \tilde{\mathbf{v}}_1 + n_s \tilde{\mathbf{v}}_1 + \tilde{n}_1 \mathbf{v}_s + \tilde{n}_1^* \tilde{\mathbf{v}}_2 + \tilde{n}_1 \tilde{\mathbf{v}}_2^*). \quad (1.15)$$

Substituting expression (1.15) into Eq. (1.14) and neglecting, as usually (i.e., slowly varying envelope), $\partial^2 \tilde{\mathbf{E}}_1 / \partial t^2$ as compared to $\omega_p \partial \tilde{\mathbf{E}}_1 / \partial t$ we find

$$-2i\omega_p \frac{\partial \tilde{\mathbf{E}}_1}{\partial t} - \omega_p^2 \tilde{\mathbf{E}}_1 + c^2 \nabla \times \nabla \times \tilde{\mathbf{E}}_1 = 4\pi e [n_0 \tilde{\mathbf{v}}_1 + n_s \tilde{\mathbf{v}}_1 + \tilde{n}_1 \mathbf{v}_s + \tilde{n}_1^* \tilde{\mathbf{v}}_2 + \tilde{n}_1 \tilde{\mathbf{v}}_2^*]. \quad (1.16)$$

To close the equation we need expressions for n_s , \mathbf{v}_s , \tilde{n}_1 , $\tilde{\mathbf{v}}_1$, \tilde{n}_2 and $\tilde{\mathbf{v}}_2$. It is obvious that the dominant term on the right-hand side of eq. (1.16) is the linear one involving $n_0 \tilde{\mathbf{v}}_1$, while the other four terms are much smaller and may be regarded to be nonlinear corrections.

Our basic assumptions are Eqs. (1.1), (1.8), and (1.9) and they allow us to introduce a hydrodynamic description for the electron fluid, that is, to use the equation of continuity and equation of motion,

$$\frac{\partial n_e}{\partial t} + \nabla \cdot (n_e \mathbf{v}_e) = 0, \quad (1.17)$$

$$\frac{\partial \mathbf{v}_e}{\partial t} + (\mathbf{v}_e \cdot \nabla) \mathbf{v}_e = -\frac{e}{m} \left(\mathbf{E} + \frac{1}{c} [\mathbf{v}_e \times \mathbf{B}] \right) - 3v_{Te}^2 \nabla \left(\frac{n_e}{n_0} \right). \quad (1.18)$$

Using inequalities (1.8) and (1.9) to linearize Eq. (1.18) in \tilde{n}_1 and $\tilde{\mathbf{v}}_1$ and assuming that the plasma is non-relativistic so that we can drop the term in the Lorentz force involving high-frequency magnetic field \mathbf{B} , we get

$$\begin{aligned} \frac{\partial \tilde{\mathbf{v}}_1}{\partial t} = & - [(\tilde{\mathbf{v}}_1 \cdot \nabla) \mathbf{v}_s + (\tilde{\mathbf{v}}_1^* \cdot \nabla) \tilde{\mathbf{v}}_2 + (\mathbf{v}_s \cdot \nabla) \tilde{\mathbf{v}}_1 \\ & (\tilde{\mathbf{v}}_2 \cdot \nabla) \tilde{\mathbf{v}}_1^*] - \frac{e}{m} \tilde{\mathbf{E}}_1 - 3v_{Te}^2 \nabla \left(\frac{\tilde{n}_1}{n_0} \right). \end{aligned} \quad (1.19)$$

To zeroth order we get from (1.19)

$$\tilde{\mathbf{v}}_1^{(0)} = -\frac{ie}{m\omega_p} \tilde{\mathbf{E}}_1, \quad (1.20)$$

and using the Poisson equation in the form

$$\text{div } \tilde{\mathbf{E}}_1 = -4\pi e \tilde{n}_1, \quad (1.21)$$

we get to the first order

$$\begin{aligned} \frac{\partial \tilde{\mathbf{v}}_1^{(1)}}{\partial t} &= \frac{ie}{m\omega_p} \left[\left(\tilde{\mathbf{E}}_1 \cdot \nabla \right) \mathbf{v}_s + (\mathbf{v}_s \cdot \nabla) \tilde{\mathbf{E}}_1 - \left(\tilde{\mathbf{E}}_1^* \cdot \nabla \right) \tilde{\mathbf{v}}_2 \right. \\ &\quad \left. - (\tilde{\mathbf{v}}_2 \cdot \nabla) \tilde{\mathbf{E}}_1^* \right] - \frac{e}{m} \tilde{\mathbf{E}}_1 + \frac{3e}{m} r_{De}^2 \nabla \left(\nabla \cdot \tilde{\mathbf{E}}_1 \right). \end{aligned} \quad (1.22)$$

We can now use (1.20) and (1.22) to obtain from Eq. (1.16) the relation

$$\begin{aligned} i \frac{\partial \tilde{\mathbf{E}}_1}{\partial t} - \frac{c^2}{2\omega_p} \nabla \times \nabla \times \tilde{\mathbf{E}}_1 + \frac{3}{2} \omega_p r_{De}^2 \nabla \cdot \nabla \cdot \tilde{\mathbf{E}}_1 - \frac{\omega_p}{2n_0} n_s \tilde{\mathbf{E}}_1 &= \\ - \frac{1}{2} i \left[\left(\tilde{\mathbf{E}}_1 \cdot \nabla \right) \mathbf{v}_s + (\mathbf{v}_s \cdot \nabla) \tilde{\mathbf{E}}_1 + \mathbf{v}_s \nabla \cdot \tilde{\mathbf{E}}_1 \right] - \frac{\omega_p}{2n_0} \tilde{n}_2 \tilde{\mathbf{E}}_1^* \\ + \frac{1}{2} i \left[\left(\tilde{\mathbf{E}}_1^* \cdot \nabla \right) \tilde{\mathbf{v}}_2 + (\tilde{\mathbf{v}}_2 \cdot \nabla) \tilde{\mathbf{E}}_1^* - \tilde{\mathbf{v}}_2 \nabla \cdot \tilde{\mathbf{E}}_1^* \right]. \end{aligned} \quad (1.23)$$

If the right-hand side of Eq. (1.23) were zero, this equation would be one of the Zakharov equations which describes both electrostatic and electromagnetic perturbations [3, 18, 19]. The terms on the right-hand side of (1.23) correspond to higher electron nonlinearities describing both electrostatic (Langmuir) and electromagnetic perturbations. The equation is a generalization of Kuznetsov's result [19], in which only potential perturbations were considered. Indeed, one readily recovers his results by putting $\tilde{\mathbf{E}}_1 = \nabla \psi$.

To close the set of equations we still need relations for n_s , \mathbf{v}_s , \tilde{n}_2 and $\tilde{\mathbf{v}}_2$. The electron motions at frequencies close to $2\omega_p$ can be described in the hydrodynamic framework as the phase velocity is much larger than the thermal velocity. Linearizing Eqs. (1.17) and (1.18) with respect to n_2 and \mathbf{v}_2 we find

$$\frac{\partial n_2}{\partial t} + n_0 \nabla \cdot \mathbf{v}_2 + \nabla \cdot (n_1 \mathbf{v}_1) = 0, \quad (1.24)$$

$$\frac{\partial \mathbf{v}_2}{\partial t} + (\mathbf{v}_1 \cdot \nabla) \mathbf{v}_1 + \frac{e}{mc} [\mathbf{v}_1 \times \mathbf{B}_1] = -\frac{e}{m} \mathbf{E}_2, \quad (1.25)$$

where \mathbf{E}_2 which represents the electric field component due to charge separation at frequencies close to $2\omega_p$ satisfies the continuity relation

$$\nabla \cdot \mathbf{E}_2 = -4\pi e n_2. \quad (1.26)$$

Using (1.20) for \mathbf{v}_1 and the appropriate Maxwell equation (1.10) for \mathbf{B}_1 we get from (1.25) the following equation for \mathbf{v}_2 , where we have retained the terms with the correct frequency dependence:

$$m \frac{\partial \mathbf{v}_2}{\partial t} = -e \mathbf{E}_2 + \mathbf{F}_2, \quad (1.27)$$

where \mathbf{F}_2 is the potential (ponderomotive or Miller, [22]) force at the second harmonic frequency $2\omega_p$. If we write

$$\mathbf{F}_2 = \tilde{\mathbf{F}}_2 \exp(-2i\omega_p t) + \tilde{\mathbf{F}}_2^* \exp(2i\omega_p t), \quad (1.28)$$

we have

$$\tilde{\mathbf{F}}_2 = -m \left((\tilde{\mathbf{v}}_1 \cdot \nabla) \tilde{\mathbf{v}}_1 + \frac{e}{mc} \left[\tilde{\mathbf{v}}_1 \times \tilde{\mathbf{B}}_1 \right] \right) = \frac{-1}{8\pi n_0} \nabla \cdot \left(\tilde{\mathbf{E}}_1 \tilde{\mathbf{E}}_1 \right). \quad (1.29)$$

We note from (1.27) that at the frequency $2\omega_p$ the driving force derives both from charge separation and from the ponderomotive force. To find n_2 we first combine Eqs. (1.24), (1.26), (1.20), and (1.21) to find $\nabla \cdot \mathbf{v}_2$ in the form

$$\nabla \cdot \mathbf{v}_2 = \frac{i}{12\pi n_0 \omega_p} \nabla \cdot \left(\tilde{\mathbf{E}}_1 \nabla \cdot \tilde{\mathbf{E}}_1 + \nabla \cdot \left(\tilde{\mathbf{E}}_1 \tilde{\mathbf{E}}_1 \right) \right), \quad (1.30)$$

and hence

$$\tilde{n}_2 = \frac{1}{6\pi m \omega_p^2} \nabla \cdot \left(\tilde{\mathbf{E}}_1 \nabla \cdot \tilde{\mathbf{E}}_1 + \frac{1}{4} \nabla \cdot \left(\tilde{\mathbf{E}}_1 \tilde{\mathbf{E}}_1 \right) \right). \quad (1.31)$$

Eqs. (1.30) and (1.31) are identical with Kuznetsov's equations [19] which were derived assuming that there were only electrostatic perturbations.

Next we must derive the "slow timescale" electron equations. As the slow timescale phase velocity v_{ph}^s will be of the order of the ion-sound speed which is small compared to the electron thermal velocity, we may assume that the averaged electron density, defined by the relation

$$\langle n_e \rangle = \langle n_0 + n_s + n_1 + n_2 + \dots \rangle = n_0 + n_s, \quad (1.32)$$

will be given by a Boltzmann distribution in the field of an effective potential U_{eff} [2, 3]. This effective potential consists of a slow-time scale charge separation potential $-e\phi_s$ and a ponderomotive potential U_{pond} obtained, like $\langle n_e \rangle$, by averaging over the fast-time scale motion:

$$U_{eff} = -e\phi_s + U_{pond}, \quad (1.33)$$

where

$$U_{pond} = \frac{e^2}{m\omega_p^2} \left(\tilde{\mathbf{E}}_1 \tilde{\mathbf{E}}_1^* \right). \quad (1.34)$$

For $\langle n_e \rangle$ we have thus

$$\langle n_e \rangle = n_0 \exp \frac{-e\phi_s + U_{pond}}{T_e}, \quad (1.35)$$

whence

$$n_s = n_0 \left[\exp \left\{ (e\phi_s - U_{pond}) / T_e \right\} - 1 \right]. \quad (1.36)$$

If the electron distribution is stationary, we get by linearizing the equation of continuity (1.17) with respect to n_s and \mathbf{v}_s and retaining only the slow-time scale terms

$$\nabla \cdot \mathbf{v}_s = -\nabla \cdot (\tilde{n}_1 \tilde{\mathbf{v}}_1^* + \tilde{n}_1^* \tilde{\mathbf{v}}_1) / n_0, \quad (1.37)$$

and hence, using (1.20) and (1.21)

$$\nabla \cdot \mathbf{v}_s = \frac{i}{4\pi m n_0 \omega_p} \nabla \cdot \left[\tilde{\mathbf{E}}_1^* \nabla \cdot \tilde{\mathbf{E}}_1 - \tilde{\mathbf{E}}_1 \nabla \cdot \tilde{\mathbf{E}}_1^* \right]. \quad (1.38)$$

To eliminate $e\phi_s$ we shall need an equation for the ion motions. As the ion temperature is lower than T_e , v_{ph}^s will be larger than the ion thermal velocity v_{Ti} and we can apply a

hydrodynamic description for the ion motion. (If $v_{ph}^s \ll v_{Ti}$, one can use the so-called "static" approximation [2].)

For the moment we shall assume that we may linearize the ion equations (see the discussion at the end of this section). We then have

$$\frac{\partial \delta n_i}{\partial t} + n_0 \nabla \cdot \mathbf{v}_i = 0, \quad (1.39)$$

$$\frac{\partial \mathbf{v}_i}{\partial t} = -\frac{e}{M} \nabla \phi_s, \quad (1.40)$$

where we have in the equation of motion omitted the pressure term, since $T_e \gg T_i$ by assumption, and neglecting the direct ion ponderomotive force (as $m/M \ll 1$) in comparison to the ambipolar "electron" force.

If we restrict ourselves to density perturbations for which $n_s \ll n_0$ - which means that we can expand and linearize Eq. (1.36) to obtain

$$\frac{n_s T_e}{n_0} + U_{pond} = e \phi_s, \quad (1.41)$$

while Poisson's equation becomes

$$\nabla^2 \phi_s = 4\pi e (n_s - \delta n_i). \quad (1.42)$$

Combining (1.41) and (1.42) to eliminate ϕ_s we have

$$n_s = \delta n_i + \nabla^2 U_{pond} / 4\pi e^2 + r_{De}^2 \nabla^2 n_s. \quad (1.43)$$

If we further assume that the spatial variations of n_s are on length scales much larger than the Debye radius, we can drop the last term on the right-hand side of Eq. (1.43) to get the departure from the quasi-neutrality, by

$$n_s = \delta n_i + \nabla^2 U_{pond} / 4\pi e^2. \quad (1.44)$$

We can now eliminate n_s and \mathbf{v}_i from (1.39), (1.40), and (1.44) and using Eq. (1.34) we find the familiar, ponderomotively driven ion-sound equation

$$\frac{\partial^2 \delta n_i}{\partial t^2} - c_s^2 \nabla^2 \delta n_i = \frac{1}{4\pi M} \nabla^2 \left(\tilde{\mathbf{E}}_1 \tilde{\mathbf{E}}_1^* \right). \quad (1.45)$$

Let us briefly remind ourselves of a fundamental requirement for the validity of our results [18, 22]. This is the requirement that the distance travelled by an electron during a time ω_p^{-1} is small compared to the characteristic fast timescale length scale k^{-1} , that is,

$$v_s \omega_p^{-1} \ll k^{-1} \quad \text{and} \quad v_1 \omega_p^{-1} \ll k^{-1}, \quad (1.46)$$

we note that we shall allow for v_1 to be more important than v_s , however, by using 1.20 and 1.38 this leads to the condition

$$\frac{W}{n_0 T_e} \ll (kr_{De})^{-2}, \quad (1.47)$$

where W is the energy density in the Langmuir wave.

The condition (1.47) also ensures that one can neglect the effect of electrons trapped in the finite-amplitude, fast time scale electric field of the wave [23]. The trapping is a special case of a strong Landau-like resonant interaction involving strong non-linear electron-orbit modifications. Trapping in spatially localized wavepackets is also negligible for sufficiently broad wavepacket spectra when condition (1.47) is satisfied. We must add that, anyway, trapping is inherently a kinetic effect so that we cannot consider it in the hydrodynamic description used here.

Under additional simplifications our equations will readily reduce to the celebrated Zakharov equations. Namely, by restricting ourselves to the potential electric field, i.e. $\tilde{\mathbf{E}}_1 = -\nabla\varphi$, dropping higher electron nonlinearities on the right hand side of (1.23) and assuming the quasi-neutrality by putting $n_s = \delta n_i$, we obtain a system of two Zakharov equations describing the nonlinear Langmuir waves coupled to the ion sound. These equations have been studied into a great depth, bringing the notion of Langmuir solitons in strong Langmuir turbulence models into focus in numerous analytical, numerical and experimental investigations. By introducing dimensionless units

$$\begin{aligned} r &= \frac{3}{2} r_{De} \sqrt{M/m} r', & t &= \frac{3}{2} (M/m) t', \\ \delta n/n_0 &= \frac{4}{3} (m/M) n, & \varphi &= (T_e/e) \sqrt{12} \varphi', \end{aligned} \quad (1.48)$$

we obtain Zakharov equations in the original form

$$\begin{aligned} \nabla^2 (\varphi_t + \nabla^2 \varphi) - \nabla \cdot (n \nabla \varphi) &= 0, \\ (\partial^2 / \partial t^2 - \nabla^2) \varphi &= \nabla^2 |\varphi|^2. \end{aligned} \quad (1.49)$$

In the one-dimensional case above equations admit the four parameter family of soliton solutions, given by

$$\varphi_x = \sqrt{2(1-\beta^2)} \lambda \operatorname{sech} [\lambda(x - \beta t - x_0)] \exp i [(\lambda^2 - \beta^2/4)t + \beta x/2 + \alpha_0]. \quad (1.50)$$

The type of these solutions is strongly influenced by the soliton velocity β which in physical units is equal to $3v_{Te}k_0r_{De}$, where k_0 is a wavenumber at the maximum in the Langmuir wavepacket spectrum (see Kuznetsov et al. [24],). For a soliton at rest, $k_0r_{De} \ll W/n_0T_e$, the electric field varies monotonically. However, when $(k_0r_{De})^2 \gg W/n_0T_e$, this is an envelope soliton with a quasi-monochromatic carrier frequency. In such a case, one can make a simplification with the slowly time variation of the envelope to arrive at the above set of Zakharov equations. In the static limit ($W/n_0T_e \ll m/M$), the Zakharov system reduce to one equation in a form of the famous nonlinear Schroedinger equation (NLS), [25],

$$\nabla^2 (\varphi_t + \nabla^2 \varphi) + \nabla \cdot (|\nabla \varphi|^2 \nabla \varphi) = 0. \quad (1.51)$$

1.3 Adiabatic Scaling and Spherical Collapse

In this part we investigate the effect of the nonlinear correction terms on the stability of spherical or circular configurations in the three- and two-dimensional cases, respec-

tively. At the end, we shall briefly discuss less symmetrical structures, while more general discussion on wave collapse will be given in a forthcoming chapter.

The spherical collapse was already discussed in Zakharov's original paper [2] but the solutions he considered were criticized by Litvak et al. [26] and by Degtyarev et al. [27]. For the spherically symmetric case Eq. (23) becomes

$$iE_t + \frac{\partial}{\partial r} \left[\frac{1}{r^{d-1}} \frac{\partial}{\partial r} (r^{d-1} E) \right] - nE - \frac{\beta |E|^2 E}{r^2} = 0, \quad (1.52)$$

where we have introduced dimensionless variables by the substitutions given in (1.48). The quantity d is the dimensionality ($d = 1, 2$ and 3) of the system, and β is the dimensionality parameter, given by

$$\beta(d=1) = 0, \quad \beta(d=2,3) = (2/3)^3 m/M. \quad (1.53)$$

The term with β comes from higher electron nonlinearities which thus do not contribute in the one-dimensional case, as was independently confirmed by Kuznetsov [19] and by Khakimov and Tsytovich [16] and Škorić and ter Haar [18] (see also [28]).

In the derivation of Eq. (1.52) we have eliminated $n_s, \mathbf{v}_s, \tilde{n}_2$ and $\tilde{\mathbf{v}}_2$ from Eq. (1.23) by using Eq. (1.30), after integrating over r , Eqs. (1.31), (1.37), and (1.38).

We shall follow the approach used in an earlier paper [21, 18] and for the moment for stationary states represent the density perturbation n as an as yet unspecified function $-Q(|E|^2)$ of the plasmon density $|E|^2$

$$n = -Q(|E|^2). \quad (1.54)$$

Of course, n satisfies the equation

$$n_{tt} - \nabla^2 n = \nabla^2 |E|^2. \quad (1.55)$$

In the static case, where the time-derivative can be neglected we have clearly

$$Q(x) = x. \quad (1.56)$$

Using (1.54) we get Eq. (1.52) simply rewritten in the form

$$iE_t + \frac{\partial}{\partial r} \left[\frac{1}{r^{d-1}} \frac{\partial}{\partial r} (r^{d-1} E) \right] + Q(|E|^2) E - \beta \frac{|E|^2 E}{r^2} = 0. \quad (1.57)$$

Eq. (1.57) has the constants of motion

$$N = \int |E|^2 d^d r, \quad (1.58)$$

the plasmon number, and

$$H = \int \left\{ |\nabla E|^2 - R(|E|^2) + \beta \frac{|E|^4}{2r^2} \right\} d^d r, \quad (1.59)$$

the Hamiltonian. In (1.59) we have $R(|E|^2)$ which is defined by the equation

$$Q(x) = \frac{dR(x)}{dx}. \quad (1.60)$$

We now consider a scaling factor $\lambda(t)$ such that

$$r \rightarrow r/\lambda, \quad E \rightarrow \lambda^{\frac{d}{2}} E, \quad (1.61)$$

this scaling leaves the plasmon number- N (action) invariant and may thus be called to be an adiabatic scaling. The Hamiltonian scales as follows

$$H \rightarrow C \int r^{d-1} dr \left\{ \lambda^2 \left| \frac{1}{r^{d-1}} \frac{\partial}{\partial r} (r^{d-1} E) \right|^2 - \lambda^{-d} R(r^d |E|^2) + \lambda^{d+2} \beta \frac{|E|^4}{2r^2} \right\}, \quad (1.62)$$

where C is a numerical factor depending on the value of d

$$C(d=1) = 1, \quad C(d=2) = 2\pi, \quad C(d=3) = 4\pi. \quad (1.63)$$

If now we assume that

$$\lim_{x \rightarrow \infty} Q(x) \propto x^\nu, \quad (1.64)$$

stability against collapse, that is, as $\lambda \rightarrow \infty$, is guaranteed, if

$$\nu < \sigma + \frac{2}{d} = \nu_{crit}, \quad (1.65)$$

where σ is a constant depending on d

$$\sigma(d=1) = 0, \quad \sigma(d=2,3) = 1. \quad (1.66)$$

Condition (1.65) changes into condition $\nu < \frac{2}{d}$ for the Zakharov equations (see, e.g. [21]) when $\beta = 0$. We also see that in the case (1.56), when $\nu = 1$, the one-dimensional case leads to stationary solutions - which are, of course, the Langmuir solitons - even without the electron nonlinearities. Finally, we note that, if the electron nonlinearities are taken into account, condition (1.65) is satisfied even for two- and three-dimensional plasmas in the case of the ponderomotive force nonlinearity (1.56). In the spherical approximation the corrections due to the higher-order electron nonlinearities thus lead to the possibility of quasi-stationary solutions also in the two- or three-dimensional case. We still need to consider, however, whether the absence of a mathematical singularity also implies the absence of a physical collapse to dimensions of the size of the Debye length, as seems to be the case judging from the experimental results of e.g. Antipov et al.[12] who formed apparently stable structures of the size of several Debye lengths.

In order to study this question we shall simply estimate the magnitude of the extra correction term in Eq. (1.48). As long as $W/n_0 T_e \ll m/M$, we can neglect the n_{tt} term in (1.55) (see [3]) so that (1.56) holds and the self-focusing term in (1.50) is simply $|E|^2 E$. If we require, say, that the correction term is an order of magnitude smaller than the self-focusing term, we have

$$\beta \frac{|E|^2 E}{r^2} \sim \frac{1}{10} |E|^2 E, \quad \text{or } r^2 \sim 10\beta, \quad (1.67)$$

whence, restoring physical dimensions, we get $r \sim 3r_{De}$.

This means that the stabilizing action of the higher-order electron non-linearities does not start to be fully effective until the spherical collapse has already proceeded quite far.

1.4 Qualitative discussion of the collapse

Before discussing the collapse of a caviton structure, that is, a localized Langmuir wave accompanied by a density depression, centred at the origin, we must draw attention that the second term in Eq. (1.50) can be written in the form $\partial^2 E/\partial r^2 + (d-1)r^{-1}\partial E/\partial r - (d-1)E/r^2$, so that the origin is a singular point of that equation, already for $\beta = 0$. One should therefore for the spherical case impose the boundary condition $E(0, t) = 0$. This may have been the reason why Degtyarev et al. [27] considered the spherical collapse of a spherical layer of radius R and thickness δ , with $\delta \ll R$, with a soliton-like field structure in the r -direction. As $\delta \gg r_{De}$, so that a fortiori $R \gg r_{De}$, the evolution of that model will not be affected by our correction term. By the same token, however, it is only possible in this model to study the very early stages of the collapse, as the condition on δ and R will soon be violated.

In the more general case (see also [26] and [29]), we could expect that there will be two regions with different dynamical properties. There will be a "core" region with a radius of the order of a few times r_{De} which is stabilized through the effect of the higher order electron non-linearities, and there will be a "shell" region which collapses towards the center (originally in [18] preceding a notion of "nucleated" collapse by [30]). As the collapse proceeds, the field amplitude increases and the condition necessary for the static approximation to hold will be violated. This means that one should consider the hydrodynamic approximation [3], but that would mean using the full equation (1.55) when W/n_0T_e approaches the value of m/M , but is still below it so that the collapse is subsonic. The self-focusing term will become increasingly important and it will drive the collapse towards the sonic, or even supersonic ($W/n_0T_e > m/M$) regime. The transition to the supersonic regime was subject to a certain amount of controversy (see [31]) as Eq.(1.55) is no longer valid for near-sonic motion. However, numerical experiments [32, 11] seem to indicate, at least for non-dissipative cases, the existence of a supersonic regime. This part of the collapse was a subject of further studies, especially the question whether such a supersonic stage could actually occur in real plasmas.

If (1.50) remains valid during the collapse we may perhaps expect in the later stages of the collapse a hydrodynamic stabilization so that stable spherical cavitons with spatial dimensions of the order of the "core" radius may be formed and these may be the structure seen by Antipov and coworkers. Strictly speaking, as soon as the value of $(W/n_0T_e)(kr_{De})^2M/m$ becomes of the order of unity, corrections to the ion motion will have to be considered ([33] and vide infra) and linearized Eqs. (1.39) and (1.40) must be replaced by the proper non-linear equations [20].

Let us finally briefly consider the general, non-spherically-symmetric case. As compared to the original Zakharov equations, we note that in Eq. (1.16) we have three extra terms. These terms are of the relative order $(kr_{De})^2$ in the static regime, but they may become important when W/n_0T_e becomes larger. For example, in the simple model of a self-similar supersonic collapse [34] we have $n_s/n_0 = \chi(W/n_0T_e)^{2/3}$, where $\chi \sim 0.1$ to 1 and for the relative magnitude of the correction terms we get $(W/n_0T_e)^{1/3}(kr_{De})^2\chi^{-1}$ which shows the possible importance of the correction terms in the hydrodynamic regime.

Chapter 2

Wave Collapse in Plasmas

2.1 Langmuir Soliton Stability and Collapse

A detailed study of the linear stability and nonlinear wave collapse of Langmuir solitons in a weakly magnetized plasma is performed [2]. An analytical investigation of the linear soliton instability with respect to long-wavelength transverse perturbation versus magnetic field effect is presented. For a more complete understanding of the growth-rate structure, a numerical solution of the eigenvalue problem that corresponds to the model equations is obtained and compared with analytical predictions. Comparison with other results is given. Furthermore, numerical results obtained by a direct simulation method in two dimensions are also presented. In a linear regime, detailed agreement with the results of the corresponding eigenvalue problem is found. In the nonlinear regime of the soliton instability all considered cases exhibit a collapse dynamics. Moreover, in the developed, highly nonlinear stage of the soliton collapse, self-similar behavior consistent with a "weak" collapse regime is found [36].

2.1.1 Introduction

One-dimensional stationary localized solitonlike wave structures were expected to be the basic elements of strong plasma turbulence [1, 11, 15, 34, 35]. In one-dimensional systems solitons are often stable, evolving rapidly from an arbitrary initial plasma state, and therefore determining the basic features of the emerging plasma turbulence. However, in real plasmas, as a rule, solitons appear to be unstable with respect to transverse perturbations [6]. In a nonlinear stage of evolution, this instability often leads to a soliton collapse, a unique nonlinear wave phenomenon of the formation of a singularity in a finite time. Accordingly, the appearance of the collapsing nonstationary wave structures (cavities) that exhibit a rapid field growth followed by an intensive spatial localization (self-focusing) results in a qualitative change of the turbulence character [30]. The dispersion relation describing linear Langmuir waves in a weak magnetic field has a form

$$\omega_k = \omega_{pe} \left[1 + \frac{3}{2} k^2 r_{De}^2 + \frac{1}{2} \frac{\omega_{ce}^2}{\omega_{pe}^2} \frac{k_{\perp}^2}{k^2} \right], \quad (2.1)$$

where ω_{ce} and ω_{pe} ($\omega_{ce} \ll \omega_{pe}$) are the electron cyclotron and the electron plasma frequency, respectively, r_{De} is the Debye radius, and k_{\perp} is the wave number component transverse to the magnetic field. It is evident that the transverse perturbation increases the wave frequency and is therefore energetically unfavorable. Accordingly, unstable modes should only correspond to long-wavelength transverse perturbations, with a frequency increase on the order of the instability growth rate. Moreover, a magnetic field increase results in an increase of the frequency of transverse oscillations and appears as a stabilizing factor.

Soliton instability in a weak magnetic field was studied in [37]. It was shown that for moving solitons with a velocity $V/v_{te} > \omega_{ce}/\omega_{pe}$ (v_{te} is the electron thermal velocity) the magnetic field produces no changes in the soliton stability apart from increasing the transverse instability length scales, according to

$$l_{\perp} \sim l_0 \frac{\omega_{ce}^2}{\omega_{pe}^2} \frac{l_0}{r_{De}},$$

where $l_0 \sim (8\pi nT/E_0^2)^{\frac{1}{2}}$, is the soliton characteristic length.

In the opposite limit, the case of a standing soliton ($V = 0$) in the long-wavelength region for the instability growth rate (γ) the following analytical solution of the corresponding eigenvalue problem [30] was obtained

$$\gamma = 2\omega_{pe} \left[\frac{E_0^2}{8\pi nT} [12 - 7\zeta(3)] - \frac{21}{4}\zeta(3) \frac{\omega_{ce}^2}{\omega_{pe}^2} \right] k_{\perp}^2 r_{De}^2, \quad (2.2)$$

where

$$\zeta(x) = \sum_n n^{-x},$$

is Riemann's zeta function.

At first sight, for sufficiently large values ($\omega_{ce}^2/\omega_{pe}^2 > 0.43E_0^2/8\pi nT$) it seems that the magnetic field stabilizes the linear instability. However, instability may reappear if one takes into account the next terms in the expansion in transverse wave number k_{\perp} . The dispersion relation (2.2) in the limit $k_{\perp} \rightarrow 0$, turns into a marginally stable mode corresponding to a small variation of the soliton amplitude. On the other hand, the expression (2.2) by itself does not appear to be sufficiently exact. In the treatment [6, 37], only the first term in the expansion $\gamma(k)$ was calculated. Moreover, the existence and solvability of the perturbation scheme, typically has not been proved, nor was the convergence of the series expansion.

Numerical results obtained by Rowland [38] indicate that the magnetic field is unable to stabilize the soliton instability. Yet, these results were based on a few values of the parameters, so it is unclear if other regions of soliton stability can exist. The influence of the magnetic field on the growth rate structure and on the transverse instability length scales remains a very important issue. These characteristics would give us an opportunity to estimate the parameters of the emerging collapsing Langmuir wave packets. The magnetic field effect on the collapse of Langmuir wave packets for different model equations has been a subject of many studies [39, 40, 41, 42].

In this section, we present a detailed study of the influence of the magnetic field on the soliton stability [36]. First, we formulate the basic model equation and discuss the physical background of the problem. Based on the variational principle, we present an analytical investigation of the growth rate structure in a linear regime for finite values of the transverse perturbation wave number. Then, we give results of the numerical solution of the corresponding eigenvalue problem. We have obtained a complete spectral structure of the growth rate and corresponding eigenfunctions. Somewhat unexpectedly, the calculated form of $\gamma(k)$ does not agree with the analytically obtained equation (1.2). We discuss the possible reason for this discrepancy, mainly due to the inadequate accuracy of the perturbation treatment. Finally, the last part is devoted to the nonlinear stage of the soliton instability which exhibits a soliton collapse. In order to study the magnetic field effect on the nonlinear stage of the soliton instability we show direct numerical simulations in two dimensions (2D). In the linear regime we find detailed agreement with the results of the corresponding eigenvalue problem. In the nonlinear regime all considered cases exhibit collapse dynamics. Moreover, in the developed, highly nonlinear stage of the soliton collapse, self-similar behavior consistent with a "weak" collapse regime is found. This work [36] differs from most of the previous studies [39, 40, 41, 42] on Langmuir collapse in terms of the model equation, initial conditions (soliton) level of nonlinearity and observed phenomena.

2.1.2 Basic Equations

Nonlinear evolution of Langmuir waves in a weak magnetic field is conveniently described by a time averaged dynamical equation for the envelope of the high-frequency Langmuir wave potential ψ , which in dimensionless units [36]

$$t \rightarrow \frac{3}{2} \frac{M}{m} \omega_{pe}^{-1} t, \quad r \rightarrow \frac{3}{2} \left[\frac{M}{m} \right]^{1/2} r_{De} r, \quad \psi \rightarrow \frac{T}{e} (12)^{1/2} \psi,$$

reads

$$\Delta (i\psi_t + \Delta\psi) - \sigma \Delta_{\perp} \psi + \nabla (|\nabla\psi|^2 \nabla\psi) = 0, \quad (2.3)$$

where $\sigma = \frac{3}{4} \omega_{ce}^2 / \omega_{pe}^2 (M/m)$, M and m are as usual the ion and the electron mass, respectively. The external magnetic field \mathbf{B} ($\omega_{ce} \equiv eB/mc$) is in the x - direction while the dimensionless equation (2.3) is valid for $\sigma \ll \frac{3}{4} M/m$. The linear part of (2.1) corresponds to the dispersion relation (1.1) while the nonlinear term is described through a static plasma response to the ponderomotive force action. We assume that the characteristic nonlinear time scales are slower than the ion-sound motions. The above is justified in a small amplitude region $E_0^2 / 8\pi nT < m/M$, i.e. in the subsonic regime.

For a more complete insight into the soliton stability problem and corresponding growth rate structure the inclusion of the ion inertia is essential (see Refs. [39, 40, 41, 42, 43]). As will be seen below, the magnetic field increase results in a growth of transverse perturbation length scales. Under the assumption that the characteristic transverse length scales are sufficiently larger than longitudinal ones, the equation (2.3) substantially simplifies to [43]

$$\frac{\partial^2}{\partial x^2} (i\psi_t + \psi_{xx}) - \sigma \Delta_{\perp} \psi + \frac{\partial}{\partial x} (|\psi_x|^2 \psi_x) = 0. \quad (2.4)$$

As mentioned above, we shall investigate stability of a planar standing soliton, given with the analytical solution of (2.1) and (2.2)

$$\psi_0 = \sqrt{2} \arctan [\sinh (\lambda x)] \exp (i \lambda^2 t), \quad (2.5)$$

where λ is the soliton strength parameter.

We study the stability of (2.3) with respect to small transverse perturbations with a potential $\psi_p = f + ig$, in a form

$$f, g \sim \exp (i \lambda^2 t + \gamma \lambda^2 t + ik \lambda y), \quad k \equiv k_{\perp} / \lambda.$$

Linearizing (2.1) on the background of the soliton (2.3) and taking scaling transformation $x \rightarrow x \lambda$, and $\sigma \rightarrow \sigma / \lambda^2$, we obtain

$$\begin{aligned} & \gamma \left[\frac{d^2}{dx^2} - k^2 \right] f + \\ & \left[\frac{d^4}{dx^4} - (1 + 2k^2) \frac{d^2}{dx^2} + k^2 (1 + \sigma + k^2) - \frac{2k^2}{\cosh^2 x} + \frac{d}{dx} \frac{2}{\cosh^2 x} \frac{d}{dx} \right] g = 0, \end{aligned} \quad (2.6)$$

$$\begin{aligned} & - \gamma \left[\frac{d^2}{dx^2} - k^2 \right] g + \\ & \left[\frac{d^4}{dx^4} - (1 + 2k^2) \frac{d^2}{dx^2} + k^2 (1 + \sigma + k^2) - \frac{2k^2}{\cosh^2 x} + \frac{d}{dx} \frac{6}{\cosh^2 x} \frac{d}{dx} \right] f = 0. \end{aligned}$$

The increment γ (growth rate) of an instability is given by the eigenvalues of the equation (2.4) corresponding to the spatially localized eigenfunctions.

In the literature there exist some standard methods of solving for $\gamma(k)$, in the long-wavelength limit, based on the local proximity of the eigenfunctions (2.4) for neutrally stable perturbations [6]. It is evident that odd and even (with respect to x) solutions of (2.4) can be treated independently. Odd modes (antisymmetric) correspond to marginally stable soliton deformations in the longwavelength region. However, for even (symmetric) modes in Ref. [37], the following analytical solution was obtained:

$$\gamma^2 = 2k^2 [12 - 7\zeta(3) - 7\sigma\zeta(3)]. \quad (2.7)$$

Due to instability the soliton is split into a number of wave packets that each exhibit a local growth of the amplitude. From the expression (2.5) it seems that for sufficiently large values of σ ,

$$\sigma > \frac{12 - 7\zeta(3)}{7\sigma\zeta(3)},$$

the magnetic field can stabilize the instability. However, as already mentioned, in a real situation this might not occur. Namely, the instability may reappear in the calculations if one takes into account the next terms in the expansion in k . It seems that standard analytical methods do not appear to be successful in that case. Therefore, we shall try to investigate the structure of the growth rate $\gamma(k)$ for finite values of k by applying an approximative variational method.

2.1.3 Variational Treatment of Soliton Stability

A basic idea of an approximative "brute force" treatment of a soliton instability in its nonlinear stage (see Trubnikov et al., [44] and references therein) is as follows. Equation (2.1) can be obtained by the variational principle [36]

$$\Delta S = 0, \quad (2.8)$$

where S is the action defined by

$$S = \int \int \left[\frac{i}{2} (\nabla \psi \nabla \psi_t^* - \nabla \psi^* \nabla \psi_t) + |\Delta \psi|^2 + \sigma |\nabla_{\perp} \psi|^2 - \frac{1}{2} |\nabla \psi|^4 \right] d\mathbf{r} dt. \quad (2.9)$$

Let us substitute ψ in (2.9) as a set of trial functions with varying parameters. In our case we chose ψ in the following form:

$$\psi_0 = \sqrt{2} \arctan \{ \sinh [\lambda (y, t) x] \} \exp [-i\varphi (y, t)], \quad |\lambda_{t,y}| \ll |\varphi_{t,y}|. \quad (2.10)$$

Accordingly, Eq. (2.9) reduces to a much simpler system of differential equations for λ and φ , which can be treated by standard analytical methods. However, the success of the above procedure essentially depends on our choice of trial functions. As already mentioned, an unstable mode appears as a local modulation of the soliton amplitude and phase. Our chosen trial function corresponds to such type of perturbation and should in a long-wavelength limit recover expression (2.7).

We substitute the trial function (2.10) into the action S , where after a straightforward procedure we obtain

$$\begin{aligned} S = \int \int \left[4\lambda\varphi_t - \frac{4}{3}\lambda^3 + 24\varphi_y^2\lambda - (\lambda_y\varphi_{yt}\lambda^{-2} - \varphi_y\lambda_{yt}\lambda^{-2} \right. \\ \left. - 2\varphi_y^2\varphi_t\lambda^{-1} - 2\varphi_{yy}^2\lambda^{-1} - 2\sigma\varphi_y^2\lambda^{-1} - 2\lambda_{yy}\varphi_y^2\lambda^{-2} \right. \\ \left. + 4\varphi_y\varphi_{yy}\lambda_y\lambda^{-2} - 2\varphi^4\lambda^{-1} \right) I_0 + 4\lambda_{yy}^2\lambda^{-2} I_2 \right] dy dt, \end{aligned} \quad (2.11)$$

where

$$I_0 = \int_0^{\infty} [\arctan(\sinh x) - \pi/2]^2 dx, \quad I_2 = \int_0^{\infty} \frac{x^2}{\cosh^2 x} dx.$$

By varying the functional S over σ and λ , it is possible to derive a system of two equations (if the initial function was appropriately chosen). We limit ourself to check if in a long-wavelength limit ($k \rightarrow 0$) of the linearized version of equations $\Delta S/\Delta\varphi = 0$, and $\Delta S/\Delta\lambda = 0$, one can recover the results of [37]. By linearizing the equations $\Delta S/\Delta\varphi = 0$, and $\Delta S/\Delta\lambda = 0$, on the background of the stationary solutions $\varphi_0 = t\lambda^2$, $\lambda_0 = const$, $\varphi = \varphi_0 + \Delta\varphi$, $\lambda = \lambda_0 + \Delta\lambda$, we get

$$-4\Delta\lambda_t - 48\lambda_0\Delta\varphi_{yy} - (2\lambda_0^{-2}\Delta\lambda_{yyt} + 4\lambda_0\Delta\varphi_{yy} + 4\lambda_0^{-2}\Delta\varphi_{yyy} - 4\sigma\lambda_0^{-1}\Delta\varphi_{yy})I_0 = 0, \quad (2.12)$$

$$4\Delta\varphi_t - 8\lambda_0\Delta\lambda + 2\lambda_0^{-2}I_0\Delta\varphi_{yyt} + 8\lambda_0^{-3}I_2\Delta\lambda_{yyy} = 0. \quad (2.13)$$

For perturbations in a form $\Delta\lambda, \Delta\varphi = \exp(\gamma t + ik y)$, after simple calculations we obtain the formula for $\gamma(k)$ as

$$\gamma^2(k) = 2 \frac{[12\lambda_0^2 - 7(\lambda_0^2 + \sigma)\zeta(3)]k^2 + 7\zeta(3)k^4}{[1 + \frac{7}{2}\zeta(3)k^2\lambda_0^{-2}]^2}. \quad (2.14)$$

It is evident that in a long-wavelength limit our result (2.14) agrees with (2.7). However, it is also obvious that the instability may reappear if we take into account the higher order terms in k . The maximum growth rate depends only weakly on σ . Accordingly, generally taken, in the framework of Eq. (2.3) the magnetic field does not stabilize the soliton stability. However, based on (2.14) for sufficiently strong magnetic fields, islands (regions) of stability around

$$\sigma = \frac{12 - 7\zeta(3)}{7\zeta(3)} \lambda_0^2,$$

should exist.

We have already emphasized that the accuracy of the above-noted variational treatment critically depends on our choice of trial functions. This procedure seems convenient to predict the rough qualitative features of the instability increment, however, hardly adequate enough to describe the fine structure of the eigenmode corresponding to (2.7). Therefore, to single out the detailed structure of the instability increment, we shall have to numerically solve the eigenvalue problem (2.6).

2.1.4 Numerical Treatment

In order to find a detailed structure of the instability increment $\gamma(k)$ it is necessary to calculate a set of eigenfunctions which vanish at infinity with the corresponding eigenvalues for γ , for different values of the perturbation wave number k and the magnetic field σ . As mentioned above, unstable modes, at least in the long-wavelength limit, correspond to a symmetric (even) type of the electric field perturbations. Accordingly, the electric potential perturbations are antisymmetric. This situation enables us to solve the system (2.6) in the interval $[0, \infty)$ with the boundary conditions [36]

$$\left. \frac{d^4 \Delta\psi}{dx^4} \right|_{x=0} = \left. \frac{d^2 \Delta\psi}{dx^2} \right|_{x=0} = 0, \quad \Delta\psi = f + ig. \quad (2.15)$$

Further, based on (2.6) the following condition is automatically satisfied:

$$\Delta\psi|_{x=0} = 0.$$

In order to find spatially localized (vanishing at infinity) solutions which satisfy (2.15) we have adopted the following method. On the right-hand side (r.h.s.) of the interval $[0, R]$, $R \gg 1$, for given k , we assume the following asymptotic solution of (2.6):

$$\Delta\psi = f + ig = C_1 \exp(k_1 x) + C_2 \exp(k_2 x), \quad (2.16)$$

where C_1 and C_2 are the arbitrary complex constants. By making use of (2.16) as boundary conditions for (2.6) it is possible to solve the system (2.6) as a Cauchy problem and to calculate the eigenfunction $\Delta\psi$ and its derivatives at the l.h.s. of the interval (at $x = 0$). As a next step, we shall define an auxiliary function $F(\gamma, C_1, C_2)$ in the following way:

$$F(\gamma, C_1, C_2) = [f^2(0) + f_{xx}^2(0) + f_{xxxx}^2(0) + g^2(0) + g_{xx}^2(0) + g_{xxxx}^2(0)]^{1/2}.$$

If F revolves at a zero point, then the obtained functions $f(x)$ and $g(x)$ appear to be the eigenfunctions and $\gamma(k)$ the corresponding eigenvalue of the system (2.6), with boundary

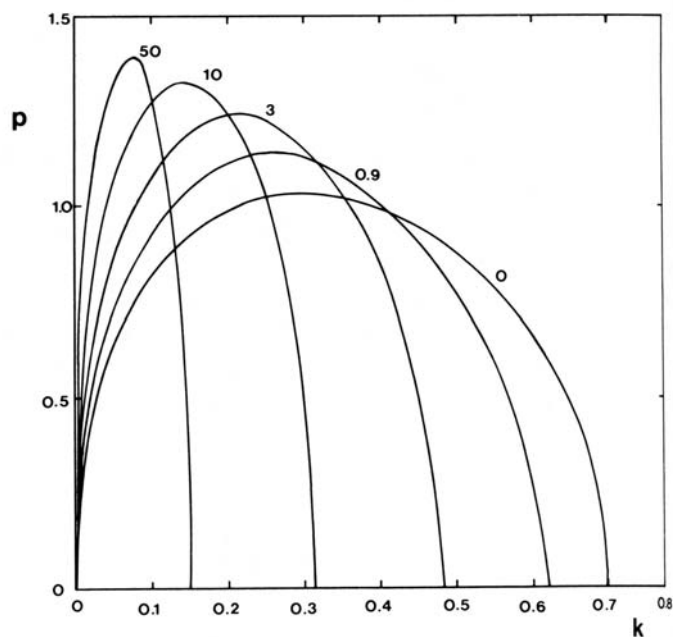


Figure 2.1: Linear growth rate (p) versus transverse perturbation wavenumber (k) for different magnetic field strengths (σ): 0, 0.9, 3, 10, and 50, [36].

conditions (2.15) and (2.16). The function F depends on five independent parameters. Based on a linearity of (2.6) it is possible to fix one of them, e.g., $ImC_1 = 1$. By varying the remaining parameters we look for a minimum of the function F . The minimization is performed by the method of steepest descent, starting with arbitrary values of γ_0 , C_1^0 and C_2^0 . Typical maximum values for f and g were equal or larger than unity. The procedure was terminated when the value of F became smaller than 10^{-3} . In order to perform calculations in the small k region, with the slowly decaying asymptotic solutions, we have chosen a substantially larger interval of calculations $R = 8$.

It has been proved that for all considered initial states a single minimum of F exists being independent on the initial conditions. Therefore, in Fig.(2.1), we plot the calculated spectrum $\gamma(k)$ for different values of σ . It is evident in (Fig.2.1), that the magnetic field increase results in a continuous change of $\gamma(k)$; its maximum shifted to the longwavelength region while the maximum value weakly increases with σ . Accordingly, the magnetic field increase leads to a growth of the transverse perturbation scale length. For larger values of l_{\perp}/l_{\parallel} , i.e., for larger magnetic fields σ , which corresponds to Eq. (2.4) the spectral dependence $\gamma(k)$ on the magnetic field strength appears to be universal:

$$\gamma(k, \sigma) = \gamma(k\sqrt{\sigma}). \quad (2.17)$$

Our calculations indicate that the transition to this universal behavior (2.17) already appears at $\sigma \sim 10$.

It is a very important fact that the numerically calculated spectral dependence differs qualitatively from the analytical formulas obtained above. Namely, numerical results

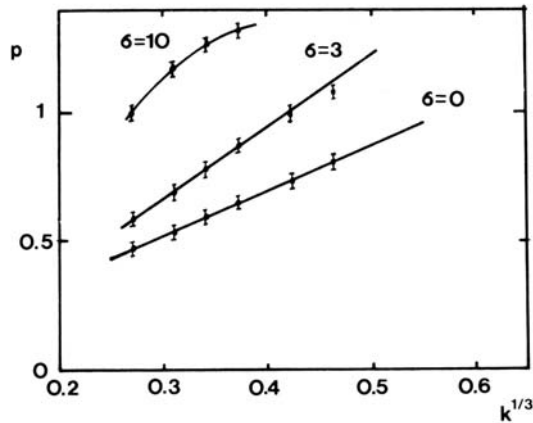


Figure 2.2: Linear growth rate as a function of transverse perturbation wavenumber ($k^{1/3}$) for magnetic field strength: 0, 3, and 10, [36].

show that the magnetic field increase does not produce an island of stability near $k = 0$; i.e., instability exists in the entire interval between $k = 0$ and the cutoff (critical) value $k = k_c$. On the other hand, the spectral structure of the growth rate in the small k region considerably differs from the analytically predicted dependence $\gamma(k) \sim k$, exhibiting a nonlinear behavior according to $\gamma(k) \sim k^{1/3}$ (see Fig.2.2).

The above situation convinces us that the formulation of the perturbation theory for the plasma soliton stability proposed in Refs. [6] and [37] does not appear to be sufficiently accurate. As an additional check of this problem we have performed further investigations in the region $k \rightarrow 0$. It seems obvious that for $k = 0$ and $\gamma = 0$, neutrally stable perturbations correspond to infinitely small variations of the soliton parameters. Accordingly, the eigenfunctions f and g of a symmetric type turn out to be

$$f = 0, \quad g = \sqrt{2} \arctan(\sinh x). \quad (2.18)$$

Our numerically calculated solutions, as $k \rightarrow 0$, continuously assume the form of (2.18).

Furthermore, we study the spectral behavior near the cutoff value k_c . Solutions of the eigenvalue problem (2.6) for $k \neq 0$ and $\gamma = 0$ were obtained in an independent way. It appears that two types of solutions exist. The first one, with the critical (cutoff) wave number $k_c = 1 - \sigma$, if $k \neq k_c$, turns into a stable mode ($\gamma^2 < 0$). The second type corresponds to an unstable branch (for $\sigma = 0$ and $k_c \simeq 0.7$) with a continuous transition for $k \neq k_c$, to a solution of the complete system (2.6).

In order to check the accuracy of our numerical method we have investigated the soliton instability in the framework of the nonlinear Schrodinger (NLS) equation. The calculated spectral form of $\gamma(k)$ coincides with the one found in [45]. In the case of the NLS equation, the soliton stability problem for a small k is solvable with the perturbation theory [6] to any order of expansion, therefore $\gamma \sim k$ for $k \rightarrow 0$, as was confirmed in our calculations.

Moreover, we have attempted to construct a novel analytical perturbation scheme which for $k \rightarrow 0$ could correctly recover the results of the above numerical calculations.

We look for a solution of (2.6) in a form of series expansion for a small k values [36],

$$\begin{aligned}\gamma &= Ak^{1/3} + \dots, \\ g &= g_0 + k^{2/3}g_{2/3} + k^{4/3}g_{4/3} + \dots \equiv g'_0 + g'_{2/3} + \dots, \\ f &= k^{1/3}(f_{1/3} + k^{2/3}f_{3/3} + k^{4/3}f_{5/3} + \dots) \equiv f'_{1/3} + f'_{3/3} + f'_{5/3} + \dots\end{aligned}\tag{2.19}$$

In the first order of the perturbation theory we get

$$\frac{d}{dx}H_+ \frac{d}{dx}f'_{1/3} = \gamma \frac{d^2}{dx^2}g'_0.\tag{2.20}$$

Further, to successive orders one obtains

$$\begin{aligned}\frac{d}{dx}H_- \frac{d}{dx}g'_{2/3} &= -\gamma \frac{d^2}{dx^2}f'_{1/3}, \\ \frac{d}{dx}H_+ \frac{d}{dx}f'_{3/3} &= \gamma \frac{d^2}{dx^2}g'_{2/3}, \\ \frac{d}{dx}H_- \frac{d}{dx}g'_{4/3} &= -\gamma \frac{d^2}{dx^2}f'_{3/3}, \\ \frac{d}{dx}H_+ \frac{d}{dx}f'_{5/3} &= \gamma \frac{d^2}{dx^2}g'_{4/3},\end{aligned}\tag{2.21}$$

where

$$\begin{aligned}H_+ &= \frac{d^2}{dx^2} - 1 + \frac{6}{\cosh^2 x}, \\ H_- &= \frac{d^2}{dx^2} - 1 + \frac{2}{\cosh^2 x}\end{aligned}$$

Finally, at the sixth order, we shall come across the terms proportional to k^2 .

$$\frac{d}{dx}H_- \frac{d}{dx}g'_{6/3} + k^2 \left[-\frac{d^2}{dx^2} + \sigma - 1 + \frac{2}{\cosh^2 x} \right] g_0 + \gamma \frac{d^2}{dx^2}f'_{5/3} = 0.\tag{2.22}$$

In that way, so far as $f'_{5/3} \sim k^5$, we have constructed the perturbation scheme for which $\gamma \sim k^{1/3}$. Although operators H_+ and H_- and their inverse counterparts are well defined, a fact that, in principle, should allow the derivation of $f'_{5/3}(x)$, the proof of the convergence of the above perturbation scheme is rather complex. A particular point lies in the fact that the expansion for a small k is justified only in the region $|x| \ll 1/k$. This is connected with a slow decay of the solution of the complete system (2.6) $f, g \sim \exp(-kx)$. Naturally, this was a reason why we try to check the proposed scheme upon our numerical calculations. It is evident from Fig.2.2, that the dependence $\gamma \sim k^{1/3}$ is obeyed with a high degree of accuracy for small k values. The deviation from the above dependence, for large σ , comes from the fact that in this case, as $\gamma = f(k\sqrt{\sigma})$, the expansion is justified for substantially smaller values of k . In Fig.2.3 we plot the dependence of $dg/dx|_{x=0}$ and $df/dx|_{x=0}$ on $k^{1/3}$. As expected from the expansion (2.19), $g_x(0) = \text{const.}$ and $f_x(0) = Bk^{1/3}$. In this way, our numerical results give strong support for the proposed perturbation scheme.

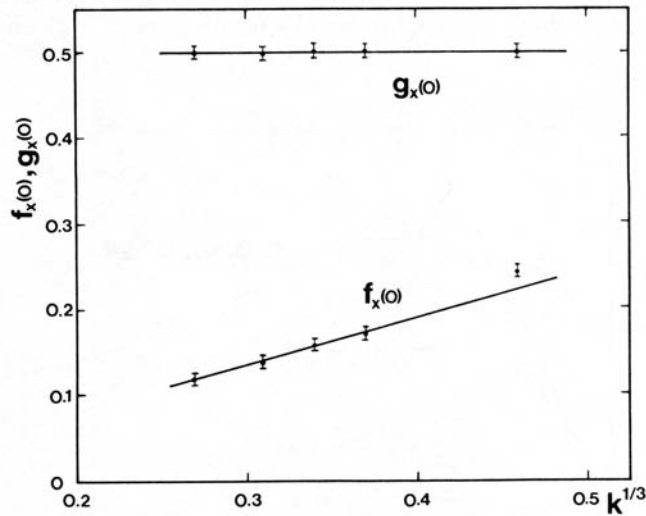


Figure 2.3: Spatial derivatives of eigenfunctions (f, g) at $x = 0$ as a function of transverse perturbation wavenumber ($k^{1/3}$), [36].

2.1.5 Nonlinear Stage of Soliton Instability

Further, we discuss a nonlinear stage of the soliton instability. In an isotropic plasma, in a linear regime, this instability results in a transverse modulation of the Langmuir soliton amplitude. The nonlinear growth of the perturbation can lead to a soliton breakup into a number of collapsing wave packets (Langmuir caviton) [46]. Therefore, in our problem, it is expected that the magnetic field can substantially affect this nonlinear stage of the soliton instability (see Refs. [39, 40, 41, 42, 43]).

In Fig.2.4 we plot the eigenfunctions of the system (2.4) calculated above that correspond to the maximum linear growth rate for different values of the magnetic field. It is evident that the increase of σ does not bring a qualitative change in a structure of the growing perturbations. Therefore, it seems reasonable to expect that the magnetic field growth just increases the transverse length scales of the wave packet leaving all basic qualitative features of the collapse process preserved.

In order to investigate the soliton instability, in particular, in its highly nonlinear stage, we have further performed a direct numerical simulation of Eqs. (2.3) and (2.4) in two dimensions ($2D$). We have used the spectral Fourier method with respect to the space coordinates with an explicit time integration scheme. The instability development was studied by imposing initial conditions in a form of the standing planar soliton (2.3) periodically perturbed in a transverse direction. For sufficiently large values of σ computations based on (2.1) and (2.2) produce very close results.

Moreover, direct simulations results are checked upon those obtained in the previous section. In the initial stage, when instability exhibits an exponential growth of the perturbation, we have chosen sufficiently small initial perturbation levels. We have used periodic boundary conditions (L_x, L_y), a numerical grid of 64×64 (checked upon 128×128

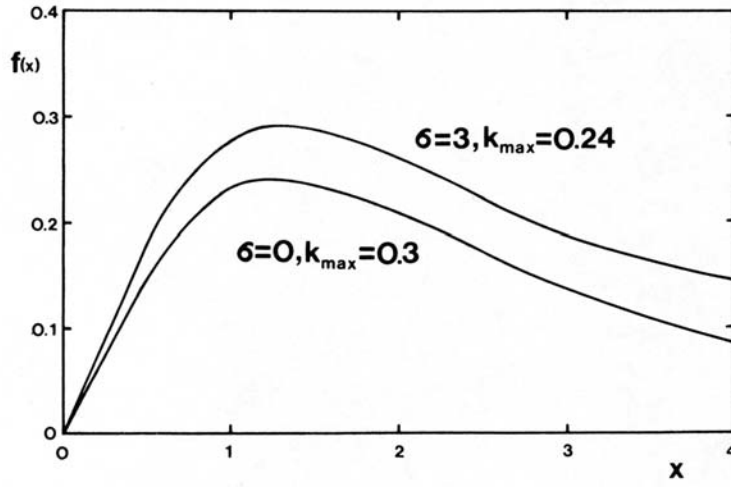


Figure 2.4: The eigenfunctions (f, g) for $\sigma = 0$ and $\sigma = 3$, [36].

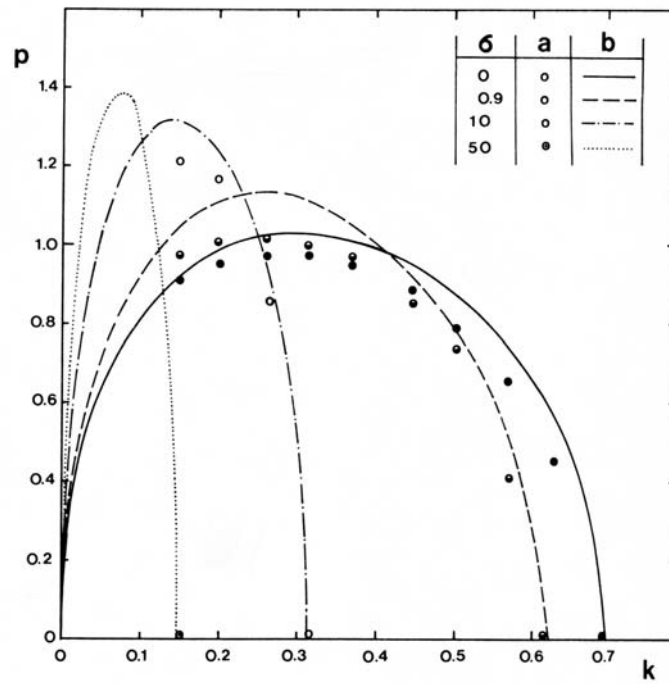


Figure 2.5: Linear growth rate (p) versus transverse perturbation wavenumber (k) for different magnetic field strengths (σ): 0, 0.9, 10, and 50. a) direct 2D simulation, b) solution of the spectral problem, [36].

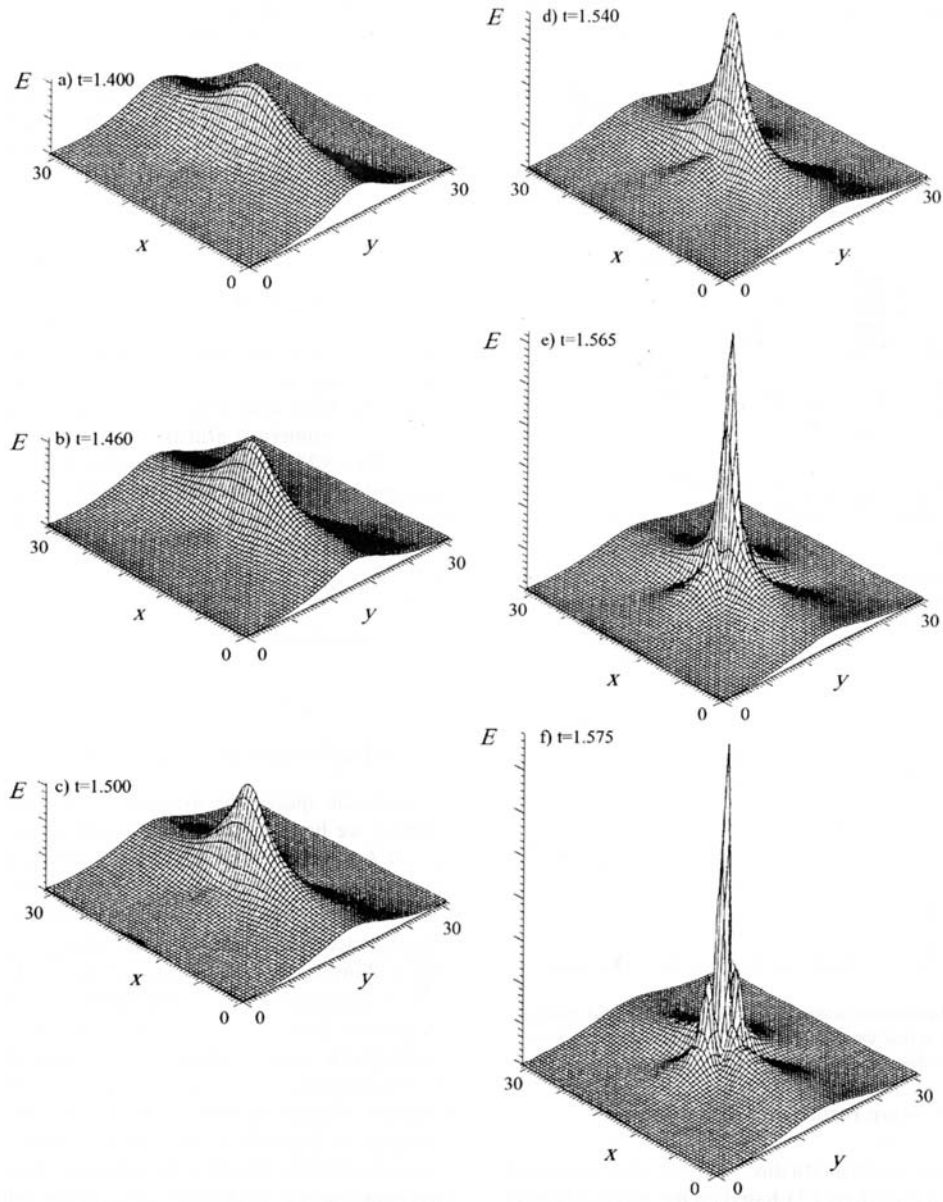


Figure 2.6: Time snapshots of the 2D soliton electric field amplitude ($E(x, y)$) during Langmuir collapse. Initial soliton strength is $\lambda = 5$ and $\sigma = 10$, [36].

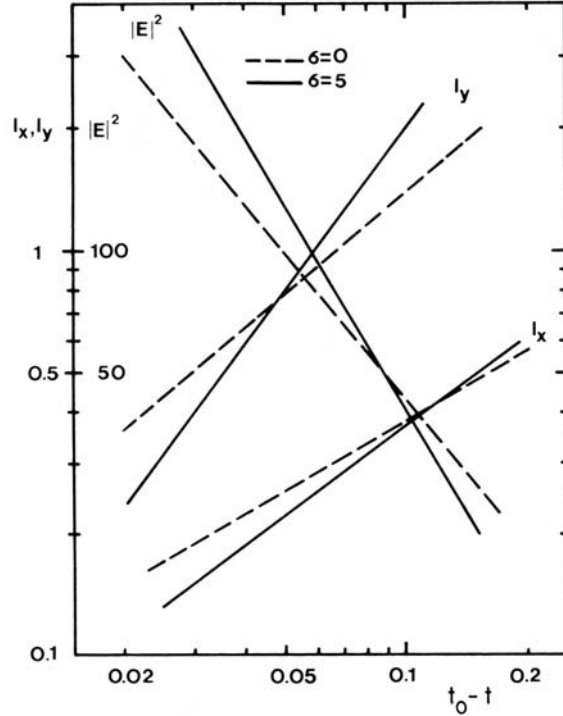


Figure 2.7: Characteristic spatial scales (l_x, l_y) and the maximum electrostatic energy density ($|E|^2$) as a function of a time interval to the collapse time ($t - t_0$). Dashed lines denote $\sigma = 0$ and solid line denote $\sigma = 5$, [36].

points, a time step of 0.001 and the perturbation level $\epsilon = 0.01$, with regularly checking the conserved integrals of (2.3) and (2.4), i.e., the plasmon number (N) and the Hamiltonian (H). In contrast to a work of Pereira, Sudan, and Denavit [46], our perturbation level ϵ was decreased [36] until the growth rate γ has become independent on ϵ . We have performed runs with different values for k and σ . However, in the range of small perturbation wave numbers ($k < 0.2$) a care must be taken, since the grid resolution can be insufficient for accurate calculations. In Fig.2.5, we compare the direct simulation results for $\gamma(k)$ with the results of numerical solutions of the eigenvalue problem (2.6). As seen on inspection the results of these two essentially independent methods of solution show satisfactory agreement. In particular, the results coincide for the values near to the cutoff wave numbers. The direct simulation results have confirmed that all linearly unstable solitons, independent of the magnetic field strength and the perturbation wave number, in their nonlinear stage enter a collapse phase. This result is consistent with e.g. work of Goldman et al. [39, 40] related to the collapse of Langmuir wave packets in a weak magnetic field with full ion dynamics. In order to illustrate this, we show typical time snapshots in Fig.2.6, of the early collapse, which exhibits the basic collapse features: the initial localization, subsequent explosive amplitude growths connected with a rapid contraction of the spatial dimensions resulting in large wave energy density. The earlier results on soliton break up and subsequent collapse in an unmagnetized plasma [46, 47] were readily recovered in our simulations for $\sigma = 0$.

An important characteristic of the collapsing wave packet is its elongation (Fig.2.7) i.e., the aspect ratio l_x/l_y . This quantity defines the energy content trapped inside the cavity, which is of considerable importance concerning the final collapse stage and the ultimate energy dissipation. Generally taken, there possibly exist solutions with a various degree of elongation [48, 36], that are also depending on the way they were initially formed.

2.1.6 Self-similarity and collapse regimes

Let us further discuss a highly nonlinear, developed stage of the collapse. A general scenario was proposed in the early work of Krasnosel'skikh and Sotnikov [43] which was based on an analytical study of a version of Eq. (2.4), which takes into account a full ion inertial response. The above is necessary in the so-called supersonic regime ($E_0^2/8\pi nT > m/M$) of the magnetized Langmuir wave collapse.

In the early stage of the soliton collapse, as long as $\omega_{ce}/\omega_{pe} \gg kr_{De}$, the transverse dimensions of the collapsing wave packet are substantially larger than the longitudinal ones, forming a highly elongated, dipole field structures. During the collapse process the transverse length scale of the cavity decreases more rapidly than the longitudinal one and therefore, when $kr_{De} \sim \omega_{ce}/\omega_{pe}$, two scales become of the same order. Accordingly, in the later stage, the magnetic field was not expected to influence the collapse development [43]. However, it is still believed that in the final collapse stage magnetic field can possibly make an effect on the cavity structure and its energy content. Indeed, our simulations seem to point in the same direction (vide infra), i.e., that in the final stage, the cavity form and the trapped energy depend on the magnetic field strength.

Further, we investigate the possible self-similar time behavior of the wave collapse process in its developed stage, following Hadžievski et al., [36]. Studies of the wave collapse have shown that a collapse process, as a unique nonlinear phenomenon of the formation of a singularity in a finite time, can be developed through two different collapse regimes: *weak* and *strong*. Originally, Zakharov and Kuznetsov [49] for the NLS equation, followed by Kuznetsov and Škorić [50] for the nonlinear upper-hybrid and lower-hybrid waves have shown that during the strong collapse regime the trapped wave energy through the collapse stage remains finite and the wave radiation from the cavity is absent. On the other hand, in the weak regime, which formally preserves zero energy into the final collapse stage, wave radiation is present. In the framework of Eq. (2.4) it has been shown that two regimes, weak and strong, exist. Both regimes near the singularity can be described by a general self-similar ansatz in the form [36]

$$\psi(\mathbf{r}, t) \rightarrow \frac{1}{(t_0 - t)^{a+ip}} f \left[\frac{z}{(t_0 - t)^b}, \frac{\mathbf{r}_\perp}{(t_0 - t)^c} \right], \quad (2.23)$$

where a, b, c , and p are the real parameters. This means that the cavity dimensions scale as

$$l_z \simeq (t_0 - t)^b, \quad l_\perp \simeq (t_0 - t)^c. \quad (2.24)$$

The number of waves localized in the cavity (N^{cav}) depends on time (in two dimensions) as

$$N^{cav} = \int \left| \frac{\partial \psi}{\partial x} \right|^2 d\mathbf{r} \sim (t_0 - t)^{2a-b+c}, \quad 2a - b + c \geq 0, \quad (2.25)$$

where for a strong collapse N^{cav} should remain constant, while for a weak collapse N^{cav} goes to zero as collapse reaches the singularity.

We shall return to the detailed classification of strong and weak collapse regimes in the next section, while here we just focus on the early collapse stage for $\omega_{ce}/\omega_{pe} \gg kr_{De}$. In this case, a simplified version of the nonlinear equations (2.4) is appropriate which accepts the following self-similar substitution [43]

$$\psi(\mathbf{r}, t) \rightarrow \frac{1}{(t_0 - t)^{ip}} f \left[\frac{z}{(t_0 - t)^{1/2}}, \frac{\mathbf{r}_\perp}{(t_0 - t)} \right], \quad (2.26)$$

where the corresponding cavity dimensions scale like

$$l_z \simeq (t_0 - t)^{1/2}, \quad l_\perp \simeq (t_0 - t).$$

However, the above self-similar ansatz describes the *weak* collapse process with a cavity plasmon number (N^{cav}) which decreases in time as

$$N^{cav} = \int \left| \frac{\partial \psi}{\partial x} \right|^2 d\mathbf{r} \sim (t_0 - t)^{1/2},$$

in the $2D$ case.

The numerical simulation of an axially symmetric version of the Krasnosel'skikh equation presented by Lipatov [48] supported the above general picture. However, conclusions concerning the late collapse stage, when the disappearing magnetic field effect supposedly switches the collapse to an isotropic type of evolution, are somewhat of a speculative nature.

In order to check the self-similar character of the collapse evolution consistent with (2.23) based on our $2D$ numerical simulation results, we vary t_0 to find the best fit for the time evolution of the maximum electric field amplitude, for different values of the magnetic field $\sigma = 0, 5, 10,$ and 15 . From (2.23), the maximum electric field amplitude squared, scales like

$$|E_{\max}|^2 \sim \frac{1}{(t_0 - t)^\alpha}, \quad \alpha = 2a + 2b. \quad (2.27)$$

Our results indicate that the self-similar evolution is exhibited also for smaller values of σ including $\sigma = 0$, with a slope $\alpha = 1.2$, which is in agreement with the results of Pereira et al. [46]. For $\sigma = 15$, they come close to the analytical predictions [50] for ($\alpha = 2$) based on Eq. (2.4). In Fig. 7, we plot in a double-logarithmic scale, the time variation of the maximum amplitude (2.27) and characteristic spatial dimensions of the collapsing cavity for $\sigma = 0$ and $\sigma = 5$. The self-similar behavior is evident, although with a changing slope:

$$\alpha_0 \simeq 1.20 \quad (\sigma = 0), \quad \alpha_5 \simeq 1.74 \quad (\sigma = 5).$$

Transverse length scales grow faster than longitudinal ones, resulting in that the initial dipole field structure tends to symmetrize. The above process gets more pronounced with the magnetic field increase. By calculating the parameters $a, b,$ and c from Fig.2.7, we

readily find the time dependence of the plasma number (N^{cav}), which based on (2.25) turns out to decrease in time, as

$$N_0^{cav} \sim (t_0 - t)^{0.20}, \quad N_5^{cav} \sim (t_0 - t)^{0.36},$$

which defines a *weak* type of collapse.

However, the self-similar features of the described collapse processes, were studied in a time interval restricted to an increase of the energy density of just up to two orders of magnitude. Therefore, the later stages of the collapse, closer to the singularity, could exhibit somewhat altered type of dynamics. As a general picture, our simulations indicate an early collapse development corresponding to a weak collapse regime. Possibly, this comes from the fact that in order to approach other, the so-called (ultra) strong collapse regime, much larger inertial interval seems necessary.

The energy content of the collapsing wave structure is of a considerable physical interest. Namely, the results indicate an altered effective absorption rate, i.e.,

$$[(k_0 r_{De}) / (\omega_{ce} / \omega_{pe})]^{1/2} \sim (E_0^2 / 8\pi nT)^{1/2} \omega_{pe} / \omega_{ce},$$

times the absorption rate for an isotropic plasma, corresponding to the increased level of the strong Langmuir turbulence. Still, a need for an experimental insight in such physical situation is of a great importance.

Subsequently, it was understood that the ultimate "burn out" process of the collapsing wave packets is expected to dissipate a finite amount of the wave energy. Namely, the structure of the weak collapse (conserving zero energy) seemed to indicate that the final stage should allow only an infinitely small value of the dissipated energy. However, in reality one expects a different situation. Further refinements in the wave-collapse theory [30], have indicated a possibility of a collapse process formed as a long-living spatially localized narrow core (hot spot) close to a singularity, which entrains the wave energy from the surrounding region ("black hole" effect). Such an effect was variably named as a "funnel effect" [30], "nucleation" or "distributed collapse" [51]. Accordingly, in our case, the solution (2.23) could supposingly be valid only in a thin region close to the singularity. At larger distances, different type of a solution could be formed providing a continuous energy influx into the singularity. More simply, in such a weak collapse dynamics a type of a "funnel" is formed entraining the energy from the outer regions.

For the Eq. (2.6) this funnel looks as an anisotropic structure. Anisotropic bi-self-similar collapse solution [52] describing a finite energy capture into an anisotropic funnel has been also predicted.

2.2 Virial Theory of Wave Collapse

The virial theorem of collapse of the large amplitude Langmuir wavepacket is proved, in a model of Zakharov equations which in the static limit reduce to the nonlinear Schroedinger equation (see, an extensive review, [25]).

The problem of plasma turbulence is of great interest both from a theoretical point of view, and from an experimental one for laboratory, fusion and astrophysical plasmas

(see, reviews [11, 34, 35], and references therein). The simplest case is that of Langmuir turbulence in an unmagnetized plasma which has been studied extensively, especially the transition from weak to strong turbulence in which the parametric modulational instability (MI), first suggested by Vedenov and Rudakov [7] and by Gailitis [8], plays a major role. In two- or three-dimensional plasmas the MI ultimately leads to Langmuir collapse [2], that is to the formation of cavitons - localized intense Langmuir wavepackets in regions of lowered plasma density - which appear unstable and can possibly collapse to the physical dimensions of a few Debye radii, when Landau damping becomes important. It should be borne in mind, however, that the Zakharov equations which describe the collapse, cease to be valid much before this final stage is reached. These equations are usually derived [2, 3, 18] on a two-fluid and two-timescale basis and they describe the evolution of nonlinear Langmuir waves coupled to ion sound by the ponderomotive force. It is the present aim to discuss the collapse dynamics of Langmuir waves and, by means of a general virial theorem, presented by Goldman and Nicholson [33], prove the condition for collapse existence. We only give an outline of our reasoning; with full details available elsewhere [2, 3, 33, 256].

We consider a hot, collisionless, uniform, non-isothermal ($T_e \gg T_i$) plasma, for nonlinear Langmuir modes with frequencies $\sim \omega_0$ close to ω_{pe} . We follow the procedure by using the standard time-averaging over the fast Langmuir wave period scale [2, 3, 256] to derive the following set of Zakharov equations for the Langmuir waves nonlinearly coupled to ion sound waves, which in the vector form, read [2, 256],

$$i\frac{\partial \mathbf{E}}{\partial t} + \frac{3}{2}\omega_0 r_{De}^2 \nabla (\nabla \cdot \mathbf{E}) - \left(\frac{c^2}{2\omega_0}\right) [\nabla \times [\nabla \times \mathbf{E}]] = \frac{1}{2}\omega_0 \left(\frac{\Delta n}{n_0}\right) \mathbf{E}, \quad (2.28)$$

$$\frac{\partial^2 \Delta n}{\partial t^2} - c_s^2 \nabla^2 \Delta n = \nabla^2 \frac{|\mathbf{E}|^2}{16\pi M},$$

where \mathbf{E} is the slowly-varying envelope of the fast-timescale electric field and Δn is the slow-timescale density variation.

Further, we restrict ourselves to a simplified version corresponding to weak amplitude case, which is valid under assumption of adiabatic ion response (neglecting the term $\partial^2 \Delta n / \partial t^2$ in the second equation) and potential (electrostatic) field \mathbf{E} , i.e. ($\nabla \times \mathbf{E} = 0$), to obtain the following nonlinear Schroedinger type of equation

$$i\frac{\partial \mathbf{E}}{\partial t} + \frac{1}{2}\nabla (\nabla \cdot \mathbf{E}) + |\mathbf{E}|^2 \mathbf{E} = 0, \quad (2.29)$$

where we have introduced, as usual, dimensionless units: $t \rightarrow t/\omega_0$, $r \rightarrow r r_{De} \sqrt{3}$, $\mathbf{E} \rightarrow (32\pi n_0 T_e)^{1/2} \mathbf{E}$.

From NLSE we can derive by the standard linear parametric instability analysis the growth rate for the modulational instability (MI) [2, 256]. To discuss the fully nonlinear evolution, self-focusing and collapse of a Langmuir wave packet we now follow Goldman and Nicholson [33] (see also Kono et al. [54]). We first of all note that Eq. (2.29) can be derived from a Lagrangian density \mathcal{L} , given by the formula (cf. Gibbons et al. [21])

$$\mathcal{L} = \frac{1}{2}i \left[\mathbf{E}^* \frac{\partial \mathbf{E}}{\partial t} - \mathbf{E} \frac{\partial \mathbf{E}^*}{\partial t} \right] - \frac{1}{2} |(\nabla \cdot \mathbf{E})|^2 + \frac{1}{2} |\mathbf{E}|^4. \quad (2.30)$$

From the Lagrangian density we readily get the energy and momentum conservation laws, in a form given in [33, 54].

$$\frac{\partial |\mathbf{E}|^2}{\partial t} + (\nabla \cdot \mathbf{s}) = 0, \quad \frac{\partial \mathbf{p}}{\partial t} + (\nabla \cdot \overleftrightarrow{\mathbf{T}}) = 0,$$

where now

$$\mathbf{p} = \frac{1}{2}i [(\mathbf{E} \cdot \nabla) \mathbf{E}^* - (\mathbf{E}^* \cdot \nabla) \mathbf{E}] = \mathbf{s}$$

$$T_{ij} = \frac{1}{2} [(\nabla \cdot \mathbf{E}) \nabla_i E_j^* + c.c.] - \frac{1}{2} \Delta_{ij} [\nabla \cdot \text{Re} \{ \mathbf{E} (\nabla \cdot \mathbf{E}) \}] + |\mathbf{E}|^4.$$

Proceeding as in [33, 54], we define the root mean square spatially averaged width $\langle \Delta r^2 \rangle^{1/2}$ ($\Delta r^2 \equiv |\mathbf{r} - \langle \mathbf{r} \rangle|^2$) of a localized wavepacket (i.e., Langmuir caviton) (using as a probability weighting function $|\mathbf{E}|^2 / \mathcal{N}$, where \mathcal{N} is the plasmon number) to get the Ehrenfest theorem,

$$\frac{\partial}{\partial t} \langle \Delta \mathbf{r} \rangle \equiv \int (|\mathbf{E}|^2 / \mathcal{N}) \mathbf{r} d^3 \mathbf{r} = \frac{\mathbf{P}}{\mathcal{N}} = \text{const.} \quad (2.31)$$

Accordingly, it is straightforward to prove the general *virial theorem*

$$\frac{\partial^2}{\partial t^2} \langle \Delta r^2 \rangle = \left[\frac{2\mathcal{H}}{\mathcal{N}} - \frac{\mathcal{P}^2}{\mathcal{N}^2} \right] - \int |\mathbf{E}|^4 d^3 \mathbf{r}. \quad (2.32)$$

By integrating twice the above equation, we find

$$\langle \Delta r^2 \rangle = At^2 + Bt + C - (2 - D) \int_0^t dt_1 \int_0^{t_1} I(t_2) dt_2, \quad (2.33)$$

where, D is the number of spatial dimensions, A is a constant of motion and B and C are integration constants,

$$I(t) = \int |\mathbf{E}|^4 d^3 \mathbf{r}, \quad A = 2\mathcal{H}/\mathcal{N} - \mathcal{P}^2/\mathcal{N}^2, \quad (2.34)$$

$$\mathcal{H} = \frac{1}{2} \int [|(\nabla \cdot \mathbf{E})|^2 - |\mathbf{E}|^4] d^3 \mathbf{r}, \quad \mathbf{P} = \int \mathbf{p} d^3 \mathbf{r}, \quad \mathcal{N} = \int |\mathbf{E}|^2 d^3 \mathbf{r}.$$

We note that, if initially $A < 0$, for the dimensionality $D \geq 2$, then $\langle \Delta r^2 \rangle$ will collapse to zero in a finite time, or physical collapse will be stopped at few r_{De} , due to Landau damping. Of course, even before such a value is reached, above model equations cease to be valid [18].

2.3 Hierarchy of Collapse Regimes in a Magnetized Plasma

A collapse classification for upper-hybrid and lower-hybrid waves in a weakly magnetized plasma is presented [50, 57, 58]. It is proved that in these nonlinear systems, three-dimensional soliton solutions do not exist. Further, it is demonstrated that the basic

criterion for the existence of the wave collapse is the unboundness of the Hamiltonian from below due to nonlinear terms. Finally, we show that there exists a hierarchy of wave collapse regimes, starting from a *weak*-collapse case which formally preserves zero wave energy into the collapse stage, and concluding with the *strong*-collapse, when the trapped wave energy remains finite [50].

2.3.1 Introduction

Studies of a theory of wave collapse show that the collapse [2, 11, 49], as a known phenomenon of the formation of a singularity in a finite time, often appears in a multi-dimensional system, although a soliton solution is usually found in an one-dimensional case. Such behaviour is found to be due the growing influence of nonlinear effects with an increase of spatial dimensionality.

A similar situation takes place in the theory of phase transitions, where the phase transition is forbidden in a low-dimensional system although it is allowed for higher dimensional cases. In a seminal paper by Zakharov and Kuznetsov [49], followed by Kuznetsov and Škorić [50], it was shown that for the nonlinear Schroedinger equation (NLSE) [25] in three dimensions (3D) there exist a hierarchy of wave-collapse regimes, starting from "weak" collapse, i.e. the most rapid regime described by the self-similar solution of the NLSE, which formally conserves zero energy into the final stage, and concluding with "strong" wave collapse in which the wave energy remains finite. Corresponding results were obtained in a work [50], which studied a different type of wave collapse in a weak dispersive medium, i.e. magnetosonic wave collapse. This situation differs from the Langmuir collapse because of a different nonlinearity of a hydrodynamic type.

In this section, we present the collapse classification for upper-hybrid (*UH*) and lower-hybrid (*LH*) waves in a weakly magnetized plasmas [50], i.e. when the electron plasma frequency ω_{pe} , is larger than the electron cyclotron frequency ω_{ce} , namely, $\omega_{pe} \gg \omega_{ce}$. First, for upper-hybrid waves, we take into account only the influence of the magnetic field on the dispersion law and use the model equation of Ref. [43]. As the lower-hybrid collapse is concerned, we describe it with a help of the self-consistent system of equations, originally derived in Ref. [55]. Further, we shall show that in these nonlinear systems, three-dimensional soliton solutions do not exist. The reason, as will appear, is connected with a type of nonlinearity which is stronger than, for instance, that in the NLSE or in the Zakharov system [2], which describes the collapse of the nonlinear Langmuir waves in an unmagnetized plasma.

2.3.2 Model Equation

First, let us consider upper-hybrid waves in a weak magnetic field ($\omega_{pe} \gg \omega_{ce}$). The dispersion law is given in the form

$$\omega(k) = \omega_{pe} \left[1 + \frac{3}{2} k^2 r_{De}^2 + \frac{1}{2} \frac{\omega_{ce}^2}{\omega_{pe}^2} \frac{k_{\perp}^2}{k^2} \right],$$

where, r_{De} is the Debye radius, k_{\perp} is the wavenumber component transverse to the magnetic field direction and \mathbf{B}_0 is directed along the z -axis. In the dispersion relation [43],

the first term describes the longitudinal electron plasma wave oscillations. Other terms are due to slower dispersive processes.

The nonlinear effect, in a weak amplitude region ($E^2/8\pi nT_e \equiv \overline{W} \ll 1$), appears to be slow with respect to fast oscillations at the plasma frequency. Therefore, we can obtain the envelope equation for the amplitude of *h.f.* oscillations, which in the dimensionless units has the form [43]

$$\Delta (i\psi_t + \Delta\psi) - \sigma\Delta_{\perp}\psi + \nabla \cdot (|\nabla\psi|^2 \nabla\psi) = 0, \quad (2.35)$$

where ψ is the slowly varying envelope of *h.f.* waves and $\sigma \equiv \frac{1}{2} \frac{\omega_{ce}^2}{\omega_{pe}^2}$. Here, we assume that $\overline{W} \ll m/M$, which means that the low-frequency density variations follow adiabatically the ponderomotive pressure induced by high-frequency waves,

$$n = -|\nabla\psi|^2. \quad (2.36)$$

Equation (2.35) can be further reduced under additional assumptions. Namely, it is known that due to weakly turbulent processes, such as induced scattering on ions or four-wave interaction, the energy transfers by cascades and condenses in the region $\omega_k \rightarrow \omega_{pe}$. In more details, it appears that these nonlinear interactions lead, in the first place, for waves with $k^2 r_{De}^2 \ll \sigma$, to a rapid decrease in k_{\perp} , and only subsequently, to a reduction of k_z down to a zero value. It means that the wave condensate must have characteristic longitudinal scales much smaller than the transverse ones, i.e., $k_{\perp} \ll k_z$. Under this assumption, equation (2.35) reduces to the following form (compare with [43])

$$\frac{\partial^2}{\partial z^2} \left[i\psi + \frac{\partial^2}{\partial z^2} \psi \right] - \Delta_{\perp} \psi + \frac{\partial}{\partial z} \left[\left| \frac{\partial \psi}{\partial z} \right|^2 \frac{\partial \psi}{\partial z} \right] = 0, \quad (2.37)$$

where without restriction we can put $\sigma = 1$ (related to a simple scaling transformation).

Analogous equations arise for *LH* waves near the LH frequency ω_{LH} . The dispersion relation for *LH* waves can be found, as

$$\omega(k) = \omega_{LH} \left[1 + k_{\perp}^2 R^2 + \frac{1}{2} \frac{m}{M} \frac{k_z^2}{k_{\perp}^2} \right],$$

where $R^2 \equiv \left[\frac{3}{4} + 3T_i/T_e \right] r_{ce}$, for $\omega_{ce} \ll \omega_{pe}$, while m and M are the electron and ion mass, respectively.

For weak intensity, as for the *UH* waves, the low-frequency density variation is related to the *h.f.* ponderomotive pressure [55, 56], through

$$n = i |\nabla_{\perp} \psi \times \nabla_{\perp} \psi^*|_z. \quad (2.38)$$

Here, as in the *UH* case, we write (2.38) in dimensionless units; ψ stands for the slowly varying envelope of the *h.f.* electric potential, and \times , denotes the vector product. The evolution equation for the envelope ψ can be found with the help of standard time-averaging over the high-frequency ω_{LH} , [2, 55].

$$\Delta_{\perp} (i\psi_t + \Delta_{\perp} \psi) - \nabla_{\perp} \cdot (|\nabla_{\perp} \psi \times \nabla_{\perp} \psi^*|_z |\hat{n} \times \nabla_{\perp} \psi|) - \phi \psi_{zz} = 0, \quad (2.39)$$

where the unit vector $\hat{n} \equiv \mathbf{B}_o/B_o$, and ϕ is a constant.

2.3.3 Nonexistence of Three-Dimensional Solitons

Now, let us study properties of Eqs. (2.37) and (2.39) in more detail [50]. As it is known, both equations are of the Hamiltonian type [24]. Accordingly, (2.37) can be represented in the form

$$i \frac{\partial^2}{\partial z^2} \psi_t = - \frac{\Delta H}{\Delta \psi^*}, \quad (2.40)$$

$$H_1 = \int \left(|\psi_{zz}|^2 + |\nabla_{\perp} \psi|^2 - \frac{1}{2} |\psi_z|^4 \right) d\mathbf{r},$$

while Eq. 2.39 is given by

$$i \Delta_{\perp} \psi_t = - \frac{\Delta H}{\Delta \psi^*}, \quad (2.41)$$

$$H_2 = \int \left(|\Delta_{\perp} \psi|^2 + |\psi_z|^2 + \frac{1}{2} |\nabla_{\perp} \psi \times \nabla_{\perp} \psi^*|^2 \right) d\mathbf{r}.$$

Besides H , the above nonlinear systems also conserve the plasmon number N : where for (2.40), $N_1 = \int |\nabla_z \psi|^2 d\mathbf{r}$, and for (2.41), $N_2 = \int |\nabla_{\perp} \psi|^2 d\mathbf{r}$. In both cases, N coincides up to a constant, with the wave energy. Equations (2.40) and (2.41) also possess conservation laws for the linear momentum and the longitudinal component of the angular momentum.

The possible stationary solutions of these equations should correspond to a soliton-like solution,

$$\psi = \psi_0(\mathbf{r}) \exp(i\lambda^2 t),$$

spatially localized, vanishing at infinity, with $\psi_0(\mathbf{r})$ being defined in the stationary limit of Eqs. (2.40) and (2.41), as follows

$$\frac{\partial^2}{\partial z^2} \left[-\lambda^2 \psi_0 + \frac{\partial^2}{\partial z^2} \psi_0 \right] - \Delta_{\perp} \psi_0 + \frac{\partial}{\partial z} (|\psi_{0z}|^2 \psi_{0z}) = 0, \quad (2.42)$$

and

$$\Delta_{\perp} (-\lambda^2 \psi_t + \Delta_{\perp} \psi) - \nabla_{\perp} \cdot (|\nabla_{\perp} \psi \times \nabla_{\perp} \psi^*|_z |\hat{\mathbf{n}} \times \nabla_{\perp} \psi) - \phi \psi_{zz} = 0, \quad (2.43)$$

where, for convenience the subscript "0" has been dropped. On the other hand, it is easy to verify that the above equations can be represented in the following variational form [24]:

$$\Delta (H + \lambda^2 N) = 0, \quad (2.44)$$

that can be readily checked on inspection. Such a representation means that the soliton should be defined as the stationary point of H for fixed N , where λ^2 plays the role of the Lagrange multiplier.

For Eqs. (2.42) and (2.43) and their variational representations, it is easy, for the soliton solution, to obtain relations between integrals I_{i1} , I_{i2} and I_{i3} , which are constituent

parts of the Hamiltonian H_i . For this purpose, we introduce the following notation: $i = 1$, stands for UH , while $i = 2$, corresponds for LH . Therefore, for the UH system

$$\begin{aligned} I_{11} &= \int |\psi_{0zz}|^2 d\mathbf{r}, \\ I_{12} &= \int |\nabla_{\perp}\psi_0|^2 d\mathbf{r}, \\ I_{13} &= \int |\psi_{0z}|^2 d\mathbf{r}, \end{aligned}$$

while for the second, LH system

$$\begin{aligned} I_{21} &= \int |\Delta_{\perp}\psi_0|^2 d\mathbf{r}, \\ I_{22} &= \int |\psi_{0z}|^2 d\mathbf{r}, \\ I_{23} &= - \int |\nabla_{\perp}\psi_0 \times \nabla_{\perp}\psi_0^*|^2 d\mathbf{r}. \end{aligned}$$

By definition, all these integrals are positive. In order to check the existence of soliton solutions, we multiply Eq. (2.42) by ψ_0^* and integrate over the hole space. One gets

$$\lambda^2 N_1 + I_{11} + I_{12} - I_{13} = 0. \quad (2.45)$$

Equation (2.45) gives the first relation between I_{11} , I_{12} and I_{13} . The others relations can be found with the help of (2.44). Let us assume the trail function of a type $\psi = \psi_0(\alpha z, \beta \mathbf{r}_{\perp})$. It is evident that

$$\frac{\partial}{\partial \alpha} (H + \lambda^2 N) |_{\alpha=\beta=1} = \frac{\partial}{\partial \beta} (H + \lambda^2 N) |_{\alpha=\beta=1} = 0.$$

Indeed, e.g. for UH waves, we can readily prove the above formula, by

$$\begin{aligned} & \frac{\partial}{\partial \alpha} (H + \lambda^2 N) = \\ & \int \left\{ \left(\frac{\partial \psi^*}{\partial \alpha} \psi_{zz} + \frac{\partial \nabla_{\perp} \psi^*}{\partial \alpha} \nabla_{\perp} \psi - \frac{\partial \psi_z^*}{\partial \alpha} \psi_z^2 \psi_z^* + \lambda^2 \frac{\partial \psi_z^*}{\partial \alpha} \psi_z + c.c. \right) \right\} d\mathbf{r} = \\ & \int \left\{ \frac{\partial \psi^*}{\partial \alpha} \left(\psi_{zzzz} - \nabla_{\perp}^2 \psi + \frac{\partial}{\partial z} (|\psi_z|^2 \psi_z) \right) + c.c. \right\} d\mathbf{r} = 0, \end{aligned}$$

for $\alpha = 1$.

Applying the above procedure for Eq. (2.42), we get

$$\begin{aligned} 3I_{11} - I_{12} - \frac{3}{2}I_{13} + \lambda^2 N_1 &= 0, \\ -2I_{11} + I_{13} - 2\lambda^2 N_1 &= 0. \end{aligned} \quad (2.46)$$

After some simple algebra, based on (2.45) and (2.46), we can show that

$$I_{12} = -2\lambda^2 N_1 < 0, \quad (2.47)$$

which contradicts the sign of I_{12} , which is positive definite. This contradiction basically implies that for the equation (2.42), stationary soliton solutions do not exist. By the same procedure, applied to (2.43), one can get corresponding relations between integrals I_{21} , I_{22} and I_{23} for LH case. They are

$$I_{21} + I_{22} - I_{23} + \lambda^2 N_2 = 0 \quad (2.48)$$

$$-I_{21} + I_{22} + \frac{1}{2}I_{23} - \lambda^2 N_2 = 0, \quad (2.49)$$

$$2I_{21} - 2I_{22} - I_{23} = 0. \quad (2.50)$$

It is easy to check again that relations (2.48)-(2.50) appear to be contradictory.

2.3.4 Necessary Condition for Wave Collapse

What is the reason for the nonexistence of 3D solitons in our models? As will be shown below, this fact is basically connected with more pronounced nonlinear effects, as compared to the type of NLSE, i.e. Zakharov equations (static limit) which follows from (2.35), after relaxing the external magnetic field effect ($\sigma = 0$). In order to illustrate, let us consider the Hamiltonian under a scaling transformation, which conserves the number of waves N . For the system (2.40), they are

$$\psi(z, \mathbf{r}_\perp) \rightarrow \frac{a^{1/2}}{b} \psi \left[\frac{z}{a}, \frac{\mathbf{r}_\perp}{b} \right], \quad (2.51)$$

while for Eq. (2.41)

$$\psi(z, \mathbf{r}_\perp) \rightarrow \frac{1}{a^{1/2}} \psi \left[\frac{z}{a}, \frac{\mathbf{r}_\perp}{b} \right]. \quad (2.52)$$

Under such a transformation the corresponding Hamiltonian becomes the function of parameters a and b .

$$H_1(a, b) = \frac{I_{11}}{a^2} + \frac{I_{12}}{b^2} a^2 - \frac{1}{2} \frac{I_{13}}{ab^2}, \quad (2.53)$$

and

$$H_2(a, b) = \frac{I_{21}}{b^2} + \frac{I_{22}}{a^2} b^2 - \frac{1}{2} \frac{I_{23}}{ab^2}. \quad (2.54)$$

Further, it is easy to check that the function $H_1(a, b)$ is unbounded from below. For this purpose let us consider the parabolic family $b = \gamma^2$, where γ is a constant. For this kind of dependence, the first two terms in $H_1(a, b)$ have the same (self-similar) dependence,

$$\frac{I_{11}}{a^2} + \frac{I_{12}}{b^2} a^2 = \frac{1}{a^2} \left[I_{11} + \frac{I_{12}}{\gamma^2} \right]. \quad (2.55)$$

As for the third nonlinear term, we get

$$\frac{1}{2} I_{13} \frac{1}{ab^2} = \frac{1}{a^5} \left[\frac{I_{13}}{2\gamma^2} \right]. \quad (2.56)$$

Under inspection, the above two terms, i.e. the dispersion and nonlinear term, show that $H_1(a, b)$ is unbounded from below. It should be stressed that the unboundedness of

Hamiltonian $H_1(a, b)$ from below is due to the nonlinear term which grows with a scale decrease, more rapidly than, for instance, in the NLSE case. This is the main reason for the nonexistence of 3D solitons. Generally taken, it is the unboundedness of the Hamiltonian that is the main signature of collapse in the known collapsing systems (see [24]). The collapse, from this point of view, corresponds to a falling down of a particle in a self-consistent potential well, when the falling time to the center of well is finite (compare with the 3D NLSE, Ref. [24]).

Similarly, it is clear that for Eq. (2.41), $H_2(a, b)$ is also unbounded from below. Here one needs to consider the curve $b = \gamma a^2$. It is evident that for this case, dispersive terms have the same self-similar behaviour, and that unboundedness is due to the nonlinear term,

$$\frac{1}{2} I_{23} \frac{1}{ab^2} = \frac{1}{a^5} \left[\frac{I_{23}}{2\gamma^2} \right]. \quad (2.57)$$

Clearly, the nonlinearity is the main cause of the collapse. Moreover, it has been shown [24].that the role of nonlinear effects tend to grow with an increase of spatial dimensionality.

2.3.5 Classification of Wave Collapse Regimes

While the unboundedness of the Hamiltonian is the necessary condition for the existence of wave collapse; however, it is not the sufficient one. On the other hand, the analogy with the free falling particle dynamics while useful and illustrative is somewhat oversimplified. Firstly, during a wave collapse, it is possible that e.g., the leaked radiation of the low-amplitude waves plays a role of effective dissipation for the cavity; i.e., spatially localized compressed density region with an intense growing wave structure. At the first sight, the radiation process seems to slow down the collapse. However, in reality we have an opposite situation. Instead of halting the collapse, the wave radiation, from the cavity with negative H , actually supports the collapse process.

Let us consider an isolated cavity with characteristic scales $l_z(t)$ and $l_\perp(t)$ with $H < 0$, emitting small amplitude waves. It is easy to verify that, for example, for system (2.40), the following estimates take place [50]:

$$\max_{\mathbf{r}} \left| \frac{\partial \psi}{\partial z} \right|^2 \geq \frac{1}{2} \frac{|H|}{N}, \quad (2.58)$$

which is a consequence of the mean-value theorem applied to I_{13} ,

$$I_{13} = \int |\psi_z|^4 d\mathbf{r} \leq \max_{\mathbf{r}} |\psi_z|^2 \int |\psi_z|^2 d\mathbf{r},$$

which is valid for an arbitrary region. Here, we may recall that for (2.40), $|\psi_z|^2$ represents the wave energy density. What happens with a cavity when we take into account the effect of wave radiation? Due to conservation of H , inside the cavity, H^{cav} evidently has to decrease; this means that, due to radiation, $H^{cav} \rightarrow -\infty$. Similarly, N as a positive definite, will decrease until it vanishes. Thus, the ratio H/N becomes infinite and so does

the maximum of the wave amplitude, according to (2.58), goes to infinity. The similar estimate takes place for the lower-hybrid waves with

$$\max_{\mathbf{r}} |\nabla_{\perp} \psi|^2 \geq \frac{1}{2} \frac{|H|}{N}. \quad (2.59)$$

From (2.59), it also follows that the small amplitude wave radiation (leakage) promotes the collapse, and that the collapse becomes more rapid.

Now we come to another interesting question about the classification of the wave collapse regimes. As was shown in Clearly, the nonlinearity is the main cause of the collapse. Moreover, it has been shown [24, 50] that basically exist two main types of wave collapse. The first one, the so-called *strong* collapse, is the case when the captured wave energy through the collapse stage remains finite and the wave radiation is absent. The other regime, *weak* collapse, is the one when the wave radiation is present.

Let us now assume that for UH waves near the singularity $\psi(\mathbf{r}, t)$ exhibits a more general self-similar behaviour,

$$\psi(\mathbf{r}, t) \rightarrow \frac{1}{(t_0 - t)^{a+ip}} f \left[\frac{z}{(t_0 - t)^b}, \frac{\mathbf{r}_{\perp}}{(t_0 - t)^c} \right],$$

where a, b, c and p are real constants. This means that the cavity size scales are

$$l_z \simeq (t_0 - t)^b, \quad l_{\perp} \simeq (t_0 - t)^c.$$

Moreover, one should note that based on the above, corresponding electric field components scale like

$$E_z \equiv \nabla_z \psi \simeq \frac{1}{(t_0 - t)^b} \psi, \quad \text{while} \quad E_{\perp} \equiv \nabla_{\perp} \psi \simeq \frac{1}{(t_0 - t)^c} \psi. \quad (2.60)$$

Substituting (2.60) in N_1 shows that the number of waves in a cavity depends on time. For Eq. (2.40) we have

$$N_1^{cav} \sim (t_0 - t)^{-2\sigma + b + 2c}, \quad \sigma = a + b.$$

In an isolated cavity, the plasmon number can only decrease in time, so

$$-2\sigma + b + 2c \geq 0. \quad (2.61)$$

The equality sign in this expression corresponds to a strong collapse, and inequality to a weak one. Then, we substitute (2.60) into Hamiltonian H_1 . This gives

$$\begin{aligned} I_{11} &\sim (t_0 - t)^{-2b} N_1^{cav}, \\ I_{12} &\sim (t_0 - t)^{-2c + 2b} N_1^{cav}, \\ I_{13} &\sim (t_0 - t)^{-2\sigma} N_1^{cav}. \end{aligned}$$

The collapse condition (2.58) leads to a second restriction on indices a, b, c ,

$$2\sigma \geq \max(2b, 2c - 2b). \quad (2.62)$$

Therefore, with condition (2.61) for σ , we have

$$b + 2c \geq 2\sigma \geq \max(2b, 2c - 2b). \quad (2.63)$$

Here the first equality, $2\sigma = b + 2c$, corresponds to the strong collapse. For this regime it is easy to see that for a fixed value of index b we get $\max \sigma = \frac{5}{2}b$ and $c = 2b$. It means that ψ obeys, in this case, the following asymptotics:

$$\psi \sim \frac{1}{(t_0 - t)^{3/2b+ip}} f \left[\frac{z}{(t_0 - t)^b}, \frac{\mathbf{r}_\perp}{(t_0 - t)^{1b}} \right]. \quad (2.64)$$

All other type of collapse belong to the weak one. The most rapid case is realized when radiation of small amplitude waves is at maximum. Such a regime corresponds to the case, for fixed index b , of the minimum of index a . Simple calculation gives $\min a = 0$ and $c = 2b$, or

$$\psi \sim \frac{1}{(t_0 - t)^{0+ip}} f \left[\frac{z}{(t_0 - t)^b}, \frac{\mathbf{r}_\perp}{(t_0 - t)^{2b}} \right], \quad (2.65)$$

It is important to note that the asymptotics (2.65) represents the self-similar solution of Eq. (2.40), with $b = \frac{1}{2}$, given in [43]. For lower-hybrid wave collapse we have the following restriction on the indices:

$$b/2 \geq a \geq b - 2c. \quad (2.66)$$

From these inequalities we can similarly obtain the relations between indices a , b and c for the strong collapse and the most rapid weak collapse. For the strong *LH* collapse simple calculations give

$$\psi \sim \frac{1}{(t_0 - t)^{b/2+ip}} f \left[\frac{z}{(t_0 - t)^b}, \frac{\mathbf{r}_\perp}{(t_0 - t)^c} \right], \quad (2.67)$$

where for fixed b , $b/4 \leq c \leq b/2$, and $\max c = b/2$. As for the most rapid weak collapse, we have

$$\psi \sim \frac{1}{(t_0 - t)^{0+ip}} f \left[\frac{z}{(t_0 - t)^b}, \frac{\mathbf{r}_\perp}{(t_0 - t)^{b/2}} \right], \quad (2.68)$$

which appears to be a self-similar substitution in Eq. (2.41) for $b = 1$, (see Refs. [56, 24]).

In conclusion, we have to underline that analytical determination of the concrete value of parameter b for the strong collapse case, for both considered models, remains open. It is possible that the value for b can be possibly found in the semiclassical limit [24].

2.4 Weak and Strong Langmuir Collapse

The self-similar evolution of weak and strong Langmuir collapse is studied by two-dimensional simulation of a soliton instability. The simulation is based on Zakharov's model of magnetized strong turbulence (UH waves) including ion dynamics. For the parameters considered, consistency with self-similar weak collapse regimes is found with no evidence of a strong Langmuir collapse [59, 60].

Preliminaries

Both for laboratory and space plasmas with a large energy content, it is typical that a state is reached where nonlinear wave effects compete with the dispersion [61, 62]. In such a physical environment spatially localized, soliton like waveforms can be formed. These structures evolve rapidly from an arbitrary initial plasma state to determine the basic features of an emerging strong plasma turbulence [17]. In one dimensional systems solitons are mostly stable, but in real plasmas, as a rule, solitary structures often appear to be unstable with respect to perturbations in a transverse direction [24, 36]. In its nonlinear stage, this instability often leads to a soliton collapse, a unique nonlinear wave phenomenon of the formation of a singularity in a finite time. In the physical sense, wave collapse corresponds to wave breaking and particle acceleration, thus playing the role of an effective heating process in a strongly turbulent plasma. Above analytical analyses of the wave collapse, based on a self-similar analysis, have revealed the hierarchy of collapse regimes. The basic distinction is between the weak collapse which formally brings the zero wave energy to the final collapse stage, and strong collapse where the initially trapped energy remains finite during the collapse [50]. In the rest, we present a numerical study in two spatial dimensions in order to check the existence of weak and strong Langmuir wave collapse and validity of self-similar solutions [50]. Our simulations are based on the above Zakharov model of strong Langmuir (UH wave) turbulence for a plasma in a weak magnetic field with the full ion dynamics .

Nonlinear Model Equations

The simplest example of strong plasma turbulence, thoroughly studied by theory, simulation and experiments, is the phenomenon of strong Langmuir turbulence (SLT), where the interacting modes are of the high-frequency Langmuir (UH) and low-frequency ion sound wave. Zakharov's model of SLT in a weakly magnetized plasma is given by two time-averaged dynamical equations [vide supra], which describe a nonlinear coupling between the Langmuir wave potential amplitude (ψ) and the ion density variation (n) . In convenient dimensionless units,

$$\begin{aligned} t &\rightarrow \frac{3}{2}\mu\omega_{pe}^{-1}t, & r &\rightarrow \mu^{1/2}r_{De}r, & \psi &\rightarrow \frac{T}{e}\mu\sqrt{12}\psi, \\ n &\rightarrow \frac{4}{3}\mu n_0 n, & \sigma &\rightarrow \frac{3}{4}\mu\left(\frac{\omega_{ce}}{\omega_{pe}}\right)^2, \end{aligned} \quad (2.69)$$

the system reads [60]

$$\begin{aligned} \nabla^2 (i \psi_t + \nabla^2 \psi) - \sigma \nabla_{\perp}^2 \psi - \nabla (n \nabla \psi) &= 0, \\ n_{tt} - \nabla^2 n &= \nabla^2 |\nabla \psi|^2 \end{aligned} \quad (2.70)$$

where ω_{ce} and ω_{pe} are the electron cyclotron and the electron plasma frequency, respectively; μ is the ion to electron mass ratio, r_{De} is the Debye radius and T is the electron temperature in energetic units. The system (2.70) is derived under an assumption that $\sigma \ll \mu$, corresponding to the physical condition of a weak magnetic field (in x -direction)

$\omega_{pe} \gg \omega_{ce}$. We note that for $\sigma = 0$, the system reduces to the original set of the curl-free Zakharov equations [24]. The vectorial form of (2.70) readily simplifies to a scalar model by replacing $(-\text{grad } \psi)$ by a scalar electric field $E(r)$. In the small amplitude (static ions) limit, the set further reduces to a single equation of the nonlinear Schroedinger (NLSE) type (see above, 2.36). However, for large Langmuir fields the inclusion of the full ion inertia is essential. A stationary, spatially localized solution of the system (2.70) in the form of a “standing” planar (1D) soliton, for the external magnetic field in the x -direction, is given by

$$\begin{aligned}\psi_s &= \sqrt{2} \arctan [\sinh (\lambda x)] \exp (i \lambda^2 t), \\ n_e &= -|\psi_{sx}|^2.\end{aligned}\tag{2.71}$$

The problem of the stability, nonlinear dynamics and collapse of Langmuir solitons was presented earlier in detail [24, 36]. In a linear regime, agreement between direct simulation and eigenvalue problem results has been obtained [36]. In the nonlinear regime, linearly unstable solitons exhibit the wave collapse. In its developed stage, Langmuir collapse is expected to follow the self-similar evolution [24]. We note that much works on the Langmuir collapse scaling were restricted to a simpler, static limit of (2.70). In distinction, we treat the full set of (2.70) accounting for the ion dynamics, that is important for large amplitude Langmuir solitons. General self-similar solution for the Langmuir potential was proposed in a form [24]

$$\psi(\mathbf{r}, t) \rightarrow \frac{1}{(t_0 - t)^{a+ip}} f\left(\frac{x}{(t_0 - t)^b}, \frac{r_\perp}{(t_0 - t)^c}\right),\tag{2.72}$$

where t_0 is the collapse time and a, b, c and p are real constants. Starting from (2.72), we find that the electric field components and maximum field energy density scale according to

$$\begin{aligned}E_x &= \nabla_x \psi \rightarrow \frac{1}{(t_0 - t)^b} \psi, \\ E_\perp &= \nabla_\perp \psi \rightarrow \frac{1}{(t_0 - t)^c} \psi, \\ |E_{\max}|^2 &\simeq \text{const.} \times \frac{1}{(t_0 - t)^{2a+2b}},\end{aligned}\tag{2.73}$$

The characteristic dimensions of the collapsing soliton (caviton) contract like

$$l_x \rightarrow (t_0 - t)^b, \quad l_\perp \rightarrow (t_0 - t)^c,$$

while the caviton plasmon number (vide infra) scales as

$$N^{\text{cav}}(t) = \int |\nabla \psi|^2 d\mathbf{r} \simeq \int E_x^2 d\mathbf{r} \rightarrow (t_0 - t)^{-2a-b+2c}.\tag{2.74}$$

In an isolated cavity, the plasmon number is conserved or decreases in time, so the following inequality must hold,

$$-2a - b + 2c > 0,$$

which in the two-dimensional case becomes

$$-2a - b + c = p > 0.$$

Generally taken, the equality sign corresponds to a *strong*, while inequality stands for a *weak* collapse regime. For more details on the collapse hierarchy and the scaling analysis, we refer to earlier papers [24].

Simulation Results and Discussions

We have performed direct numerical simulations of nonlinear equations (2.70) based on the spectral Fourier method with respect to two spatial dimensions with an explicit time integration. The initial condition is chosen in a form of a standing planar soliton (2.71), perturbed in a transverse, y -direction [60], as given by

$$\psi_x(t=0) = \psi_{sx}(t=0)(1 + 2\epsilon \cos ky),$$

where the initial ion density is taken to satisfy the adiabatic matching, in order to shorten plasma transients. We have used periodic boundary conditions (L_x, L_Y), a numerical grid 64×64 points (checked upon 128×128) and the perturbation level $\epsilon = 0.01$, performing a regular numerical check of conserved integrals of motion in (2.70; the plasmon number (N))

$$N = \int |\nabla\psi|^2 d\mathbf{r}, \quad (2.75)$$

and the Hamiltonian (H)

$$H = \int \left(|\nabla^2\psi|^2 + \sigma |\nabla_{\perp}\psi|^2 + n |\nabla\psi|^2 + \frac{1}{2} |\nabla\phi|^2 + \frac{1}{2} n^2 \right) d\mathbf{r}, \quad n_t = \nabla^2\phi. \quad (2.76)$$

To study the space-time dynamics of the soliton instability we have performed runs with different values of k, λ and σ . The simulations have confirmed that all linearly unstable solitons [36, 59] in the nonlinear stage enter the collapse phase. Typical space-time evolution of the soliton collapse was illustrated in Fig.2.6. Further, we show temporal evolution of the soliton amplitude in Fig.2.8. The initial, linearly unstable phase is followed by an explosive growth; entering a self-similar stage of a Langmuir collapse. The case, $k = 0.15$, corresponds to the most linearly unstable perturbation. Further, in order to check if the self-similar character of the collapse is consistent with (2.72) we vary t_0 to find the best fit with simulation data for the maximum electric field and corresponding soliton dimensions l_x and l_y (Fig.2.9). We measure the values of the scaling parameters α ($\alpha = 2a + 2b$), b and c to find β . In all considered cases we have found good agreement with the self-similar solution (2.72), as indicated by the power law dependence in Fig.2.9. In our simulations of the inertial phase of the Langmuir collapse, for various values of k, λ and σ , weak collapse ($\beta > 0$) is regularly observed, with no evidence of the strong Langmuir collapse. Increase of the magnetic field speeds up the amplitude growth and the transverse contraction rate; however, these effects are suppressed for a larger soliton strength.

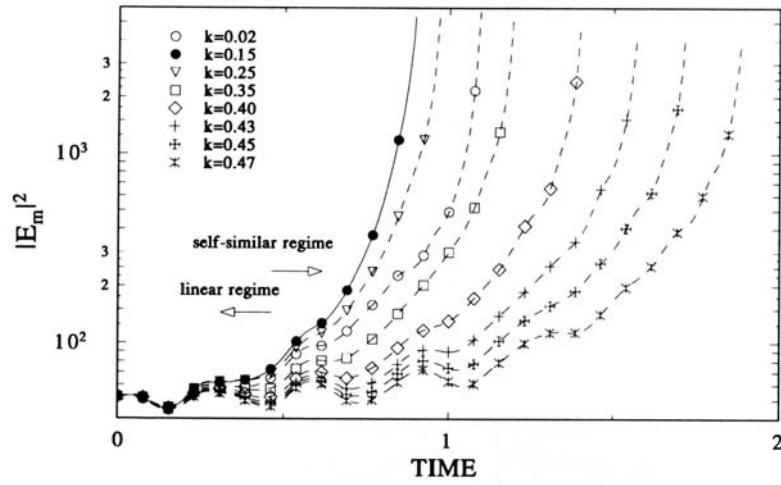


Figure 2.8: Maximum soliton amplitude in time for different transverse perturbation wavenumbers. The soliton strength is $\lambda = 5$ and $\sigma = 3$, [60].

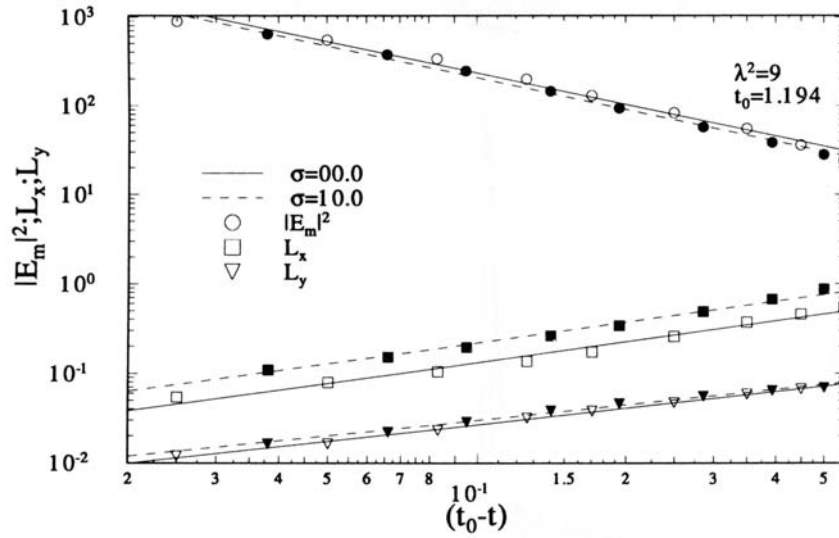


Figure 2.9: Characteristic spatial scales (l_x, l_y) and the maximum soliton energy as a function of time interval ($t - t_0$). Numerical fits (lines) of 2D simulation data (points), [60].

Apart from contributing to a general theory of Langmuir turbulence, the above results can be readily applied to studies of SLT in ionospheric, auroral and solar plasmas [61, 62]. In these applications varying signatures of anisotropic wave power spectra, heated particle tail, etc., are obtained by space observations and computer simulations [63, 64, 65, 66, 67, 68, 69, 70, 71, 72, 74, 75]. In order to make estimates and certain predictions and to justify proposed application models, one can readily turn to the above results on self-similar properties of the magnetized SLT.

Chapter 3

Spatiotemporal Complexity in Plasmas

Nonlinear systems with an infinite number degrees of freedom are readily described by partial differential equations. Behaviour of such systems exhibits a rich variety of dynamical structures in space and time with coherent, as well as, chaotic features [76]. Nearly conservative systems and dissipative systems represent two distinctive highly important categories. In dissipation dominated systems often a limited number of equilibrium states is available resulting in formation of patterns due to rapid system relaxation under strong dissipative processes. However, both, for nearly conservative and dissipative systems, evolution in an infinitely dimensional phase space can approach attractors that are low-dimensional [77, 78]. An important family of partial differential equations includes nonlinear evolution equations, such as: KdV equation, NLS equation, Zakharov's equation, Ginzburg-Landau, Sine-Gordon, Kuramoto-Shivashinsky, as well as the three-wave interaction (3WI), which possess a remarkable nonlinear class of soliton solutions. These equations including a lowest order of nonlinearity describe some of basic generic interactions in physics, and nature, in general [79, 80, 81].

3.1 Spatiotemporal Effects in Three-Wave Interaction

A nonlinear resonant interaction of three waves in space and time is readily represented by a system of coupled equations

$$\begin{aligned}\frac{\partial a_0}{\partial t} + V_0 \frac{\partial a_0}{\partial x} &= -a_1 a_2 + i\delta_0 a_0, \\ \frac{\partial a_1}{\partial t} + V_1 \frac{\partial a_1}{\partial x} &= a_0 a_2^* + i\delta_1 a_1, \\ \frac{\partial a_2}{\partial t} + V_2 \frac{\partial a_2}{\partial x} &= a_0 a_1^* - \Gamma a_2 + i\delta_2 a_2 - i\sigma |a_2|^2 a_2.\end{aligned}\tag{3.1}$$

where V_i and δ_i , ($i = 0, 1, 2$) is group velocity and linear phase shift, respectively; while Γ and σ corresponds to linear damping and nonlinear phase shift (detuning) of a_2 complex

amplitude, respectively. It is a simplified version of the more general system, assuming linear damping and nonlinear shift put to zero for first two waves, i.e., $\Gamma_1 = \Gamma_2 = 0$ and $\sigma_1 = \sigma_2 = 0$. A basic mathematical formulation and physical background of resonant wave interactions in plasmas have been explored before. For example, for infinitely thin layer, analytical solutions can be found [82]. Moreover, a general tendency of 3WI to transit to deterministic chaos has been already early recognized [83, 84, 85]. Further, we shall concentrate on full space-time aspects of nonlinear three-wave interactions and route to dynamical complexity and saturation in a *finite* plasma system [81, 85, 86].

3.1.1 Time-Only Problem in Three Wave Interaction

In a *time-only* dependent case in three-wave interaction (3WI) ($\partial/\partial x = 0$) the system of equations (3.1) reduces to:

$$\begin{aligned}\frac{da_0}{dt} &= -a_1 a_2 + i\delta_0 a_0, \\ \frac{da_1}{dt} &= a_0 a_2^* + i\delta_1 a_1, \\ \frac{da_2}{dt} &= a_0 a_1^* + i\delta_2 a_2 - i\sigma |a_2|^2 a_2 - \Gamma a_2.\end{aligned}\tag{3.2}$$

In order to solve the above system it is convenient to represent the complex amplitudes in terms of two real variables, for the amplitude and phase of the interacting waves [86], respectively, i.e.

$$a_i(t) = A_i(t)e^{i\phi_i(t)}, \quad i = 0, 1, 2$$

where $A_i(t) = \sqrt{|a_i|^2}$ is the amplitude and $\phi_i(t)$ is the phase of the wave.

Accordingly, the system of equations (3.2) becomes

$$\begin{aligned}\frac{dA_0}{dx} &= -A_1 A_2 \cos \phi, \\ \frac{dA_1}{dx} &= A_0 A_2 \cos \phi, \\ \frac{dA_2}{dx} &= A_0 A_1 \cos \phi - \Gamma A_2, \\ \frac{d\phi}{dt} &= \left(\frac{A_1 A_2}{A_0} - \frac{A_0 A_2}{A_1} - \frac{A_0 A_1}{A_2} \right) \sin \phi + \delta + \sigma A_2^2,\end{aligned}\tag{3.3}$$

where $\phi(t) = \phi_0 - \phi_1 - \phi_2$ is the total phase, while $\delta = \delta_0 - \delta_1 - \delta_2$ is the total linear phase shift. The above system of four ordinary differential equations in dissipation free case (for $\Gamma = 0$), satisfies the following conservation relations :

$$\begin{aligned}m_0 &= n_0(t) + n_1(t) = \text{const.} \\ m_1 &= n_0(t) + n_2(t) = \text{const.} \\ A_0 A_1 A_2 \sin \phi - \frac{\sigma}{4} A_2^4 - \frac{\delta}{2} A_2^2 &= C = \text{const.}\end{aligned}\tag{3.4}$$

where $n_i(t) = (A_i(t))^2$. The first two equations are of the well-known *Manley–Rowe* type, while the third one is derived from the phase dependence equation in (3.3). Therefore, the system of four equations can reduce to a single differential equation for an independent variable $n_0(t)$

$$\frac{dn_0(t)}{dt} = -2 \left[(m_1 - m_2) \left(\frac{\sigma^2}{16} (m_1 - n_0)^3 - \frac{\sigma\delta}{4} (m_1 - n_0)^2 - \frac{\delta^2}{4} (m_1 - n_0) + n_0(m_0 - n_0) \right) \right]^{\frac{1}{2}}, \quad (3.5)$$

where m_0, m_1 and C are determined by the initial conditions for the wave amplitudes and phase, at $t = 0$. For $\Gamma \neq 0$, we get two independent variables and the system becomes nonintegrable. In the case $\Gamma = 0$, there are two independent variables represented by the first and the third equation in (3.5), which now reads

$$\frac{d}{dt} \left(A_0 A_1 A_2 \sin \phi - \frac{\sigma}{4} A_2^4 - \frac{\delta}{2} A_2^2 \right) + \Gamma (A_0 A_1 A_2 \sin \phi - \sigma A_2^4 - \delta A_2^2) = \text{const..}$$

In a simplified, dissipation free case ($\sigma = \delta = \Gamma = 0$), the solution of (3.5) after integration is found in a form of the *Jacobian* elliptic functions [87, 88],

$$\begin{aligned} n_0(t) &= \text{sn}^2 \left(-\sqrt{1+\epsilon}(t-t_0), \frac{1}{\sqrt{1+\epsilon}} \right), \\ n_1(t) &= (1+\epsilon) \text{dn}^2 \left(-\sqrt{1+\epsilon}(t-t_0), \frac{1}{\sqrt{1+\epsilon}} \right), \\ n_2(t) &= \text{cn}^2 \left(-\sqrt{1+\epsilon}(t-t_0), \frac{1}{\sqrt{1+\epsilon}} \right), \end{aligned} \quad (3.6)$$

with a period:

$$T = \frac{2K \left(\frac{1}{\sqrt{1+\epsilon}} \right)}{1+\epsilon} \xrightarrow{\epsilon \rightarrow 0} \frac{\ln \frac{16}{\epsilon}}{\sqrt{1+\epsilon}}, \quad (3.7)$$

for the initial conditions

$$n_0(0) = 1 \geq n_1(0) = \epsilon \geq n_2(0) = 0. \quad (3.8)$$

The period T is taking values between 2.09 and $+\infty$ (for $\epsilon = 1$ and $\epsilon = 0$, respectively), where $K(\gamma) \in [\frac{\pi}{2}, \infty)$ (complete elliptic integral of the first kind) for $\gamma \in (0, 1)$, with the relation for γ given as

$$\gamma = \frac{1}{\sqrt{1+\epsilon}}.$$

The aperiodic solution ($T \rightarrow \infty$) reads

$$\begin{aligned} n_0(t) &= \tanh^2(-(t-t_0)), \\ n_1(t) &= n_2(t) = \sec^2(-(t-t_0)), \end{aligned} \quad (3.9)$$

The type of solution (3.9) is analogous to the localized soliton solution with a "pump" amplitude A_0 , which satisfies the following boundary conditions [89]

$$A_0(\infty) = 1, \quad A_1(\infty) = 0, \quad A_2(\infty) = 0,$$

The soliton like solution exists also in the case $\sigma, \delta \neq 0$. with the complete analysis found elsewhere, which predicts a possible complete wave action transfer from the pump to two "daughter" waves for a particular choice of parameters.

Introducing the phase shifts brings new terms in just the last equation of the system (3.3). As a consequence the phase is no longer stationary, instead it is given by the equation

$$\sin \phi(t) = \frac{\frac{\sigma}{4}A_2^3 + \frac{\delta}{2}A_2}{A_0A_1}, \quad \text{with } C = 0,$$

In the limit $\sigma \rightarrow 0, \delta \neq 0$, the solution is

$$\begin{aligned} n_0 &= \frac{\alpha - \beta}{2} + \frac{2 - \alpha + \beta}{2} sn^2 \left(-\sqrt{\beta}(t - t_0), \gamma \right), \\ n_1 &= 1 + \epsilon - n_0, \\ n_2 &= 1 - n_0, \end{aligned}$$

where

$$\begin{aligned} \alpha &= 1 + \epsilon + \delta^2/4, \\ \beta &= \sqrt{\alpha^2 - \delta^2}, \\ \gamma &= \sqrt{\frac{2 - \alpha + \beta}{2\beta}}, \end{aligned}$$

with a period

$$T = 2 \frac{K(\gamma)}{\sqrt{\beta}},$$

which in the case $\sigma \rightarrow 0$, reduces to (3.7).

Periodic solution is found both, for zero and nonzero phase shifts, however, in the limiting case $\delta = 0, \sigma \rightarrow 0$, period becomes

$$T \approx T_{\sigma=0} - \frac{\sigma^2}{8},$$

where $T_{\sigma=0}$ is the period found for $\sigma = 0$.

Assuming $\sigma = \delta = 0$, with $\Gamma > 0$, no analytical solutions is found. However, necessary condition for the existence of oscillatory type of solutions in the asymptotic case of weak and strong damping can be found. In the weakly damped case ($\Gamma \ll 2$) solutions are given [87] by the *Jacobian* elliptic functions with damped modulus

$$\begin{aligned} n_0 &= m \operatorname{cd}(t, m), \quad n_1 = \frac{m_c}{\operatorname{dn}(t, m)}, \quad n_2 = m m_c \operatorname{sd}(t, m), \\ m &= u_{10} e^{-\frac{\Gamma t}{2}}, \quad m_c = (1 - m^2)^{\frac{1}{2}}, \end{aligned}$$

while in a strong damping case ($\Gamma \gg 2$), type of degenerated solutions is found.

$$n_0 = \frac{f}{(1+f^2)^{\frac{1}{2}}}, \quad n_0 = \frac{1}{(1+f^2)^{\frac{1}{2}}}, \quad n_2 = [1 - e^{-\Gamma t}] \frac{f}{\Gamma(1+f^2)},$$

where $f = u_{00}/u_{10}e^{-t/\Gamma}$.

In the case $\Gamma \neq 0, \sigma = \delta = 0$, above system (3.2) is written, as

$$\begin{aligned} \frac{da_0}{dt} &= -a_1 a_2, \\ \frac{da_1}{dt} &= a_0 a_2^*, \\ \frac{da_2}{dt} &= a_0 a_1^* - \Gamma a_2. \end{aligned} \tag{3.10}$$

By multiplying (3.10) with corresponding complex conjugate variables after a straightforward procedure and by introducing $n_i(t) = |a_i(t)|^2$, we get

$$n_0(t) + n_1(t) = \text{const.}$$

With initial conditions (3.8) and ansatz

$$a_0(t) = \alpha_0 \cos \phi(t),$$

where $\alpha_0 = \sqrt{1 + \epsilon}$, expression for wave amplitude $a_1(t)$ is found

$$a_1(t) = \alpha_0 \sin \phi(t).$$

After substitution into the system of equations (3.10), it results in

$$a_2(t) = \phi(t)'$$

and further substituting into the third equation in (3.10) gives the ordinary differential equation of the second order for $\zeta(t) = 2\phi(t)$

$$\zeta'' + \Gamma \zeta' - \alpha_0^2 \sin \zeta = 0,$$

that can be further reduced to a system of two first order differential equations for unknown variables $\zeta(t), y(t)$

$$\begin{aligned} \zeta' &= y, \\ y' &= -\Gamma y + \alpha_0^2 \sin \zeta, \quad \alpha_0 = \sqrt{1 + \epsilon}. \end{aligned} \tag{3.11}$$

The fixed points of the above system (3.11) are

$$(\zeta, y) = (k\pi, 0), \quad k = 0, \pm 1, \pm 2, \dots$$

The characteristics of the fixed points can be determined by solving the eigen-value problem

$$\lambda^2 + \Gamma\lambda - \alpha_0^2 \cos \zeta = 0,$$

where λ is the corresponding eigen-value.

For the fixed points

$$(\zeta, y) = ((2n + 1)\pi, 0), \quad n = 0, \pm 1, \pm 2, \dots$$

eigen-values are found, as

$$\lambda_{1,2} = \frac{-\Gamma \pm \sqrt{\Gamma^2 - 4\alpha_0^2}}{2}.$$

For $\Gamma^2 \geq 4\alpha_0^2$, λ takes negative values and fixed points are stable nodes; for $\Gamma^2 \leq 4\alpha_0^2$ eigen-values are calculated as

$$\lambda_{1,2} = \frac{-\Gamma \pm i\sqrt{4\alpha_0^2 - \Gamma^2}}{2}$$

and fixed points are stable focii, which in a limiting case $\Gamma \rightarrow 0$ give oscillatory solutions with a period $2\pi/\sqrt{1 + \epsilon}$.

For the fixed points

$$(\zeta, y) = (2n\pi, 0), \quad n = 0, 1, 2, \dots$$

corresponding eigen-values are

$$\lambda_{1,2} = \frac{-\Gamma \pm i\sqrt{4\alpha_0^2 + \Gamma^2}}{2}$$

that gives $\lambda_1 < 0$ and $\lambda_2 > 0$, actually the fixed point of a saddle-node type

By introducing nonzero phase shift δ , in the equation (3.3) analogous search for oscillatory solutions can be performed, based on the pseudo-potential method [86]. For example, in the limit of vanishing $\delta \rightarrow 0$, oscillatory solution with frequency Ω is found

$$\Omega = \sqrt{V_1 V_2} \left(1 + \epsilon^2 \frac{V_0}{V_1} + \epsilon^4 \frac{V_0^2}{V_1^2} \right)^{\frac{1}{4}}.$$

3.1.2 Space-Only Problem in Three Wave Interaction

In a stationary (steady state, $\frac{\partial}{\partial t} = 0$) case, three-wave interaction system of equations (3.11), becomes

$$\begin{aligned} V_0 \frac{da_0}{dx} &= -a_1 a_2 + i\delta_0 a_0, \\ V_1 \frac{da_1}{dx} &= a_0 a_2^* + i\delta_1 a_1, \\ V_2 \frac{da_2}{dx} &= a_0 a_1^* + i\delta_2 a_2 - \Gamma a_2 - i\sigma |a_2|^2 a_2. \end{aligned} \tag{3.12}$$

This system of equations for space-only case (3.12) for $V_i > 0$, is analogous to the above time-only case (3.3). However, the change of sign in V_1 , will transform the initial value problem to a more demanding boundary value problem in a finite media. Introducing boundary conditions at two different boundaries results in a qualitative change in the eigen-value spectrum. More precisely, equations for amplitudes and phase become

$$\begin{aligned}
\frac{du_0}{dx} &= -u_1 u_2 \cos \phi, \\
\frac{du_1}{dx} &= u_0 u_2 \cos \phi, \\
\frac{du_2}{dx} &= u_0 u_1 \cos \phi - G u_2, \\
\frac{d\phi}{dx} &= \left(\frac{u_1 u_2}{u_0} - \frac{u_0 u_2}{u_1} - \frac{u_0 u_1}{u_2} \right) \sin \phi + \delta + \Delta u_2^2,
\end{aligned} \tag{3.13}$$

with the following anzats being introduced

$$\begin{aligned}
u_i(x) &= \frac{1}{\sqrt{V_j V_k}} a_i(x) \equiv u_i(x) e^{i\phi_i(x)}, \quad i, j, k = 0, 1, 2, \\
\phi(t) &= \phi_0(x) - \phi_1(x) - \phi_2(x), \\
\delta &= -\frac{\delta_0}{V_0} - \frac{\delta_1}{V_1} + \frac{\delta_2}{V_2}, \Delta = \frac{\sigma V_0 V_1}{V_2} \text{ and } G = \frac{\Gamma}{V_2}.
\end{aligned} \tag{3.14}$$

Solution of the system for $\Gamma = \delta = \Delta = 0$, is given in terms of *Jacobian* elliptic functions

$$\begin{aligned}
n_0(x) &= dn^2(x, \sqrt{r}), \\
n_1(x) &= r cn^2(x, \sqrt{r}), \\
n_2(x) &= r sn^2(x, \sqrt{r}),
\end{aligned} \tag{3.15}$$

with a parameter r which corresponds to a reflectivity. Solutions appear to be oscillatory, with a period

$$T = 2K(\sqrt{r}), \tag{3.16}$$

while in a case $r \rightarrow 1, T \rightarrow \infty$, which is the spatially aperiodic solutions, given by

$$\begin{aligned}
n_0(x) &= \sec h^2(x), \\
n_1(x) &= r \sec h^2(x) \\
n_2(x) &= r th^2(x).
\end{aligned} \tag{3.17}$$

If $\Gamma = \Delta = 0$, but $\delta \neq 0$, solutions are found as

$$\begin{aligned}
n_0(x) &= 1 - n_2(x), \\
n_1(x) &= r - n_2(x), \\
n_2(x) &= \frac{\alpha - \eta}{2} \operatorname{sn}^2 \left(\sqrt{\frac{\alpha + \eta}{2}} x, \sqrt{\frac{\alpha - \eta}{\alpha + \eta}} \right)
\end{aligned} \tag{3.18}$$

where $\alpha = 1 + r + \delta^2/4$ and $\eta = \sqrt{\alpha^2 - 4r}$, with a period

$$T = \frac{2K \left(\sqrt{\frac{\alpha - \eta}{\alpha + \eta}} \right)}{\sqrt{\frac{\alpha + \eta}{2}}}, \tag{3.19}$$

which in the limit $\delta \rightarrow 0$, reduces to (3.16).

In the finite system, solutions have to satisfy the nonzero boundary conditions, given as

$$n_1(L) = \epsilon, \tag{3.20}$$

where L is the length of a system. In a general case, the spectrum of eigen-values is countably finite. However, depending on whether $\epsilon = 0$ or $\epsilon \neq 0$, different implications follow.

In the case $\epsilon = 0$, it was shown that for $\Gamma = \delta = \Delta = 0$, of all possible solutions, only, the so-called fundamental mode exists and is asymptotically stable [90, 91] (it corresponds to 1/4 period of the *Jacobian* elliptic solution)

$$L = K(\sqrt{r}). \tag{3.21}$$

Based on L values, the reflectivity of the fundamental mode is calculated as

$$\begin{aligned}
r &= 4 \frac{L - L_0}{L_0}, \quad L \geq L_0 = \frac{\pi}{2} \frac{\sqrt{V_1 V_2}}{\gamma_0}, \\
r &= 1 - 16e^{-2L}, \quad L \geq 2L_0,
\end{aligned}$$

where $L \geq L_0$, is the condition for neglecting the convective amplification of the noise (ϵ), found in the linear parametric analysis [92, 93]. Moreover, for δ and/or Δ values different from zero, it was found that solutions exist only for nonzero ϵ values. The system (3.13) with nonzero damping ($\delta = \Delta = 0, G \neq 0$) has stationary solution related to a aperiodic fundamental mode [94]. Condition for existence of nontrivial stationary state, which is a saturated decay instability, corresponds to instability threshold found from a linear parametric theory (constant pump). Marginal stability condition [88] is found as

$$L = \frac{\left[\frac{\pi}{2} + \sin^{-1} \left(\frac{\beta}{2} \right) \right]}{\left(1 - \frac{\beta^2}{4} \right)^{\frac{1}{2}}},$$

with $\beta = L_0/L_a$, where L_a is the longitudinal absorption rate. Instability is of the absolute or convective type, respectively, depending on whether $\beta < 2$ or $\beta > 2$.

3.1.3 Spatiotemporal Evolution in Three-Wave Interaction

The three-wave interaction in space and time is written in a known form (3.1)

$$\begin{aligned}\frac{\partial a_0}{\partial t} + V_0 \frac{\partial a_0}{\partial x} &= -a_1 a_2 + i\delta_0 a_0, \\ \frac{\partial a_1}{\partial t} + V_1 \frac{\partial a_1}{\partial x} &= a_0 a_2^* + i\delta_1 a_1, \\ \frac{\partial a_2}{\partial t} + V_2 \frac{\partial a_2}{\partial x} &= a_0 a_1^* - \Gamma a_2 + i\delta_2 a_2 - i\sigma |a_2|^2 a_2.\end{aligned}\tag{3.22}$$

Assuming that $V_0, V_1, V_2 > 0$, the system (3.22) describes 3WI as an initial value problem at one point in space-time. However, the case of e.g., $V_0, V_2 > 0$ and $V_1 < 0$, moves one condition to other boundary (finite or infinite), which leads to a two-point boundary problem. Qualitative difference in these two cases, was discussed above, for time-only versus space-only 3WI model.

In seminal papers, Fuchs [87, 88] has investigated stationary solution for (3.22) system ($\partial/\partial t = 0$) for a zero phase shift and zero damping. The solutions found are of the *Jacobian* elliptic function type, with the existence of particular solution defined by the condition (3.20). To exclude the convective noise growth (ε), i.e. to concentrate on the absolute instability regime, noise level is taken to zero, so that condition (3.20) taken with (3.8) becomes

$$cn(L, \sqrt{r}) = 0,$$

where L is the system length and r is the reflectivity.

From the characteristics of the *Jacobian* elliptic cosine function [95], it follows

$$L = (2n + 1)K(\sqrt{r}),\tag{3.23}$$

with $n = 0, 1, 2, \dots$ and $K(\sqrt{r})$ one quarter of the *Jacobian* cosine. Since $K(\gamma), \gamma = \sqrt{r}$, is growing monotonically from $\pi/2$ to ∞ , for γ between 0 and 1, it is evident that if $L < \pi/2$ then $r = 0$. On the other hand, for $L > \pi/2$ unique solutions are found (3.22), such that

$$1 > r_0 > r_1 > r_2 > \dots > r_{N-1} > 0,\tag{3.24}$$

where $2N - 1$ is largest odd integer part of $2L/\pi$.

Fundamental solution is the only eigen-function which is definite continuous for all $L \in (0, \infty)$. For $L \in (0, \pi/2)$ one gets trivial solution ($r = 0$). For $L > \pi/2$, if $K(\sqrt{r}) \rightarrow \infty$ and $r \rightarrow \infty$, the fundamental mode continually evolves into

$$u_{0,1} \longrightarrow \sinh x, \quad u_2 \longrightarrow \tanh x,$$

that is a unique solution for the semi-infinite system case ($L \rightarrow \infty$). Quantities $u_i (i = 0, 1, 2)$ are introduced through (3.24).

Stability analysis of the system (3.22) was given in [90] by using the perturbation treatment, for $\delta_{0,1,2} = \sigma = \Gamma = 0$. Transformation to a system of equations for amplitudes and phases of three waves is performed, which are real quantities, by substituting

$$a_i(x, t) = A_i(x, t) e^{i\phi_i(x, t)}$$

where A_i and ϕ_i , is the amplitude and phase of the wave ($i = 0, 1, 2$), respectively.

Amplitude-phase equations are represented by

$$\begin{aligned} \frac{\partial A_0}{\partial t} + V_0 \frac{\partial A_0}{\partial x} &= -A_1 A_2 \cos \phi, \\ \frac{\partial A_1}{\partial t} + V_1 \frac{\partial A_1}{\partial x} &= A_0 A_2 \cos \phi, \\ \frac{\partial A_2}{\partial t} + V_2 \frac{\partial A_2}{\partial x} &= A_0 A_1 \cos \phi, \\ A_0 \left(\frac{\partial \phi_0}{\partial t} + V_0 \frac{\partial \phi_0}{\partial x} \right) &= A_1 A_2 \sin \phi, \\ A_1 \left(\frac{\partial \phi_1}{\partial t} + V_1 \frac{\partial \phi_1}{\partial x} \right) &= A_0 A_2 \sin \phi, \\ A_2 \left(\frac{\partial \phi_2}{\partial t} + V_2 \frac{\partial \phi_2}{\partial x} \right) &= A_0 A_1 \sin \phi, \end{aligned} \quad (3.25)$$

where the total phase shift is $\phi = \phi_0 - \phi_1 - \phi_2$.

The stability of (3.25) was analyzed by the Lyapunov stability theory. Linearized equations around the equilibrium (steady state), i.e. $\dot{A}_i = 0, \dot{\phi}_i = 0$ are analyzed. Stationary solutions are written as $Y_m^{(n)}$, $m = 1, \dots, 6$ (indices denote, wave amplitude (1, 2, 3) and phase (4, 5, 6), respectively, while $n = 0, 1, \dots, N - 1$, for N given by (3.24). Actually, stationary solution (3.25) is defined as a vector

$$Y_m^{(n)} = (S_\alpha^{(n)}, 0), \alpha = 0, 1, 2,$$

where $S_\alpha^{(n)}$ are stationary amplitudes with the corresponding zero phase (vide supra). Then, a general solution appears as

$$Y_m = (A_\alpha, \phi_\alpha), \text{ where } \alpha = 0, 1, 2, \quad m = 1, 2, \dots, 6.$$

Departure from an equilibrium is given by

$$y_m = Y_m - Y_m^{(n)}, \quad m = 1, 2, \dots, 6.$$

where after substituting in (3.25) gives a set of equations for small perturbations of the wave amplitude and phase y_m , as

$$\frac{\partial y_m}{\partial t} + V_m \frac{\partial y_m}{\partial x} = f_m(Y_1, \dots, Y_6), \quad (3.26)$$

In [90], decoupling of amplitude and phase perturbations from equilibrium was revealed. Therefore, asymptotic stability of the fundamental mode is studied, by independently analyzing the stability of amplitude and phase to small perturbations in (3.26). Analysis of phase perturbations has shown that in a vicinity of the fundamental mode, perturbation

phases couple resulting in a stability, contrary to a case of unstable phase perturbations of the non-fundamental mode. Furthermore, stability of the fundamental mode to amplitude perturbations was performed by WKB (Wentzel-Kramers-Brillouin) procedure. Still, above perturbation analysis is not adequate for a system evolving far from the equilibrium state. Stability of the fundamental mode was confirmed in a classical paper by Harvey and Schmidt [91]. Time evolution is numerically calculated by perturbing the fundamental as well as non-fundamental mode solutions that satisfy the condition (3.20). In all considered cases the system, in the time of γ_0^{-1} saturates to the fundamental mode.

Introducing the linear and nonlinear phase shift terms in the system of equations (3.25), in the steady state ($\partial/\partial t \rightarrow 0$), conserved quantities (invariants) are calculated as

$$\begin{aligned} m_0 &= V_0 n_0(x) - V_1 n_1(x) = \text{const.}, \\ m_1 &= V_0 n_0(x) + V_2 n_2(x) = \text{const.}, \\ K(x) &= A_0 A_1 A_2 \sin \phi - \frac{\sigma}{4} A_2^4 - \frac{\delta}{2} A_2^2 = \text{const.} \end{aligned} \quad (3.27)$$

with $n_i(x) = A_i(x)^2$, $i = 0, 1, 2$. For boundary conditions

$$n_0(0) = 1, n_1(L) = 0, n_2(0) = 0 \quad (3.28)$$

the third invariant becomes $K(0) = 0$. However, at the other boundary $x = L$, from (3.20), one calculates $K(L) \neq 0$; which breaks the invariance condition, i.e., $K(x) \neq \text{const.}$, hence, contradicts our basic assumption of the steady state. This simple argument, due to Škorić [96], based on a nonlinear phase mismatch, explains a generic cause of nonstationarity in 3WI processes, such as, e.g. nonlinear stimulated Raman (also Brillouin) instability saturation in laser plasma interactions [97, 98].

3.1.4 Convective and Absolute Instability

Investigation of a system stability against perturbations in a finite region of space requires a solution of a boundary value problem [81, 86, 99].

$$u(x, t) = \frac{1}{2\pi} \sum_{s=1}^{\infty} \int_{-\infty}^{\infty} u_s(k, 0) e^{[i\omega_s(k)t - ikx]} dk, \quad (3.29)$$

where $u_s(k, 0)$ is the wave number spectrum of an initial perturbation, with a summation done over all eigenmode wave numbers.

Exponential growth in time of the particular k -components still do not guarantee that the perturbation grows in a specific point in space. Namely, perturbations can while growing propagate out of the unstable region. This is a *convective* instability. However, if among exponentially growing perturbations there are those that do not leave the finite region, i.e. which continuously grow in each point in space; this is a condition of an *absolute* instability. More formally, if

$$\lim u(x, t) \longrightarrow \infty, \quad x \in (x_1, x_2),$$

where $u(x, t)$ is a perturbation (x_1 and x_2 are boundaries of the unstable region), instability is absolute. However, if

$$\lim u(x, t) \longrightarrow 0, \quad x \in (x_1, x_2),$$

this instability is convective.

Obviously, the feature of an instability will depend on our choice of the frame of reference. If the observer travels together with a perturbation, in a new moving frame such instability will appear as absolute. On the contrary, in a system with an absolute instability, with a change to new variables, $t_n = t$, $x_n = x - v_0 t$, instability transits into a convective one. To determine the instability character by analyzing the dispersion relation is not an easy task. However, for a large class of systems described by the hyperbolic partial differential equations (*PDE*), it will be sufficient to find in the (x, t) plane, the boundaries of the perturbation propagation which correspond to the characteristics of the *PDE* with a maximum and minimum slope. This is a basic of the method of characteristics [99]. The essence of the method of characteristics is that characteristics are determined by the asymptotes of dispersion curves in a linear problem. Characteristics and asymptotes have the same slope in the phase space (x, t) and (ω, k) , respectively. Moreover, for hyperbolic systems, where the number of asymptotes with a finite slope is equal to the number of normal modes (eigen-modes), it is possible, based on the form of dispersion curves to determine the character of the instability. If the asymptotes point out in opposite directions, the instability is absolute and *vice versa*. For the basic system of equations, one gets

$$\frac{\partial u_i}{\partial t} + \sum_{k=1}^n a_{ik}(u) \frac{\partial u_k}{\partial x} + b_i(u) = 0, \quad i = 1, 2, \dots, n, \quad (3.30)$$

where u_i are system variables, $a_{ik}(u), b_i(u)$ are nonlinear functions of u_i , equation of characteristics is therefore

$$Det(a_{ik} - V\delta_{ik}) = 0, \quad (3.31)$$

with V -*tangens* of the inclination angle on the t - axis.

Linearized system of equations (3.30) is described by the dispersion relation

$$Det\left(a_{ik} - \frac{\omega}{k}\delta_{ik} - \frac{1}{k}\delta_{ik}\right) = 0, \quad b_{ik} = \frac{\partial b_i}{\partial u_k} \Big|_{u_k=u_0}, \quad (3.32)$$

which coincides with (3.31) for $k \rightarrow \infty$, where the slope of the dispersion curves is identical to a slope of the characteristics.

For the parametric instability in a plasma, important effect comes from the spatial localization of the pump in the unstable region controlled by the finite pump extent or phase mismatch due to a spatial non-uniformity. If of the convective type, locally growing instability can propagate out of the unstable region before the substantial amplitude growth is achieved. For the absolute instability, amplitude will grow exponentially until other nonlinear effects start to play their role.

Discussion on absolute versus convective instability for the decay instability in a uniform medium can be found in [100]. To determine the character of the instability it is

sufficient to observe the long-time behavior of the a_1 -scattered amplitude at $x = 0$, the point at which the instability was initiated. Furthermore, if $a_1(t \rightarrow \infty, 0) \rightarrow 0$, instability is convective; otherwise, for $a_1(t \rightarrow \infty, 0) \rightarrow \infty$, the instability is absolute. Long-time evolution is determined by the character of the poles in the dispersion relation $D(p, k) = 0$. Analysis has shown that $V_1 V_2 > 0$, gives the convective instability, while for $V_1 V_2 < 0$, absolute instability appears, if the additional condition is satisfied, namely

$$\frac{\gamma_0^2 l^2}{|V_1 V_2|} > \frac{\pi^2}{4}. \quad (3.33)$$

where γ_0 is the uniform linear parametric instability growth rate and l is the length of the system.

3.2 Complexity in Laser Plasma Instabilities

The spatiotemporal evolution of stimulated Raman backscattering in a bounded, uniform, weakly dissipative plasma is analyzed [98, 101, 102, 103]. The nonlinear model of a three-wave interaction involves a quadratic coupling of slowly varying complex amplitudes of the laser pump, the backscattered and the electron plasma wave. The corresponding set of coupled partial differential equations with nonlinear phase detuning that is taken into account is solved numerically in space time with fixed nonzero source boundary conditions. The study of this open, convective, weakly confined system reveals a distinctive quasiperiodic transition to spatiotemporal chaos via spatiotemporal intermittency. In the analysis of transitions a dual scheme borrowed from fields of nonlinear dynamics and statistical physics is applied. An introduction of a nonlinear three-wave interaction to a growing family of paradigmatic equations which exhibit a route to turbulence via spatiotemporal intermittency is outlined [104].

3.2.1 Introduction

The nonlinear three-wave interaction (3WI) as a physical concept, in its variety of appearances, has found its application in hydrodynamics, nonlinear optics, and plasma physics [81]. It occurs whenever waves encounter a resonance in a physical space, i.e., fulfill frequency and wave vector matching conditions. Stimulated Raman scattering (SRS) in plasma is a paradigm of a three-wave interaction related to a nonlinear coupling of intense laser light (pump) to the electron plasma wave (EPW) and the scattered light, shifted in wave number and frequency [81]. It has been studied to a great extent both experimentally and theoretically, largely because of its practical application in a search for a future energy source based on inertial confinement thermonuclear fusion induced by intense laser beams. That is, SRS belongs to a family of underdense plasma instabilities, which can have a detrimental effect on the efficiency of laser energy deposition into a fusion target. The well-developed parametric theory [97, 105] gives basic values of SRS instability threshold, growth rates in its initial stage, and some insight into long time spatiotemporal evolution in saturated regimes [98, 105, 106, 107, 108, 109]. However, in contemporary high-intensity laser plasma experiments, SRS has often displayed rich and

exciting physics, not predicted by the parametric theory, such as a spiky-burstlike signal, anomalously low reflectivity, and spectral gaps and broadenings, as well as incoherent (irreproducible) dynamics [109]. With increasing evidence that SRS often transits from convective to absolute instability in typical laser fusion target-plasma experiments, the problem of nonlinear saturation has become a focus of many SRS studies. Various models, based on different physical mechanisms, have been recently attempted, pointing to a strongly nonlinear dynamics of the EPW as a key factor that determines the nature of saturated SRS states [110, 111, 112, 113]. In particular, an inherent feature of strongly nonlinear SRS to transit from a coherent (regular) to chaotic (turbulent) dynamics has been anticipated recently [85, 98, 109]. In this Chapter, transition from a coherent to a strongly nonlinear incoherent regime, or spatiotemporal chaos (STC) [114], is explored for saturated SRS in typical laser fusion conditions. This study follows the work by these authors [94, 98, 102, 103] on nonlinear saturation of SRS in a plasma layer as a paradigm of a ubiquitous 3WI in a dissipative, weakly confined spatially extended system, which can exhibit extensive chaos [85, 114]. The corresponding set of coupled partial differential equations (PDEs), with nonlinear phase detuning of the EPW taken into account, is solved numerically in space time with rigid nonzero source boundary conditions [115]. Through the variation of physical (laser and plasma) parameters, in particular by increasing the pump strength, this open, convective system is driven toward a spatiotemporal chaos. A route via steady state and periodic regime with quasiperiodic transition to spatiotemporal intermittency is observed, for review see also, [116, 117].

The spatiotemporal intermittency (STI) in which periodic or quasiperiodic, coherent (laminar) oscillations are interrupted by chaotic (turbulent) bursts is a widely observed phenomenon in spatially extended systems [114, 118, 119] with effectively many degrees of freedom, for example, in hydrodynamic systems (Rayleigh-Benard convection, surface waves, and open pipe flows [120]). This state should be contrasted with the weak or phase turbulence, where there is a competition between localized coherent structures in the sense that one mode dominates energetically, then another takes over, and so on. These localized structures occur at random within the physical domain, which retains a rather homogeneous structure as, for example, in Rayleigh-Benard convection, and such dynamics is usually low dimensional. As such, weak turbulence is closest to the so-called low dimensional chaos in which the system displays incoherence only in time while the spatial structure remains quasi frozen by the confined boundaries [121]. The spatiotemporal intermittency, on the other hand, is further characterized by dominant macroscopic scales in space-time, which can, generally taken, be identified as the coherent (length, time) scales in distinction to fully developed turbulence, where there are no predominant macroscopic scales. In addition to experiments in hydrodynamics, the spatiotemporal intermittency is frequently encountered in PDE simulations of routes to chaos generic to nonlinear dissipative extended systems [114, 118], modeled by, for example, the Kuramoto- Shivashinsky equation, the Swift- Hohenberg equation, and coupled map lattices [122], to name a few. The STI state displays the coexistence of patches of turbulence immersed in the rest of the structure still in the laminar state; the continuous transition amounts to a progressive increase of the turbulent fraction through the variation of control parameters [118]. In this case turbulence is strong locally and affects only a part of a physical space, which can be very small, e.g., at the ST1 threshold [118]. For completeness, we are reminded

that in nonlinear plasma physics an extensively developed theory of weak turbulence is available, starting from the early 1960s. This theory is built on a quasilinear concept of weakly interacting, weakly nonlinear plasma modes of random phases [123]. The rest of this Chapter is organized as follows. Firstly, the one-dimensional model of the nonlinear SRS is presented. Next, classical diagnostics from dynamical systems theory to analyze the time-only aspect of the backscattered wave evolution is introduced. Further, the spatiotemporal aspect of the system and analysis of the corresponding patterns and the correlation functions is performed. Moreover, dimension and entropy that quantify the spatiotemporal behavior and identify the route to spatiotemporal intermittency and chaos is introduced. Finally, coarse graining the degrees of freedom into binary variables such that the local space-time regions are labelled as either chaotic or laminar, and the techniques from the theory of phase transitions and critical phenomena is used to identify the transition from spatiotemporal intermittency to spatiotemporal chaos [102].

3.2.2 Nonlinear 3WI Paradigm for SRS

Laser plasma interactions are a useful test bed for exploring rich variety of strongly nonlinear plasma phenomena. As a rule, they include a number of important three-wave resonant instability models, involving the strong laser pump parametric coupling to plasma eigen-modes. These instabilities are mostly of a decay type, where the energy transfer from the laser pump to lower frequency daughter waves typically involves the electrostatic plasma modes (i.e., electron plasma wave and ion sound wave). In laser fusion, great concern is related to stimulated Raman and Brillouin scattering on electron plasma waves and ion sound waves, respectively, which can result in undesirable loss of laser energy at the target and production of energetic particles [97, 100, 124].

In propagation of an incident electromagnetic wave (laser) through an under-dense plasma ($n \leq n_{cr}$, i.e., $\omega_0 \geq \omega_{pe}$), the pump can easily excite plasma eigen-modes which exist at the noise level. In an isotropic, unmagnetized warm plasma (vide infra, Section 4), three basic linear eigen-modes are available:

- electromagnetic (transverse) wave

$$\omega^2 = \omega_{pe}^2 + k^2 c^2,$$

- electron plasma (longitudinal) wave, with

$$\omega^2 = \omega_{pe}^2 + 3k^2 v_{te}^2,$$

- ion-acoustic (sound) wave

$$\omega^2 = c_s^2 k^2,$$

where, $\omega_{pe}^2 = e^2 n_0 / \varepsilon_0 m_e$, the electron plasma frequency, $v_{te}^2 = kT_e / m_e$, electron thermal velocity, and $c_s^2 = zT_e / m_i$, ion sound velocity.

Stimulated Raman backscattering is a 3WI resonant instability of the laser pump against excitation of an electron plasma wave and another electromagnetic (laser) wave which propagates in the backward direction. Therefore, being possible for laser frequency $\omega_0 \geq 2\omega_{pe}$, or in other words, at plasma density below the quarter critical, $n \leq n_{cr}/4$.

Stimulated Raman scattering (SRS) is of great relevance in contemporary laser plasma research and will be next studied in more detail.

The one-dimensional model of SRS, assumes a uniform plasma layer of thickness L , irradiated by a laser beam from $x < 0$, which enters the plasma at $x \geq 0$, boundary.. The EPW and the scattered light are allowed to grow from their thermal noise levels (ε_1 and ε_2 , respectively). Moreover, the EPW is subjected to a weak dissipation characterized by the linear damping rate ν_e . The nonlinear 3WI model derived here for the case of SRS describes the spatiotemporal evolution of complex amplitudes of the pump (a_0), scattered (a_1) and EPW (a_2) in a weakly coupling approximation. These equations are obtained from Maxwell's and fluid vlasma equations in WKB approximation, assuming the resonant matching between frequencies and wave numbers of three waves ($\omega_0 = \omega_1 + \omega_2$, $\mathbf{k}_0 = \mathbf{k}_1 + \mathbf{k}_2$) closely satisfying the corresponding linear dispersion relations

$$\omega_{0,1}^2 = \omega_{pe}^2 + k_{0,1}^2 c^2, \quad \omega_2^2 = \omega_{pe}^2 + 3k_2^2 v_{te}^2, \quad (3.34)$$

where indices 0, 1, and 2 stand for the pump, scattered, and EPW, respectively; ω_{pe} for electron plasma frequency; and v_{te} for electron thermal velocity. For the case of *backscattering*, which is of most practical importance, the corresponding set of 3WI equations reads [102]

$$\begin{aligned} \frac{\partial a_0}{\partial \tau} + V_0 \frac{\partial a_0}{\partial \xi} &= -a_1 a_2, \\ \frac{\partial a_1}{\partial \tau} - V_1 \frac{\partial a_1}{\partial \xi} &= a_0 a_2^*, \\ \frac{\partial a_2}{\partial \tau} + V_2 \frac{\partial a_2}{\partial \xi} &= \beta_0^2 a_0 a_1^* - \Gamma a_2 + i\delta |a_2|^2 a_2, \end{aligned} \quad (3.35)$$

with time and space variables $\tau = \omega_0 t$, $\xi = x/L$, where the dimensionless amplitudes of the coupled waves are related to the physical quantities, electric fields E_0 and E_1 of the two electromagnetic waves, and EPW-driven electron density fluctuation δn_e ,

$$\begin{aligned} a_0(\xi, \tau) &= \frac{ck_2}{4\omega_0} \left[\frac{\omega_{pe}}{\omega_1} \right]^{\frac{1}{2}} \frac{E_0(x, t)}{\mathcal{E}_0}, \\ a_1(\xi, \tau) &= \frac{ck_2}{4\omega_1} \left[\frac{\omega_{pe}}{\omega_0} \right]^{\frac{1}{2}} \frac{E_1(x, t)}{\mathcal{E}_0}, \\ a_2(\xi, \tau) &= \frac{\omega_{pe}^2}{4\omega_0 \sqrt{\omega_0 \omega_1}} \frac{\delta n_e(x, t)}{n_0}, \end{aligned} \quad (3.36)$$

\mathcal{E}_0 denotes the vacuum pump electric field amplitude, and n_0 the equilibrium plasma density. Normalized group velocities and the damping rate Γ are expressed by

$$V_0 = \frac{c^2 k_0}{\omega_0^2 L}, \quad V_1 = \frac{c^2 k_1}{\omega_0 \omega_1 L}, \quad V_2 = \frac{3k_2 v_{te}^2}{\omega_0 \omega_{pe} L}, \quad \Gamma = \frac{\nu_e}{2\omega_0}. \quad (3.37)$$

and the laser pump strength is given by the ratio of the electron quiver velocity in a laser pump field to the speed of light

$$\beta_0 \equiv \frac{v_{osc}}{c} = \frac{e\mathcal{E}_0}{m_e \omega_0 c}. \quad (3.38)$$

We note an additional self-modal nonlinearity in the equation for EPW, given in the form of a nonlinear phase detuning (shift) $\sim \delta |a_2|^2$, which is due to large amplitude nonlinear EPWs excited through the SRS process [97, 110, 111, 112, 113]. In present-day laser-plasma interaction experiments, high intensity lasers induce large amplitude EPWs. For short pulse, ultra high intensities, relativistic correction to the electron mass makes it necessary to include a nonlinear detuning term in (3.35) [89, 126, 127]. On the other hand, an analogous nonlinear term could be due to nonlinear density modulation involving pondermotive coupling of EPWs to ion sound in the saturation of long-pulse SRS via Langmuir decay instability.

While relativistic correction to electron plasma frequency directly adiabatically induces nonlinear detuning of the wave resonance, density modulation has a more complex time-dependent effect due to ion dynamics [106, 107, 108]. For high-intensity relativistic laser plasma interaction, the corresponding model studied by some authors [126, 89, 127] calculates a relativistic frequency shift δ , given as

$$\delta = \frac{3\omega_0^2\omega_1}{c^2\omega_{pe}k_2^2}. \quad (3.39)$$

We also note the relevance of our model (3.35) to relativistic beat wave interactions [89, 126, 127].

To approach the absolute regime of the backward SRS instability, there is a minimum plasma length L_0 , i.e., basic amplification length or scattering length. In dimensionless units, the absolute instability condition for backward SRS, can be written as

$$\frac{\omega_0 L}{c} \frac{\beta_0}{\beta_{te}} > \frac{2\pi}{\alpha} \sqrt{\frac{3\sqrt{11-2\alpha}}{\sqrt{11-\alpha^2} + \sqrt{11-2\alpha}}}, \quad (3.40)$$

where $\alpha = \omega_{pe}/\omega_0 = \sqrt{n_0/n_{cr}}$, and $\beta_{te} = \sqrt{T_e(\text{keV})/511}$.

As discussed, the standard conservative form ($\delta = 0$, $\Gamma = 0$) of 3WI in one dimension is integrable [81]. However, with an introduction of dissipation ($\Gamma > 0$), closed form analytical solutions are not available and a numerical solution is the only alternative. A spatially uniform (time-only) version of (3.35) has been studied in detail, and it was shown to exhibit a low-dimensional chaos under restricted conditions [84] (see 5.2.4). Naturally, as indicated above, the spatially extended model of 3WI is more difficult to investigate. Only recently, the 3WI have been solved and studied in space time. These results have revealed rich physical behavior of saturated regimes corresponding to low-dimensional chaos as well as to STC [85, 98, 114].

The most useful information on the SRS is contained in the reflectivity R , which designates a fraction of incident laser intensity reflected backward [102],

$$R = \frac{V_0 |a_1(0)|^2}{V_1 |a_0(0)|^2} \quad (3.41)$$

with its maximum value normalized to unity in the stationary case. To solve (3.35), appropriate initial and boundary conditions are required. We choose physically realistic boundary conditions, while the choice of the plasma slab length satisfies the criterion for

the occurrence of the absolute instability. The wave amplitudes obey the corresponding initial and nonzero source fixed boundary conditions,

$$\begin{aligned} a_0(x, 0) &= 0 \quad (\text{for } x > 0), a_0(0, t) = A_0 \\ a_1(x, 0) &= a_1(L, t) = \varepsilon_1 A_0 \quad a_2(x, 0) = a_2(x, t) = 0 \end{aligned} \quad (3.42)$$

where A_0 follows from (3.36) for $E_0(0) = \mathcal{E}_0$.

A series of numerical simulations of model (3.35), by means of a central difference method, has been performed for different system (laser and plasma) parameters within physically realistic values. The accuracy of the centered-time, centered-space numerical scheme has been checked at each temporal step by using the modified Manley-Rowe conservation relations [81, 105, 115], which follow from (3.35).

The following parameters are chosen: $V_0 = 9.5 \times 10^{-3}$, $V_1 = 8.8 \times 10^{-3}$, $V_2 = 2.9 \times 10^{-4}$, $\Gamma = 1.6 \times 10^{-6}$, $\delta = 3.5$ and $\varepsilon_1 = 10^{-2}$, corresponding to typical laser plasma conditions [97, 102, 107]: $n_0 = 0.1n_{cr}$, $T_e = 1keV$, $L = 100c/\omega_0$ and $\nu_e/\omega_{pe} = 10^{-5}$.

3.2.3 Bifurcations and Low-Dimensional Chaos

In the time-only aspect of the SRS we follow the evolution of the backscattered wave. For the present exposition we study the bifurcation sequence while the incident pump wave amplitude, as a control parameter, is varied. The justification for this choice of the control parameter lies in the fact that the variation of the plasma slab length, keeping the incident laser beam amplitude fixed, leads to the same bifurcation sequence. The variation of the damping term on the other hand, alters only the quasiperiodic regime, as discussed below, and the same effect is observed when plasma density is changed. The robustness of the scenario was checked by varying the plasma slab length up to a factor of 5, by changing the damping term by two orders of magnitude [94], $(10^{-6} - 10^{-4}) \nu_e/\omega_{pe}$ and varying the plasma density within the interval $(0.001n_{cr} - 0.1n_{cr})$.

As the relative pump strength β_0 increases, starting from the value 0.01, the attractor changes according to the symbolic sequence

$$FP \rightarrow P \rightarrow QP \rightarrow I \rightarrow C$$

where FP stands for unimodal fixed point, P for periodic, QP for quasiperiodic, I for intermittent, and C for chaos. The quantitative boundaries in β_0 between successive attractors are depicted in Fig. 3.1.

The fixed point bifurcates to a stable limit cycle [Fig. 3.2(c)] through a supercritical Hopf bifurcation. As the relative pump strength is further increased, an additional spatial mode occurs, which is apparently associated with the second frequency in the quasiperiodic dynamics observed in the interval $(0.026 < \beta_0 < 0.029)$. The corresponding second frequency occurring for the EPW can be accounted for by the appearance of a traveling wave [Fig. 3.8(b)]. Within this finite parameter range, a mode locking occurs in which two incommensurate frequencies become related by a ratio of integers and the winding number, defined as the ratio of the two frequencies, is equal to 5. The corresponding

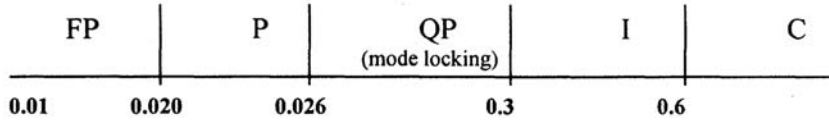


Figure 3.1: The bifurcation sequence as a function of relative pump strength, [102].

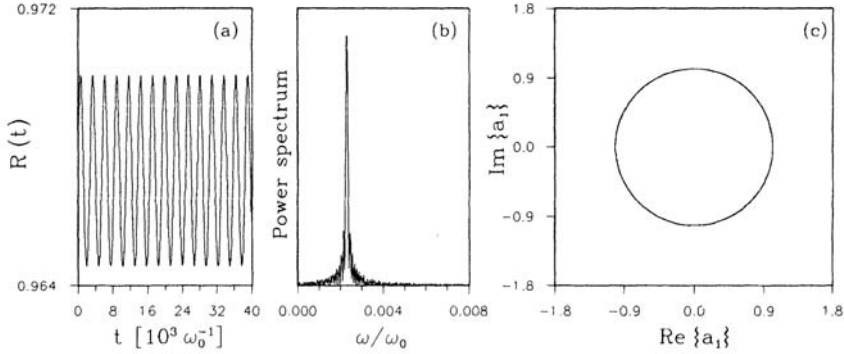


Figure 3.2: (a) Stimulated Raman backscattering reflectivity, (b) power spectrum and (c) phase diagram for $\beta_0 = 0.02534$, [102].

phase space representation, a 2-torus, is represented in Fig. 3.3(c). Harmonics f_n , appearing in the power spectrum of the quasiperiodic evolution, are related to the two main frequencies by $f_n - f_0 = n (f_1 - f_0)$, where f_0 is the frequency of the peak to the left of the most energetic frequency f_1 [Fig. 3.3(b)]. The weak nonlinear effects stabilize the 2-torus trajectory in the vicinity of the former periodic trajectory, which although linearly unstable remains visible, disclosing a beautiful illustration of another supercritical Hopf bifurcation. At this point, it should be noted that the increase of the damping term leads to the bifurcation sequence in which the quasiperiodic regime occurs without frequency locking, which can be explained on the basis that increased damping suppresses the evolution of the traveling mode. With further increase in β_0 , the manifestation of another degree of freedom occurs through the destruction of torus without appearance of the third frequency [Figs. 3.4(b) and 3.4(c)]. An interesting feature of this new regime is the existence of two metastable regions of the attractor, namely, "laminar" parts that retain almost unchanged a quasiperiodic nature and intermittent chaotic bursts. In the power spectra plots, the power spectrum of intermittent regime exhibits an increasing noise level [Figs. 3.4(b) and 3.5(b)]. As the control parameter is further increased, the fraction of time spent in laminar regions decreases, and fully developed temporal chaos sets in, as reflected in the broadband power spectrum [Fig. 3.6(b)]. Finally, the correlation dimension values obtained by the standard Grassberger-Procaccia algorithm [128] establish the low-dimensional nature of these attractors. The dimension increases from 1 (periodic) through 2.28 (quasiperiodic) to 3.7-4.7 (intermittent and chaotic).

All of the dynamical system diagnostics presented in this section analyzed the tem-

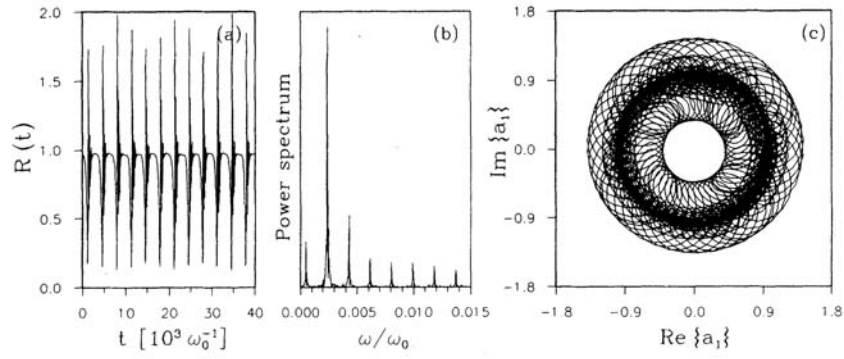


Figure 3.3: Reflectivity, (b) power spectrum and (c) phase diagram for $\beta_0 = 0.027$, [102].

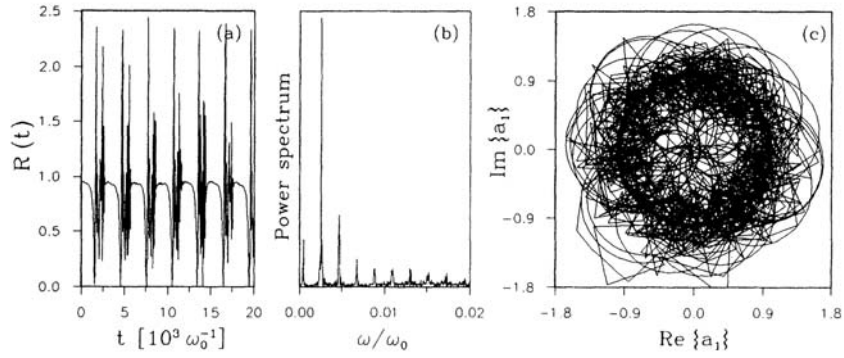


Figure 3.4: (a) Reflectivity, (b) power spectrum and (c) phase diagram for $\beta_0 = 0.03$, [102].

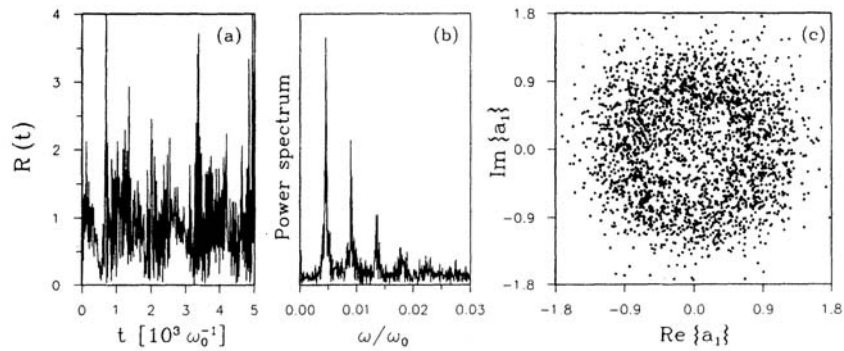


Figure 3.5: (a) Reflectivity, (b) power spectrum and (c) phase diagram for $\beta_0 = 0.05$, [102].

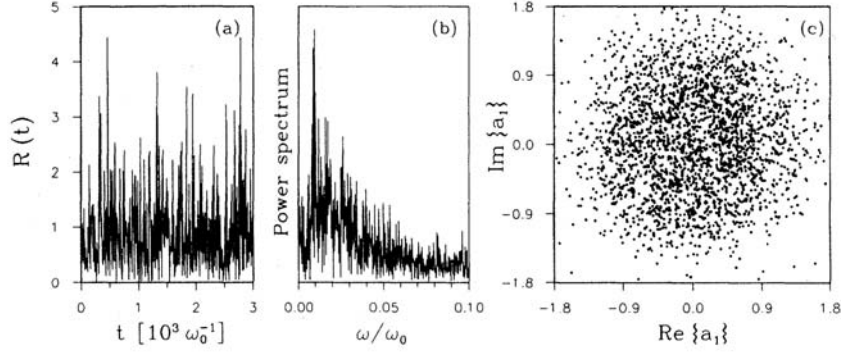


Figure 3.6: (a) Reflectivity, (b) power spectrum and (c) phase diagram for $\beta_0 = 0.1$, [102].

poral aspect of the backscattered wave at the left boundary of the plasma slab. For a system of partial differential equations (3.35), the temporal aspects must be correlated with spatial information, and more detailed insight is gained from the analysis of spatiotemporal patterns and the corresponding correlation functions. This is the subject of the next section.

3.2.4 Spatiotemporal Wave Patterns

The simulation results of the stimulated Raman backscattering dynamics exhibit spatiotemporal intermittency and spatiotemporal chaos and are described in terms of correlation functions having spatial and temporal scales. The numerically observed spatial states involved in the bifurcation sequence include coherent states, traveling waves, and intermittent and chaotic states. The global picture of both spatial and temporal attracting states for various spatiotemporal regimes for the backscattered wave and the EPW are listed in Table I. In general, the qualitative space-time behavior of the pump wave is almost identical to the corresponding patterns of the scattered wave. This is due to the fact that the coherent structures of the backscattered wave are determined by the incident pump wave, while the features of the EPW represent the outcomes of the interaction processes that take place between the pump and the backscattered wave. We give here a more detailed account of these spatiotemporal structures. For small values of the relative pump strength, the spatial structure resembles a semi-humplike structure that increases in size as the damping term (Γ) decreases. The mirrorlike symmetry of the scattered wave structure and the EPW structure with respect to each other is evident in Fig. 3.7. In next regime, a spatially periodic structure of the scattered wave superimposed on one-half of the hump occurs at regular time intervals, while no such structure can be noticed for the EPW. Further increase of the control parameter β_0 brings forth the appearance of the propagating EPW mode and flattening of the underlying spatial structure for both waves. The striking feature of the scattered wave pattern in this regime is the breatherlike coherent excitation oscillating in time [Fig. 3.8(a)]. As β_0 increases and leaves the parameter range corresponding to the mode locking temporal behavior, the most interesting feature is the change in spatial symmetry, particularly for the EPW. As the relative pump strength increases, the temporal translational symmetry of the backscattered co-

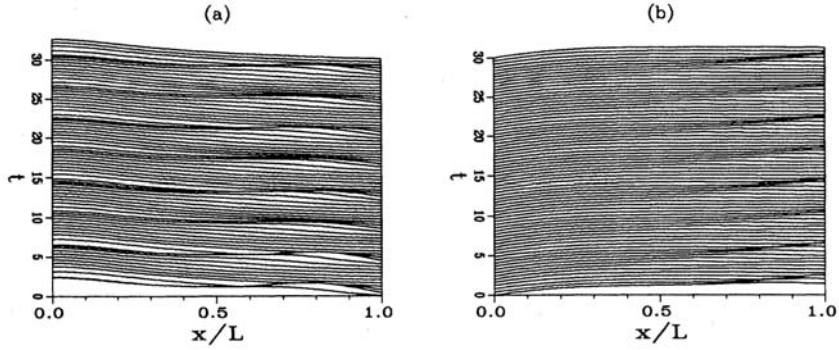


Figure 3.7: Space-time patterns of (a) backscattered wave and (b) electron plasma wave for $\beta_0 = 0.02534$, [102].

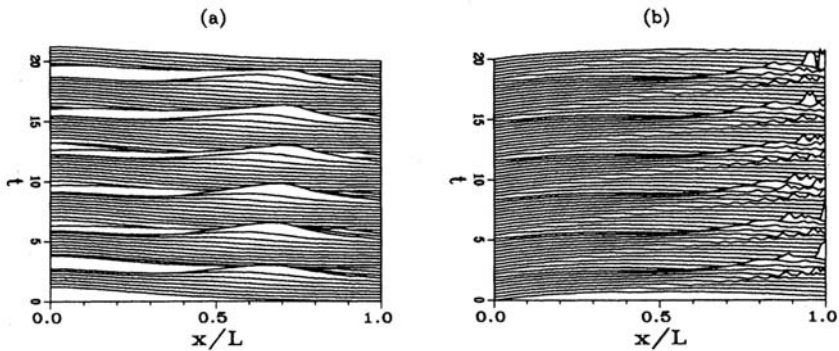


Figure 3.8: Space-time patterns of (a) backscattered wave and (b) electron plasma wave for $\beta_0 = 0.027$, [102].

herent structures breaks up more dramatically than the corresponding one of the EPW. A common feature of all four regimes is the same number of coherent structures in the time direction.

The transition from the spatiotemporal intermittency to spatiotemporal chaos (Fig. 3.11) is continuous in the sense that, as the threshold is approached from below, the number of turbulent domains slowly increases, accompanied with the breakup of laminar domain fronts. The autocorrelation functions for the two regimes (Figs. 3.9, 3.10, and 3.12) clearly show that the correlations fall off gradually both in time and in space. The well-defined correlation lengths (times) for these two regimes indicate that the dynamics is uncorrelated for lengths (times) greater than these characteristic values. The fact that the group velocity of the EPW is 30 times smaller than the backscattered wave velocity has important implications on the spatiotemporal characteristics of the corresponding wave patterns. The correlation length of the EPW is consequently approximately 30 times smaller than the correlation length of the backscattered wave (Figs. 3.10). Autocorrelation functions provide clear qualitative, although quantitatively not adequate, evidence of spatiotemporal chaos. Moreover, to determine the control parameter value at which the transition from intermittency to chaos occurs, methods from the theory of critical phe-

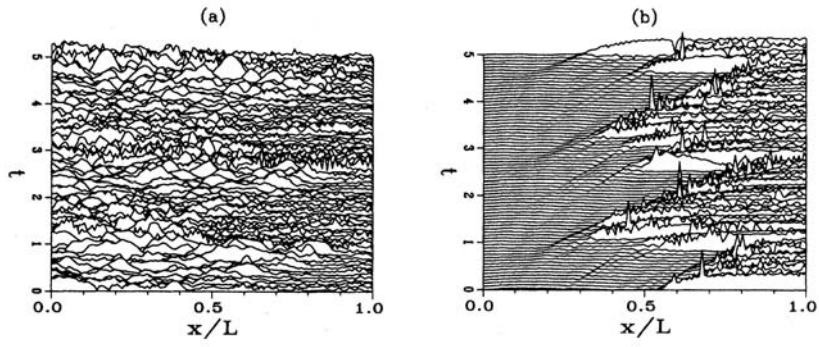


Figure 3.9: Space-time patterns of (a) backscattered wave and (b) electron plasma wave for $\beta_0 = 0.06$, [102].

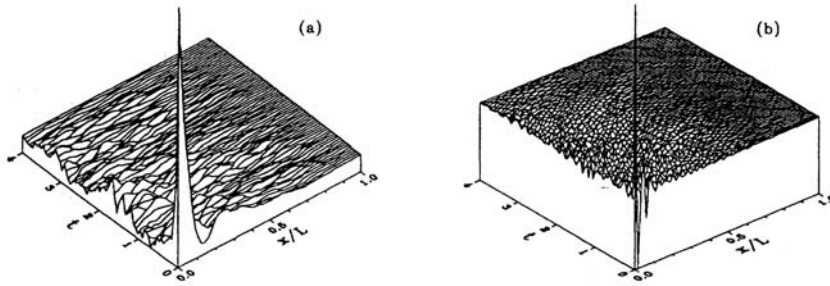


Figure 3.10: Autocorrelation functions for (a) backscattered wave and (b) electron plasma wave for $\beta_0 = 0.06$, [102].

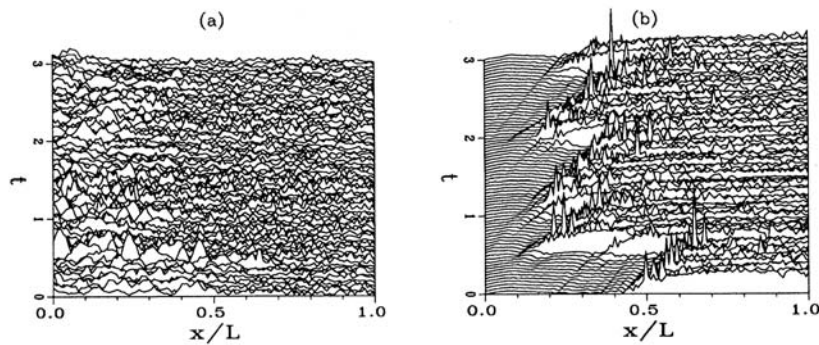


Figure 3.11: Spatiotemporal patterns of for (a) backscattered and (b) EPW for $\beta_0 = 0.1$, [102].

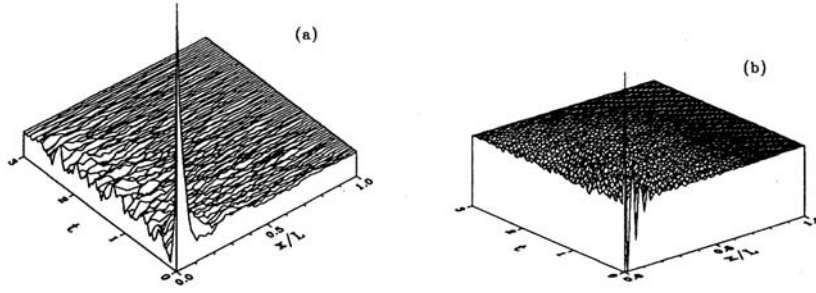


Figure 3.12: Autocorrelation function for (a) backscattered and (b) EPW for $\beta_0 = 0.1$, [102].

nomena and phase transitions will be used. These aspects of the analysis are addressed in the next two sections.

3.2.5 Quantitive Signatures of Spatiotemporal Regimes

To better understand the transition from regular to chaotic dynamics, the relationship between the spatial and temporal degrees of freedom in the system is essential. In this study we choose the local approach on the attractor of the EPW in order to define the spatiotemporal quantities such as dimension and entropy. The approach is characterized by determination of local orthogonal directions on the attractor (the local topological dimensionality) along which the local data points are distributed. The embedding space, and hence the attractor, is reconstructed with reference to spatial dependence. That is, embedding procedure consists in taking time series of each spatial location as one component of the embedding vector, and the number of spatial locations determines the embedding dimension. The centers defining local regions on the attractor are randomly selected in such a way that they nearly cover the entire surface of the attractor. The local dimension is determined by the rank of the local data matrix defined by the preselected number of nearest neighbors for each local center. The number of nearest neighbors is determined by the condition that the local region they define is linear and their number usually varies between 30 and 50. The test for local linearity consists in successively decreasing the number of points in the local region until further decrease does not decrease the number of dominant orthogonal directions [129]. The rank of the local data matrix is determined by the singular value decomposition (SVD). If the local data matrix is labeled \mathbf{U} , then the singular values λ_i of \mathbf{U} are equal to the square roots of the eigenvalues of the data covariance matrix $\mathbf{R} = \mathbf{U}^T \mathbf{U}$, and the number of nonzero singular values (eigenvalues) determines the local topological dimension of the attractor. Since it is almost impossible to obtain exactly zero eigenvalues either in numerical simulations or from experimental data, the main challenge in this approach is to determine the threshold below which an eigenvalue should be considered to be zero. The topological dimension of the whole attractor is calculated as the weighted average of local dimensions, i.e.,

$$\langle D \rangle = n_1 d_1 + n_2 d_2 + \dots + n_s d_s,$$

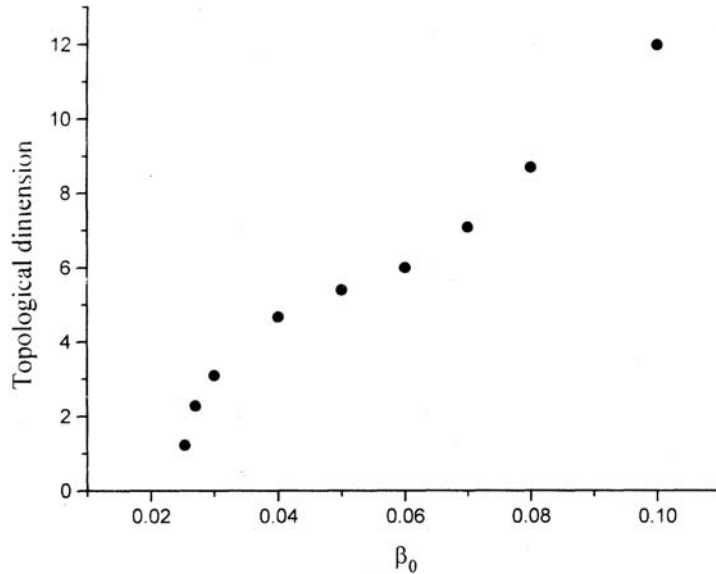


Figure 3.13: Topological dimension of EPW versus β_0 , [102].

where $n_i = m_i/N$, m_i is the number of local regions in which dimension d_i occurs, and N is the total number of local regions. Hence, as the local dimension is an integer value, the topological dimension of the whole attractor may be fractal in nature. Note that because of the nature of the embedding procedure, the dimension defined in such a way reflects the spatial and temporal dynamics simultaneously.

The separation of true signal from noise is accomplished using the method formulated on the basis of an information-theoretic criterion. Two such methods, the Akaike information criterion [130] and the minimum descriptive length of Risannen [131], have been extensively used in signal processing applications, particularly for the determination of the number of signals in high resolution arrays. However, since the Akaike information criterion tends to overestimate and the minimum descriptive length tends to underestimate the number of signal sources, active research is going on to overcome the shortcomings of these two criteria. In our approach we have used the modified information-theoretic criterion, which does not show these deficiencies, and an interested reader can find a complete account of this method in Ref. [132]. The resulting topological dimensions for various spatiotemporal patterns of the SRS are presented in Fig. 3.13. As more and more active modes take part in the dynamics, the dimension correspondingly changes and various spatiotemporal bifurcations may be identified through the dimension changes. Another important aspect of dimension calculations for extended systems, namely, density of dimension $\rho \equiv D(L)/L$, where L is the size of the system, has been verified as independent of L , and details of the growth rate of dimension as a function of the system size have been reported elsewhere [101].

Using the same embedding procedure, we have applied the Grassberger-Procaccia algorithm for calculating the widely used correlation dimension. The obtained results show very good agreement with the results for topological dimension for low-dimensional dy-

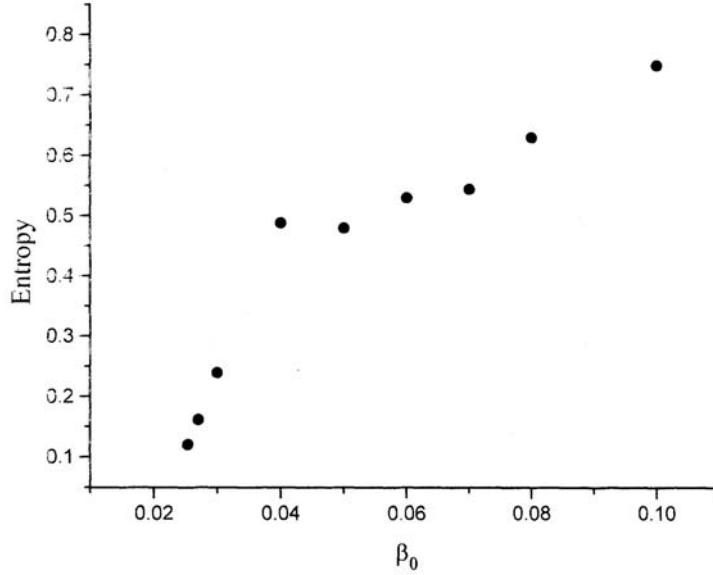


Figure 3.14: Entropy of EPW for values of pump β_0 , [102].

namics ($d < 8$). For higher dimensional dynamics the correlation dimension is inaccurate because of the intrinsic limitations of the algorithm. That is, the upper bound permitted by the algorithm is $2 \log_{10} N$, where N is the time dimension of the embedding matrix (length of the time series) [133]. In general, however, the advantages of local analysis of topological properties of the attractor are particularly evident in identifying important topological features due to, for example, thin directions, which may indicate that the corresponding attractor cross section is a Cantor set, or the effects due to the limited amount of data [134]. Moreover, the criterion for separating signals from noise is the integral part of this approach, while the correlation dimension, as well as other metric and probabilistic dimensions, are quite sensitive to the presence of noise. Note that SVD is often used as a noise reduction procedure before applying the correlation dimension algorithm. That is, the few dominant eigenvalues in the singular value spectrum are retained based on the certain arbitrary criterion, such as by counting those singular values (eigenvalues) that exceed a certain percentage of the largest singular value (eigenvalue), usually $\geq 95\%$ [135]. In either case, SVD is applied globally, while the information is lost on the local effects on noise, which can be of significant importance for thin directions on the attractor.

Important indicators of the sensitivity to initial conditions of the system are Lyapunov exponents, which represent the growth rates of edges of an infinitesimal tangent space to the trajectory of an attractor. In terms of singular values λ_i , the local Lyapunov exponents scale approximately as $\ln \lambda_i$. Hence, the number of local Lyapunov exponents is equal to the local topological dimension, and the number of positive local Lyapunov exponents averaged over the attractor increases with the increase of the control parameter, as well as with the system size.

The singular value decomposition of the spatiotemporal data matrix corresponds to

the spectral decomposition of the signal into spatial and temporal orthogonal modes,

$$u(x, t) = \sum_{i=1}^N \lambda_i \phi_i(x) \psi_i(t), \quad (3.43)$$

with

$$\lambda_1 \gg \lambda_2 \dots > 0,$$

and

$$(\phi_i, \phi_j) = (\psi_i, \psi_j) = \delta_{i,j},$$

which converges in norm. The pair (ψ_i, ψ_j) defines a spatiotemporal structure of energy λ_i^2 [136]. The relative energy of each structure is given as the ratio of one structure energy to the total energy of the signal [136, 137].

$$p_i = \lambda_i^2 / \sum_{i=1}^N \lambda_i^2 \quad (3.44)$$

Here the characterization of the eigenvalue spectrum is based on the principle that the information contained in the eigenvalues can be interpreted as a probability distribution, so that each eigenvalue can be viewed as an indication of how likely it is to identify a spatiotemporal structure within the whole spectrum. Based on the information-theoretic definition of entropy, the normalized entropy can be defined as

$$H(u) = - \lim_{k \rightarrow \infty} \frac{1}{\ln k} \sum_{i=1}^k p_i \ln p_i. \quad (3.45)$$

Because of the normalizing factor $1/\log k$, the entropy is defined in the range between 0 and 1. If the dynamics of the system is such that only one eigenvalue is different from zero (i.e., the energy is concentrated in only one eigenvalue), the spatiotemporal entropy is equal to 0, indicating the lowest level of complexity. On the other hand, if the energy is equidistributed, i.e., all eigenvalues are the same, the global entropy is equal to 1, indicating the highest possible complexity. In analogy with the local topological dimension, we can calculate local entropy while the global entropy can be obtained by ensemble averaging over the attractor. The spatiotemporal entropy of the EPW as a function of relative pump strength is presented in Fig. 3.14. The entropy evolves from a value close to zero corresponding to the steady (laminar) state; increases as new coherent structure emerge and the energy spreads out on the eigenvalues; and approaches the value of 0.76, where many structures carry similar amounts of energy. Both the entropy and the topological dimension display a clear distinction between STI and STC, and additional work is necessary to relate the local aspects of these two quantities to the universal characteristics of spatiotemporal intermittency and chaos in various physical systems.

3.2.6 Transition from Spatiotemporal Intermittency to Spatiotemporal Chaos

A method to locate a parameter threshold value is based on the coarse graining of the space-time data into binary values, according to which local spatiotemporal regions are

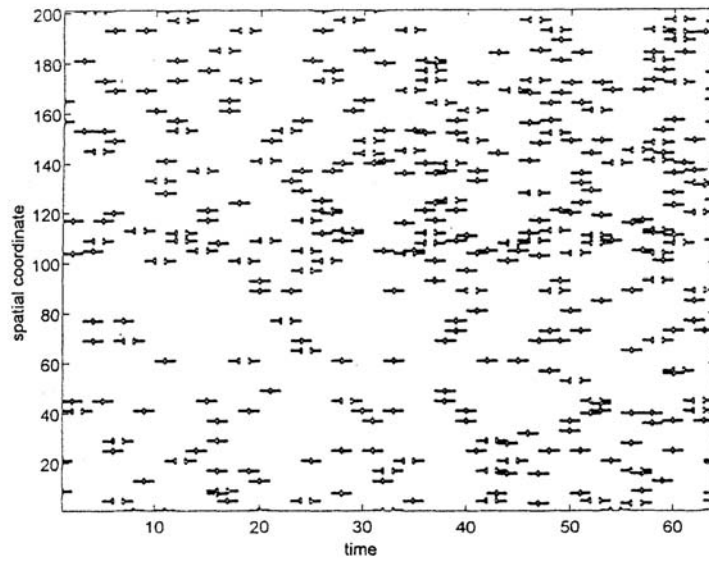


Figure 3.15: Spatiotemporal pattern in binary reduction for $\beta_0 = 0.06$, near intermittency threshold, [102].

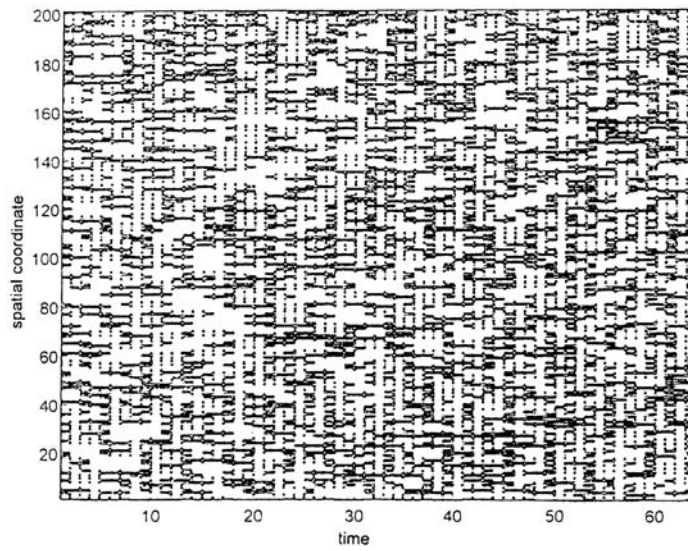


Figure 3.16: Spatiotemporal pattern in binary reduction for $\beta_0 = 0.1$, well in the turbulent regime, [102].

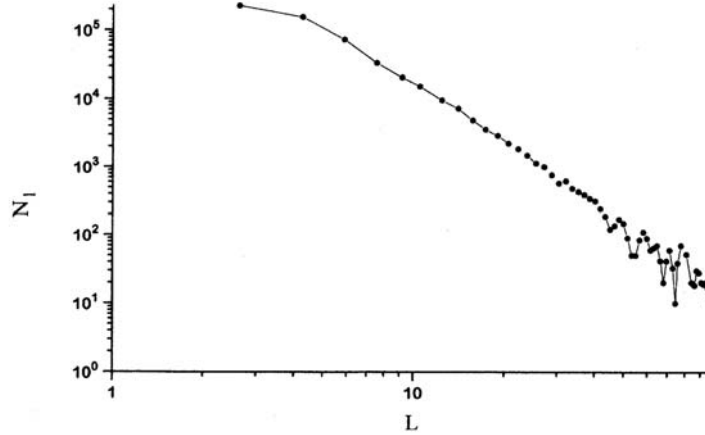


Figure 3.17: Histogram of laminar domains sizes for $\beta_0 = 0.06$, near the threshold, [102].

labeled only as either laminar or chaotic [138, 139]. Since in the laminar (quasiperiodic) regions the local amplitude is lower than in turbulent regions, by setting an arbitrary cutoff a binary representation may be obtained that easily distinguishes between chaotic and nonchaotic domains. The obtained representation seems to be independent on the precise cutoff value within the accuracy of the calculation. The two-state representation for the regimes corresponding to $\beta_0 = 0.06$ and $\beta_0 = 0.1$ are presented in Figs. 3.14 and 3.15, respectively. Assuming an analogy to directed percolation [140], the laminar phase corresponds to a state where chaotic (turbulent) states percolate through the lattice until the size in the time direction, the time-correlation length, is reached. Directed percolation is known for exhibiting a continuous (second order) phase transition, usually characterized by a critical exponent that scales the variation of the order parameter near the transition point. The order parameter in this framework is defined as the mean number of laminar or turbulent domains. The distribution of sizes of laminar domains, or the corresponding distribution of sizes of clusters of laminar sites, defines a correlation length (or size) that characterizes the patterns; Figs. 3.16-3.18, clearly confirm the existence of a critical threshold value. Near the threshold ($\beta_0 = 0.06$), the distribution of sizes of laminar domains is characterized by the power law behavior (with the characteristic exponent of the order of 3.0), while deep in the chaotic region ($\beta_0 = 0.1$) the behavior follows the exponential behavior with the characteristic exponent 1.5. An analogous statistical analysis was performed for the time domain distributions, and the temporal approach displays features similar to those obtained for the spatial distributions. The threshold in this case remains approximately the same ($\beta_0 = 0.06$), although the exponents are different. The distribution follows an algebraic decay, with a characteristic exponent 3.2, while above the threshold the decay is exponential with the characteristic exponent 1.2.

3.2.7 Conclusions

A study of the open, convective, weakly confined dissipative model of SRS as a paradigm of 3WI in an extended system was presented. The numerical simulation reveals a particularly beautiful example of a quasiperiodic route, accompanied by frequency locking, to

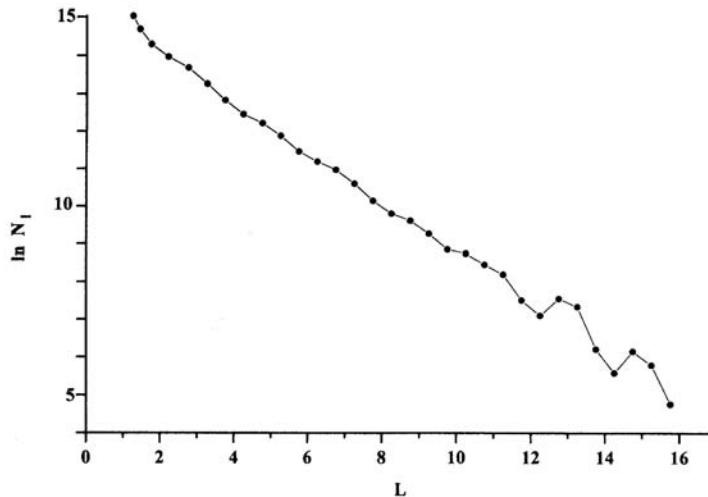


Figure 3.18: Histogram of laminar domains sizes for $\beta_0 = 0.1$, well in the turbulent regime, [102].

spatiotemporal chaos via spatiotemporal intermittency [102]. The striking feature of this scenario is intermittency in both space and time scales, with laminar regions exhibiting the quasiperiodic nature of the preceding attracting state, as distinguished from the chaotic domains by the change in spatial symmetry. The occurrence of the second frequency in the power spectrum of the quasiperiodic regime is apparently due to the appearance of a new spatial mode in the case of the backscattered wave (traveling wave in the case of the electron plasma wave), suggesting a complex interplay between spatial and temporal degrees of freedom. Changes in the topological dimension of the chaotic attractor can be directly correlated with changes in the number of active modes, and a similar conclusion is valid for the spatiotemporal entropy. An important item of information provided by this analysis is that it supports the view that the route to low-dimensional chaos represents the main dynamical frame on which the route to spatiotemporal chaos is built. The coarse graining of the space-time data into binary variables enables the use of the methods from the theory of critical phenomena to draw qualitative parallels between the transition from spatiotemporal intermittency to spatiotemporal chaos and directed percolation. The final claim in this section establishes the place of 3WI in the growing family of physical phenomena that display the intermittent route to spatiotemporal chaos [114].

3.3 Self-Organization in a Dissipative Three-Wave Interaction- Saturated SRS Paradigm

A nonlinear three-wave interaction in an open dissipative plasma model of a stimulated Raman backscattering is studied. An anomalous kinetic dissipation due to electron trapping and plasma wave breaking is accounted for in a hybrid kinetic-fluid scheme. We simulate a finite plasma with open boundaries and vary a transport parameter to examine a route to spatio-temporal complexity. An interplay between self-organization at micro-

kinetic and macro-fluid scales is found through quasi-periodic and intermittent evolution of dynamical variables, dissipative structures and related entropy rates. A consistency with a general scenario of self-organization is examined [124, 125].

3.3.1 Introduction

In recent papers on complexity and self-organization in plasmas a profound underlying structure in strongly nonlinear and complex plasma phenomena was revealed [141, 142]. Self-organization is a generic process of a creation of order in a nonlinear far-from-equilibrium system open to an environment [143]. Free energy supply, nonlinear instability and structural bifurcation which result in dissipation, entropy production and its subsequent removal from a system are key governing points [142, 143]. The above concept, as a working hypothesis, was successfully applied in studies of markedly diverse phenomena of the macro-scale MHD and micro-kinetic self-organization in plasmas. For a continual pumping of free energy and efficient excess entropy removal, generic self-organization to an intermittent state was found [142, 143].

In this section we examine an open convective dissipative model of a stimulated Raman backscattering. In fluid simulations (*vide supra*), rich spatio-temporal complexity, which exhibits transition to intermittency and chaos following a quasiperiodic route was revealed [102]. Detailed analysis of spatiotemporal patterns, examining the partition of energy among coherent structures has found a growing complexity and chaos as the pumping increases. However, based on general advancements in studies of plasma complexity [141, 143] it appears plausible that due to turbulence related anomalous dissipation, self-organization to a state of reduced complexity should be realized. To emulate the effect of entropy balance a hybrid three-wave interaction model that includes a phenomenological kinetic dissipation via particle trapping and wave breaking, a model, originally proposed by [104, 124].

3.3.2 Physical Preliminaries on Nonlinear Kinetic SRS

A resonant nonlinear three-wave interaction, as a physical concept, is a paradigmatic phenomenon which has found applications [81, 114, 123]. Stimulated scattering in a plasma represents a wide class of three-wave interactions related to nonlinear coupling of a finite amplitude electromagnetic pump wave to the electrostatic plasma (electron and/or ion) wave and the scattered electromagnetic wave [105]. Assuming that resonant matching between frequencies and wave numbers are satisfied, the pump parametrically excites the stimulated growth of the daughter waves from their thermal noise level.

Stimulated Raman scattering involves parametric coupling of an electromagnetic pump to an electron plasma wave and a scattered electromagnetic wave [97]. Various applications in laboratory: laser and radio-frequency wave driven plasmas, as well as in space and astrophysical plasmas were attempted [144, 145, 146, 147, 148]. Here, a nonlinear evolution of a stimulated Raman backscattering in an open dissipative plasma model is examined. Generally taken, we have shown invariants breaking points to an onset of non-stationarity for conditions of nonlinear phase detuning (3.39). Spatiotemporal complexity in a fluid model of stimulated Raman backscattering in a bounded weakly dissipative

plasma was attempted in [102]. A continual increase in complexity with a control parameter (e.g., pump strength) was predicted by this model as shown above, thus establishing its place in a family of paradigmatic physical phenomena that display an intermittent route to spatio-temporal chaos [114]. However, the effects of anomalous Raman dissipation and plasma electron heating followed by entropy expulsion, were omitted. It is a purpose of this section to introduce a plausible entropy inventory by a phenomenological modelling of anomalous kinetic dissipation related to Raman complexity, following [124]. In long saturated regimes, self-organization (SO) generic to an open dissipative system under a continuous free energy supply is expected [141].

Extensive studies of nonlinear stimulated Raman backscattering have been performed by analytics, fluid and particle simulations [97, 105, 144], and references therein. In a strongly driven case, Raman instability exponentiates until arrested by nonlinear and dissipative effects. The saturation comes, basically, through pump depletion and/or higher-order nonlinearities as well as kinetic dissipation related to electron trapping and plasma wave breaking [97, 105, 144]. While pump depletion is readily included in fluid modelling, the latter effects are inherently kinetic. However, after more than three decades of intensive particle simulation studies, nonlinear Raman scattering is understood to possess relatively clear, albeit anomalous overall features.

As a result of electron trapping and breaking of large plasma waves a hot tail-suprathermal electron population is generated. The corresponding velocity of hot (fast) electrons roughly equals the phase velocity of the electron plasma wave. As a general feature, two temperature (Maxwellian like) electron distribution is recorded, for the thermal-bulk and suprathermal-hot tail electron distributions. Energy exchange and hot component thermalization leads to an increase of the bulk temperature at the expense of plasma wave dissipation. However, actual details of this overall scenario are determined by complex wave turbulence and the electron transport, both influenced strongly by boundary and other plasma conditions. This qualitative understanding of anomalous Raman features has enabled useful scaling relations and semi-empirical formulas, typically extracted by averaging over time and shots of short-run particle simulation data. Generally taken, a realistic long time saturation (e.g., 10 000 plasma wave periods) does not appear to be assessable to even top performance particle simulations due to required computation time and limitations of the numerical scheme involving large number of particles [97, 151, 150].

It is this situation that has motivated us to address a problem of anomalous Raman in a long time evolution. A potential saturation to self-organizing plasma states using a general concept of complexity in plasmas in a system open to an environment is presented [124]. Firstly, a phenomenological hybrid fluid model to try to emulate basic physics of anomalous Raman scattering, as a precursor to state-of-the-art future particle simulation with open boundaries, is introduced.

At this point, we refer to an example of extensive analysis of nonlinear Raman saturation by Rose et al., [144, 145, 146]. In distinction to a simple adiabatic cubic nonlinearity (e.g., relativistic type) in our model equation for the electron plasma wave, these author(s) introduce nonlinearly coupled Langmuir-ion wave dynamics. Based on Zakharov's fluid model, processes like Langmuir decay, wave collapse and density modification are included in such description.. One- and two-dimensional (1-2D) simulations allowed comparison with realistic laser-plasma experimental conditions. In comparison, a weakly

coupled three-wave interaction model which include basic kinetic effects in 1D Raman model will be shown below. Although simple, kinetic dissipation gets self-consistently coupled with nonlinear Raman dynamics to study self organized saturated states. An important fact appeared, that both of mentioned approaches predict an intensity dependent spectral broadening and incoherence paradigm for Raman backscatter spectrum, as recently observed in number of experiments and simulations [144, 152, 153].

3.3.3 A Three-Wave Dissipative Interaction Model

Stimulated Raman backscattering in a plasma is a paradigm of a three-wave parametric interaction where by a strong electromagnetic wave (0- laser pump) decays into an electron plasma wave (2) and backscattered wave (1) downshifted in frequency. This nonlinearly coupled 3WI process obeys a resonant matching condition for wave frequencies and wave numbers.

In the one-dimensional case, which is of main importance, the linear parametric Raman backscatter growth rate is given

$$\gamma_0 \approx 0.5\beta_0\sqrt{\alpha/(1-\alpha)}\omega_0, \quad (3.46)$$

where α is the ratio between the electron plasma frequency and the frequency of the pump:

$$\alpha = \omega_{pe}/\omega_0 = \sqrt{n/n_{cr}} \quad (3.47)$$

and the quantity β_0 , as shown earlier, is a relative pump strength.

In a bounded, uniform, fully ionized plasma, the spatio-temporal evolution of the coupled waves' normalized, slowly-varying complex amplitudes $a_i(\xi, \tau)$ governed by the known set of partial differential equations in dimensionless units, as presented in the previous chapter, namely

$$\frac{\partial a_0}{\partial \tau} + V_0 \frac{\partial a_0}{\partial \xi} = -a_1 a_2, \quad (3.48)$$

$$\frac{\partial a_1}{\partial \tau} - V_1 \frac{\partial a_1}{\partial \xi} = a_0 a_2^*, \quad (3.49)$$

$$\frac{\partial a_2}{\partial \tau} + V_2 \frac{\partial a_2}{\partial \xi} + \gamma a_2 + i\sigma |a_2|^2 a_2 = \beta_0^2 a_0 a_1^*, \quad (3.50)$$

where time and space coordinates are as usual, measured in units ω_0^{-1} and L^{-1} respectively, with plasma wave damping rate given by γ . Ions are kept fixed to preserve the plasma quasineutrality. Damping of the light waves is neglected, while T designates the bulk electron temperature directly proportional to EPW group velocity, $V_2 \sim T_e$, (3.37). An important feature of the system (3.48-3.50) is the self-modal cubic term in the plasma wave equation. It appears as a nonlinear phase shift due to a detuning of a large amplitude plasma wave. A time-only (space-only) version of (3.48-3.50) was discussed before in detail, and it was shown to exhibit bifurcation to a low-dimensional chaos under restricted conditions. The spatially extended model is of a more physical significance and have revealed rich complexity related to low-dimensional as well as spatio-temporal chaos [85, 102, 114].

The system (3.48-3.50) can be solved in space-time for standard initial and finite boundary conditions. In the loss-free steady state with zero phase shift, it predicts the well known elliptic function solutions, together with three (Manley-Rowe) conserved integrals [102, 123]. However, it was shown above that for a nonzero phase shift ($\sigma > 0$) in finite boundaries, the third phase involving invariant is broken (3.27). Thus a violation of the steady-state assumption, points to a nonstationary Raman saturation. Indeed, subsequent evolution exhibits a quasiperiodic route to low dimensional intermittency to finally result in a fully developed spatiotemporal chaos, in previous fluid model. However, we note that in a physical sense chaotic dynamics is related to plasma wave breaking followed at a kinetic level by a strong nonlinear electron acceleration and heating. In turn, hot electrons can Landau damp freshly SRS driven plasma waves to suppress and strongly alter Raman instability evolution and possibly limit the level of kinetic complexity. To perform studies in this direction a phenomenological hybrid 3WI dissipative SRS model is introduced. The set of 3WI equations is solved simultaneously with simple model equations for hot and bulk plasma heating. In this way, effective damping $\gamma(t)$ and the electron temperature $T(t)$ in 3WI, appear as dynamical variables, in contrast with a standard model that assumes a constant plasma background. Therefore, dissipative effects on a long time Raman saturation and kinetic self-organization in an open system can be emulated [124].

3.3.4 Kinetic-Hybrid Scheme

It was chosen to simulate conditions relevant to anomalous Raman saturation in an open system, which means allowing an energy exchange between an interaction region and the plasma environment. To emulate basic kinetic effects missed by the earlier fluid 3WI model of (3.48-3.50), a phenomenological “hybrid” scheme which includes generation of hot electrons, that are trapped and accelerated in large amplitude plasma wave was introduced [124]. Assuming that a part of plasma wave energy is transferred to electrons that are resonant with the forward propagating electron plasma wave, hot electron generation equation together with a 3WI set (3.48-3.50) can be numerically solved. As a consequence, the suppression of Raman instability by hot electrons through a Landau damping is found. We further assume that the effective damping (γ term) of plasma waves is due to both linear Landau damping on hot electrons and nonlinear term, due to bulk electron acceleration via electron trapping in large EPW. Finally, a simple total energy balance equation to model bulk heating via the redistribution of the absorbed energy between bulk (thermal) and hot (suprathermal) electrons is added. It seems that, although straightforward, this idea appears to be a rare attempt to treat a rather complex, inherently kinetic regime of anomalous Raman by a simple fluid-based model. Simplifying the electron transport to spatially averaged dynamics a hybrid like coupled mode scheme that includes effects of both thermal and hot electrons on Raman instability is introduced. Open boundaries are carefully accounted for, thus enabling to model conditions of both current-free streaming and inhibited electron transport. A brief check of the model performance against particle simulation is done, in order to try closer fits by adjusting a free transport parameter in the scheme. In that way, a longtime Raman saturation in an open system is addressed, an important question that remains difficult to answer even by highest performance particle

simulations [97, 150].

We start by assuming the electron distribution function, including thermal (bulk) and hot component, to be approximated by bi-Maxwellian electron distribution [97, 124]:

$$F(x, t, v) = n_h(x, t) f_h(v) + n_b(x, t) f_b(v), \quad (3.51)$$

where n_h and $n_b (\gg n_h)$ stand for slowly varying hot and bulk electron density, respectively, with each $f_i(v)$ normalized to unity. We assume that the total hot electron current includes a source term due to trapped resonant electrons (in the thermal Maxwellian tail). Therefore we write

$$\begin{aligned} j_h(x, t) &= \int_{hot} v F(v) dv = n_h(x, t) \int_{-\infty}^{\infty} v f_h(v) dv \\ &+ n_b(x, t) \int_{v_{ph}-v_{tr}}^{v_{ph}+v_{tr}} v f_b(v) dv, \end{aligned} \quad (3.52)$$

where v_{ph} is the plasma wave phase velocity and v_{tr} is characteristic velocity of resonant electrons ($v \sim v_{ph}$) with orbits trapped in a trough of a large amplitude plasma wave (a_2) (in physical units, $v_{tr}(t) \sim (2eE_2/mk_2)^{1/2}$), where the maximum E_2 amplitude allowed is limited by the plasma wavebreaking condition [97, 110, 111].

Equation of continuity for hot electrons is written in a standard form

$$\frac{d}{dt} n_h(x, t) \equiv \frac{\partial}{\partial t} n_h(x, t) + \nabla \cdot j_h = 0, \quad (3.53)$$

or after performing the spatial average by integration, defined as

$$\langle \dots \rangle_L = \frac{1}{L} \int_0^L (\dots) dx, \quad (3.54)$$

where $n_h(t)$ is hot electron density averaged over the plasma length L , we obtain

$$\frac{d}{dt} n_h(x, t) + \frac{1}{L} j_h(x, t) \Big|_0^L = 0. \quad (3.55)$$

Using the electron current one gets equation for the hot electron generation

$$\frac{d}{dt} n_h(t) = \frac{n_b(L, t)}{L} \int_{v_{ph}-v_{tr}(L, t)}^{v_{ph}+v_{tr}(L, t)} v f_b(v) dv - \kappa n_h(t), \quad (3.56)$$

We note $v_{tr}(0, t) = 0$, due to the boundary condition for a plasma wave. The loss term is due to electrons which escape through open plasma boundaries, with the transport coefficient $\kappa = kv_h/L \approx kv_{ph}/L$ and coefficient k equal to 1 and 2 for a free streaming and a Maxwellian flow, respectively. We now proceed to evaluate the effective damping rate in the plasma wave equation (3.50). We assume that a total damping is due to both linear Landau and nonlinear (trapping and wave breaking) effects, namely, the total damping rate: $\gamma(t) = \gamma_{Landau} + \gamma_{nl}$, where for the linear Landau term we shall use a standard

formula appearing in the literature [97] Further, we introduce the spatially integrated plasma wave energy density, through

$$W(t) = \frac{1}{L} \int_0^L \frac{1}{8\pi} |E(x,t)|^2 dx. \quad (3.57)$$

The rate of the electron plasma wave energy dissipation through linear and nonlinear processes is

$$2\gamma W(t) = 2\gamma_{Landau} W(t) + \frac{mn_b(L,t)}{2L} \int_{v_{ph}-v_{tr}(L,t)}^{v_{ph}+v_{tr}(L,t)} v^3 f_b(v) dv, \quad (3.58)$$

where an integral term, gives a nonlinear contribution to a plasma wave damping, thus effectively determining the value of γ_{nl} .

Finally, equation for the total energy balance between the plasma wave, the thermal and hot electron component, by starting from a general conservation law (w_i denotes energy, ϕ_i denotes energy flux) is given

$$\frac{d}{dt} \sum_i w_i(x,t) = \frac{\partial}{\partial t} \sum_i w_i(x,t) + \text{div} \sum_i \phi_i(x,t) = 0. \quad (3.59)$$

For spatially averaged (integrated) quantities one has to evaluate the energy flux at open boundaries

$$\frac{d}{dt} \sum_i W_i(x,t) + \frac{1}{L} \sum_i \Phi_i(x,t) \Big|_0^L = 0. \quad (3.60)$$

For our system, the plasma wave, thermal and hot electron component: $W_i(t) \Rightarrow W + E_{th} + E_h$, the electron bulk and hot energy densities are simply: $E_{th} = n_b T_b$ and $E_h = n_h T_h$; and the average energy flux, is given by $\Phi_{th} = \pm v_{th} E_{th}$ and $\Phi_h = \pm v_h E_h$. For the Maxwellian distribution the above energy flux has to be multiplied by a weighting factor $\simeq 0.65$. However, in real plasmas, an inhibited energy flux is modified by a parameter $k \sim (0 - 1)$; in a largely heuristic model of a highly complex electron energy transport [97]. The \pm sign indicates the flux direction at the plasma boundary (at $x = 0, L$). By using the above expressions, the equation for the thermal energy variation is given as

$$\frac{d}{dt} [n_b(t) T_b(t)] = 2\gamma W(t) - \frac{d}{dt} [n_h(t) T_h(t)] - \frac{k}{L} [\Phi_{th} + \Phi_h - \Phi_q] \Big|_0^L, \quad (3.61)$$

where we have introduced Φ_q as the return flux of fresh (cold) ambient electrons through an open plasma boundary (*vide infra*). We note in passing, a simplified form of (3.55) with respect to a lack of a finite relaxation time, that is normally required for a heat transfer via e.g. hot-bulk electron collisions.

3.3.5 Open Boundary Model

A simulation model with boundaries open to electromagnetic waves and plasma electrons is introduced. Accordingly, a transport between an interaction region and a large surrounding plasma environment is allowed. For electrons which escape from an interaction

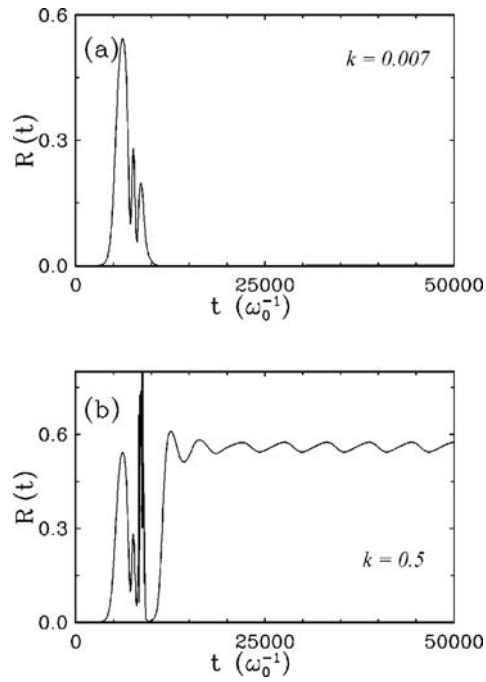


Figure 3.19: Raman reflectivity in time versus transport parameter k , for (a) closed (inhibited transport) and (b) open system, [124].

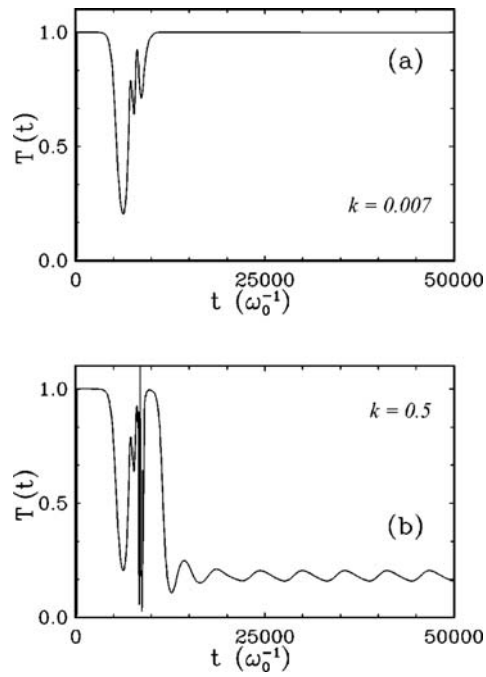


Figure 3.20: Raman reflectivity in time versus transport parameter k , for (a) closed (inhibited transport) and (b) open system, [124].

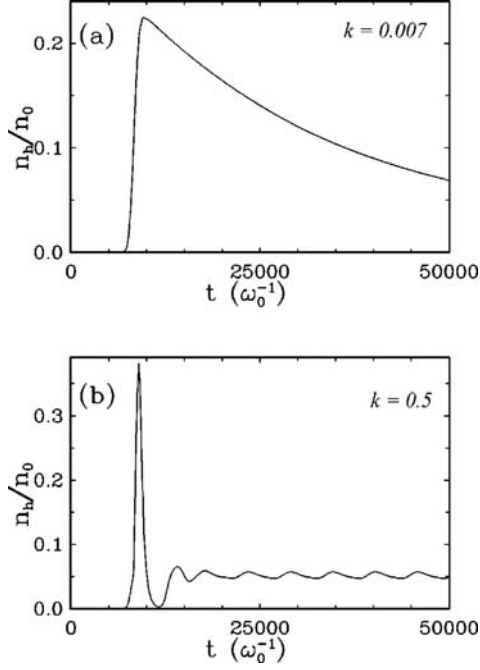


Figure 3.21: Hot electron density variation in time for (a) closed and (b) open system, [124].

layer (length L) fresh ambient electrons are re-injected in order to preserve the plasma quasineutrality. Accordingly, a long-time Raman saturation could be observed under conditions with physically realistic current free boundaries.

A straightforward procedure is briefly sketched. The total electron current at the boundary is written as an algebraic sum of the outgoing and the incoming components: $J_{tot} = J_{out} + J_{in}$, with $J_{out} = J_{th} + J_h$, for thermal and hot electron contributions. Further, $J_{in} = n_q v_0$, where $n_q v_0$ stands for a current of ambient electrons streaming into a plasma layer. By requiring the total current at the boundary to be zero, one readily evaluates J_{in} in terms of the thermal and hot components. The energy flux carried by ambient electrons (with temperature T_0) is simply $\Phi_q \simeq J_{in} T_0$, making the calculation of the loss term in the thermal balance equation an easy task.

In further text, we refer to the above model as the "open" one, in contrast with the "closed" plasma model where an electron transport is inhibited by a build up of a space charge. The latter case corresponds to e.g. plasma-vacuum boundary, with the energy flux (Φ), coefficient restricted to low values (few percent). As for the Maxwellian with an open boundary we get the factor, $k \sim 0.65$; one should expect a wide range of dynamical regimes between these two extreme transport cases [97].

3.3.6 Micro-Scale and Macro-Scale Self-Organization

The Raman complexity obtained in simulations is briefly analyzed. Parameters of the "standard case" studied in depth in a fluid 3WI model are chosen (vide supra) [102, 124].

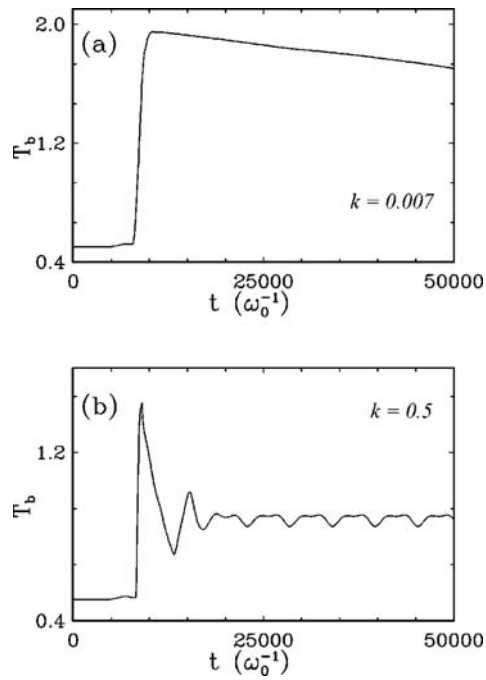


Figure 3.22: Bulk electron temperature in time versus k for (a) closed and (b) open system, [124].

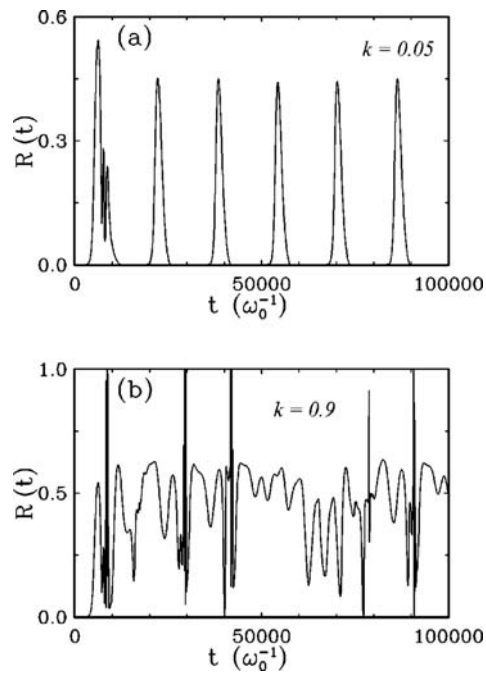


Figure 3.23: Raman reflectivity in time shows complexity of (a) quasiperiodic and (b) intermittent type, [124].

Initial plasma parameters are: the electron density is 0.1 of the critical density, the electron temperature of 0.5 keV and the plasma length $L = 100c/\omega_0$. Further, the electron transport coefficient k is taken to be the basic *control* parameter. A continuous pumping is applied to observe different saturated states for an open and closed (isolated) system. Typically, the reflection and transmission coefficients in time, as well as the evolution of hot electron density and bulk temperature, are plotted. The pump strength is equal to 0.025. For two cases of an open ($k = 0.5$) and nearly closed ($k = 0.007$) plasma system, after transient pulsations reflectivity saturates to a quasisteady state. As expected, the transmittivity follows the same scenario. However, while for the open system reflectivity saturates to a high-finite value, in a strongly confined-closed system reflectivity quickly drops to zero due to a complete Raman suppression (see Figs. 3.19 and 3.20). More precise insight into a phase space dynamics finds out that, while the closed system saturates to an exact steady state (*fixed point*), in the open case, small periodic oscillations (*limit cycle*) are present. Moreover, in the latter case, the moderate hot electron population, which is locked to a finite-plasma wave as a source of hot electrons, saturates to a quasisteady state. In distinction, in the closed system, hot density is high and nonstationary, typically an order of magnitude higher than above, rapidly generated during an abrupt dissipation of Raman driven large plasma waves (Fig. 3.21). It gradually relaxes in later times, due to a convective cooling through the boundaries. Similar to hot population, important difference exists in the bulk temperature evolution. In the open system, temperature saturates to a steady-state, moderately above an initial-ambient temperature. This is due to a continual energy input via kinetic dissipation balanced by efficient convection losses. In the closed system, rapid and large temperature rise is observed, to reach its maximum by halting Raman instability, later to experience slow cooling through transport inhibited boundaries (Fig. 3.22).

Further, by carefully varying a control parameter k , generic structural bifurcations along the route to complexity are studied (see Figs. 3.23-3.26). For $k = 0.05$, in the system, a bifurcation to a new state of kinetic self-organization is revealed. Structural instability transits to a quasiperiodic dynamical state, observed readily as a train of temporal pulses in the reflectivity and transmittivity. Hot electron population follows, with strong quasi-periodic pulsations peaked around 20% of the initial electron density. On the other hand, the bulk temperature, after its initial growth, exhibits strong sawtooth oscillations reminiscent of the MHD type observed in magnetically confined fusion plasmas. By further exploring a parameter space for the open system with $k = 0.9$ a transition to a quasiperiodic dynamics, interrupted by chaotic bursts is found. Closer insight into the attractor space finds irregular portion of the dynamics, pointing to an intermittent nature of this regime. Indeed, hot electrons are intermittently ejected in a form of intense jet spikes ($T_h \sim 22 \text{ keV}$) as a striking feature of this type of kinetic self-organization (Fig. 3.25). Bulk temperature follows an intermittent scenario, by exhibiting quasiperiodic (QP) fluctuations, somewhat above its initial value (Fig. 3.26). Finally, a temporal route to complexity by plotting a phase space attractor for the hot electrons is shown (Fig. 3.27). By varying a transport parameter k ($0.7 - 0.9$) a gradual onset of complexity and chaos is revealed, starting with typical “stretching and folding” features of the periodic trajectories.

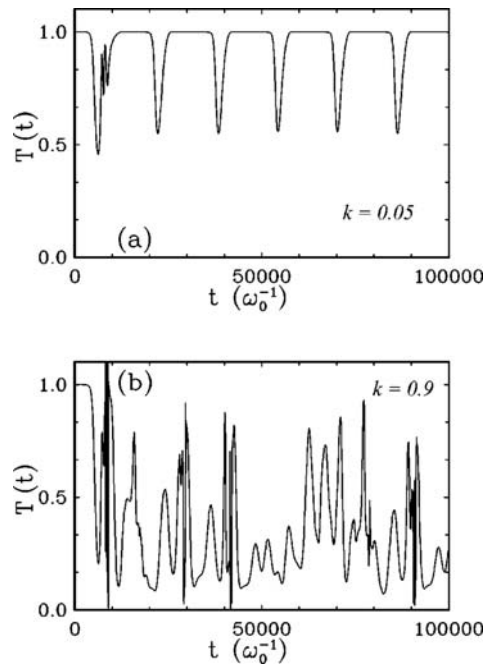


Figure 3.24: Raman transmittivity in time for (a) quasiperiodic and (b) intermittent regime, [124].

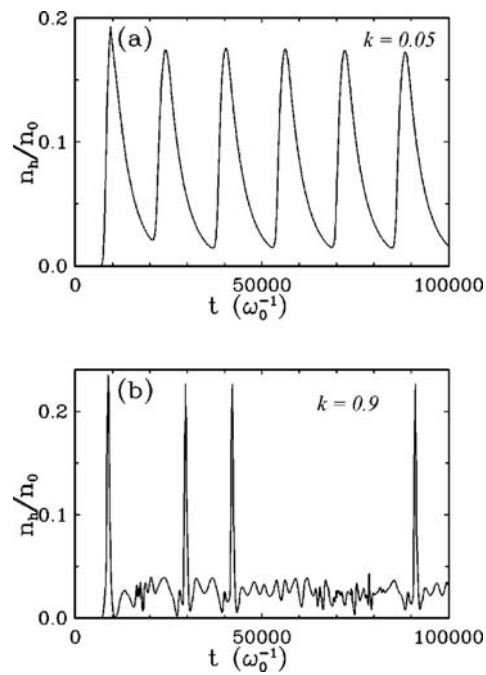


Figure 3.25: Hot electron density in time shows (a) quasiperiodic and (b) intermittent pulsations, [124].

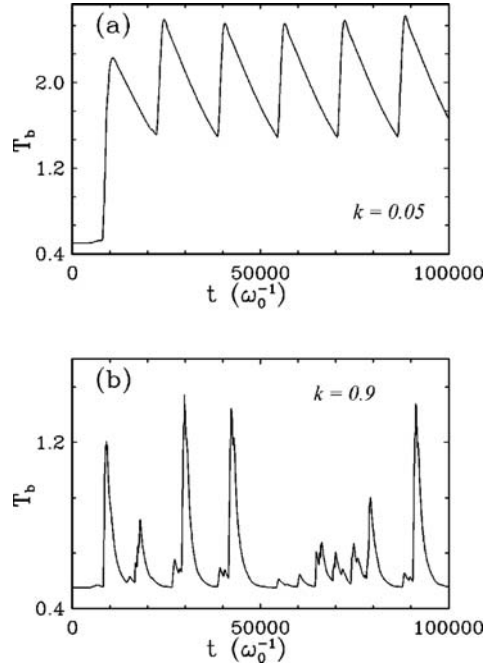


Figure 3.26: Bulk electron temperature in time exhibits (a) sawtooth and (b) intermittent pulsations, [124].

3.3.7 Dissipative Structures and Entropy Rate

Self-organization (SO) in strongly nonlinear far-from equilibrium systems can lead to a creation of ordered states that reflect an interaction of a given system with its environment. These dynamical structures or patterns, named dissipative structures to stress the crucial role of dissipation in their creation, have become a central theme of the science of complexity [141, 143]. On the other hand, there is a fundamental role of the entropy, in particular, the rate of entropy change in an open system. The rate of entropy production and its removal basically governs self-organization features of a system. A large amount of effort has been spent in attempts to relate the entropy rate extrema to structural bifurcations and transitions between different ordered states [141, 143].

First, focus is at self-organized dissipative structures developed at macro scales. Indeed, in above model, basic wave and fluid density variables were assumed to vary slowly in space-time. Therefore, we expect that original spatiotemporal profiles, found in simulations, should correspond to large dissipative structures, self-organized at macroscale levels. As an illustration, we plot the plasma wave profile (Fig. 3.28), in particular, to reveal a genuine spatiotemporal nature of an intermittent regime as compared to regular dynamical regimes of the steady-state and QP type. Spatiotemporal complexity of quasi-steady and traveling wave patterns with regular and chaotic features is found in different states of self-organization.

However, a hybrid nature of this model will also allow to recover kinetic type properties of self-organization. By using an analytical dependence of the electron Maxwellian distribution on varying hot (bulk) temperature and density (3.51) a genuine picture of

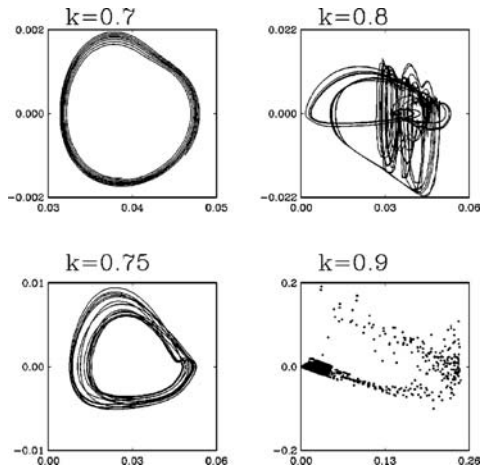


Figure 3.27: Phase diagrams for hot electrons, show stretching and folding of orbits reminiscent of chaos, [124].

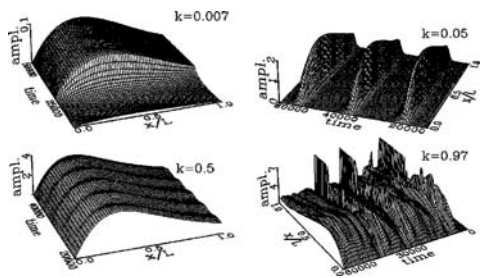


Figure 3.28: Spatiotemporal dissipative structures of electron plasma wave for different k values exhibit a varying level of complexity; from the steady-state via quasi-periodic to intermittent regimes, [124].

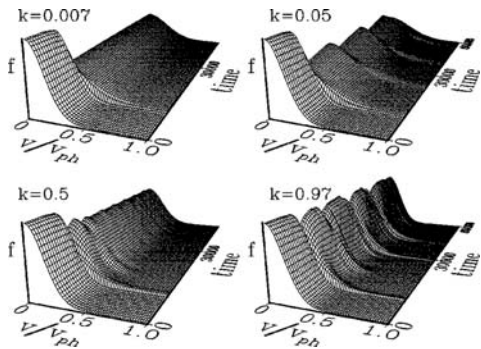


Figure 3.29: 3D view of $f_e(v)$ for different saturated regimes reveals micro-kinetic SO of both thermal and suprathermal electron components, [124].

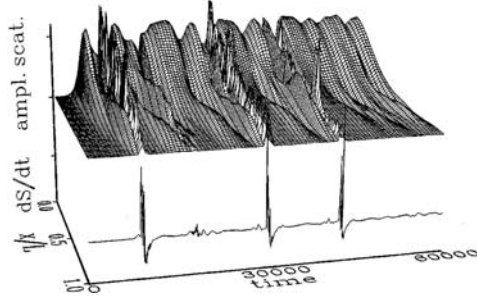


Figure 3.30: Dissipative plasma wave structures vs. entropy rate in time. Positive entropy rate jumps coincide with onset of chaos, while negative bursts indicate transition to a laminar phase of SO at macro-scales, [124].

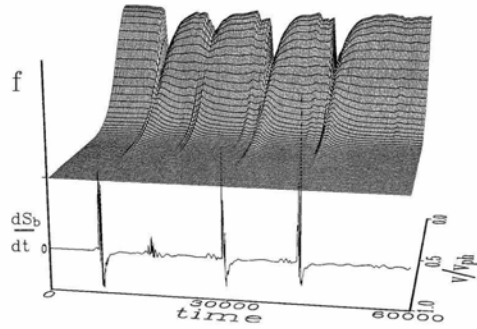


Figure 3.31: Intermittent electron distribution function versus entropy rate in time. Similar to Fig. 3.30, structural bifurcations at micro-scales coincide with entropy rate extrema, [104].

kinetic self-organization at plasma microscales is exposed. To show the self-organization featuring micro-levels, the electron velocity distribution function is plotted. In Fig. 3.29 a three-dimensional view of the electron velocity distribution in time for different saturated Raman regimes is shown, as indicated by values of parameter k . Kinetic self-organization of varying complexity is revealed in thermal and hot regions of the electron distribution. Furthermore, one can observe a complex connection and interplay between self-organization at *macro* and *micro* levels in a plasma.

Finally, in Fig. 3.30 the entropy rate $dS(t)/dt$ in time together with a spatio-temporal profile of the scattered wave energy is presented. To calculate the entropy S related to electron distributions as: $S(t) = S_b(t) + S_h(t)$, one uses

$$S_i(t) = - \int_0^L dx \int_{-\infty}^{\infty} dv f_i(x, v, t) \ln f_i(x, v, t), (i = b, h). \quad (3.62)$$

For an intermittent regime, featuring an interchange between chaotic and laminar phases, clear evidence of structural transitions corresponding to the maximum (positive) and minimum (negative) entropy rate is found. As a striking example of self-organization in an open system, a rapid entropy increase which coincides with an onset of a chaotic

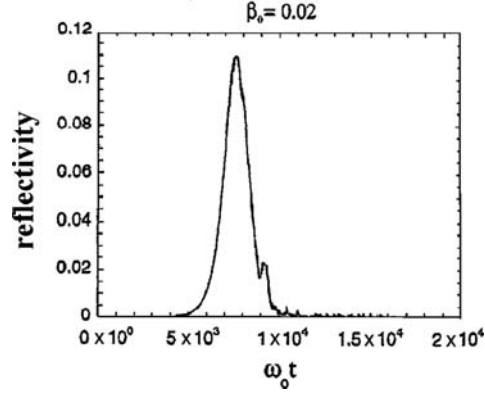


Figure 3.32: Raman reflectivity in time from $1\frac{1}{2}D$ EM particle-in-cell simulations, for laser pump of 0.02 shows remarkable agreement with Fig. 3.19 (a) obtained from 3WI hybrid model, [151].

phase is revealed. Subsequent anomalous dissipation and entropy growth is halted by a sudden entropy expulsion into the environment. Negative burst in entropy rate indicates a bifurcation from a chaotic, back to a laminar quasiperiodic phase. An intermittent nature of this regime is shown through a repetitive pattern of behavior. We note that complex spatiotemporal dissipative wave structures are mapped onto a more simple entropy rate time series. Intervals of near zero entropy rate during a laminar phase, mean a net balance between the entropy production and the expulsion. This appears to be an example of a stationary nonequilibrium state possibly realized in a strongly nonlinear open system [143].

3.3.8 Summary

In summary, above simple findings appear to be early indication of a generic intermittent scenario in a kinetic self-organization of anomalous Raman instability. Although phenomenological rather than rigorous, above dissipative 3WI open model has self-consistently accounted for the entropy production and removal, for both thermal and suprathermal electrons. In this way, rich transient Raman complexity gradually gets self-organized and attracted to definite saturated dynamical states, such as: steady-state, quasi-periodic and intermittent ones. At this point, one is able to claim a type of consistency with the working hypothesis and general scenario of self-organization in plasmas. As a further step, an important justification for such hybrid modeling of saturated Raman complexity by the open boundary particle simulation may be expected [149]. As an illustration, we show in Fig. 3.32, particle-in-cell simulation data for a model of an isolated plasma slab (thin foil layer) in a vacuum [151]. For the same parameters as above, particle simulations evidently support the Raman reflectivity patterns (Fig. 3.19) for a nearly closed ($k = 0.007$) plasma system; recovering also quasi-periodic incoherent spectra similar to those shown above. Generally taken, intensity dependent route to incoherent SRS spectral broadening consistent with this model has been also observed in relativistic laser-plasma interaction experiments, see e.g., Refs. [152, 153].

Chapter 4

Relativistic Plasma Interactions

Ever since the much acclaimed paper of Akhiezer and Polovin [154] plasma theorists have been attempting to comprehend complex dynamics related to the propagation of high and ultra-high intensity electromagnetic (EM) radiation through a plasma. This topic was successfully revisited a number of years later by Kaw and Dawson [155] whose analysis threw more light on the propagation of coupled longitudinal-transverse waves of arbitrary intensity. The high phase velocity case was soon solved exactly by Max and Perkins [156]. The problem of relativistic laser-plasma interactions is of particular interest concerning the fast ignition concept relevant to contemporary laser inertial confinement fusion research [157, 158]. Moreover, the understanding of relativistic laser pulse evolution in a plasma is basic to many new applications, including optical-field-ionized x-ray lasers [159], plasma-based electron accelerator schemes [160, 161], as well as, the interpretation of some astrophysical phenomena (see [162], and references, therein). Currently, the field of relativistic laser matter interaction has diverged in two main broad directions; the first, related to laser fusion, high energy densities and laboratory astrophysics, and the second, related to ultra high field science, high energy particle acceleration and photon beam and ultra-fast attosecond phenomena [163]. Many of these applications require stable channel guiding of intense laser beams over longer distances, without significant energy losses [164]. The pioneer workers in this field [154, 155, 156], did not consider the stability of the plane-wave solutions, related to nonlinear interaction between normal plasma modes. However, in a highly nonlinear system we have to deal with nonlinearly coupled modes under various plasma conditions.

4.1 Electronic Parametric Wave Coupling

In a plasma exists a number of instabilities that can be classified as parametric excitations of resonantly coupled waves [165]. This is a multi-wave process since in practice an externally driven pump wave can interact with a whole spectrum of waves in a plasma. However, in most cases the process can be well described as three wave interaction as long as certain resonant triplet of waves evolves (almost) independently of the others. The three-wave interaction is the lowest-order nonlinear effect for a system approximately described by a linear superposition of discrete waves. In order for nonlinear 3WI to occur, the wave frequencies and wave vectors must satisfy matching conditions

$$\omega_- = \omega_0 - \omega_1, \quad \mathbf{k}_- = \mathbf{k}_0 - \mathbf{k}_1, \quad (4.1)$$

where modes "0" and "1" represent pump and plasma waves and mode "-" represent scattered wave (Stokes wave). When the pump amplitude exceeds a certain threshold, the remaining two waves which are initially at noise level start growing absorbing energy from the pump wave. In addition to the above wave triplet described by (4.1), another, usually weaker triplet having two waves in common with the first one can be observed in experiments and simulations. The resonant conditions for this wave triplet are

$$\omega_+ = \omega_0 + \omega_1, \quad \mathbf{k}_+ = \mathbf{k}_0 + \mathbf{k}_1, \quad (4.2)$$

where ω_+ denotes upshifted frequency by the frequency ω_1 . This wave is known as anti-Stokes wave. The fact that the triplets (4.1) and (4.2) share two waves can be used as a concept to control the chaos in three-wave coupling [102, 166]. There is a rich experimental and theoretical support in laboratory and space plasmas for nonlinear wave-wave interactions that involve EM waves, Langmuir waves and ion-acoustic waves. The decay schemes for these processes are

- (i) photon \longrightarrow photon + Langmuir wave
- (ii) photon \longrightarrow photon + ion-acoustic wave

where the first type of the decay is known as stimulated Raman scattering (SRS) and the second type as stimulated Brillouin scattering (SBS). These scattering processes are of particular interest to inertial confinement fusion since the fusion targets are characterized by large regions of an underdense plasma. Much works have been devoted to stimulated Raman and Brillouin scattering instabilities, concerning their ability to serve as a source of high energetic particles which may preheat the core of a fusion pellet. The stimulated scattering can be large enough to reflect a significant part of the laser light and thus to decrease the laser efficiency at the target [167]. As has been shown by experiments and computer simulations there can be a rich interplay between these two instabilities [168, 169, 170]. In present-day laser-fusion research SRS instability is of a major concern [168, 171, 172, 173].

4.1.1 Stimulated Raman Scattering

The stimulated Raman scattering is a parametric decay of an incident EM wave (ω_0, k_0) into a scattered light (ω_s, k_s) and an electron plasma (Langmuir) wave (ω_{EPW}, k_{EPW}) . The matching conditions [97, 174], for the frequencies and wave numbers are

$$\omega_0 = \omega_s + \omega_{EPW}, \quad k_0 = \pm k_s + k_{EPW}, \quad (4.3)$$

respectively, where

$$k_0 = \frac{\omega_0}{c} \left(1 - \frac{n}{n_{cr}} \right)^{1/2}, \quad (4.4)$$

$$k_s = \frac{\omega_s}{c} \left(1 - \frac{\omega_p^2}{\omega_s^2} \right)^{1/2}, \quad (4.5)$$

+ (-) denotes forward (backward) scattering, n is the density, $n_{cr} = n\omega_0^2/\omega_p^2$ is the critical density and $\omega_p = (ne^2/(\varepsilon_0 m))^{1/2}$ is the plasma frequency. In the low-temperature limit the dispersion equation for Langmuir wave is $\omega_{EPW}^2 = \omega_p^2 + 3k_{EPW}^2 v_t^2$, where $v_t = (T/m)^{1/2}$ is the electron thermal velocity and T is the temperature.

In the process of SRS, the EM pump wave is scattered by ripples of the electron plasma density. A ponderomotive force that arises due to the beats of the pump and scattered light further enhances these density ripples. There is a positive feedback loop and therefore an instability can occur. However, since the minimum frequency of EM waves in a plasma is ω_p , as can be seen from the frequency matching condition ($\omega_0 > 2\omega_p$), SRS instability can occur for electron densities $n < 0.25n_{cr}$. Note that this condition can be shifted to higher densities due to the presence of highly energetic particles or/and due to large amplitude electromagnetic waves.

The phase velocity of the plasma wave produced during parametric interaction can be slow enough to reach back into the tail of the background plasma electron distribution function. The tail electrons can obtain energy from the wave by becoming trapped in the electron plasma wave and damping it. In fact, this dominantly occurs for stimulated Raman backward scattering (B-SRS) where the phase velocity of the electron plasma wave for low density is $v_{ph} \approx \frac{\omega_p}{2k_0}$. For stimulated Raman forward scattering (F-SRS) the phase velocity is nearly the velocity of light and a very low number of particles have initial energy to be trapped and accelerated. However, when the pump wave propagates through a plasma for a large enough distance, a large amplitude electron plasma wave can be driven producing a significant number of high energetic electrons.

4.1.2 Relativistic Dispersion Relation for Cold Plasma

In order to obtain insight into relativistic parametric instabilities, in this section we derive a hybrid dispersion equation for EM wave scattering in an unmagnetized homogeneous cold plasma, [175, 176]. The ions are fixed as a cold plasma background and dynamics of electrons is relativistic. We assume that the radiation field is linearly polarized ($\mathbf{E} = E\mathbf{e}_y$) and consists of a pump wave

$$\mathbf{A}_0 = \frac{1}{2}A_0\mathbf{e}_y e^{i(\mathbf{k}_0 \cdot \mathbf{x} - \omega_0 t)} + c.c. \quad (4.6)$$

and two daughter waves

$$\mathbf{A}_+ = \frac{1}{2}A_+\mathbf{e}_y e^{i(\mathbf{k} \cdot \mathbf{x} - \omega t)} e^{i(\mathbf{k}_0 \cdot \mathbf{x} - \omega_0 t)} + c.c. \quad (4.7)$$

$$\mathbf{A}_- = \frac{1}{2}A_-\mathbf{e}_y e^{-i(\mathbf{k} \cdot \mathbf{x} - \omega^* t)} e^{i(\mathbf{k}_0 \cdot \mathbf{x} - \omega_0 t)} + c.c. \quad (4.8)$$

propagating in x direction. Here, \mathbf{A} is the vector potential, index "0" denotes the laser wave, while "+" and "-" stand for daughter waves, Stokes ($\omega - \omega_0$, $\mathbf{k} - \mathbf{k}_0$) and anti-Stokes

$(\omega + \omega_0, \mathbf{k} + \mathbf{k}_0)$, respectively. The amplitudes of the scattered waves are assumed to be much smaller than the amplitude of the pump wave ($A_+, A_- \ll A_0$). As one can see the frequency and wave vector matching conditions are included in expressions (4.7) – (4.8), so ω and k represent respectively the frequency and wave vector of ES wave. The starting point for the description of the interaction of these waves in a cold plasma fluid are Maxwell equations

$$\mathbf{E} = -\nabla\phi - \frac{\partial\mathbf{A}}{\partial t}, \quad (4.9)$$

$$\mathbf{B} = \nabla \times \mathbf{A}, \quad (4.10)$$

$$\nabla \times \mathbf{B} = \mu_0\mathbf{j} + \varepsilon_0\mu_0\frac{\partial\mathbf{E}}{\partial t}, \quad (4.11)$$

the continuity equation

$$\frac{\partial n}{\partial t} + \nabla \cdot (n\mathbf{v}) = 0, \quad (4.12)$$

and the relativistic equation of motion

$$m\frac{d\gamma\mathbf{v}}{dt} = -e(\mathbf{E} + \mathbf{v} \times \mathbf{B}), \quad (4.13)$$

where \mathbf{E} and \mathbf{B} are the electric and magnetic fields, ϕ is the scalar potential, \mathbf{j} is the current density, n is the electron density, \mathbf{v} is the velocity and γ is the relativistic Lorentz factor.

Using vector identity $\nabla \times (\nabla \times \mathbf{A}) = \nabla(\nabla \cdot \mathbf{A}) - \nabla^2\mathbf{A}$, from Maxwell equations one can obtain

$$\frac{1}{c^2}\frac{\partial^2\mathbf{A}}{\partial t^2} - \nabla^2\mathbf{A} + \nabla\left(\frac{1}{c^2}\frac{\partial\phi}{\partial t} + \nabla \cdot \mathbf{A}\right) = \mu_0\mathbf{j}, \quad (4.14)$$

and, on the other hand, the equation of motion (4.13) can be rewritten as

$$\frac{\partial\gamma\mathbf{v}}{\partial t} = \frac{e}{m}\left(\nabla\phi + \frac{\partial\mathbf{A}}{\partial t}\right) - c^2\nabla\gamma. \quad (4.15)$$

Here, equations (4.13), (4.14) and (4.15) will be examined order by order in the amplitudes of the incident waves¹, by writing,

$$\mathbf{j} = -en\mathbf{v} = \mathbf{j}^{[1]} + \mathbf{j}^{[2]} + \mathbf{j}^{[3]} + \dots \quad (4.16)$$

where

$$\mathbf{j}^{[1]} = -en_0\mathbf{v}^{[1]}, \quad (4.17)$$

$$\mathbf{j}^{[2]} = -en_0(\mathbf{v}^{[2]} + n^{[1]}\mathbf{v}^{[1]}), \quad (4.18)$$

$$\mathbf{j}^{[3]} = -en_0(\mathbf{v}^{[3]} + n^{[1]}\mathbf{v}^{[2]} + n^{[2]}\mathbf{v}^{[1]}), \quad (4.19)$$

¹The approach presented in this section is in fact weakly-relativistic since it requires an expansion of the relativistic factor. A fully relativistic approach can be used in the case of circularly polarized EM waves since the amplitude of the electric field and the electron quiver velocity remain constant.

and

$$\gamma \approx 1 + \frac{1}{2} \frac{v^2}{c^2} + \dots = 1 + \frac{1}{2} \frac{(\mathbf{v}_0 + \mathbf{v}_+ + \mathbf{v}_-)^2}{c^2} + \dots \quad (4.20)$$

Using renormalization $e\mathbf{A}/m \rightarrow \mathbf{A}$ and radiation gauge $\nabla \cdot \mathbf{A} = 0$, in first-order of perturbations we have

$$\mathbf{v}_\perp^{[1]}(\omega_0, k_0) = \mathbf{A}_0, \quad (4.21)$$

$$\mathbf{v}_\perp^{[1]}(\omega + \omega_0, k + k_0) = \mathbf{A}_+, \quad (4.22)$$

$$\mathbf{v}_\perp^{[1]}(\omega - \omega_0, k - k_0) = \mathbf{A}_-^*, \quad (4.23)$$

where "*" denotes complex conjugate. No density fluctuations are produced in first-order, $n^{[1]} = 0$.

In second order from the continuity equation and equations (4.14) and (4.15) we write, respectively,

$$\frac{\partial n^{[2]}}{\partial t} + \nabla \cdot \mathbf{v}_\parallel^{[2]} = -\nabla(n^{[1]}v_\parallel^{[1]}) = 0, \quad (4.24)$$

$$\frac{1}{c^2} \nabla \frac{\phi^{[2]}}{\partial t} = -\frac{\mu_0 n_0 e^2}{m} \mathbf{v}_\parallel^{[2]}, \quad (4.25)$$

($e\phi/m \rightarrow \phi$), and

$$\frac{\partial \mathbf{v}_\parallel^{[2]}}{\partial t} = \nabla \phi^{[2]} - \frac{1}{2} \nabla_\parallel (\mathbf{v}_\perp^{[1]} \cdot \mathbf{v}_\perp^{[1]}), \quad (4.26)$$

so that we have

$$\mathbf{v}_\parallel^{[2]} = \frac{1}{2} \frac{k\omega}{\omega^2 - \omega_p^2} (\mathbf{v}_\perp^{[1]} \cdot \mathbf{v}_\perp^{[1]})_\omega, \quad (4.27)$$

$$\phi^{[2]} = -\frac{1}{2} \frac{\omega_p^2}{\omega^2 - \omega_p^2} (\mathbf{v}_\perp^{[1]} \cdot \mathbf{v}_\perp^{[1]})_\omega, \quad (4.28)$$

$$n^{[2]} = \frac{1}{2} \frac{k^2}{\omega^2 - \omega_p^2} (\mathbf{v}_\perp^{[1]} \cdot \mathbf{v}_\perp^{[1]})_\omega. \quad (4.29)$$

The beating of the pump and scattered waves give perturbations of the plasma quantities at $(2\omega_0, 2k_0)$:²

²From equations (4.30) – (4.32) one can obtain the following expressions for perturbations in the longitudinal direction at $(2\omega_0, 2k_0)$ [177, 178],

$$v_\parallel^{[2]}(2\omega_0, 2k_0) = -E_0 \frac{e^2}{m^2} \frac{k_0}{\omega_0} \frac{1}{4\omega_0^2 - \omega_p^2} \cos 2(k_0x - \omega_0t),$$

$$E^{[2]}(2\omega_0, 2k_0) = E_0^2 \frac{e}{m} \frac{\omega_p^2}{2\omega_0^2} \frac{k_0}{4\omega_0^2 - \omega_p^2} \sin 2(k_0x - \omega_0t),$$

$$n^{[2]}(2\omega_0, 2k_0) = -E_0^2 \frac{e^2}{m^2} \frac{k_0^2}{\omega_0^2} \frac{1}{4\omega_0^2 - \omega_p^2} \cos 2(k_0x - \omega_0t).$$

$$\mathbf{v}_{\parallel}^{[2]}(2\omega_0, 2k_0) = \frac{2k_0\omega_0}{4\omega_0^2 - \omega_p^2}(\mathbf{A}_0 \cdot \mathbf{A}_0), \quad (4.30)$$

$$\phi^{[2]}(2\omega_0, 2k_0) = -\frac{1}{2} \frac{\omega_p^2}{4\omega_0^2 - \omega_p^2}(\mathbf{A}_0 \cdot \mathbf{A}_0), \quad (4.31)$$

$$n^{[2]}(2\omega_0, 2k_0) = \frac{2k_0^2}{4\omega_0^2 - \omega_p^2}(\mathbf{A}_0 \cdot \mathbf{A}_0), \quad (4.32)$$

at $(\omega + 2\omega_0, k + 2k_0)$:

$$\mathbf{v}_{\parallel}^{[2]}(\omega + 2\omega_0, k + 2k_0) = \frac{(k + 2k_0)(\omega + 2\omega_0)}{(\omega + 2\omega_0)^2 - \omega_p^2}(\mathbf{A}_0 \cdot \mathbf{A}_+), \quad (4.33)$$

$$\phi^{[2]}(\omega + 2\omega_0, k + 2k_0) = -\frac{\omega_p^2}{(\omega + 2\omega_0)^2 - \omega_p^2}(\mathbf{A}_0 \cdot \mathbf{A}_+), \quad (4.34)$$

$$n^{[2]}(\omega + 2\omega_0, k + 2k_0) = \frac{(k + 2k_0)^2}{(\omega + 2\omega_0)^2 - \omega_p^2}(\mathbf{A}_0 \cdot \mathbf{A}_+), \quad (4.35)$$

at $(\omega - 2\omega_0, k - 2k_0)$:

$$\mathbf{v}_{\parallel}^{[2]}(\omega - 2\omega_0, k - 2k_0) = \frac{(k - 2k_0)(\omega - 2\omega_0)}{(\omega - 2\omega_0)^2 - \omega_p^2}(\mathbf{A}_0^* \cdot \mathbf{A}_-^*), \quad (4.36)$$

$$\phi^{[2]}(\omega - 2\omega_0, k - 2k_0) = -\frac{\omega_p^2}{(\omega - 2\omega_0)^2 - \omega_p^2}(\mathbf{A}_0^* \cdot \mathbf{A}_-^*), \quad (4.37)$$

$$n^{[2]}(\omega - 2\omega_0, k - 2k_0) = \frac{(k - 2k_0)^2}{(\omega - 2\omega_0)^2 - \omega_p^2}(\mathbf{A}_0^* \cdot \mathbf{A}_-^*), \quad (4.38)$$

and at (ω, k) :

$$\mathbf{v}_{\parallel}^{[2]}(\omega, k) = \frac{k\omega}{\omega^2 - \omega_p^2}(\mathbf{A}_0^* \cdot \mathbf{A}_+ + \mathbf{A}_0 \cdot \mathbf{A}_-^*), \quad (4.39)$$

$$\phi^{[2]}(\omega, k) = -\frac{\omega_p^2}{\omega^2 - \omega_p^2}(\mathbf{A}_0^* \cdot \mathbf{A}_+ + \mathbf{A}_0 \cdot \mathbf{A}_-^*), \quad (4.40)$$

$$n^{[2]}(\omega, k) = \frac{k^2}{\omega^2 - \omega_p^2}(\mathbf{A}_0^* \cdot \mathbf{A}_+ + \mathbf{A}_0 \cdot \mathbf{A}_-^*). \quad (4.41)$$

Since $A_{\pm} \ll A_0$, the second (longitudinal) harmonics of the scattered waves $[2(\omega \pm \omega_0), 2(k \pm k_0)]$ can be neglected.

In third order the total currents at the frequencies and wave vectors of the pump and scattered waves are derived. Since we have

$$\frac{\partial^2 \mathbf{A}}{\partial t^2} - c^2 \nabla^2 \mathbf{A} = -\omega_p^2 \mathbf{v}^{[1]} + \frac{e}{m\epsilon_0} \mathbf{j}^{[3]}, \quad (4.42)$$

one can obtain an amplitude dependent dispersion equation for the pump wave. At the peak of the wave amplitude we have

$$\omega_0^2 = \omega_p^2 \left[1 - \frac{\beta^2}{4} \left(\frac{3}{2} - \frac{2c^2 k_0^2}{4\omega_0^2 - \omega_p^2} \right) \right] + c^2 k_0^2, \quad (4.43)$$

where $\beta = \frac{eE_0}{m\omega_0 c}$ is the laser strength. As we can conclude from equation (4.43), a high intensity wave introduces a relativistic shift in its natural frequency (or a shift in the wave number). For very low densities $\omega_0 \gg \omega_p$, the amplitude dependent part of equation (4.43), can be approximated as $\frac{\beta^2}{4}$, whereas near the critical density $\omega_0 \approx \omega_p$, this term is $\approx \frac{3\beta^2}{8}$.

For the scattered waves, on the other hand, we have

$$\mathcal{D}_+ A_+ = \Gamma \mathcal{D}_1^+ A_+ - \Gamma \mathcal{D}_2 A_-^*, \quad (4.44)$$

$$\mathcal{D}_- A_-^* = \Gamma \mathcal{D}_1^- A_-^* - \Gamma \mathcal{D}_2 A_+, \quad (4.45)$$

where $\Gamma = \frac{\omega_p^2 \beta^2}{4}$ and $\mathcal{D}_\pm = [(\omega \pm \omega_0)^2 - \omega_p^2 - c^2(k \pm k_0)^2]$,

$$\mathcal{D}_1^\pm = \left(\frac{c^2 k^2}{\omega^2 - \omega_p^2} + \frac{c^2 (k \pm 2k_0)^2}{(\omega \pm 2\omega_0)^2 - \omega_p^2} - 3 \right),$$

$$\mathcal{D}_2 = \left(\frac{c^2 k^2}{\omega^2 - \omega_p^2} + \frac{2c^2 k_0^2}{4\omega_0^2 - \omega_p^2} - \frac{3}{2} \right).$$

Finally, equations (4.44) and (4.45) can be combined to give the hybrid dispersion equation

$$\mathcal{D}_- \mathcal{D}_+ = \Gamma (\mathcal{D}_- \mathcal{D}_1^+ + \mathcal{D}_+ \mathcal{D}_1^-) + \Gamma^2 (\mathcal{D}_2^2 - \mathcal{D}_1^+ \mathcal{D}_1^-). \quad (4.46)$$

Note that the term $\sim \Gamma^2$ can be neglected.

Solutions of the Relativistic Dispersion Relation

The hybrid dispersion equation (4.46) is a sixth order equation in ω . It was solved numerically for a broad range of densities and laser strengths as a function of the real wave number k normalized to the wave number of the pump wave k_0 . The solutions of the dispersion equation [176], the real ω_r and imaginary part ω_i (the temporal growth rate) of the ES wave frequency ω are normalized to the frequency of the pump wave ω_0 .

In Fig.4.1 the solutions of the hybrid equation (4.46) are shown for plasma density $n = 0.1n_{cr}$ and laser strengths (a) $\beta = 0.3$ and (b) $\beta = 0.6$. The solution for $k/k_0 > 1$ is associated with the backward stimulated Raman scattering (B-SRS) instability, whereas the solution $k/k_0 < 1$ represents the forward stimulated Raman scattering (F-SRS) instability. The temporal growth rate for B-SRS and F-SRS instabilities are distinct for considered parameters. Moreover, instability branches are well separated in k space. For sufficiently high laser intensity, the relativistic correction to the mass of electrons oscillating in the incident electric field causes the relativistic modulational instability (RMI) [179]. The source of the RMI is the dependence of the wave dispersion on the amplitude

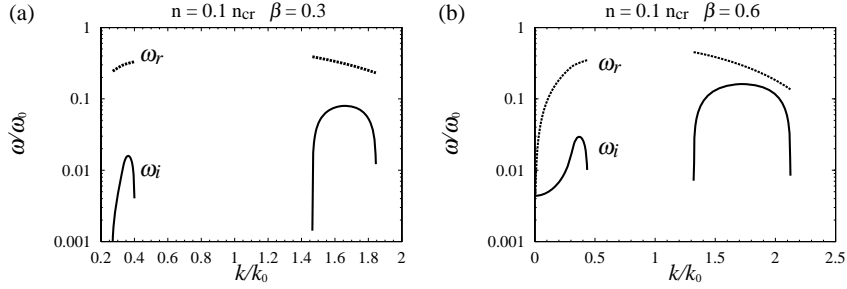


Figure 4.1: Solutions of the hybrid dispersion equation (equation 4.46) for $n = 0.1n_{cr}$ and laser strengths (a) $\beta = 0.3$ and (b) $\beta = 0.6$. The solid lines are the growth rate (ω_i) and the dashed lines are the real part of the frequency (ω_r). The frequencies and wave numbers are normalized to ω_0 and k_0 , respectively, [176].

of waves (see equation (4.43)). The consequent effect is that small perturbations of the original wave envelope become narrower and larger following an accumulation of the wave energy into a smaller space [179]. In Fig.4.1b, the low-frequency, low-wave-number tail connected to F-SRS branch corresponds to this instability. The relativistic modulation propagates in the direction of the incident large-amplitude EM wave.

In view of the Stokes and anti-Stokes sidebands, it should be pointed out that the contribution of the anti-Stokes wave (4.7) to B-SRS can be neglected, since this wave is non-resonant for backward scattering. For F-SRS and RMI both waves, Stokes (4.8 and anti-Stokes (4.7), give the contribution. In particular for $k/k_0 \ll 1$, the amplitude of the anti-Stokes wave is of order of the amplitude of the Stokes wave ($A_+ \approx A_-$) [180].

For higher electron densities, $n = 0.2n_{cr}$ (Fig. 4.2) and $n = 0.25n_{cr}$ (Fig.4.3) the solutions are plotted for several laser strengths, (a) $\beta = 0.2$, (b) $\beta = 0.3$, (c) $\beta = 0.4$ and (d) $\beta = 0.6$. As we can see, for $n = 0.2n_{cr}$ (Fig.4.2a) there is a gap between Raman branches that disappears with increasing the laser strength (Fig.4.2b). The RMI branch appears for higher EM wave intensities with a gap that separates the RMI and SRS instability (Fig.4.2c). Further increasing the incident wave intensity results in merging of all branches (Fig.4.2d). The behavior of the solutions shown in Fig.4.3 is similar to the behavior described above, although it should be noted that the backward and forward Raman branches are already connected for $\beta = 0.2$.

In general, as one can conclude from Figs. 4.1-4.3, for $n \leq 0.25n_{cr}$ the RMI has a lower growth rate than the SRS instability. For low plasma densities the B-SRS instability is the leading instability. With increasing density or/and laser strength the Raman branches get closer and merge. As is expected, an increase in the laser strength increases the growth rates of the instabilities.

As an illustration of the solutions in the range of densities $n > 0.25n_{cr}$, in Fig.4.4 we show unstable solutions of the hybrid dispersion equation for $n = 0.4n_{cr}$ and laser strengths $\beta = 0.4$ (Fig.4.4a), $\beta = 0.422$ (Fig.4.4b), $\beta = 0.45$ (Fig.4.4c) and $\beta = 0.6$ (Fig.4.4d). As we can see, in a plasma with density $> 0.25n_{cr}$, when SRS is halted, only the RMI is found (figure 4.4a). However, an increase in the laser strength results in the appearance of the B-SRS branch, relativistically shifted to high densities (Fig.4.4b). For

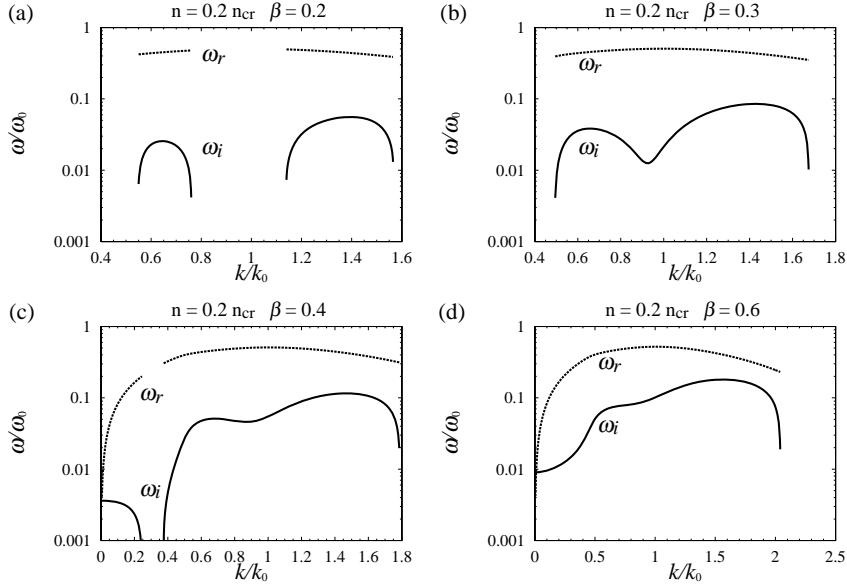


Figure 4.2: Solutions of the hybrid dispersion equation (equation 4.46) for $n = 0.2n_{cr}$ and laser strengths (a) $\beta = 0.2$, (b) $\beta = 0.3$, (c) $\beta = 0.4$ and (d) $\beta = 0.6$. The solid lines are the growth rate (ω_i) and the dashed lines are the real part of the frequency (ω_r). The frequencies and wave numbers are normalized to ω_0 and k_0 , respectively, [176].

higher laser strengths, the SRS instability again becomes the leading instability (Fig.4.4c). Finally, the RMI and SRS instability branches merge (Fig.4.4d).

4.1.3 Summary

As one can conclude, a relativistic EM wave is unstable in a plasma, with different regimes that depend on density (and other parameters) and EM wave intensity. In general, B-SRS is the leading instability. F-SRS competes with B-SRS for higher densities. When SRS is halted ($n > 0.25n_{cr} + \text{relativistic shift}$) only the RMI can grow. As it was shown, the relativistic description of parametric instabilities introduces a broadening of unstable regions in k space and merging of unstable regions of different instabilities. Although the laser strengths considered here are somewhat larger than allowed by expansion (4.20), the obtained results show good agreement with previously reported results. The majority of these results have been obtained under various approximations such as: cold plasma, weak relativistic effects, circular polarization, very low density plasma, the quasistatic approximation, one dimensional scattering geometry, etc. [175, 180, 181, 182, 183, 184]. A unified three-dimensional approach to the problem of electron parametric instabilities of relativistically intense laser light in a cold plasma, including harmonic generation is presented in [185].

At the end, it should be pointed out that the hybrid dispersion equation (4.46) was solved for real values of the wave number (the initial value problem). This corresponds, strictly speaking, to the case when the interacting waves always stay in the plasma (an

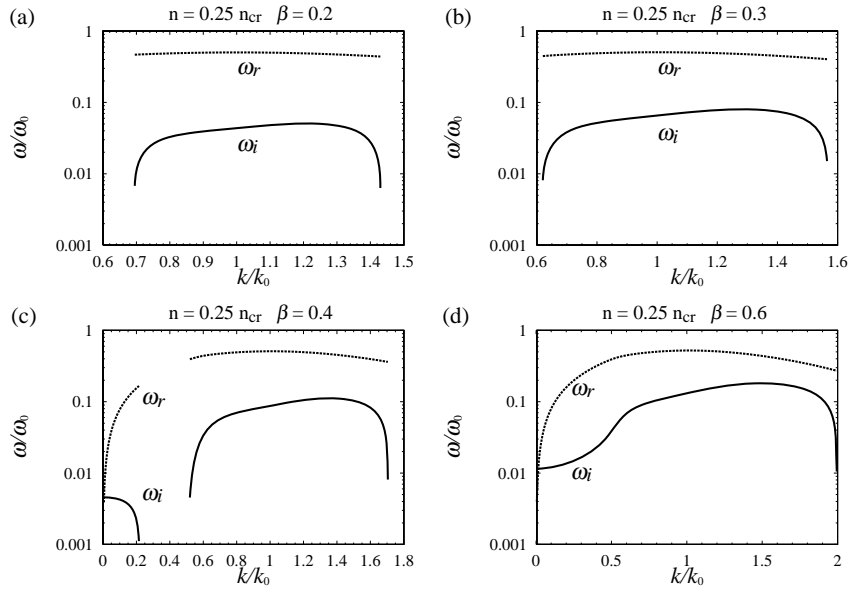


Figure 4.3: Solutions of the hybrid dispersion equation (equation 4.46) for $n = 0.25n_{cr}$ and laser strengths (a) $\beta = 0.2$, (b) $\beta = 0.3$, (c) $\beta = 0.4$ and (d) $\beta = 0.6$. The solid lines are the growth rate (ω_i) and the dashed lines are the real part of the frequency (ω_r). The frequencies and wave numbers are normalized to ω_0 and k_0 , respectively, [176].

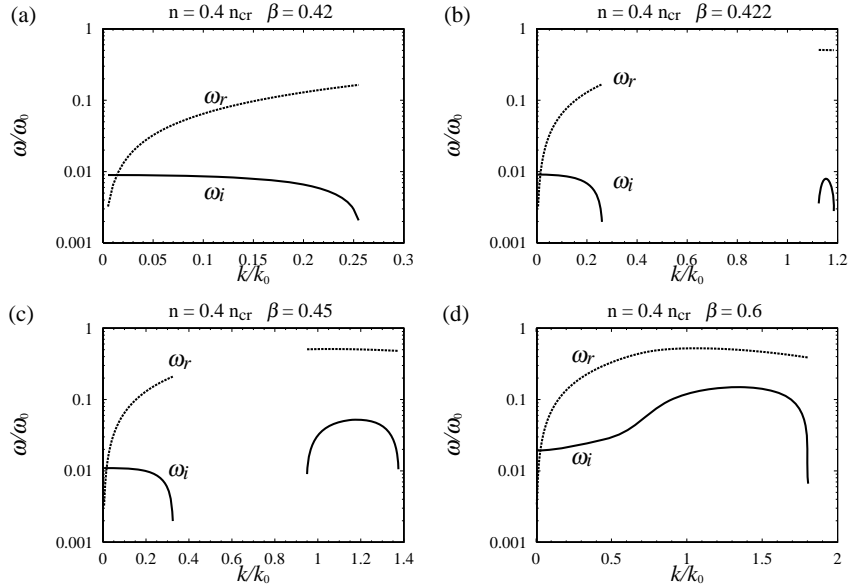


Figure 4.4: Solutions of the hybrid dispersion equation (equation 4.46) for $n = 0.4n_{cr}$ and laser strengths (a) $\beta = 0.42$, (b) $\beta = 0.422$, (c) $\beta = 0.45$ and (d) $\beta = 0.6$. The solid lines are the growth rate (ω_i) and the dashed lines are the real part of the frequency (ω_r). The frequencies and wave numbers are normalized to ω_0 and k_0 , respectively, [176].

infinite or periodic plasma model) [105]. Complications arise from the fact that in the case of real (finite) plasmas the waves involved in the interaction escape from the interaction region. Therefore we get the boundary value problem with additional complexity. In the following sections by using computer simulations we shall consider the propagation of intense EM waves in a finite homogeneous plasma.

4.2 Computer simulations

Numerical modeling is crucial to our understanding of complex plasma phenomena. The basic idea of computer simulations is to numerically solve an evolution of a plasma system by using mathematical equations that basically describe the system on an accepted physical level. This approach to plasma complexity enables a numerical plasma experiment with detailed diagnostics. Such numerical experiments are of a great value for understanding results from the real ones. Simulations are also used for experiments that cannot be performed in the laboratory either due to their size or due to the characteristic time scale of certain physical processes. However, simulations are not a substitution for laboratory and space experiments and observations. They are restricted by computer performances and usually we can only sample limited set of initial conditions. Nevertheless, computer *simulation* fills a large gap between *theory* and *experiment* and by combining these three approaches it is possible to obtain detailed information on complex processes in plasmas. Today's supercomputers offer an excellent platform for various simulation methods, thus developing rapidly the third methodology of scientific research.

During last decades various types of simulation approaches in plasmas have been introduced. Among these are: a magneto-hydro-dynamics code, fluid code, Vlasov and particle-in-cell codes, etc. In general, these simulation codes are based on kinetic or/and fluid description of plasmas. Fluid simulations work by solving numerically the fluid (hydrodynamic) equations whereas kinetic simulations are based on the plasma kinetic equation (Vlasov equation) or on particle simulation. The particle simulation computes the motion of charged particles, interacting with each other and with externally applied fields. The hybrid code is a combination of these two approaches: e.g., particle model is used for ions and dynamics of electrons is treated by using the fluid model.

In laser-fusion oriented research two simulation approaches evolved and became widely used: Vlasov simulations and prevailing particle-in-cell simulations (PIC). Vlasov simulation method provides a much lower noise level than PIC simulations. However, Vlasov simulations are very expensive for investigations of high intensity wave-plasma interactions in 2-3D, since the phase space required by this simulations becomes very large.

4.2.1 Particle-in-cell simulations

Electromagnetic relativistic particle-in-cell (PIC) simulations [150, 186], are a powerful tool for studying strong laser-plasma interaction. The simulation method for EM relativistic PIC is based on Maxwell equations

$$\nabla \cdot \mathbf{E} = \frac{\rho}{\varepsilon_0}, \quad (4.47)$$

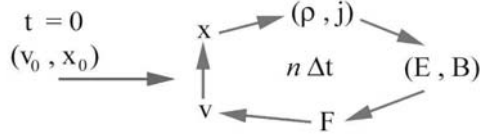


Figure 4.5: The basic cycle of a particle simulation code.

$$\nabla \cdot \mathbf{B} = 0, \quad (4.48)$$

$$\nabla \times \mathbf{E} = -\frac{\partial \mathbf{B}}{\partial t}, \quad (4.49)$$

$$\nabla \times \mathbf{B} = \mu_0 \mathbf{j} + \frac{1}{c^2} \frac{\partial \mathbf{E}}{\partial t}, \quad (4.50)$$

closed by the relativistic equation of particle motion

$$\frac{d(\gamma \mathbf{v})}{dt} = \mathbf{F} = q(\mathbf{E} + \mathbf{v} \times \mathbf{B}), \quad (4.51)$$

where ρ is the charge density, \mathbf{j} is the current density and μ_0 is the magnetic permeability. In a PIC simulation, plasma is represented by a large number of quasi-particles each of which models the action of a large number of physical particles. While coordinate and particle velocities remain continuous quantities in this simulation scheme, the electric and magnetic fields and the charge and current densities are discretized on a spatial grid. The simulation cycle starts with some appropriate initial conditions for the particle positions and velocities. This initial choice of conditions is related with the "geometry" of the physical problem which is in the focus. In Fig.4.5, a basic computational cycle is shown. From particle positions and velocities at each time step, we compute the charge and current densities (ρ, \mathbf{j}) on the spatial grid. These computations require some weighting methods at the grid points that are dependent on particle positions. Next, using Maxwell equations we calculate electric and magnetic fields (\mathbf{E}, \mathbf{B}) and then use these fields, again performing a weighting, to find the Lorentz force \mathbf{F} and advance in time the particle velocities \mathbf{v} and positions \mathbf{x} .

The choice of code characteristics, i.e. time step and length of grids, should provide good accuracy and stability to make simulations correct over many computational cycles. The time step should be small enough to resolve the highest frequency in the problem and the choice of grid length should be fine enough to resolve the Debye length. Furthermore, to avoid nonphysical results due to the finite difference approximation used to solve equations (4.47)-(4.51), the time step Δt and the grid spacing Δx have to satisfy the following inequality (Courant condition) [150, 186, 187],

$$\Delta x > c\Delta t. \quad (4.52)$$

Thus, the time step and the grid spacing should be chosen in such a way that the particles during one time step cannot cross a distance larger than the size of the cell.

4.3 Weakly Relativistic Electromagnetic Solitons

Relativistic electromagnetic (EM) solitons in laser driven plasmas were analytically predicted and found by particle simulations [154, 188, 189, 190, 191, 192, 193]. Relativistic solitons are EM structures self-trapped by locally modified plasma refractive index via two effects: the relativistic electron mass increase and the electron density drop by the ponderomotive action of intense laser light [154, 189]. A large effort was put into studies of one-dimensional (1D) relativistic EM solitons in an ultraintense laser interaction with underdense and overdense plasmas [194, 195, 197, 198, 199, 200, 201]. For laser pulses longer than the electron plasma wave wavelength, spatially modulated depleted pulse, due to stimulated Raman scattering, readily in nonlinear stage breaks-up into a slow train of ultra-short 1D relativistic EM solitons [191, 194, 195]. Moreover, soliton acceleration toward the plasma-vacuum interface can produce bursts of reflected low-frequency EM radiation [230]. Recently, circularly polarized subcycle relativistic EM solitons were found and studied in 2D and 3D by particle simulations [195, 196]; while the ion motion influence on dynamics and the lifetime of 1D and 2D relativistic solitons was investigated in [195, 197].

Evolution of a relativistic laser pulse in a long-scale moderately underdense plasma was studied analytically and by computer simulation [194, 195, 197, 198]. While the circular polarization case was investigated in much detail [193, 197, 198, 199, 200], here, we treat a more complex linear polarization case. Linearly polarized laser light sets electrons into longitudinal motion by relativistic Lorentz force generating coupled longitudinal-transverse wave modes. In this situation, by relativistic fluid and particle simulations for a long laser pulse, we have recently analyzed nonlinear interplay between forward and backward stimulated Raman scattering and relativistic modulational instability [194]. Parametric down-cascade evolves into a weak turbulence, which saturates into a photon condensate at the bottom of the light spectrum. This phenomenon, similar to Langmuir condensate, corresponds to strong energy depletion and a laser beam break-up, as observed in many simulations. In the final stage of saturation, behind the pulse front, the train of intense ultra-short standing relativistic solitons is formed. It was estimated, for ultra-short laser pulses [195], that 30 to 40% of the laser energy can be trapped inside these low-frequency electromagnetic solitons creating a significant channel for laser beam energy conversion. Below, the problem of existence, stability and dynamics of linearly polarized electromagnetic solitons is studied by an one-dimensional analytical model for a weak relativistic nonlinearity. A simple dynamical equation of the nonlinear Schrödinger (NLS) type, with two extra nonlocal (derivative) nonlinear terms is derived. The conserved quantities, the photon number and the Hamiltonian, are calculated and a soliton solution in an implicit form is found analytically. Further, the soliton stability is examined and compared with the circular polarization case. Analytical results are confirmed by numerical simulations of the derived NLS model, as well as, of fully relativistic nonlinear equations. Finally, the saturation amplitude and the frequency for large relativistic solitons observed in numerical simulations are analytically estimated, [201].

4.3.1 Dynamical Equations

The relativistic wave equation and the cold electron momentum equation, in terms of vector and scalar potential (\mathbf{A} and ϕ , respectively), in the *Coulomb* (radiation) gauge, where $\nabla \cdot \mathbf{A} = 0$, are written as [202]

$$\nabla^2 \mathbf{A} - \frac{1}{c^2} \frac{\partial^2}{\partial t^2} \mathbf{A} = -\frac{4\pi}{c} \mathbf{J}_\perp, \quad (4.53)$$

where \mathbf{J}_\perp is the transverse component of the total electron current $\mathbf{J} = \mathbf{J}_\perp + \mathbf{J}_\parallel = en\mathbf{v}$, where n is the electron density and ions assumed to be fixed, and

$$\frac{\partial \mathbf{p}}{\partial t} + (\mathbf{v} \nabla) \mathbf{p} = e \nabla \phi + \frac{e}{c} \frac{\partial}{\partial t} \mathbf{A} - \frac{e}{c} \mathbf{v} \times (\nabla \times \mathbf{A}), \quad (4.54)$$

where $\mathbf{p} = \gamma m \mathbf{v}$, is the electron momentum, \mathbf{v} , is the electron velocity and $\gamma = (1 + p^2/m^2 c^2)^{1/2}$ is the relativistic Lorentz factor. The relativistic electron momentum equation can be transformed by using the vector identity which after a straightforward algebra gives

$$\frac{\partial}{\partial t} \left(\mathbf{p} - \frac{e}{c} \mathbf{A} \right) = e \nabla \phi - mc^2 \nabla \gamma + \mathbf{v} \times \left[\nabla \times \left(\mathbf{p} - \frac{e}{c} \mathbf{A} \right) \right], \quad (4.55)$$

that is the equation for the generalized momentum $\left(\mathbf{p} - \frac{e}{c} \mathbf{A} \right)$. By taking the *curl* of the above relation, one can readily conclude that if $\nabla \times \left(\mathbf{p} - \frac{e}{c} \mathbf{A} \right)$ is equal to zero initially, it will remain zero at later times. Therefore, an important relation, $\mathbf{p}_\perp = \frac{e}{c} \mathbf{A}$, is found, which after a substitution in \mathbf{J}_\perp , simplifies the wave equation in terms of the vector potential \mathbf{A} , [89, 204].

Accordingly, in one dimensional case, relativistic wave equation, the continuity equation and the electron momentum equation, read [201],

$$\left(\frac{\partial^2}{\partial t^2} - c^2 \frac{\partial^2}{\partial x^2} \right) a = -\frac{\omega_p^2 n}{n_0 \gamma} a, \quad (4.56)$$

$$\frac{\partial n}{\partial t} + \frac{\partial}{\partial x} \left(\frac{np}{m\gamma} \right) = 0, \quad (4.57)$$

$$\frac{\partial p}{\partial t} = -eE_\parallel - mc^2 \frac{\partial \gamma}{\partial x}, \quad (4.58)$$

where $a = eA/mc^2$ is the normalized vector potential in y direction, n is the electron density, p is the electron momentum in x direction, $\gamma = (1 + a^2 + p^2/m^2 c^2)^{1/2}$, E_\parallel is the longitudinal electric field, n_0 is the initial electron-ion density and $\omega_p = (4\pi e^2 n_0/m)^{1/2}$ is the electron plasma frequency.

In a weakly relativistic limit for $|a| \ll 1$ and $|\delta n| \ll 1$ we expand the right hand side of the (4.56) and introduce the normalized perturbed electron density $\delta n = (n - n_0)/n_0$ and dimensionless variables $x \rightarrow (c\omega_p^{-1})x$ and $t \rightarrow (\omega_p^{-1})t$ to obtain [199],

$$\left(\frac{\partial^2}{\partial t^2} - \frac{\partial^2}{\partial x^2} \right) a = - \left(1 + \delta n + \frac{a^2}{2} \right) a. \quad (4.59)$$

Further, by combining the linearized equations of continuity (4.57) and the electron momentum (4.58) we get for the perturbed electron density [199],

$$\frac{\partial^2 \delta n}{\partial t^2} + \delta n = \frac{1}{2} \frac{\partial^2}{\partial x^2} a^2. \quad (4.60)$$

In distinction to circular polarization [9,13], linearly polarized waves have odd harmonics of the vector potential a and even harmonics of the electron density δn [154, 199]. Further, we introduce the slow time varying complex envelopes in a form

$$a = \frac{1}{2} [Ae^{-it} + A^*e^{it}]; \quad \delta n = N_0 + \frac{1}{2} (N_2e^{-i2t} + N_2^*e^{i2t}). \quad (4.61)$$

and find the envelopes N_0 and N_2 by substituting (4.61) into (4.60) and collecting the zero and second harmonic terms (e^{-i2t})

$$N_0 = \frac{1}{4} (|A|^2)_{xx}; \quad N_2 = -\frac{1}{6} (A^2)_{xx}, \quad (4.62)$$

where subscripts x designates derivations with respect to x -coordinate.

By substituting (4.61) and (4.62) into the wave equation (4.59) and collecting first harmonic terms (e^{-it}) we obtain the wave equation for the vector potential envelope A ,

$$i \frac{\partial A}{\partial t} + \frac{1}{2} A_{xx} + \frac{3}{16} |A|^2 A - \frac{1}{8} (|A|^2)_{xx} A + \frac{1}{48} (A^2)_{xx} A^* = 0. \quad (4.63)$$

The eq. (4.63) has a form of the generalized nonlinear Schrödinger (NLS) equation [205] with two extra nonlocal (derivative) nonlinear terms. We can derive the conserved quantities [201, 206]: photon number P

$$P = \int |A|^2 dx, \quad (4.64)$$

and Hamiltonian H

$$H = \frac{1}{2} \int \left\{ |A_{xx}|^2 - \frac{3}{16} |A|^4 - \frac{1}{8} [(|A|^2)_x]^2 - \frac{1}{12} |A|^2 |A_x|^2 \right\} dx. \quad (4.65)$$

We further look for a stationary and localized solution of (4.63) in a form

$$A = \alpha(x) e^{i\lambda^2 t}, \quad (4.66)$$

with the boundary conditions

$$\alpha(\pm\infty) = 0, \quad \alpha(x) < \infty. \quad (4.67)$$

Under the assumptions (4.66) and (4.67) the first integration of (4.63) gives

$$(\alpha_x)^2 = 2 \frac{\alpha^2 \lambda^2 \left(1 - \frac{3}{32} \frac{\alpha^2}{\lambda^2}\right)}{1 - \frac{\alpha^2}{3}}. \quad (4.68)$$

Additional integration of (4.68) gives a localized soliton solution in an implicit form

$$\pm\lambda x = \frac{1}{2\sqrt{2}} \ln \frac{\sqrt{1 - \frac{3}{32}\frac{\alpha^2}{\lambda^2}} + \sqrt{1 - \frac{\alpha^2}{3}}}{\left| \sqrt{1 - \frac{3}{32}\frac{\alpha^2}{\lambda^2}} - \sqrt{1 - \frac{\alpha^2}{3}} \right|} - \frac{4}{3}\lambda \ln \frac{\frac{1}{3}\sqrt{32\lambda^2 - 3\alpha^2} + \sqrt{1 - \frac{\alpha^2}{3}}}{\sqrt{\left|1 - \frac{32}{9}\lambda^2\right|}}, \quad (4.69)$$

with a soliton amplitude $a_0 = \frac{4\sqrt{2}}{\sqrt{3}}\lambda$.

This is linearly polarized soliton with a vector potential a oscillating with the frequency $\omega = 1 - \lambda^2$, slightly below the plasma frequency.

For the soliton strength λ above the critical value $\lambda \geq \lambda_c = \frac{3}{4\sqrt{2}}$ ($a_0 \geq \sqrt{3}$) the solution (4.66) has a form of a "cusp" soliton [16]; the centrally highly pointed waveform. In the small amplitude limit $\lambda \ll \lambda_c$ one neglects the non-local (ponderomotive) terms and the solution (4.66) becomes the well-known secant hyperbolic (NLS) soliton.

4.3.2 Relativistic Soliton Stability

To check the stability of the soliton (4.66) we use the Vakhitov-Kolokolov stability criterion [205, 207]

$$\frac{dP_0}{d\lambda^2} > 0, \quad (4.70)$$

where P_0 is the soliton photon number defined by (4.64). The function $P_0(\lambda)$ for the soliton solution (4.69) is calculated analytically as

$$P_0(\lambda) = \frac{16\sqrt{2}}{3}\lambda + 2 \left(1 - \frac{32}{9}\lambda^2\right) \ln \frac{1 + \frac{4\sqrt{2}}{3}\lambda}{\left|1 - \frac{4\sqrt{2}}{3}\lambda\right|}. \quad (4.71)$$

The curve $P_0(\lambda)$, shown in Figure 1, represents the stationary solutions of (4.63) which correspond to the minimum of the Hamiltonian H for the fixed photon number P .

According to the condition (4.70) the soliton (4.69) turns out to be stable in the region $\lambda < \lambda_s \approx 0.44$ ($a_0 < a_s \approx 1.44$) indicating that cusp solitons are also unstable ($\lambda_s < \lambda_c$). More generally, we can now conclude that small amplitude linearly polarized solitons ($a_0 < 1$) within the weakly relativistic model (4.59)-(4.60) are stable.

On the other hand, for *circularly* polarized EM waves, fully nonlinear relativistic soliton solution of (4.56) and (4.57) has been analytically found [9,13], as

$$a(x, t) = \frac{2\lambda \cosh(\lambda x)}{\cosh^2(\lambda x) - \lambda^2} \exp(i\sqrt{1 - \lambda^2}t), \quad (4.72)$$

with $a(x, t) = a_y + ia_z$, where indices denote y and z components of the vector potential.

The soliton amplitude is $a_0 = \frac{2\lambda}{1 - \lambda^2}$ and frequency $\omega = \sqrt{1 - \lambda^2}$. However, in the circular polarization case ω is the angular velocity of the rotation of the polarization plane (with constant amplitude) while for the linear polarization it stands for the frequency of the oscillating vector potential.

A condition for the electron density greater than zero imposes a constraint on the maximum soliton amplitude, as $a_0 < \sqrt{3}$ and frequency $1 > \omega > \sqrt{\frac{2}{3}}$ ($0 < \lambda < \sqrt{3}/3$).

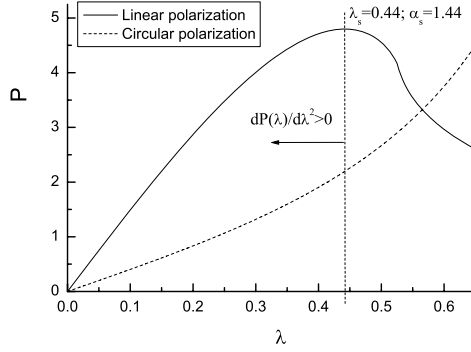


Figure 4.6: Photon number $P_0(\lambda)$ variation for solitons with linear and circular polarization with an illustration of the Vakhitov-Kolokolov stability criteria, [201].

To further check the stability of the circularly polarized solitons (4.72) we can use the similar procedure as for the case of linearly polarized solitons. Therefore, the corresponding soliton photon number $P_0(\lambda)$ reads

$$P_0(\lambda) = \frac{4 \arctan\left(\frac{\lambda}{\sqrt{1-\lambda^2}}\right)}{(1-\lambda^2)^{3/2}} + \frac{4\lambda}{1-\lambda^2}, \quad (4.73)$$

while according to the Vakhitov-Kolokolov stability criterion (4.71) we conclude that the circularly polarized solitons remain stable ($\frac{dP_0}{d\lambda^2} > 0$) inside the whole region $0 < a_0 < \sqrt{3}$ of existence (Fig.4.6). However, this approach is valid only for the limited class of circularly polarized perturbations and does not give an answer for arbitrary perturbations. Our first analytical studies on the stability of the circularly polarized solitons under arbitrary perturbations reveal that the circularly polarized perturbations are the special case given as a trivial solution of the corresponding eigen value problem.

The shape of the curve $P_0(\lambda)$ (Fig.4.6) for the linearly polarized solitons predicts the existence of the soliton instability region $\lambda > \lambda_s \approx 0.44$. However, the Vakhitov-Kolokolov criterion just solves a linear stability problem for solitons indicating a presence of exponentially growing or decaying modes; therefore, giving no prediction about the subsequent nonlinear evolution of unstable solitons or about stability of the localized structures with arbitrary profiles. According to the nonlinear analysis [208], for the generalized NLS equation with a similar shape of the corresponding curve $P_0(\lambda)$, beside the stationary solution there exist two other regimes of the soliton dynamics: (a) soliton collapse and (b) long-lived relaxation oscillations around the stable soliton amplitude. In our case, due to the local cubic nonlinear (NLS) term in (4.63), one can plausibly expect such dynamical regimes. However, the presence of two extra nonlocal nonlinear terms in (4.63) indicates the possible existence of some other dynamical states.

4.3.3 Numerical Results

In order to check analytical results and prediction of the regimes of the soliton dynamics we performe direct numerical simulation of the model equation (4.63) using a numerical

algorithm based on the split-step Fourier method [209], originally developed for the NLS equation. The main feature of the split-step Fourier method is numerical calculation of the spatial derivatives in the Fourier space in each integration time step. In our case, the spatial derivative of the additional nonlinear term (nonlocal term) is also calculated in the Fourier space.

Numerical results prove that the initially launched solitons (4.69) with the soliton parameters inside the stability region $\lambda < \lambda_s \approx 0.44$ remains stable. Solitons with parameters outside the stability region evolve toward the corresponding stable soliton with long-lived relaxation oscillations. The evolution of the initially launched soliton with amplitude $a_0 \approx 1.6$ ($\lambda \approx 0.2$) outside the stability region is shown on Fig. 4.7a. A similar behavior exhibit initially perturbed solitons with photon number $P < P_{\max} = P_0(\lambda_s) \approx 4.79$ inside the stability region $\lambda < \lambda_s$ or different localized structures with small deviation from the stable equilibrium state. As an example of such dynamics, the time evolution of two Gaussian structures with different amplitudes but with the same photon number $P = 2.875$ are shown on Fig. 4.7b and Fig. 4.7c. The evolution in both cases is long-lived relaxation oscillations around the stable soliton amplitude (4.69) with $\lambda \approx 0.2$ ($a_0 \approx 0.653$) which corresponds to the exact value of the photon number $P = 2.875$. These dynamical regimes exist also in NLS equation and they are analytically predicted and numerically confirmed in [209]. However, when the initial perturbation increases, the period grows with oscillations becoming strongly nonlinear to exhibit new types of long-lived localized dynamical structures (Fig. 4.7d). Further deviation from the stable equilibrium state can lead to a rapid aperiodic growth of the amplitude and the soliton collapse (Fig.4.7e).

The understanding of different dynamical regimes is important for an insight into the low-frequency process of formation of stable relativistic solitons behind the laser pulse front inside the photon condensate [194]. More detailed determination of the regions in the parameter plane (P, λ) or separatrix curves in the phase space for different dynamical regimes would require additional analytical and numerical study which is out of the scope of this paper.

4.3.4 Ultra-Relativistic Solitons

Above considerations related to linearly polarized solitons were restricted to a weakly relativistic regime, therefore being not applicable for describing large amplitude solitons observed numerically in [8]. For that purpose we have to use a different approach. A direct numerical simulation of the fully nonlinear relativistic one-dimensional fluid-Maxwell system (4.56)-(4.58) was performed to study propagation of a long, strong relativistic laser pulse in a uniform, underdense plasma. Our algorithm based on the second order accuracy Lax-Wendorff method and leap-frog central scheme [194], was exploited. Linearly polarized pico-second pulse was launched into a plasma (10 evolution of the mean pulse energy and other plasma parameters was followed. Numerical results given in Fig.4.9 show the spatiotemporal evolution of the pulse energy, revealing the generation of a train of intense ultra-short relativistic (almost) standing EM solitons inside the photon condensate ($\omega < \omega_p$). Large relativistic solitons at a late time instant, after propagation of the pulse, are shown in Fig.4.8. In Fig.4.10 two characteristic neighboring solitary structures

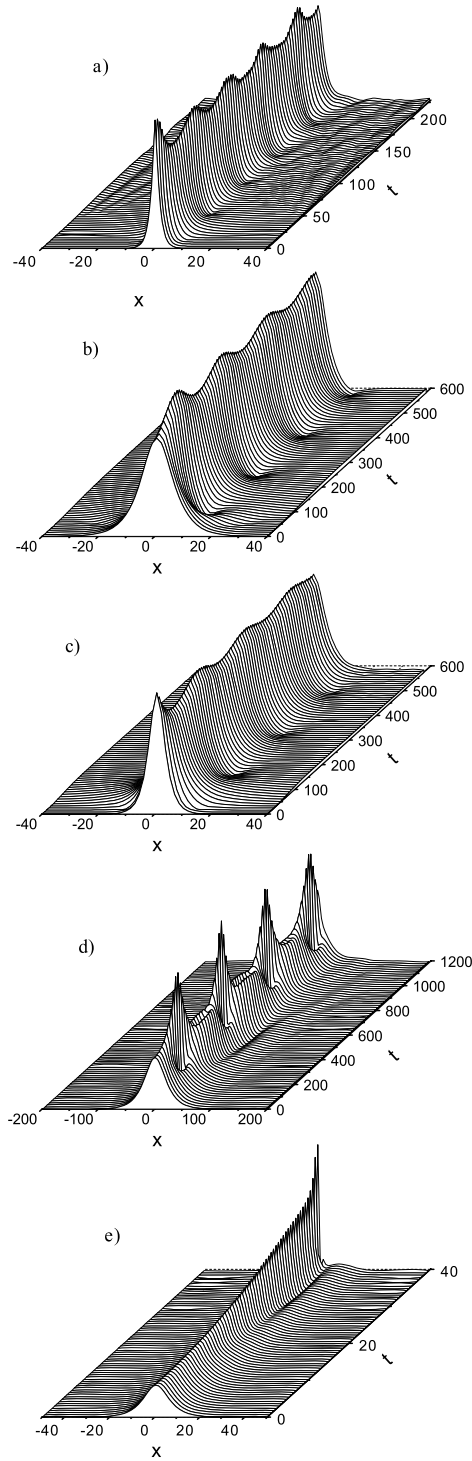


Figure 4.7: Spatiotemporal evolution of different initial structures a) Soliton in the instability region with amplitude $A_0 = 1.6$; b) Gaussian structure with amplitude $A_0 = 0.536$ and photon number $P = 2.875$; c) Gaussian structure with amplitude $A_0 = 0.536$ and the same photon number as in (b); d) An example of oscillating dynamical structures and e) An example of collapse dynamics, [201].

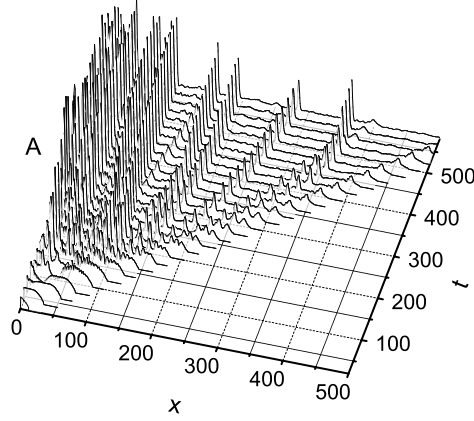


Figure 4.8: Ultra-relativistic standing solitons formed behind the short laser pulse ($T = 1.5ps$; $a_0 = 0.6$, [201]).

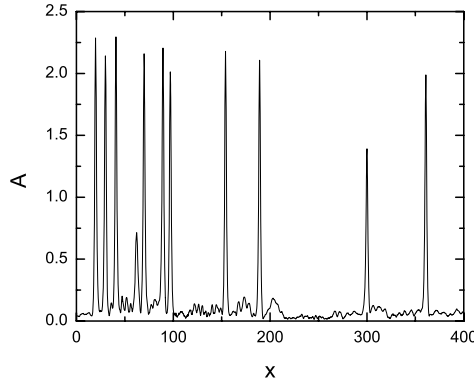


Figure 4.9: Spatiotemporal EM energy density inside a photon condensate; from 1D fluid-Maxwell simulation of laser pulse ($a_0 = 0.5$) propagation (from left to right) in a underdense plasma ($n_0 = 0.1n_{cr}$) show slowing intense solitary structures, [201].

$A_s(x)$ are presented, along with electron density $\delta n_s(x)$ and the associated longitudinal momentum $p_x(x)$. Simulations clearly reveal that apart from stable small amplitude solitons, the family of large relativistic solitons, saturating at $A_0 \approx 2.5$ exists as well. The saturated value of the soliton amplitude depends on the laser intensity a_0 as well as on other parameters, e.g. the laser pulse duration. However, our study has shown that the soliton amplitude typically saturates at $A_0 \approx 2.9$ for intensities $a_0 \approx 0.7 - 0.8$.

As earlier analytical model fails for large amplitudes we have used a different approach to estimate saturating values of the vector potential and its corresponding frequency. Namely, our numerical data strongly support the following substitution

$$\begin{aligned} a(x, t) &= A(x) \cos(\omega t); & p(x, t) &= P(x) \sin(2\omega t); \\ \delta n(x, t) &= N_0(x) + N_2(x) \cos(2\omega t) \end{aligned} \quad (4.74)$$

Neglecting p^2 in γ , but retaining p in the motion equation, after a simple trigonometric transformation we get

$$\gamma = \sqrt{1 + a^2} = \sqrt{\left(1 + \frac{A^2}{2}\right) + \frac{A^2}{2} \cos(2\omega t)}. \quad (4.75)$$

The first term under the square root is larger than the absolute value of the second term, allowing the approximate expansion

$$\gamma \approx \gamma_A + \frac{A^2}{4\gamma_A} \cos(2\omega t), \quad (4.76)$$

where $\gamma_A = \sqrt{1 + A^2/2}$. Furthermore, under approximations (4.74-4.76) the following set of equations can be obtained

$$\begin{aligned} A_{xx} &= \left[\frac{5\gamma_A^2 - 1}{4\gamma_A} - \frac{\omega^2}{2}(3\gamma_A^2 - 1) + \frac{\gamma_A^2 + 2}{4\gamma_A^4} A_x^2 + \omega \frac{3\gamma_A^2 - 1}{2\gamma_A} P_x \right] A \\ N_0 &= \frac{A_{xx} A}{2\gamma_A} \left(1 - \frac{A^2}{8\gamma_A^2} \right) + \frac{A_x^2}{2\gamma_A^3} \left(1 - \frac{3A^2}{8\gamma_A^2} \right) \\ N_1 &= \frac{A_{xx} A}{2\gamma_A} \left(1 - \frac{A^2}{4\gamma_A^2} \right) + \frac{A_x^2}{2\gamma_A^3} \left(1 - \frac{3A^2}{4\gamma_A^2} \right) + 2\omega P \\ P &= \frac{\omega(1 + \gamma_A^2) A A_x}{2\gamma_A^2 \left(4\omega^2 \gamma_A - N_0 + \frac{A^2}{16\gamma_A^2} N_1 \right)} \end{aligned} \quad (4.77)$$

Solving the above system under assumption that maximum soliton amplitudes saturate at $\delta n = -1$ ($n = 0$) gives the result $A_0 = 2.67$ for $\omega_0 = 0.72$ close to the values obtained by direct numerical simulation of the fully relativistic system ($A_0 \approx 2.9$ and $\omega_0 \approx 0.73$). The difference in these results can come from, e.g. neglecting higher harmonics in A and consequently in γ . Nevertheless, we have demonstrated the existence of large linearly polarized electromagnetic solitons with an estimate for the soliton parameters A_0 and ω_0 .

In conclusion, we have investigated existence and stability of 1D relativistic electromagnetic solitons in a cold underdense plasma, and have analytically found solutions and regions of stability of linearly polarized relativistic EM solitons in agreement with the relativistic fluid-Maxwell and particle simulations [194]. Analytical estimates gave the maximum amplitude and the frequency of large relativistic solitons close to simulation data. Difference in linear and circular polarization was singled out, e.g., in a role of the 2nd harmonic term in the relativistic γ -factor present for the linear polarization. The question of multi-dimensional effects, such as e.g. transverse stability of 1D solitons for symmetry breaking perturbation [59], deserves further attention.

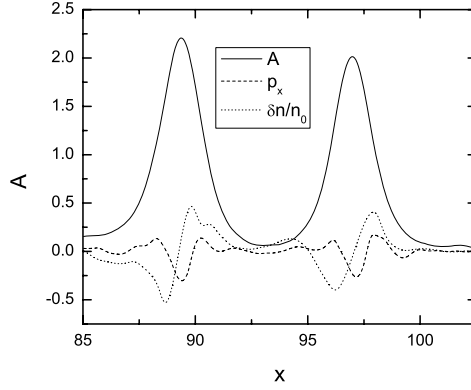


Figure 4.10: Two neighboring solitons with the corresponding vector potential $A_s(x)$, density perturbation $\delta n_s(x)$ and linear momentum $P_x(x)$.

4.4 Stimulated Raman Scattering Cascade into Photon Condensation

The interaction of a relativistic laser pulse with an underdense plasma is investigated by fluid-Maxwell and particle-in-cell simulations. A nonlinear interplay between backward and forward stimulated Raman scattering instabilities produces a strong spatial modulation of the light pulse and the down cascade in its frequency spectrum. The Raman cascade saturates by a unique photon condensation at the bottom of the light spectrum near the electron plasma frequency, related to strong depletion and possible break-up of the laser beam. In the final stage of the cascade-into-condensate mechanism, the depleted downshifted laser pulse gets gradually transformed into a train of ultra-short relativistic light solitons, [194].

4.4.1 Introduction

Linearly polarized relativistic EM radiation sets plasma electrons into the longitudinal motion by the strong $(\mathbf{v} \times \mathbf{B})$ forces changing the nature of electromagnetic wave (EMW) to a coupled longitudinal-transverse mode. So are one dimensional (1D) electronic parametric instabilities : stimulated Raman forward- and backward-scattering (F-SRS and B-SRS, respectively) and relativistic modulational instability (RMI) [105, 211, 174, 212]. They do not appear isolated, but are often nonlinearly interlinked with other instabilities [180, 185]. Here, we shall mostly discuss F-SRS and B-SRS induced by picosecond, moderate to high intensity laser pulses in long length-scale plasmas. Particular attention will be paid to the effects of their mutual interplay and couplings to RMI. This results in rich 1D dynamics, reflecting in a spectral broadening and cascading process which transfers the incident laser energy to higher order scattering modes. Along the propagation beam, there is typically a Raman cascade in the light spectrum from fundamental (laser) frequency toward lower frequencies. The first Stokes line is significant, however, further with laser propagation it becomes a new pump, which decays via a secondary Raman scatter-

ing. This cascade process is halted around the plasma frequency, the cutoff frequency for light propagation. We find that continuing instability growth through stimulated Raman cascade downshifts a power maximum from the fundamental to the bottom of the light spectra. This unique stimulated photon condensation following a Raman cascade, appears as a striking consequence of the relativistic laser instabilities. This is similar to a situation with the Langmuir condensate in a weak turbulence theory [2, 11] where a condensate is due to a Langmuir decay spectral cascading down to small wave numbers. As is well known, among these electronic instabilities, the SRS type is particularly significant concern, because the excited electron plasma wave (EPW) has a high phase velocity of order the velocity of light (F-SRS), it can produce very energetic electrons after the damping of EPW, such electrons can preheat the fuel in laser fusion applications [97].

The SRS instability can be most simply characterized as the resonant decay of an incident laser EM wave (ω_0, k_0) into a scattered *Stokes* EM wave (ω_s, k_s) plus an EPW (ω_{epw}, k_{epw}) (Langmuir wave) with the following matching conditions for frequencies and wave numbers,

$$\omega_0 = \omega_s + \omega_{epw}, \quad k_0 = \pm k_s + k_{epw}$$

Here, $+k_s$ and $-k_s$ denote stimulated forward and backward Raman scattering (F-SRS/B-SRS), respectively.

In addition to the above wave triplet described by the above equation for SRS, usually, another weaker resonant three-wave coupling process with the first *anti-Stokes* scattered EM wave, can be observed in experiment and simulation.

$$\omega_s = \omega_0 + \omega_{epw}, \quad \pm k_s = k_0 + k_{epw}$$

By this three-wave coupling, one can obtain an upshifted frequency by the electron plasma wave frequency ω_{epw} .

An EM wave which propagates in a plasma has dispersion relation $\omega_0^2 = \omega_{pe}^2 + k_0^2 c^2$, EPW has dispersion relation $\omega_{epw}^2 = \omega_{pe}^2 + 3k_{epw}^2 v_{the}^2$, here, c , ω_{pe} and v_{the} are speed of light, electron plasma frequency and electron thermal velocity, respectively. The minimum frequency for EM wave propagating inside plasma is ω_{pe} , so it is clear that the SRS instability requires that

$$\omega_0 \geq 2\omega_{pe} \implies n \leq \gamma n_{cr}/4 \quad (4.78)$$

where n and n_{cr} are the plasma density and the critical density for EM wave propagating in plasma, respectively, γ is relativistic Lorentz factor.

When these scattered EM waves, *including Stokes and anti-Stokes modes*, propagating inside plasma backward or forward, if their intensities exceed the corresponding thresholds of three-wave coupling processes, like the incident laser EM wave, they become new pumps, new instabilities then can be excited. Further, the new excited scattered EM waves to excite new instabilities if the corresponding thresholds are still exceeded successively. A stimulated Raman cascade process with the following frequency and wave number matching conditions,

$$\omega_{s,j} = \omega_0 \pm j\omega_{epw} \quad ; \quad \pm k_{s,j} = k_0 \pm jk_{epw}$$

then therefore takes place in intense laser-plasma interaction. The scattered EM waves include, not only the first-, second-, \dots , high-order Stokes modes ($j = -1, -2, \dots$), but also the first-, second-, \dots , high-order anti-Stokes modes ($j = 1, 2, \dots$), respectively.

When a relativistic laser propagates in underdense plasma, B-SRS and F-SRS can develop, they do not appear isolated but are often interconnected [194]. A nonlinear interplay between B-SRS and F-SRS produces a strong spatial modulation of the laser pulse and stimulated Raman cascade in its frequency spectra of scattered EM waves. The continuing instability growth through stimulated Raman cascade downshifts the power maximum from the fundamental to the bottom of the EM wave spectra. It gets saturated by the photon condensation mechanism, related to strong depletion and possible break-up of the laser beam. In the final stage of the cascade-into-condensation mechanism, the depleted downshifted laser pulse gradually transforms into a train of ultra-short relativistic EM solitons [194, 213].

When making a comparison between homogeneous temporal instability growth rates of B-SRS and F-SRS in a weakly relativistic case, we conclude that their ratio is roughly $(n_e/n_c)^{3/4}$, where n_c is the critical electron density, which means that the Raman back-scatter growth time is 5 – 30 times shorter than its forward-scatter counterpart when the plasma density is varied from $0.1n_c$ to $0.01n_c$. However, it should be noted that B-SRS becomes saturated efficiently at a very early stage of evolution, while F-SRS and RMI can get close and even merge to a unique F-SRS/RMI instability, which competes with the B-SRS instability in the process of anomalous absorption of laser energy. B-SRS saturation can occur due to pump depletion (for parameters applied here) or due to particle trapping, which could be dominant in low density plasmas.

All of above processes were intensively studied by theory and simulations [182, 214, 215, 199, 183]. However, due to analytical difficulties related to nonlinear electron dynamics and anharmonicity in the plasma response for linearly polarized light as compared to circularly polarized laser light, the former has received less theoretical consideration. So, an attempt to solve a fully nonlinear system of cold electron-fluid and Maxwell equations for 1D propagation of high-intensity, linearly polarized laser light in a uniform underdense plasma is presented. Further, detailed analysis is performed by 1D (2D) PIC simulations [194, 216]. The PIC method can follow the exact evolution of the laser light and plasma waves and particles on short time scales, much less than the laser period.

4.4.2 Relativistic Fluid-Maxwell Simulation

A long laser pulse enters the plasma and propagates in the x -direction, inducing both transverse and longitudinal electron motion. We consider only a purely one-dimensional case, in which the EM field is described by longitudinal (E_x) and transverse (E_y) electric field components and magnetic field B_z . For further treatment it is convenient to normalize all the physical quantities to dimensionless values by introducing light-speed units. We express length x in $c\omega_0^{-1}$ and time t in ω_0^{-1} units, and normalize the electron fluid velocity v , momentum p , fields E and B , vector potential A , and density n_e to $c, mc, mc\omega_0 e^{-1}, m\omega_0 e^{-1}, mce^{-1}$, and n_0 , respectively. Here c, m, e, ω_0 , and n_0 designate, as usual, the vacuum speed of light, electron mass and (absolute) electron charge, laser light frequency, and initial uniform electron density, respectively. In this way, Maxwell equations in 1D

reduce to [194],

$$\frac{\partial E_x}{\partial t} = \frac{n_e p_x}{\gamma}, \quad (4.79)$$

$$\frac{\partial E_y}{\partial t} + \frac{\partial B_z}{\partial x} = \frac{n_e A}{\gamma}, \quad (4.80)$$

$$\frac{\partial B_z}{\partial t} + \frac{\partial E_y}{\partial x} = 0, \quad (4.81)$$

$$\frac{\partial A}{\partial t} = -E_y, \quad (4.82)$$

in dimensionless units, while the cold electron fluid quantities are described by the continuity and electron motion equations

$$\frac{\partial n_e}{\partial t} = -\frac{\partial}{\partial x} \left(\frac{n_e p_x}{\gamma} \right), \quad (4.83)$$

$$\frac{\partial p_x}{\partial t} = -E_x - \frac{\partial \gamma}{\partial x}, \quad (4.84)$$

where $\gamma = (1 + p_x^2 + A^2)^{1/2}$, the transverse momentum p_y is replaced by the vector potential A , under Coulomb gauge (Sect. 12.2.1); with immobile ions as a neutralizing background. Unlike the weakly relativistic case amplitude case (weak pump case and linear stability analysis) in the strong-pump limit considered here, the only exact analytical solution of the system of equations (4.79)-(4.84) can be found for idealized circularly polarized EM pump. Direct numerical solving of the above system has not been performed often in the past [217]. So, effort has been invested into a construction of a stable numerical scheme for solving the 1D system (4.79)-(4.84) in a fully relativistic form, without any approximations. The fluid equations were treated by the second-order accuracy Lax-Wendroff method. As for the EM fields, a leap-frog-type central scheme was applied, with simultaneous calculation of all values, assisted by averaging exact electric and magnetic fields to approximate mesh node values at every space and time step.

In order to study the properties of backward and forward propagating EM waves; reflectivity R and transmittivity T are introduced at spatial point

$$R(x, t) = (F^-) / E_0^2, T(x, t) = (F^+) / E_0^2, \quad (4.85)$$

where F^+ and F^- are forward and backward propagating EM fields

$$F^\pm = E_y \pm B_z. \quad (4.86)$$

The aim of the simulation is to study penetration of a long ($> psec$) linearly polarized relativistic laser pulse into a long ($L > 1mm$) moderately dense ($n_e < n_c/4$) plasma, as relevant for fast ignition in laser fusion. A relative laser intensity a_0 was varied in the interval $0.1 - 1$, where

$$a_0 = eE_0/m_e\omega_0c \simeq 8.85 \times 10^{-10} I^{1/2} \lambda_0, \quad (4.87)$$

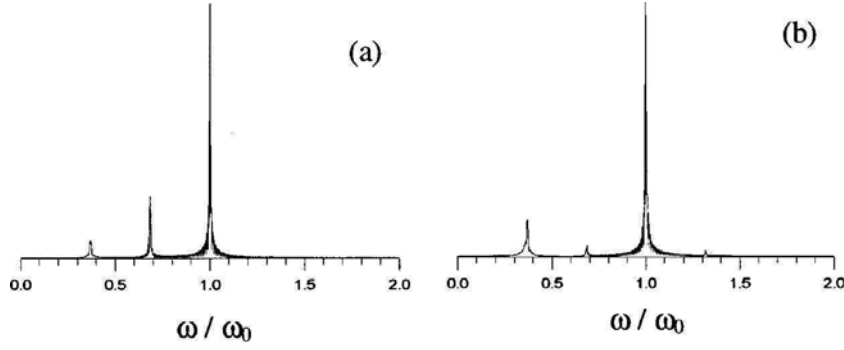


Figure 4.11: Frequency spectra of forward propagating laser pulse at point in space, (a) $x = 60\lambda_0$ and (b) $x = 200\lambda_0$, respectively inside plasma for $a_0 = 0.1$ and $n_e = 0.1n_c$, [194].

laser intensity I is given in W/cm^2 , and λ_0 laser wavelength in microns (μm); therefore, roughly, the intensity range $10^{16} - 10^{18}W/cm^2$, was covered for laser light wavelength of $1\mu m$.

For lower pump intensity ($a_0 = 0.1$) and the plasma density $n_e < 0.1 n_c$, forward-propagating stimulated Raman scattering in a linear regime occurs, with Stokes component in the frequency spectrum far dominant over anti-Stokes one Fig.4.11. Along the propagating beam, there is a cascade in the light spectrum from fundamental (laser) ω_0 —frequency toward lower frequencies. The first Stokes line is significant, however, along the propagation path, the Stokes mode further decays via a secondary Raman scattering. This cascade process is eventually halted near the electron plasma frequency—the cutoff for the light propagation.

Further, the laser intensity a_0 was raised to higher values of 0.2 and 0.3. Fig.4.12, demonstrates the spatial profile of the laser beam energy (averaged over the laser period) at different moments of time. Although, still a moderately relativistic case, typically strong spatial modulation, pulse depletion and break up takes place. The characteristic nonlinear modulation spatial scale is $2\pi c/\omega_p$ or here, about ($\sim 3\lambda_0$) corresponding to F-SRS/RMI processes [194]. Similar relativistic modulation effects are regularly observed in particle simulations with ultra-short pulse high intensity laser pulses [187, 214, 199, 183, 218, 219]. Having a significant growth rate, the predominantly convective B-SRS instability (in the pulse frame) develops at the pulse front and saturate over short distance in a back of the pulse. Strong backscattering depletes the body of a pulse by creating like a notch at some point in the pulse [218].

In addition, two-dimensional PIC simulations have been performed to find qualitative agreement with the above behavior [194]. The simulation box of $(200\lambda_0 \times 50\lambda_0)$ with uniform cold plasma and density $n_e = 0.1n_c$ is put in vacuum. In Fig.4.13 the 2D laser pulse EM energy profile is plotted at three moments in time. Again, laser pulse break-up is observed at roughly the same spot as seen in earlier fluid simulations. Further, Fig.4.14 gives a view of transmitted light spectrum, together with a spectral intensity at the central axis (top). Raman cascade containing first anti-Stokes and first and second Stokes sidebands, is clearly revealed. Continuing the study by extensive 1D PIC simulations,

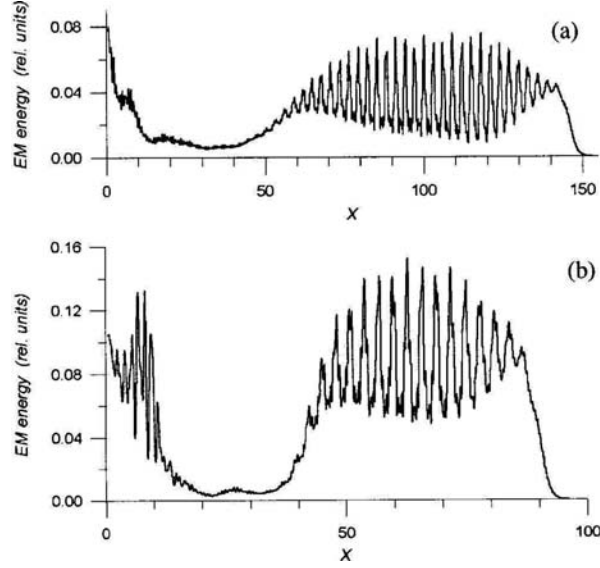


Figure 4.12: Spatial distribution of laser EM energy density for (a) $a_0 = 0.2$, $n_e = 0.1n_c$ at $t = 160T_0$ and (b) $a_0 = 0.3$, $n_e = 0.1n_c$ at $t = 100T_0$, from fluid simulation, [194].

remarkable spectral properties are observed, pointing to their general complex character (Fig.4.15). Namely, B-SRS spectra reveal the SRS cascade toward lower frequency mode numbers, gradually down-shifting the maximum to the bottom of the spectrum. This unique stimulated photon condensation following the Raman cascade is a striking example of complexity in relativistic laser-plasma interactions, as was qualitatively predicted in Chapter 11 on 3WI dynamics [124]. Indeed, above scenario is well consistent with 3WI model of B-SRS with the relativistic frequency shift, which by increasing laser intensity can trigger nonlinear bifurcations on the route to spatio-temporal turbulence, as was first proposed by Škorić et al, [98, 102, 124, 151] (vide supra). In order to give a wider parameter survey, F-SRS and B-SRS spectra are shown in Fig.4.16, revealing the *Raman cascade into photon condensation* with a spectral energy accumulation at the cut-off frequency.

Next, the relativistic 1D EM particle simulations of the SRS, Raman cascade, transition from Raman cascade into photon condensation and the generation of large amplitude relativistic EM soliton, by linearly-polarized intense laser interacting with a underdense uniform plasmas, are presented in more detail [216].

4.4.3 Particle Simulations

One-dimension and three-velocity (all quantities depend on x -coordinate and the particle momenta have three components) fully relativistic EM particle-in-cell (1D3V-PIC) code is used. The total length of simulation system is $3L$ (c/ω_0), where c and ω_0 are the speed of light and the laser EM frequency in vacuum, respectively. The L long plasma begins at $x=0$ and ends at L , in the front and rear side of the plasma layer, there are two L long vacuum regions. Ions are initially placed as a neutralizing background and are kept

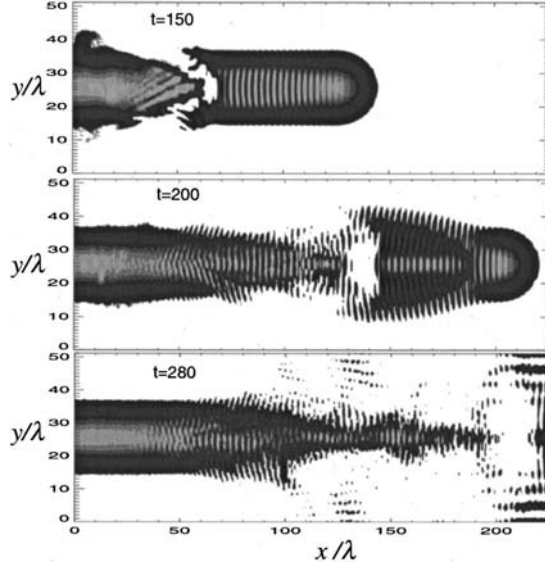


Figure 4.13: 2D distribution of EM energy density at three moments in time during pulse propagation ($a_0 = 0.2$, $n_e = 0.1n_c$) from 2D PIC simulation. Laser pulse break up is clearly observed, [194].

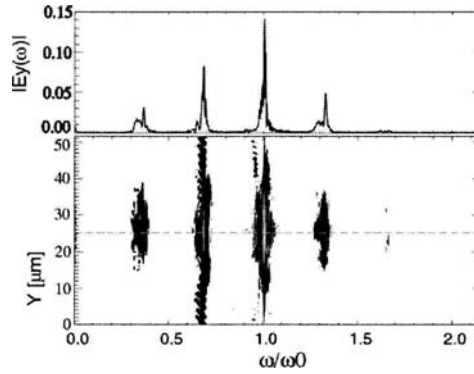


Figure 4.14: Transmitted light spectrum variation in transverse direction (bottom) and spectral distribution on the axis (top) from 2D PIC simulation of Fig.4.13.

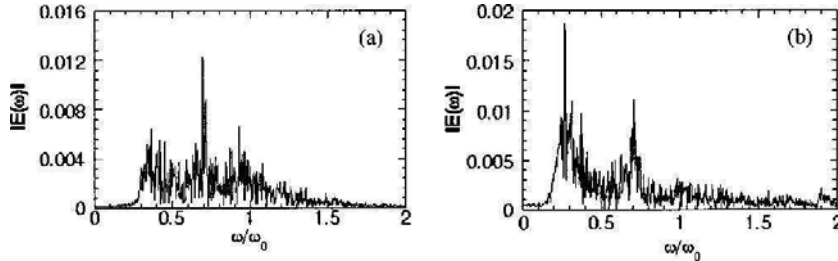


Figure 4.15: B-SRS spectra from 1D PIC simulation for parameters of Fig.4.14; (a) $a_0 = 0.2$ and (b) $a_0 = 0.3$ ($n_e = 0.1n_c$), [194].

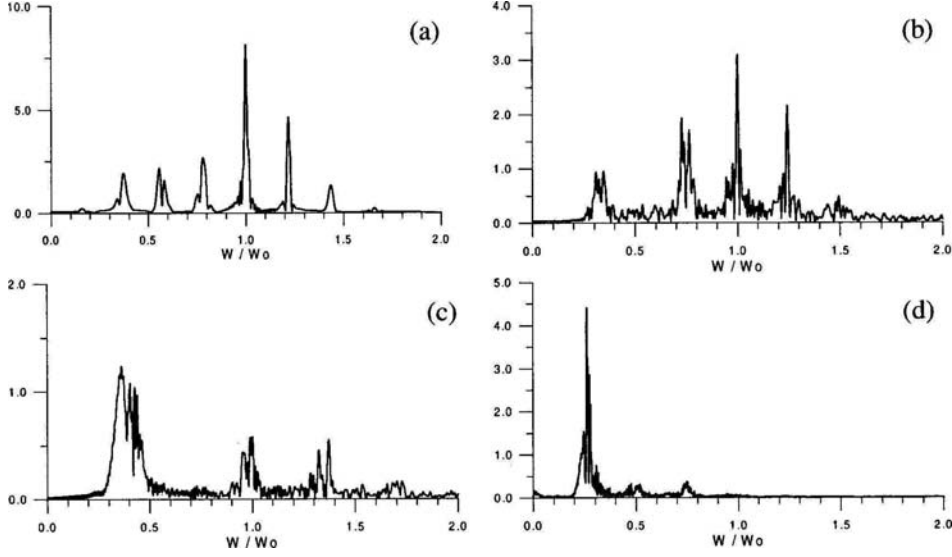


Figure 4.16: Forward-SRS spectra from 1D PIC for (a) $a_0 = 0.2$, $n_e = 0.05n_c$, (b) $a_0 = 0.5$, $n_e = 0.07n_c$, (c) $a_0 = 0.3$, $n_e = 0.13n_c$ and backward-SRS spectrum, (d) $a_0 = 0.4$, $n_e = 0.07n_c$, [194].

immobile. The number of cells is 10 per $1 c/\omega_0$ and 80 particles are put in each cell. The linearly-polarized laser with the electric field E_0 along the y -direction is launched at the position where $200c/\omega_0$ long distance before plasma. Its normalized amplitude is $a_0 = eE_0/m_e\omega_0c$, where e and m_e are the electron mass and charge, respectively. The electrons which enter vacuum region build a potential barrier that prevents electrons of leaving the plasma. For these electrons as well as for outgoing EM waves, two $100c/\omega_0$ long additional numerical damping regions are used [216].

It should be noted that, in the following parts of this paper, by taking the EM fields at the front and rear positions both are $100c/\omega_0$ long distance away from plasma, the spectra for both frequency and wavenumber, the reflectivity and the transmissivity, and the temporal growth of all EM modes are calculated, respectively. The time, electric field and magnetic field are normalized to the laser period $2\pi/\omega_0$, $m\omega_0c/e$ and $m\omega_0/e$, respectively; the time is taken zero, $\omega_0t = 0$, when the laser arrives at the vacuum-plasma boundary.

Stimulated Raman Cascade into Photon Condensation

Our first simulation are performed by taking plasma density $n = 0.03n_{cr}$, plasma length $L = 1000c/\omega_0$, temperature $T_e = 1.0keV$ and the normalized laser amplitude $a = 0.3$, respectively.

The long plasma is initially uniform in density and the intense laser pulse is radiated continuously in our simulations. There is enough time for the growth of instabilities and rich interplay between many relativistic electronic parametric instabilities, such as F-SRS, B-SRS and RMI [194, 216]. When an intense laser propagates in underdense plasma, SRS can be first excited by the intense laser EM wave coupling into a scattered EM wave

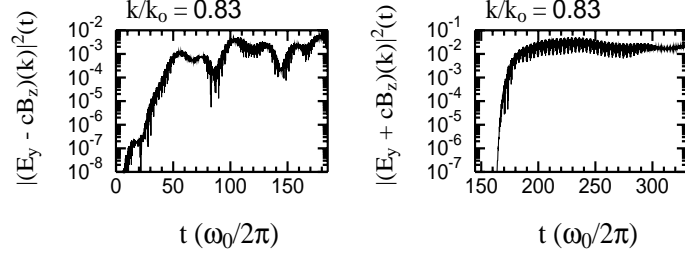


Figure 4.17: The temporal growth for reflected EM wave (left plot) and transmitted EM wave (right plot) both measured in vacuum in the case of plasma $n = 0.03n_{cr}$, $L = 1000c/\omega_0$, $T_e = 1.0keV$ and laser amplitude $a = 0.3$, respectively. From Fig. 4.18 to Fig. 4.22 the same simulation parameters are used, [216].

plus an EPW. In such a low plasma density, as shown in Fig.4.17, in the early linear growth stage, B-SRS has lower growth rate and longer growth time than that of the F-SRS, it gets saturated efficiently at a very early stage of evolution due to plasma heating and trapping. With time goes on, F-SRS and RMI can get close and merge to unique F-SRS/RMI instability, after that, which can compete with the B-SRS instability.

The frequency spectra and wave numbers for reflected EM, transmitted EM and ES waves are plotted in Fig.4.18, respectively. One can see that, during the SRS process, the excited dominant ES wave is EPW with frequency $\omega_{pe} \approx 0.17\omega_0$; the corresponding scattered Stokes EM wave has its frequency $\omega_s \approx 0.83\omega_0$. The wave numbers for both backward and forward scattered EM waves are $k_s \approx 0.83k_0$, the EPW have two dominant peaks, the first peak with $k_{epw} \approx 1.83k_0$ for B-SRS and the second peak with $k_{epw} \approx 0.17k_0$ for F-SRS, respectively. Therefore, for both B-SRS and F-SRS, they can well-explained by three-wave resonant coupling decay with the corresponding matching conditions for frequency $\omega_0 = \omega_s + \omega_{epw}$ and for wave number $k_0 = k_s + k_{epw}$ are well-satisfied.

It should be noted that, in our low plasma density case, the wavenumbers measured in vacuum nearly equal to that which measured inside plasma.

Fig.4.19 (top) shows the snapshots for the energy density of EM field, it demonstrates the spatial distribution of transverse EM energy density, in its early stage, B-SRS radiates its EM energy through soliton-like structures, as shown in Fig.4.19, which corresponds to the peaks in the reflectivity plot. When the unique F-SRS/RMI instability dominate and can compete with the B-SRS instability, as a result, the strong spatial self-modulation of the order of $2\pi c/\omega_{pe} \approx 5.8\lambda_0$ which comes from F-SRS/RMI instability and the depletion of the laser pulse are taken place and observed from Fig.4.19 (bottom).

In a linear regime, B-SRS and F-SRS Stokes sidebands in the spectra are far dominant over the anti-Stokes modes. Following that, there is a clear stimulated forward Raman cascade process, as nicely shown in Fig.4.21. The scattered Stokes EM waves include the first- to fifth-Stokes modes. In addition, the first- to fourth- anti-Stokes modes can also be observed. As expected, at early times, laser driven cascade shows descending spectral intensity toward higher harmonics. The stimulated forward Raman cascade is eventually halted at the cut-off, close to the background electron plasma frequency $0.15\omega_0$. The spectral gap between the laser fundamental and the lowest Stokes mode is apparent (Fig.4.21

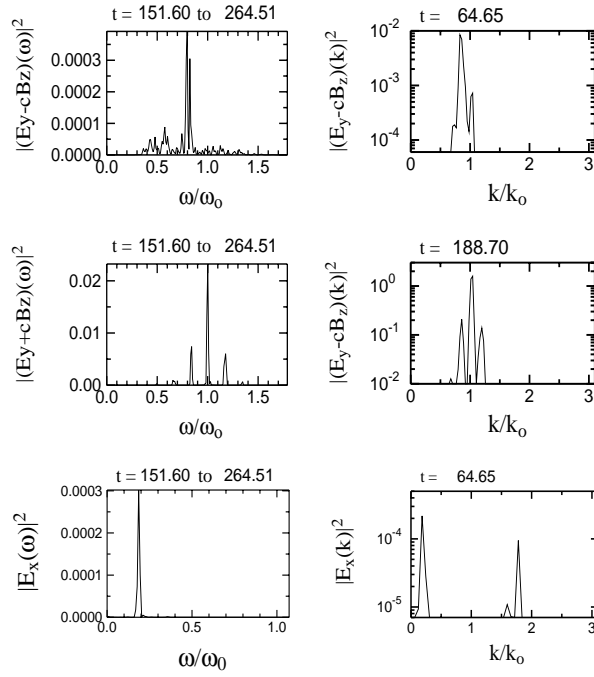


Figure 4.18: The frequency spectra for the reflected and transmitted EM waves both measured in vacuum and for ES wave measured inside plasma. The wavenumbers for electric field E_y and for ES field E_x both measured inside plasma, [216].

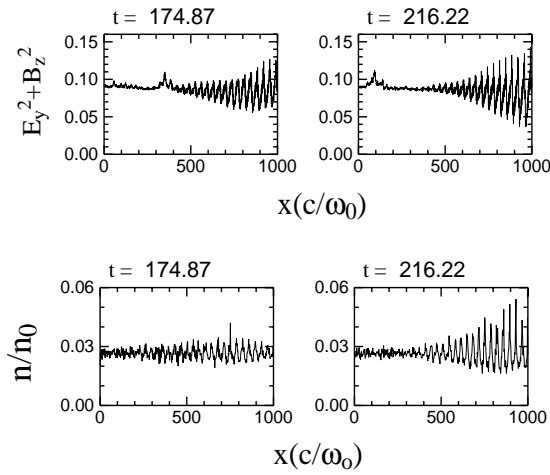


Figure 4.19: The snapshots for energy density of EM field $E_y^2 + B_z^2$ (averaged over laser period) and plasma density n/n_0 , [216].

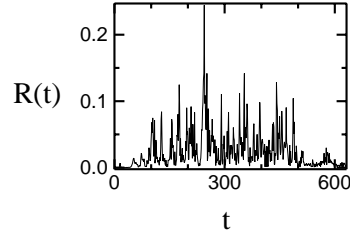


Figure 4.20: The temporal reflectivity of EM wave measured in vacuum, [216].

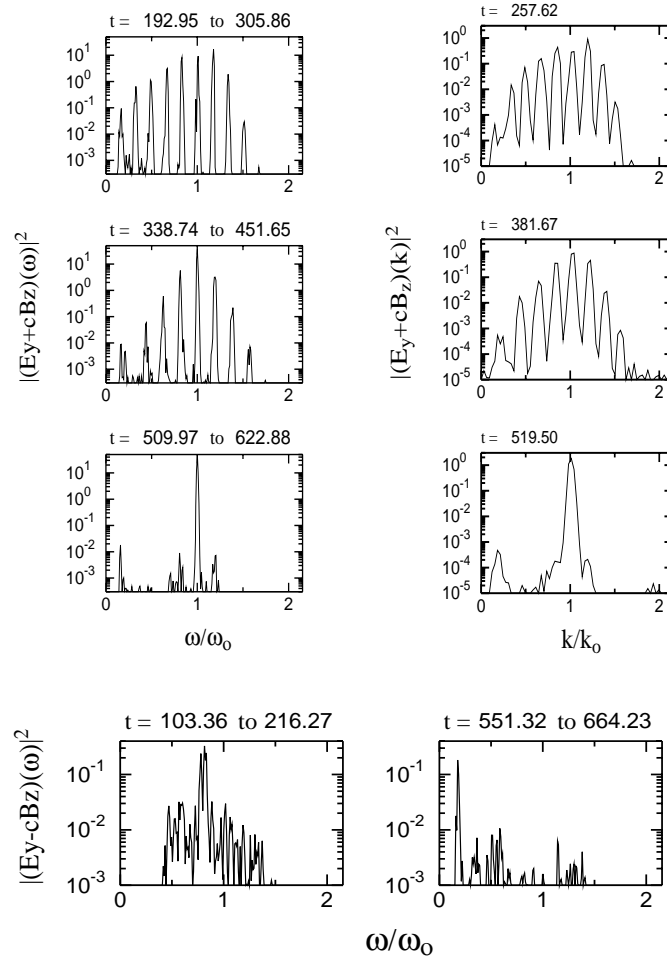


Figure 4.21: The frequency and wavenumber spectra of transmitted EM wave measured in vacuum (top); the frequency spectra of reflected EM wave (bottom), [216].

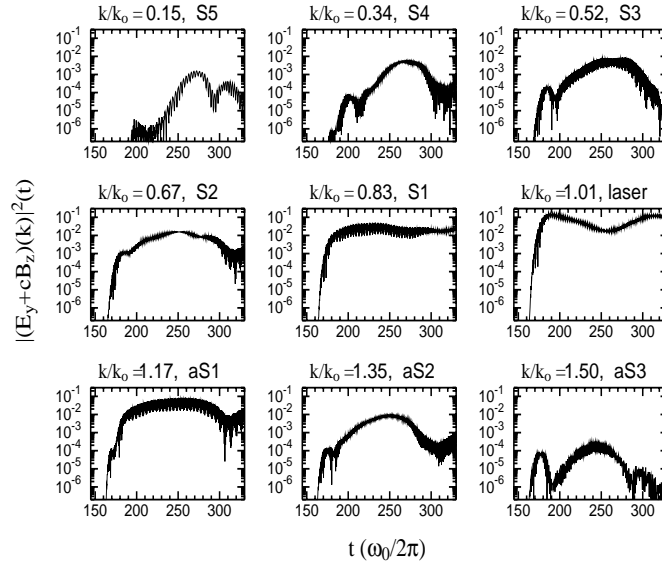


Figure 4.22: The temporal growth of transmitted EM Stokes (S) and anti-Stokes (aS) modes, [216].

and below). Continuous laser energy transfer by Raman cascade to low-frequency self-trapped EM mode further enhances the unique photon condensate.

From the frequency and wavenumber spectra of backscattered EM wave, stimulated backward Raman cascade still can be observed, which include both Stokes and anti-Stokes EM modes, however, it does not reveal a clear Raman cascade process like shown in stimulated forward Raman cascade process due to complex backscattered EM wave. Another interesting feature is that, there is the broadening of the backscattered EM spectra, from laser frequency to the perturbed electron plasma frequency. In the meantime, the reflectivity exhibits a spiky behavior, as shown in Fig.4.20, which is a result of condensation and modulational instability generating spiky turbulence [194].

To illustrate the onset and growth of the stimulate forward Raman cascade, the plots for the temporal evolution of dominant Stokes and anti-Stokes EM modes measured in vacuum, are given in Fig.4.22. The fundamental laser EM mode has a clear depletion of the EM energy which corresponds to the depression in the temporal evolution plot of laser EM mode. Both for Stokes and anti-Stokes EM modes, high-order mode with low growth rate grows later in time than of the low-order mode. Another fact is that, there is clear second growing process with the decrease of EM mode, this perhaps comes from the transition from high-order mode to low-order one. In the later time, the continuing instability growth through stimulated Raman cascade downshifts a power maximum from the fundamental to the bottom of the EM wave spectra. They clearly reveal a tendency of a transition from the Raman cascade regime to regimes of energy accumulation nearly at the perturbed electron plasma frequency which is the cutoff frequency for EM wave propagating in plasma, the so-called photon condensation.

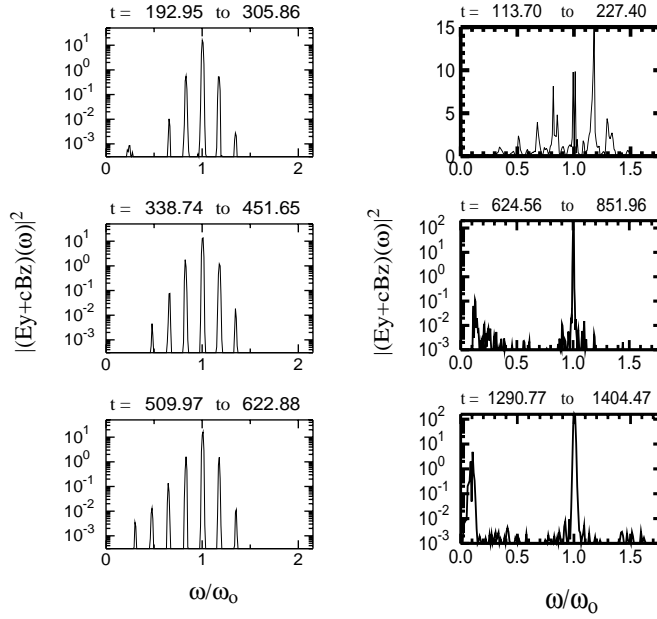


Figure 4.23: The frequency spectra of transmitted EM wave, for $n = 0.03n_{cr}$, $L = 1000c/\omega_0$, $T_e = 1.0keV$; for laser amplitude $a = 0.2$ (left) and $a = 0.4$ (right), [216].

Effect of Laser Intensity on SRS Cascade into Photon Condensation

What role does the laser intensity play in SRS evolution and stimulated Raman cascade into photon condensation? To understand this question, several simulations have been performed only by changing laser amplitude. As shown in Fig.4.23, the frequency spectra of transmitted EM wave for laser amplitude $a = 0.2$ and $a = 0.4$, respectively, are presented here.

It is clear that the cascade-to-condensation transition becomes more pronounced with increasing laser intensity [194]. In the lower laser amplitude case, few Stokes and anti-Stokes EM modes are excited, further, with decreasing laser amplitude, the stimulated Raman cascade into photon condensation and even SRS do not take place. In the higher

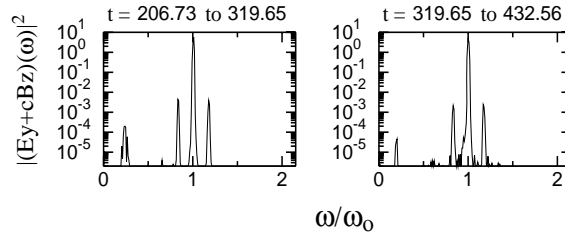


Figure 4.24: The frequency spectra of transmitted EM wave, for $n = 0.03n_{cr}$, $L = 1000c/\omega_0$, $T_e = 1.0keV$ and $a = 0.1$, [216].

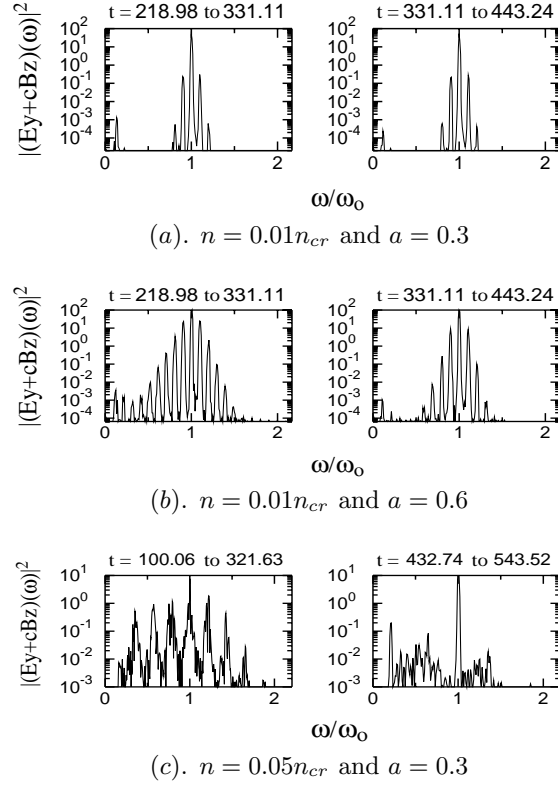


Figure 4.25: The frequency spectra of transmitted EM wave for different plasma density and for fixed $L = 1000c/\omega_0$ and temperature $T_e = 1.0keV$. For (a) $n = 0.01n_{cr}$ and $a = 0.3$, (b) $n = 0.01n_{cr}$ and $a = 0.6$, (c) $n = 0.05n_{cr}$ and $a = 0.3$, [216].

intensity case, more Stokes and anti-Stokes modes are excited with short growing and persistent time than that in the lower laser amplitude case; however, the bandwidth of the modes become larger than that in the lower amplitude case, further with increasing laser amplitude, the modes will merge each other, which quickly suppresses the growth of the above processes.

For much lower laser intensity $a = 0.1$, as shown in the Fig.4.24, there is no much Stokes and anti-Stokes EM modes to be excited. In addition to natural laser EM mode, only three other modes, i.e., the first Stokes EM mode, first anti-Stokes EM mode and the mode at electron plasma frequency ω_{epw} , are excited.

In a low density plasma, in the regions of strong photon-condensation, first, large portion of electrons are pushed away due to the large ponderomotive force of EM field, the resulted electron density redistribution results in nonlinearity; second, dispersion effect comes into play an important role due to the electron mass increase relativistically by their responding to the intense EM field [198]. Therefore, in addition to various instabilities, these effects can lead to many well-known nonlinear phenomena, for example, the generation of relativistic EM soliton [196, 220].

As shown in Fig.4.26, the soliton has regular EM and ES structure in space, i.e., its ES field E_x has one-cycle structure, the corresponding transverse electric field E_y is the half-

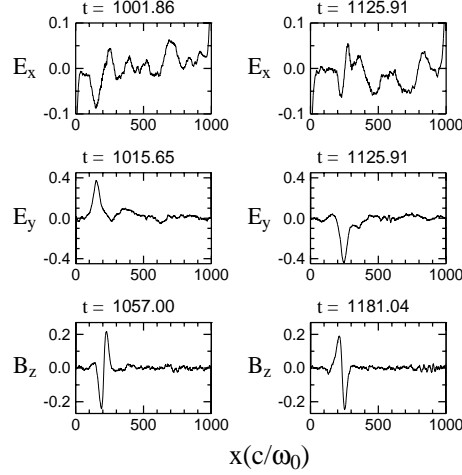


Figure 4.26: The snapshots for ES field profile (averaged over EPW wavelength) and EM field structures (averaged over laser period) in the case of plasma $n = 0.03n_{cr}$, $L = 1000c/\omega_0$, $T_e = 1.0keV$ and laser amplitude $a = 0.5$, respectively, [216].

cycle and the magnetic field B_z is the one-cycle structure, respectively. And the spatial EM field structure is oscillatory in time, but the ES field structure is not. The explanation comes directly from Maxwell's equations. The Faraday law gives $B_z \sim \partial E_y / \partial x$; indeed, the x -derivative of the Gaussian soliton profile E_y gives B_z in Fig.4.26. Similarly, from the Poisson equation, integration over x of the Gaussian density cavity leads to the ES field E_x in Fig.4.26. Moreover, PIC data and analytics, e.g., equations (4-7) of [201], show that zero-harmonic term dominates the electron density perturbation. Therefore, the Poisson equation gives the corresponding non-oscillatory ES field structure, like E_x in Fig.4.26; from which we know that, the size of EM soliton is about $5\lambda_0$, which approximately equals to the electron plasma wavelength $\lambda_{pe} = c/\omega_{pe}$. About the ES and EM structures of soliton, it has been discussed in Ref. [221, 222, 223], the acceleration of soliton also has been explained there, i.e., in addition to the inhomogeneity of plasma density, the acceleration of relativistic EM solitons can depend upon, not only the incident laser amplitude, but also upon the plasma length.

In conclusion, fully relativistic EM 1D-PIC simulation results on the SRS, stimulated Raman cascade and the transition from Raman cascade into photon condensation, induced by linearly-polarized intense laser interacting with underdense homogeneous plasmas were shown. At appropriate laser amplitude and plasma conditions, large relativistic EM soliton forms due to the strong photon condensation.

4.5 Ultra Relativistic EM Solitons in Intense Laser Interaction with a Low Density Plasma

Ultra relativistic electromagnetic solitons due to strong photon condensation, induced by a linearly polarized intense laser interacting with an underdense uniform collisionless plasma, are studied by particle simulations. In homogeneous plasma, both standing and accelerated solitons are observed. It is found that the acceleration of the solitons depends upon not only the laser amplitude but also the plasma length. The electromagnetic frequency of the solitons is between half- and one-time of the unperturbed electron plasma frequency. The electrostatic field inside the soliton has a one-cycle structure in space, while, the transverse electric and the magnetic fields have half- and one-cycle structures, respectively. The acceleration of the solitons is briefly discussed.

4.5.1 Introduction

The mechanism of the relativistic EM soliton formation and its structure have been analytically investigated and observed by particle simulation of the interaction of intense laser radiation with underdense and overdense plasmas [193, 201, 224, 225, 226, 227, 228]. The EM solitons found in one-dimensional (1D) and two-dimensional (2D) particle simulations consist of slowly or non-propagating electron density cavities inside which an EM field is trapped and oscillates coherently with a frequency below the unperturbed electron plasma frequency, and with a spatial structure corresponding to half a cycle (subcycle soliton) [229]. In homogeneous plasmas, EM solitons have been found to exist for a long time, close to the regions where they were generated, and eventually decay due to their interaction with fast particles and the transforming their energy into fast particles. In inhomogeneous plasmas, EM solitons are accelerated with the acceleration proportional to the gradient of the plasma density towards the low density side. When an EM soliton reaches some critical plasma region, for example, the plasma-vacuum interface, it radiates its energy away in the form of a short burst of low-frequency EM radiation [230]. The interaction of two 2D solitons leads to their merging and the resulting soliton retains the total energy of the two merged solitons [195, 198, 231].

In previous section, we mainly paid attention at SRS cascade scattering and the transition from Raman cascade into photon condensation [216]. As a follow up of above work, here, we will concentrate on and present 1D-PIC simulation results of the large, ultra relativistic EM solitons due to strong photon condensation following that stimulated Raman cascade, induced by a linearly polarized intense laser pulse in long underdense plasma. The standing, backward-, and forward-accelerated EM solitons are observed. It is found that in homogeneous plasma the acceleration of the EM solitons depends upon both the laser amplitude and the plasma length. The EM frequency of the solitons is between half- and one times of the background electron plasma frequency. The ES field inside the soliton has a one-cycle structure in space, while the transverse electric and magnetic fields have half-cycle and one-cycle structures, respectively. The acceleration of the EM solitons are briefly discussed. Finally, the influences of the plasma temperature and the ion dynamics on the formation of the EM solitons are investigated.

4.5.2 Ultra Relativistic EM Solitons

A one-dimensional and three-velocity fully relativistic EM particle-in-cell (1D3V-PIC) code is used in our simulations. The length of the plasma layer is L (c/ω_0), which begins at $x=0$ and ends at $x = L$, where c and ω_0 are the speed of light and the laser frequency in vacuum, respectively; at the front and rear side of the plasma, there are two L long vacuum regions. Ions are initially placed as a neutralizing background and are kept immobile. The number of cells is 10 per $1 c/\omega_0$ and 80 particles are put in each cell. The linearly polarized laser pulse, which with the electric field E_0 along the y direction and the normalized amplitude $a = eE_0/m_e\omega_0c$, is launched at the distance $200c/\omega_0$ from the plasma front interface, where e and m_e are the electron mass and electron charge, respectively. The plasma electrons which enter the vacuum region build a potential barrier that prevents more electrons leaving the plasma. For outgoing electrons as well as EM waves, two $100c/\omega_0$ long additional numerical damping regions are used.

The time, electric field, and magnetic field are normalized to the laser period $2\pi/\omega_0$, $m_e\omega_0c/e$, and $m_e\omega_0/e$, respectively. The time is taken as zero, $\omega_0t = 0$, when the unit-step laser pulse arrives at the front vacuum-plasma boundary.

All simulations are performed by using an underdense homogeneous low density plasma, $n = 0.032n_{cr}$. The unit-step intense laser pulse is injected continuously; there is enough time for growth, development, and rich interplay between many relativistic electronic parametric instabilities, such as the stimulated backward Raman scattering (B-SRS), stimulated forward Raman scattering (F-SRS), and the relativistic modulational instability (RMI), etc. [194, 216].

In such laser plasma conditions, SRS can be first excited by the intense laser EM wave coupling into a scattered EM wave plus an EPW. In the early linear stage, B-SRS has a lower growth rate and longer growth time than that of the F-SRS. B-SRS irradiates its EM energy through spiky-like temporal structures and becomes saturated at an early stage due to electron heating by trapping and EPW breaking. At later times, F-SRS and RMI become closer and merge to a unique F-SRS/RMI instability, which can later dominate and compete with the B-SRS instability; as a result, a strong spatial self-modulation of the order of $2\pi c/\omega_{pe} \approx 5.6\lambda_0$ and depletion of the laser pulse will take place. Following that SRS, there is a clear stimulated Raman cascade scattering with the excitation of higher-order Stokes and anti-Stokes mode EM waves [216]. At early times, the laser pump driven Raman cascade develops a descending spectrum toward higher order harmonics. The Raman cascade is eventually halted at the lowest Stokes harmonic, close to the perturbed electron plasma frequency. In the later time, the continuing instability growth and laser energy transfer through Raman cascade downshifts EM energy from the fundamental to the bottom of the EM frequency spectrum, i.e., the low frequency trapped EM mode. It reveals a tendency to transition from the Raman cascade regime to EM energy accumulation, i.e., the so-called photon condensation [194, 102, 151, 232, 233]. The cascade-to-condensation transition becomes more pronounced with increasing laser amplitude and increasing plasma density.

In the regions of strong photon-condensation, first, a large part of the electrons is pushed away by the ponderomotive force of the EM field, creating a local electron density cavity; second, the relativistic electron mass increases, both locally reducing the plasma

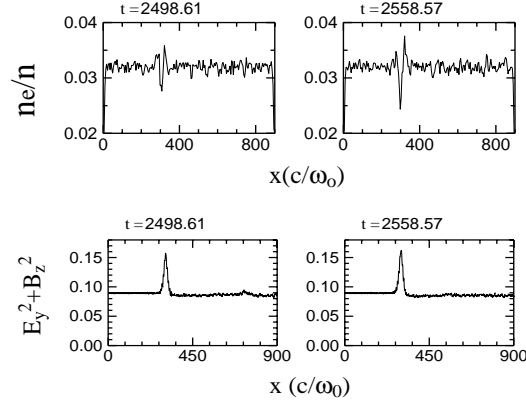


Figure 4.27: The snapshots for electron density n/n_e and for EM energy density $E_y^2 + B_z^2$ averaged over laser wavelength λ_0 in the case of plasma $n = 0.032n_{cr}$, $L = 900c/\omega_0$, $T_e = 350eV$ and laser amplitude $a = 0.3$, respectively, [222].

refractive index and resulting in self-trapping of EM energy. Therefore, at proper laser amplitude conditions, due to strong photon condensation, the well-known physical phenomenon of nonlinear EM energy localization in the form of the relativistic coherent EM soliton becomes possible. Since the photon number in the Raman cascade is conserved, the frequency downshift results in a correspondingly large increase in the amplitude of the lowest harmonics [194, 216, 196, 220].

Standing EM Soliton

In the case of plasma density $n = 0.032n_{cr}$, length $L = 900c/\omega_0$, temperature $T_e = 350eV$ and laser amplitude $a = 0.3$, following that stimulated Raman cascade scattering and strong photon-condensation, the snapshots for electron plasma density n/n_e and EM energy density $E_y^2 + B_z^2$ are shown in Fig.4.27. A spatially localized, non-propagating electron density cavity is created. Inside the density cavity, an EM field is trapped and oscillates coherently; that is, a large amplitude relativistic EM soliton is formed. There is no the gradient of the plasma density, therefore, the formed EM soliton belongs to the standing case, and exists within our simulation time, close to the regions where it was generated [230].

In Fig.4.28, the frequency spectra for ES field E_x and EM field E_y , which are trapped inside the soliton, are plotted. In addition to the laser fundamental and the excited perturbed EPW, the EM component with frequency $\omega_{sol}^{EM} \approx 0.13\omega_0 \approx 0.72\omega_{pe}$ and the ES component with frequency $\omega_{sol}^{ES} \approx 0.87\omega_0$ are observed, respectively. If only from the point of view of the frequency, it seems that, one can explain this phenomenon roughly by a three-wave resonant coupling process during the existence of the EM soliton. The size of the EM soliton is about $\Delta x_{sol} \approx \lambda_{epw} \approx 5.6\lambda_0$, where λ_{eaw} and λ_0 are the electron plasma wavelength and laser wavelength in vacuum, respectively. As shown in Fig.4.29, the ES field E_x , which is trapped inside the soliton, has a one-cycle structure in space, while the corresponding transverse electric field E_y has a half-cycle and the magnetic field B_z a

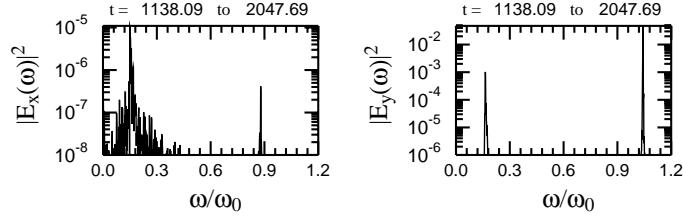


Figure 4.28: The spectra of ES field and EM field which trapped inside soliton region. The simulation parameters are the same as used in Fig.1, [222].

one-cycle structure, respectively. The spatial EM field structure is oscillatory in time, but the ES field structure is not [194, 216]. In our simulations, laser amplitude was weakly to moderately relativistic ($a < 1$), however, the created EM solitons are indeed largely ultra-relativistic, and the maximum amplitude of the EM soliton grows with increasing laser amplitude and saturates at roughly similar maximum amplitude (ultra-relativistic) $a_{sol}^{max} \approx 5 - 6$ [216].

It should be stated here, that the EM soliton field frequency is $0.13\omega_0$, smaller than the background electron plasma frequency $\omega_{pe} \sim 0.18\omega_0$. This comes from the strong relativistic effect, which makes the electron mass increase from m_e to γm_e , and can then decrease electron plasma frequency from ω_{pe} to $\omega_{pe}/\gamma^{1/2}$. Therefore, it is possible that localized EM structure, with frequency smaller than background ω_{pe} , can exist and propagate inside plasma.

By keeping the plasma parameters unchanged and increasing the laser intensity only, EM soliton scenarios appeared to be different from the above standing case. Both, the backward-accelerated and forward-accelerated EM solitons are observed [222, 234].

Backward- and Forward Accelerated EM solitons

In two cases where the laser amplitude $a = 0.4$ and $a = 0.5$ (see Fig.4.30 for laser amplitude $a = 0.4$), following Raman cascade and strong photon-condensation, a spatially localized large amplitude EM soliton due to strong photon-condensation begins to form. However, the soliton dynamics appears to be different from that of the standing soliton case; the observed EM soliton is now accelerated backwards towards the plasma-vacuum interface. After arriving at the plasma-vacuum interface, it radiates its energy away in the form of a short burst of low-frequency intense EM wave, due to a non-adiabatic interaction with the plasma-vacuum boundary. During the radiation of the EM soliton, as a result, one can observe a very high transient reflectivity larger than that of the B-SRS process (Fig.4.30, top). In the higher laser amplitude $a = 0.5$ case, the story is the same as that for the laser amplitude $a = 0.4$ case, i.e., a spatially localized backward-accelerated large amplitude EM soliton can be still observed. However, due to the larger acceleration, the "lifetime" of the EM soliton inside the plasma is shorter than that of the laser amplitude $a = 0.4$ case. Similarly, a very high transient reflectivity, larger than that of the B-SRS process, can be also observed during the radiation of the EM soliton.

By analyzing the frequency spectra in vacuum after the radiation of the EM soliton,

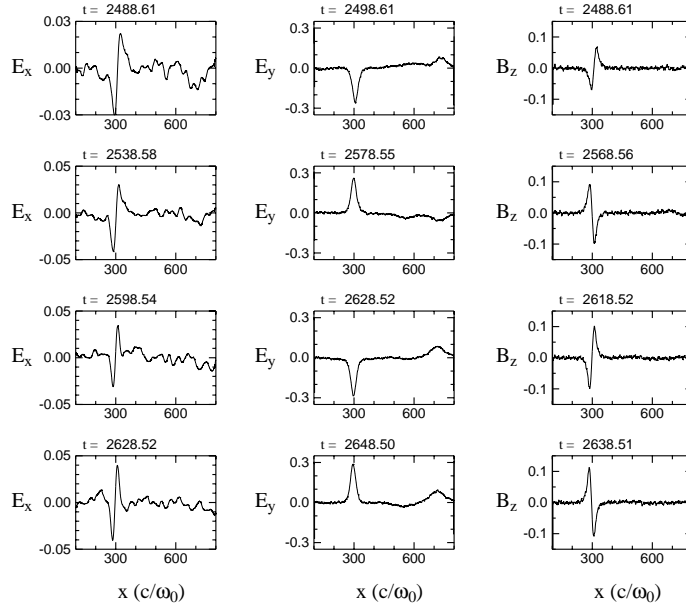


Figure 4.29: The snapshots for ES field structure (averaged over the EPW wavelength λ_{epw}) and EM field structure (averaged over the laser wavelength λ_0). The simulation parameters are the same as used in Fig.4.27, [222].

we can obtain that the EM frequencies of the soliton are $\omega_{sol}^{EM} \approx 0.67\omega_{pe}$ for the laser amplitude $a = 0.4$ case, and $\omega_{sol}^{EM} \approx 0.61\omega_{pe}$ for the laser amplitude $a = 0.5$ case, respectively [222].

If we further increase the laser amplitude to $a = 0.6$ and $a = 0.7$, the most interesting phenomenon is that the observed EM solitons are neither the standing ones nor the backward-accelerated ones, rather, the large amplitude EM solitons are now accelerated forward.

The scenarios before the formation of the EM solitons are the same as stated before, i.e., due to strong photon-condensation, as shown in Fig.4.31, for laser amplitude $a = 0.6$. A spatially localized large amplitude EM soliton can be still formed. However, the interesting feature is that the observed EM soliton now accelerates in the forward direction. Again, after the EM soliton arrived at the plasma-vacuum interface, it radiated its energy away in the form of a short burst of low-frequency EM waves. As expected, a very high transient transmissivity during the radiation of the EM soliton can be detected as shown in Fig.4.31 (top). For higher intensity $a = 0.7$ the situation is the same as for $a = 0.6$ case.

Similarly, by analyzing the frequency spectra in vacuum after the radiation of the EM soliton, we found that the EM frequencies of the soliton are $\omega_{sol}^{EM} \approx 0.56\omega_{pe}$ for the laser amplitude $a = 0.6$ case, and $\omega_{sol}^{EM} \approx 0.50\omega_{pe}$ for the laser amplitude $a = 0.7$ case, respectively [222].

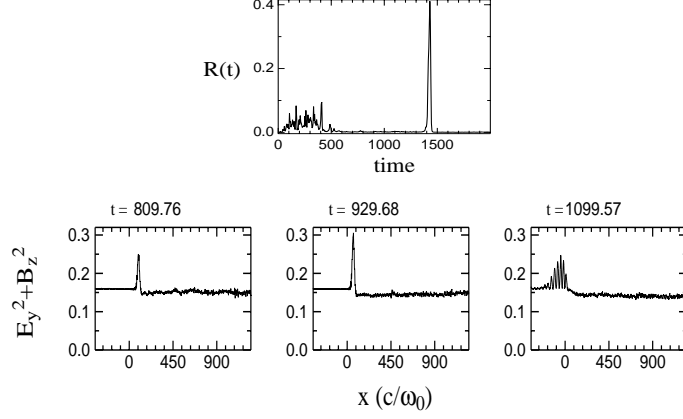


Figure 4.30: The snapshots for reflectivity and EM energy density $E_y^2 + B_z^2$ (averaged over laser wavelength λ_0) in the case of plasma $n = 0.032n_{cr}$, $L = 900c/\omega_0$, $T_e = 350eV$ and laser amplitude $a = 0.4$, respectively, [222].

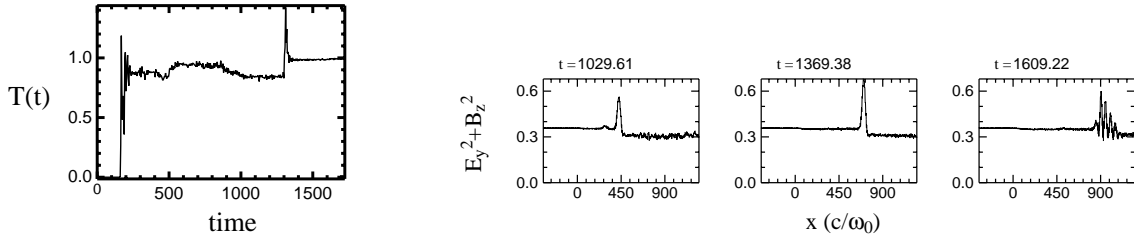


Figure 4.31: The snapshots for transmissivity and EM energy density $E_y^2 + B_z^2$ (averaged over laser wavelength λ_0) in the case of plasma $n = 0.032n_{cr}$, $L = 900c/\omega_0$, $T_e = 350eV$ and laser amplitude $a = 0.6$, respectively, [222].

Merging of Two Ultra Relativistic EM Solitons

By performing many simulations, we also found that, in the case of the plasma density $n = 0.032n_{cr}$, length $L = 1400c/\omega_0$, temperature $T_e = 350eV$ and laser amplitude $a = 0.3$, as shown in the Fig.4.32, two spatially localized large amplitude EM solitons emerge and coexist inside the plasma. After their formation, the two EM solitons both are accelerated backward with different accelerations, as time goes on, the back one can overtake the front one. After that, the two EM solitons then merge together to form a new EM soliton, which with the large amplitude nearly equals the sum of the two EM solitons. This newly formed large amplitude EM soliton exists and does not separate again within our simulation time

To conclude, the formation of both the standing and the accelerated large amplitude EM solitons due to strong photon condensation, induced by linearly polarized intense laser interacting with an underdense uniform collisionless plasma, is studied by 1D-PIC particle simulations. We found that, in addition to the inhomogeneity of the plasma density, the acceleration of the EM solitons depends upon both the laser amplitude and

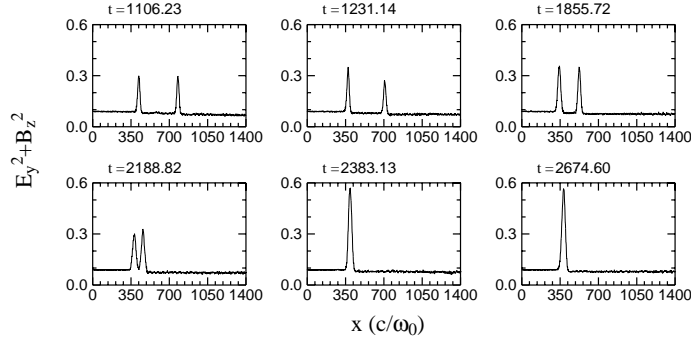


Figure 4.32: The snapshots for EM energy density $E_y^2 + B_z^2$ averaged over laser wavelength λ_0 in the case of plasma density $n = 0.032n_{cr}$, length $L = 1400c/\omega_0$, temperature $T_e = 350eV$ and laser amplitude $a = 0.3$, respectively, [222].

the plasma length. The EM frequency of the solitons is between half- and one-time of the unperturbed electron plasma frequency. The transverse electric field E_y , magnetic field B_z , and ES field E_x inside the soliton have half-, one-, and one-cycle structures in space, respectively.

4.6 Stimulated Electron Acoustic Scattering in High Intensity Laser Plasma Interaction

The propagation of a laser light through an under-dense plasma is an active research topic. Much works have been devoted to stimulated Raman and Brillouin scattering instabilities, concerning their ability to produce energetic particles which can preheat the core of a fusion pellet. The stimulated scattering from an electron plasma wave (EPW) (Raman scattering -SRS) or ion acoustic wave (IAW) (Brillouin scattering -SBS) can be large to reflect a significant part of the laser light and decrease the coupling efficiency at the target. As was shown by experiments and computer simulations there can be a rich interplay between these two instabilities [169, 168, 170]. Although understanding of basic principles of laser parametric coupling to the EPW and IAW is quite satisfactory, the quantitative predictions are often in large disagreement with observations from real experiments. There was a recent upsurge of interest to explain unexpectedly high SRS reflectivity obtained in experiments emulating conditions of National Ignition Facility targets [235, 236].

4.6.1 On the Electron Acoustic Waves

Recently, D. S. Montgomery *et al.* reported observation of a novel stimulated electron-acoustic wave scattering (SEAS) to explain "single hot spot" experiments performed at Trident laser facility [237, 238]. Namely, in the linear theory, the so-called electron-acoustic wave (EAW) exists, i.e. a strongly damped linearized Vlasov-Maxwell (VM)

mode whose phase velocity is between an EPW and an IAW; often neglected in studies of wave-plasma instabilities. However, analytical studies of non-linear one-dimensional VM solutions have found that strong electron trapping can occur even for small amplitude electrostatic wave, resulting in undamped non-linear travelling waves (BGK-like) [240, 241] or, with an inclusion of small dissipation, in weakly damped travelling solutions [241]. The main difficulty in resolving SEAS from the standard SRS in laser-plasma experiments is that the backscattered light spectrum can cover the nearly continuous broad range of frequencies due to a simultaneous growth of instabilities at different spatial locations in a non-uniform plasma, complex wave-plasma dynamics due to the system length, etc. The first observation of backward SEAS and reinterpretation of earlier experimental results from low plasma densities [237, 238], has encouraged further investigation of domains and conditions for SEAS. However, under reported conditions the energy in the SEAS mode still remained well below (3000 times) the observed backward SRS level.

4.6.2 Stimulated Raman and Acoustic Wave Scattering

Further, excitation of SEAS and its interconnection with SRS instability is investigated by particle simulation of a propagation of a linearly polarized laser through a plasma layer placed in vacuum. An electromagnetic relativistic 1d3v PIC code was used. The number of grids was 25 per $1c/\omega_0$ (ω_0 is the laser frequency), with minimum 50 particles/grid. The length of a simulation system was $220c/\omega_0$ and ions were kept immobile as a neutralizing background. The electrons which enter vacuum build a potential barrier that prevents other electrons of leaving the plasma. However, due to strong heating some energetic electrons can reach boundaries of the system. For these electrons, as well as for electromagnetic waves additional damping regions were used. In number of simulations, besides stimulated Raman backscattering, we have observed an intense reflection recognized as SEAS instability, with its main contribution in regions with over-critical density for ordinary SRS. Strong SEAS reflection, which can several times exceed SRS reflectivity, is followed by large heating of a plasma, which was the first report of such a plasma behavior given by [176, 242, 243, 244, 245].

From our simulation data SEAS is identified as a resonant three-wave parametric interaction [165] involving the laser pump (ω_0, k_0), the backscattered lightwave (ω_s, k_s) and the trapped electron-acoustic wave (EAW) (ω_a, k_a). In the linear instability stage, resonant conditions $\omega_0 = \omega_s + \omega_a$ and $k_0 = -k_s + k_a$ are well satisfied, while electromagnetic waves (pump and Stokes wave) satisfy standard dispersion equation $\omega_{0,s}^2 = \omega_p^2 + c^2 k_{0,s}^2$. The backscattered wave is always found to be driven near critical, i.e. $\omega_s \approx \omega_p$ which implies $k_s \approx 0$ and $V_s \approx 0$ ($\omega_p = (ne^2/(\epsilon_0 m \gamma))^{1/2}$ is the plasma frequency, γ is the relativistic factor, and $V_s = c^2 k_s / \omega_s$ is the light group velocity). Therefore, the Stokes sideband is a slowly propagating, almost standing electromagnetic wave. The above decay scheme is observed for a wide range of laser intensities, plasma densities and temperatures. It is known that high temperatures can significantly alter the growth rates and sometimes suppress parametric instabilities [250]. However, according to [241], efficient excitation of trapped EAW ($\omega_a < \omega_p$), is to be expected in the range $v_{ph}/v_t = 1 - 2$ (v_{ph} and $v_t = (T/m)^{1/2}$ are the phase and electron thermal velocities). Thus, for SEAS excitation at the threshold, high thermal velocity which closely match the EAW phase velocity is important.

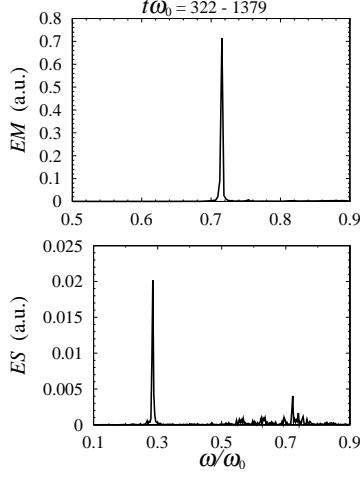


Figure 4.33: Spectrum of electromagnetic (top) and electrostatic (bottom) waves in the plasma layer ($n = 0.6n_{cr}$, $L = 40c/\omega_0$) for time interval $t\omega_0 = 322 - 1379$. The initial electron thermal velocity is $v_t/c = 0.28$, [242].

To illustrate an onset and growth of SEAS instability, spectra of electromagnetic-light (EM) waves and electrostatic (ES) waves are plotted in Figs. 4.33- 4.34.

Fig.4.33 shows discrete spectra in an early phase of SEAS instability. The density and the plasma length are $n = 0.6n_{cr}$ ($n_{cr} = n(\omega_0/\omega_p)^{1/2}$) and $L = 40c/\omega_0$, respectively, the longitudinal thermal velocity is $v_t/c = 0.28$ and the laser strength is $\beta = (eE_0)/(mc\omega_0) = 0.3$ (E_0 is the amplitude of the electric field). The backscattered EM wave grows at the electron plasma frequency $\omega_p \approx 0.72\omega_0$ (the laser pump line at $\omega/\omega_0 = 1$ is not shown), while corresponding EAW is at $\omega_0 - \omega_p \approx 0.28\omega_0$. Note that apart from ES noise around a natural plasma mode ($\omega_p \approx 0.72\omega_0$), ponderomotively driven non-resonant modes are also present (not shown in Fig.4.33) at 2-nd, $\omega = 2\omega_0$ and $k = 2k_0$ ($v_{ph}/c \approx 1.44$), as well as at zero-harmonic [177, 178]. From obtained data, it follows that the phase velocity of the EAW is $v_{ph}/c = (\omega_0 - \omega_p)/k_0 \approx 0.41$.

In Fig.4.34 nonlinearly broadened EM and ES spectra of fully developed SEAS are shown for a plasma with $n = 0.4n_{cr}$, $L = 40c/\omega_0$, $v_t/c = 0.20$ and laser strength $\beta = 0.3$. The instability growth results in the plasma frequency decrease and strong electron heating which tends to suppress the further growth. Above is reconfirmed in the post -SEAS stage, after the instability was halted (vide infra). Once EAW has died off, dominant ES response is weak EPW, which peaks at perturbed $\omega_p \approx 0.54\omega_0$ (the decrease of 0.06 from the initial state), while the decreased Stokes sideband appears at $\omega_s \approx 0.58\omega_0$. Moreover, a blue-shifted, modulated and incoherently broadened EM spectrum (Fig.4.33) seems consistent with the 3WI backscatter complexity induced by the nonlinear phase shift, as was predicted by one of these authors [102, 151, 236].

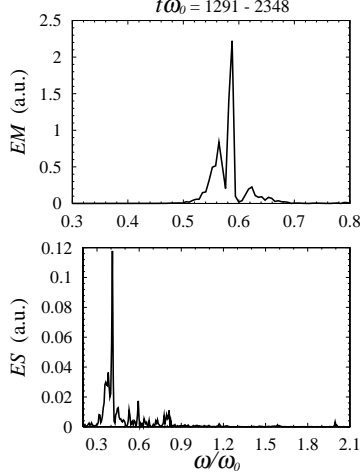


Figure 4.34: Spectrum of electromagnetic (top) and electrostatic (bottom) waves in the plasma layer ($n = 0.4n_{cr}$, $L = 40c/\omega_0$) for time interval $t\omega_0 = 1291 - 2348$. The initial electron thermal velocity is $v_t/c = 0.2$, [242].

4.6.3 SEAS Model

We propose a SEAS model as a resonant parametric coupling of three waves $a_i(x, t) \exp[i(k_i x - \omega_i t)]$, in a weakly varying envelope approximation [102, 105],

$$\frac{\partial a_0}{\partial t} + V_0 \frac{\partial a_0}{\partial x} = -M_0 a_s a_a, \quad (4.88)$$

$$\frac{\partial a_s}{\partial t} - V_s \frac{\partial a_s}{\partial x} = M_s a_0^* a_a, \quad (4.89)$$

$$\frac{\partial a_a}{\partial t} + V_a \frac{\partial a_a}{\partial x} + \Gamma_a a_a = M_a a_0^* a_s, \quad (4.90)$$

where $V_i > 0$ are the group velocities, Γ_a is damping rate for EAW ($\Gamma_0 = \Gamma_s = 0$ for light waves is used), $M_i > 0$ are the coupling coefficients and a_i are the wave amplitudes, where $i = 0, s, a$, stand for the pump, backscattered wave and EAW, respectively. Since considered model is a short plasma, in order to get high reflectivity, instability needs to be absolute. With standard boundary conditions $a_0(0, t) = E_0$, $a_s(L, t) = a_a(0, t) = 0$, the backscattering becomes an absolute instability if

$$L/L_0 > \pi/2, \quad (4.91)$$

[91, 105], where $L_0 = (V_s V_a)^{1/2}/\gamma_0$ is the interaction length and $\gamma_0 = E_0(M_s M_a)^{1/2}$ is the uniform growth rate. Since observed $V_s \approx 0$ for the backscatter, the condition (4.91) is readily satisfied ($L_0 \approx 0$). Explicit form of (4.88) and (4.89) is easy to get (light waves), however for EAW (4.90) no linear dispersion relation in analytical form exists [237, 240, 241, 251]. Since damping rate $\Gamma_a \neq 0$, the EAW is characterized by the longitudinal

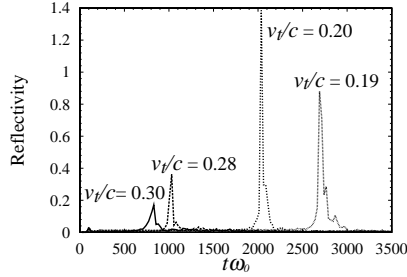


Figure 4.35: Reflectivity in time from the plasma layer ($n = 0.4n_{cr}$, $L = 40c/\omega_0$) for different initial electron thermal velocities v_t/c and $\beta = 0.3$, [242].

absorption length $L_a = V_a/\Gamma_a$, SEAS-backscatter instability becomes absolute under an extra condition [105],

$$L_0/L_a < 2. \quad (4.92)$$

In a linear theory EAW is a highly damped mode, so the absorption length L_a is taking small values. However, as concluded earlier, the key factor for an onset and growth of SAES is nearly critical "standing" backward Stokes wave ($L_0 \approx 0$), so that $V_s \approx 0$ satisfies (4.91) and also minimizes the threshold E_0 for SEAS instability [242], $\gamma_0 > 0.5\Gamma_a(V_s/V_a)^{1/2}$.

4.6.4 Simulations

The temperature effect can be clearly seen near the threshold intensity for SEAS ($\beta \sim 0.3$). Since the longitudinal thermal velocity of electrons can easily increase due to e.g. the Raman instability, the temperature in transverse direction was set to 500eV, with a longitudinal temperature taken as a control parameter. However, we note, that the SEAS instability was readily observed for isotropic distribution, as well. Just above the threshold, high electron temperature may be essential for an instability growth. This is illustrated by Fig.4.35 in which reflectivity ($R = \langle S_r \rangle / \langle S_0 \rangle$, S_r and S_i are Poynting vectors for reflected and incident wave, respectively, and $\langle \rangle$ denotes time averaged values) are shown for $\beta = 0.3$, $n = 0.4n_{cr}$, $L = 40c/\omega_0$ at several temperatures, $v_t/c = 0.19, 0.20, 0.28$ and 0.30 . There is an optimum temperature for perfect matching with an excited EAW which results in a maximum SEAS reflectivity. For $v_t/c = 0.2$ observed reflectivity is very high - nearly 140% of the incident laser light. One calculates $v_{ph}/v_t \approx 2.64, 2.50, 1.84$ and 1.72 for $v_t/c = 0.19, 0.20, 0.28$ and 0.30 , respectively. For temperatures $\leq v_t/c = 0.18$ and $\beta = 0.3$ the instability was not observed during time period of $t\omega_0 = 5000$.

For laser intensities well above the threshold there appears no need for high electron temperatures to excite SEAS. For example, already at $T = 500\text{eV}$, with a strong relativistic pump $\beta = 0.6$, $n = 0.6n_{cr}$ and $L = 40c/\omega_0$ instability develops fast and quickly saturates within $t\omega_0 = 500$. In Fig.4.36, time evolution of SEAS reflectivity and the electron distribution function $f(v_x/c)$ for the initial ($t\omega_0 = 0$) and the state after the instability ($t\omega_0 = 1000$) are plotted. This effect, seems related to relativistic interactions, important for e.g. fast ignitor research, and will deserve future attention. First estimates

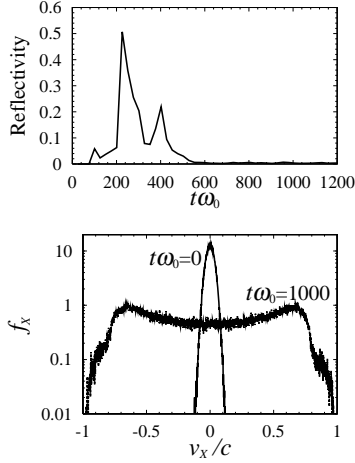


Figure 4.36: Reflectivity in time (top) and electron velocity distribution (bottom) in the plasma layer ($n = 0.6n_{cr}$, $L = 40c/\omega_0$, $\beta = 0.6$) for $t\omega_0 = 0$ and $t\omega_0 = 1000$ (after the instability), [242].

point out at the relativistic-nonlinear frequency shift (NLFS) of the electrostatic wave driven by a laser, as a possible cause [177, 178]. At relativistic intensity, large NLF generates broad ES harmonics which can cover resonant EAW frequency. SEAS resonance is broadened, while instability can grow rapidly, instead from a low background noise, directly from a finite ES harmonic, seeded by a laser. As seen in Fig.4.36, SEAS produces large relativistic heating which deforms an initial Maxwellian into "water-bag" alike distribution and generates highly energetic electrons with main contribution near $v = \pm v_{ph}$ of the EAW.

Finally, we briefly address a question of coexistence and interrelation between SRS and SEAS. The simulated system consists of two connected underdense plasma layers L_1 and L_2 , of the length $L_1 = 20c/\omega_0$ and $L_2 = 80c/\omega_0$ with corresponding densities $n_1 = 0.2n_{cr}$ and $n_2 = 0.6n_{cr}$, respectively. Initial temperature is taken at 500eV. Our choice of densities makes L_1 strongly active for Raman instability, while L_2 (overdense for SRS) is practically in a role of a heat sink. Simulations show common picture, an excitation of strong SRS marked by intermittent reflectivity pulsations (see Fig.4.37, $t\omega_0 < 1000$) [102, 151, 236]. The instability eventually gets suppressed by strong heating of supra-thermal and bulk electrons. Since hot electrons quickly escape the Raman region (L_1) they enter and heat the sink (L_2). Moreover, a striking feature emerges at late times, with a reflection of a second intense pulse much larger than the original Raman signal (Fig.4.33, $t\omega_0 \approx 2700$). This is readily identified as SEAS which originates from the large "sink", once the temperature has grown to resonate with EAW to enable excitation of SEAS. Therefore, SEAS mediated by SRS becomes a dominant process, as an example of a complex interplay possibly relevant to our understanding of future experiments.

In summary, in first particle simulations in a plasma not accessible to SRS, strong isolated SEAS reflection from trapped EAW was observed near the electron plasma frequency. A three-wave parametric model was discussed, in particular, a role of a standing

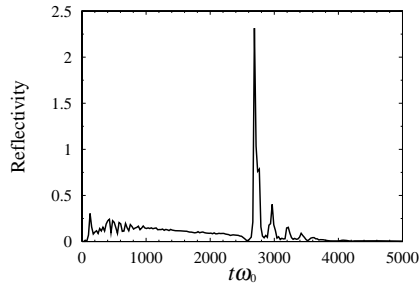


Figure 4.37: Time history of the reflectivity from two connected plasma layers ($n_1 = 0.2n_{cr}$, $L_1 = 20c/\omega_0$, $n_2 = 0.6n_{cr}$, $L_2 = 80c/\omega_0$, $\beta = 0.3$). Initial reflectivity bursts from ordinary SRS in L_1 are followed at late times by a huge SEAS pulse generated in L_2 , which was heated by hot electrons from L_1 , [242].

Stokes sideband for excitation of an absolute SEAS instability. While in reported experiments [237] SEAS to SRS signal ratio was smaller than 10^{-3} , we find conditions in which SEAS dominates over standard SRS. Further study of SEAS role, e.g in relativistic laser-plasmas, deserves future attention.

4.7 Stimulated Trapped Electron Acoustic Wave Scattering, EM Soliton and Ion-Vortices in Subcritical Plasmas

Stimulated trapped electron acoustic wave scattering by a linearly polarized intense laser in a subcritical plasma is studied by particle simulation. The scattering process is a three-wave parametric decay of the laser pump into a critical Stokes electromagnetic sideband wave and the trapped electron acoustic wave (see, previous section). As the ion acoustic wave grows in time it breaks locally, followed by a large relativistic electromagnetic soliton. A new phenomenon, MeV ion-vortex in ion phase-space forms by local electromagnetic and electrostatic fields inside the soliton. It is found that the electron acoustic wave mode is similar to the kinetic electrostatic electron nonlinear waves, [234].

4.7.1 Introduction

As indicated above, in addition to the standard SRS, a new type of stimulated backscattering, involving the so-called electron acoustic waves (EAWs) was recently reported in single hot spot experiments [237, 238]. At relativistic intensities it was first exposed by Nikolić, Škorić, et al., by particle-in-cell (PIC) simulations in subcritical plasmas [242, 244]. More recently, by PIC simulations, Valentini, O’Neil and Dubin have investigated the excitation of EAWs and the stability of the EAWs against decay, and found that the EAW is a nonlinear wave with a carefully tailored trapped particle population, and the excitation process must create the trapped particle population [252]. Previous authors examining

the linear Vlasov dispersion relation, already noted two ES branches, corresponding to the well-known, high-frequency EPW, and a low-frequency Landau damped branch, termed electron acoustic waves (EAWs), whose frequency and phase velocity are between an ion-acoustic wave (IAW) and an EPW [246, 247].

Relativistic solitons, predicted by a theory and observed in simulations, are localized electromagnetic (EM) structures self-trapped by a locally modified plasma refractive index through the relativistic electron mass increase and the electron density depletion by the ponderomotive force of a strong laser pulse. In homogeneous plasmas, standing solitons persist for a long time, and eventually decay due to interaction with fast electrons. In inhomogeneous plasmas, solitons get accelerated with an acceleration proportional to the gradient of the plasma density towards the low density side. When the soliton reaches a plasma-vacuum interface, it radiates away its energy in the form of a short intense low-frequency burst of EM radiation [197, 216, 230, 248]. Ion acceleration by EM solitons, due to the energy gain during the ion interaction with the slow-varying EM fields trapped inside the soliton, has been studied in the past. EM soliton propagating with a high speed, for the purpose of particle acceleration, could provide the wakeless regions with regular electric and magnetic fields, with which particles can interact and gain net energy, transforming the soliton energy into the energy of the fast particles [248].

In this section, stimulated trapped electron acoustic wave scattering (T-SEAS) instability induced by a linearly polarized intense laser interacting with a plasma layer at a subcritical density range ($n_{cr}/4 < n/\gamma < n_{cr}$, which is overdense for standard SRS, where γ is relativistic factor), is studied by 1D PIC simulations, [234]. This instability takes place whether the ion dynamics is taken into account or not. Still, with ion dynamics, an excited ion acoustic wave grows in time and breaks, accompanied by a large relativistic EM soliton. As a new phenomenon, a MeV energy ion-vortex structure in the momentum phase-space forms by localized EM and ES soliton fields. Ion-vortices both in homogeneous and in inhomogeneous plasmas are found. Previously, PIC simulations of subcritical plasmas by Adam *et al.*, [180, 249] concentrated on electron effects in early stages of relativistic SRS parametric instability in 1D and 2D model, in particular. We found similar electron effects in 1D, still, they lack spectral data to test EPW/EAW nonlinear dispersion. We note, that, e.g. the electron hole detected in Fig. 3, [180, 249], could be related to a relativistic EM soliton structure, as revealed in this work. Also, in the asymptotic stage, their reference to "... ES component being strongly Landau damped ..." could be an actual evidence of EAWs (p. 4767, Ref. [249]). As will be discussed, this electron acoustic wave (EAW) mode is similar to the kinetic electrostatic electron nonlinear (KEEN) waves, which are stable, nonlinear, multimode coherent structures in plasmas as was introduced by Afeyan et al.[253].

4.7.2 Simulation Model

In our simulations, fully relativistic EM 1D-PIC code is used. The $100 c/\omega_0$ long plasma begins at $x = 0$ and ends at $x = 100 c/\omega_0$; at the front and rear sides of the plasma layer, there are two $200c/\omega_0$ vacuum regions, where c and ω_0 is the speed and carrier frequency of laser pulse, respectively. The number of cells is 20 per $1 c/\omega_0$, 100 electrons and 100 ions are put in each cell. Plasma density is $n = 0.6n_{cr}$, where n_{cr} is the critical

density. The electron and ion temperature are $T_e = 5T_i = 1keV$, and with the mass ratio is $m_i/m_e = 1836$. Linearly polarized laser plane wave, with electric field E_0 along the y direction and normalized laser amplitude $a = eE_0/m_e\omega_0c = 0.6$, is initialized at $x = -50 c/\omega_0$, where m_e and e are the electron mass and electron charge, respectively. The time, electric field, and magnetic field are normalized to $2\pi/\omega_0$, $m_e\omega_0c/e$, and $m_e\omega_0/e$, respectively; time is taken as zero, $t = 0$, when laser pulse arrives at the front vacuum-plasma boundary. In the plots, the ES field E_x is averaged over electron plasma wavelength $\lambda_{pe} = c/\omega_{pe}$, EM fields E_y , B_z and EM energy density $E_y^2 + B_z^2$ are averaged over laser wavelength $\lambda_0 = c/\omega_0$, respectively.

4.7.3 Stimulated Trapped Electron Acoustic Wave Scattering

Plasma density is taken beyond $n > 0.25n_{cr}$, so that the standard SRS is excluded. We found when the laser amplitude $a > 0.4$, T-SEAS instability takes place. In a linear stage, as shown in Fig.4.38, its spectrum is well explained by a resonant three-wave parametric decay of an intense laser pump into the slow backscattered Stokes EM sideband and the trapped EAW. The backscattered Stokes EM wave in vacuum region is found to be driven critical, i.e., near the relativistic electron plasma frequency $\omega_s = 0.62\omega_0 \approx \omega_{pe}/\gamma^{1/2}$, where $\gamma = \sqrt{1+a^2}$ is relativistic factor, while the corresponding EAW has the frequency $\omega_{eaw} \approx 0.40\omega_0 < \omega_{pe}$. The wavenumber for EM wave inside the plasma has two peaks; one with $k_s^p \approx 0.12k_0$ another with $k_0^p \approx 0.80k_0$, which correspond to backscattered and laser EM waves, respectively; while, the wavenumber for EAW is $k_{eaw} \approx 0.92k_0$; here, $k_0 = \omega_0/c$ is the wavenumber of laser light in vacuum. We further assume the relativistic electron plasma frequency as $\omega_{pe}^* \approx 0.61\omega_0$, which is smaller than the initial laser pump induced $\omega_{pe}/\gamma^{1/2} \approx 0.69\omega_0$, since, in the region of intense EM and EAW waves, larger relativistic effect reduces the local electron plasma frequency. The EM waves for both pump and Stokes mode satisfy the standard dispersion relation $\omega_{0,s}^2 = \omega_{pe}^{*2} + c^2(k_{0,s}^p)^2$. Then, in the early T-SEAS instability, the matching conditions for both the frequency $\omega_0 = \omega_s + \omega_{eaw}$ and the wavenumber $k_0^p = -k_s^p + k_{eaw}$ appear to be satisfied. Note that the natural relativistic electron plasma mode $\omega_{pe}/\gamma^{1/2} \approx 0.69\omega_0$ is also weakly excited.

During the T-SEAS instability, as shown in Fig.4.39 (top), large portion of electrons is trapped in the ES potential of the large EAW, this is why a term 'T-' before 'SEAS' is put. In a nonlinear saturation, there is a rapid growth and strong localization of the Stokes EM wave by forming narrow intense spiky EM structures with downshifted laser light trapped inside, as shown in Fig.4.39 (bottom). The train of relativistic EM spikes gets eventually irradiated through the front vacuum-plasma boundary in a form of an intense reflection burst of the downshifted laser light. The large trapped EAW excited inside plasma with low phase velocity quickly heats up bulk electrons to relativistic energies, which will eventually suppress T-SEAS instability. To illustrate the onset and growth of the T-SEAS instability, in Fig.4.40, the plots for the temporal evolution of the dominant backscattered EM mode $|E_y(k)|^2$ and EAW mode $|E_x(k)|^2$, both measured inside the plasma, are given. One can see the temporal evolution clearly; after the early linear phase a nonlinear process then follows while further growth of EM and ES wave gets saturated. If we assume, for both EM and ES mode harmonics, the linear parametric growth in the form $E_k(t) \sim E_k(0)e^{\gamma t}$; then, by using our data, we can estimate their

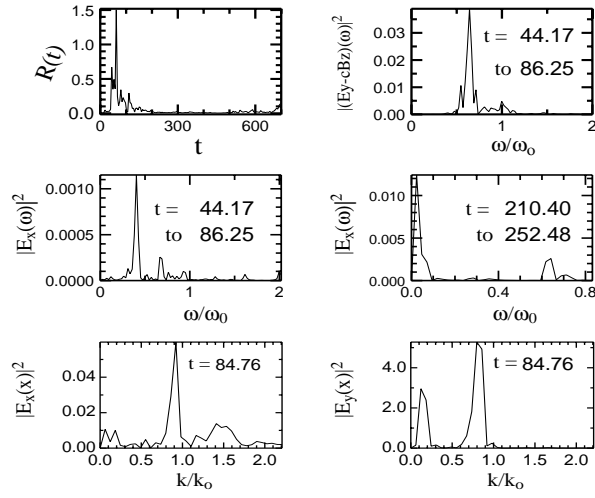


Figure 4.38: Reflectivity and frequency spectrum for the reflected EM wave (top); frequency spectra of the ES wave inside plasma (middle); and wavenumber spectra for the electric fields E_x and E_y both measured inside plasma (bottom), respectively, [234].

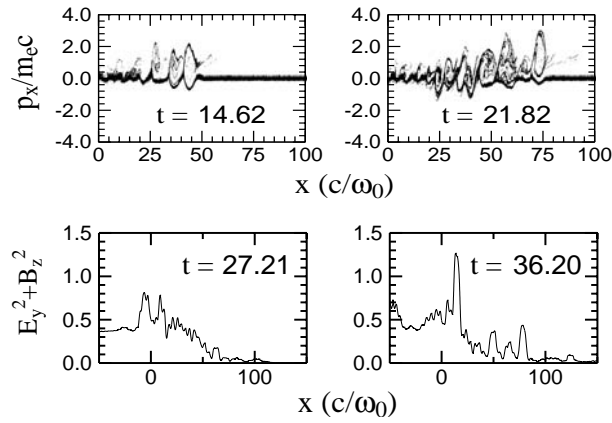


Figure 4.39: Snapshots for electron phase space $x \sim p_x$ (top) and EM energy density $E_y^2 + B_z^2$ (bottom), respectively, [234].

corresponding growth in the initial stage of T-SEAS instability. The growth rate for the backscattered EM mode is $\gamma_s \approx 0.176\omega_s = 0.113\omega_0$, the corresponding growth rate for EAW is $\gamma_{eaw} \approx 0.267\omega_{eaw} = 0.107\omega_0$, respectively.

In order to clarify the T-SEAS instability growth, we follow a simple model [232, 91, 102, 244, 242], for parametric coupling between three waves $a_i(x, t)\exp[i(k_i x - \omega_i t)]$, satisfying the frequency and wave number resonant matching conditions, which for weakly varying envelopes in dimensionless units reads:

$$\partial a_i / \partial t + V_i \partial a_i / \partial x + \Gamma_i a_i = M_i a_j^* a_k \quad (4.93)$$

where $V_i > 0$ are group velocity ($i, j, k = 0, s, eaw$ denote pump EM, backscattered EM, and EAW modes, respectively), Γ_{eaw} is an effective damping rate for EAW; $\Gamma_0 = \Gamma_s = 0$ for EM waves is used. $M_i > 0$ are the coupling coefficients and a_i are the wave amplitudes. With standard open boundary conditions $a_0(0, t) = E_0$ and $a_s(L, t) = a_{eaw}(0, t) = 0$, the backscattering grows as an absolute instability, only if $L/L_0 > \pi/2$, where $L_0 = (V_s V_{eaw})^{1/2} / \gamma_0$ is the interaction length and $\gamma_0 = E_0 (M_s M_{eaw})^{1/2}$ is the uniform growth rate. The group velocity of the backscattered EM wave is $-V_s = c^2 k_s / \omega_s \approx 0.19c$; even if we assume that the group velocity for EAW is so large that $V_{eaw} \approx c$ and a very small uniform growth rate $\gamma_0 \approx 0.1\omega_0$ (the growth rates for both backscattered EM wave and EAW are greater than $0.1\omega_0$, as have been shown above), then the $L_0 \approx 4.3c/\omega_0$. So a posteriori, for plasma length $L = 100c/\omega_0$, the condition $L/L_0 > \pi/2$ for the absolute instability to take place, is readily satisfied. This means that intensive T-SEAS instability can indeed develop as observed for our simulation conditions.

The EAW mode found in our simulation is very similar to the kinetic electrostatic electron nonlinear (KEEN) waves. The KEEN waves, which were reported by Afeyan et al. [253], are stable, long-lived nonlinear, multimode coherent structures in plasmas, which can only be driven by sufficiently strong electric fields. The frequency of the excited KEEN waves is in a band around the electron acoustic frequency. In the case of KEEN waves, no flattened electron velocity distribution function need be invoked and no single mode behavior is observed [253]. However, in our case, we found that the observed EAW is nearly a single mode, as in Fig.4.38 the peaked frequency spectra of the ES wave shown. Also, the kinetic effects play an important role on the stimulated EAW scattering, due to the large electron relativistic heating by T-SEAS process, the initial Maxwellian distribution then deforms into "water-bag" alike distribution and generates highly energetic electrons with main contribution near the phase velocity $\pm v_{ph}$ of the EAW.

4.7.4 Electromagnetic Soliton and Ion-Vortices

We found that early T-SEAS instability behavior is similar, whether the ion dynamics is taken into account or not. However, with ion dynamics, for times longer than ion period $2\pi/\omega_{pi}$, the IAW is excited and persists in time [248]. Already, before the IAW onset, electron trapped orbits (EAW) are well developed [249], (Fig.4.40) to be rapidly destroyed by strong EM transverse and ES longitudinal fields and stochastic heating to relativistic energies. The IAW peak in our early spectrum is hard to detect, as the strong trapped EAW is dominant. Once the T-SEAS instability is halted, as in Fig.4.38 (middle)

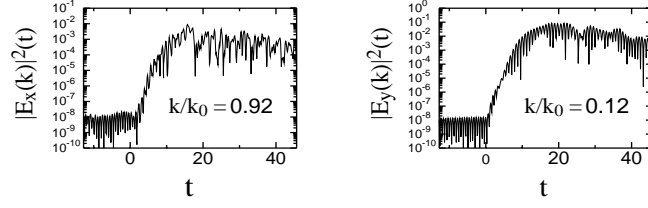


Figure 4.40: Temporal growth for EAW mode E_x and backscattered EM mode E_y both measured inside plasma, respectively, [234].

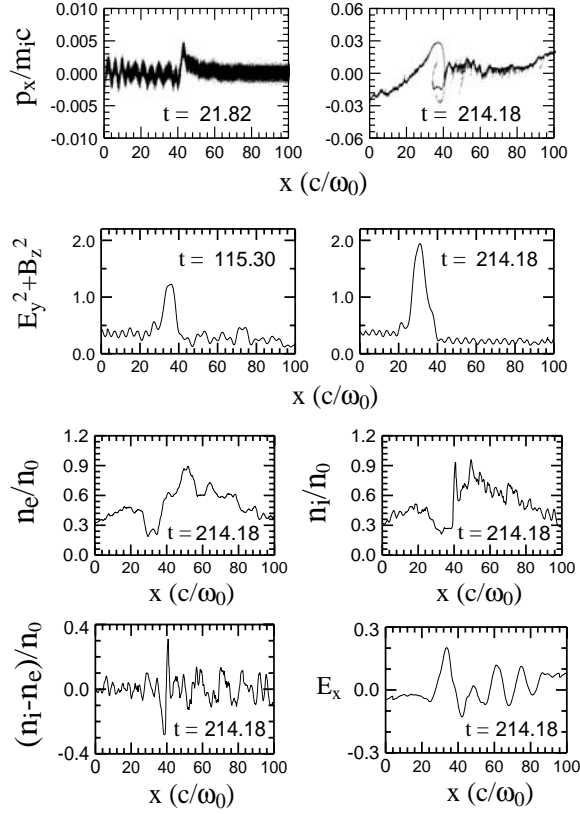


Figure 4.41: Snapshots for ion phase-space, EM energy density $E_y^2 + B_z^2$, plasma density, and ES field E_x , respectively, [234].

the ES spectrum shows, the IAW mode with frequency $\omega_{iaw} \approx 0.023\omega_0$, which approximately equals to the natural ion plasma frequency $\omega_{pi} = (m_e/m_i)^{1/2}\omega_{pe} \approx 0.021\omega_0$, can be observed, clearly. The excited IAW propagates forward driven basically by two effects: direct laser ponderomotive force (PF) action on ions and by much stronger, indirect effect, due to relativistic electron dynamics, through fields (currents) created in the violation of plasma quasi-neutrality. It is clear that a complete picture of such a complex paradigm of multi-scale nonlinear interactions can be revealed only by relativistic PIC simulations. Still, the direct PF effect is visualized in Fig.4.41 (top, left), where early IAW is modulated by PF, i.e. wavenumber equal to the 2nd harmonic of laser light. Furthermore, a growing nonlinearity and slow finite velocity of driven IAWs quickly leads to a strong steepening of the wavefront and its eventual break-up. At later times, at $t > 21.82$, as observed in Fig.4.41, ion orbits begin to overturn, close to $x = 40 c/\omega_0$ point, while the steep IAW density shock wave front breaks. After that, by EM energy localization in the density cavity, one EM soliton is nucleated at the same position and continues to grow in time to saturate at $t \approx 252.94$ with the maximum EM energy $E_y^2 + B_z^2 \approx 2.5$. During its growth, firstly, large number of electrons are expelled from the high EM field region by the relativistic ponderomotive force ($\sim \partial\gamma/\partial x$) [201]. At the front of the soliton ($x \approx 40 c/\omega_0$) at $t = 214.18$, because of large inertia, slow ions pile up and one sharp ion density peak is formed. Simultaneously, electrons do not accumulate at the front and rear side, because of their small inertia. Then, at the narrow region around the soliton front edge $x \approx 40 c/\omega_0$, a net positive charge forms, as the $(n_i - n_e)/n_0$ plot in Fig.4.41 shows. Behind the ion density peak, namely inside the soliton region, to preserve the charge neutrality, more electrons will be pushed away to balance the ion density peak by the ES field of the charge separation. Thus, a net negative charge region forms. This charge distribution results in a double layer structure, as in Fig.4.41 the ES field E_x plot shows. Both, the relativistic EM soliton field and the local large E_x sheath field via interplay can strongly accelerate or decelerate ions. Ions with initial negative velocity inside the soliton are reflected by sharp ion density peak, will first experience a deceleration process, and then accelerated again by soliton fields; while ions with positive velocity experience just the reverse processes. As a result, as the ion phase-space plot at $t = 214.18$ shows in Fig.4.41, eventually, a trapped ion-vortex (ion-hole) structure is formed.

The size of the ion-vortex is close to the soliton width, i.e., $\Delta x_{vortex} \approx \Delta x_{soliton} \approx 1 \sim 2\lambda_{pe}$. The maximum ion-vortex energy is large, in the range $1 \sim 2$ MeV. Qualitatively, an early excess charge in the electron density hole appears to trigger ion-vortex formation; analogous to a large water eddy caused by the hole at the river bottom. We can roughly estimate the maximum ion energy by simply assuming that ions are initially accelerated in the effective planar capacitor (capacity-C) with plates (area-A) at the soliton width (d) on the potential ($U=Q/C$) due to a locally expelled total electron (hole) charge (Q). This appears consistent with the ES profile (E_x in Fig.4.41), in the soliton cavity region ($x \approx 25 - 40 c/\omega_0$). By using $C = \epsilon_0 A/d$, rough estimates for d and $Q = e\delta n_e A d$ readily predict the few MV range.

As an intense laser pulse propagates through the plasma layer, electrons spontaneously and via interactions with the laser spread out into vacuum by forming the charge separation ES fields at both boundaries; ions tend to follow electrons to keep the charge neutrality. As a result, the plasma density will decrease from the center to both bound-

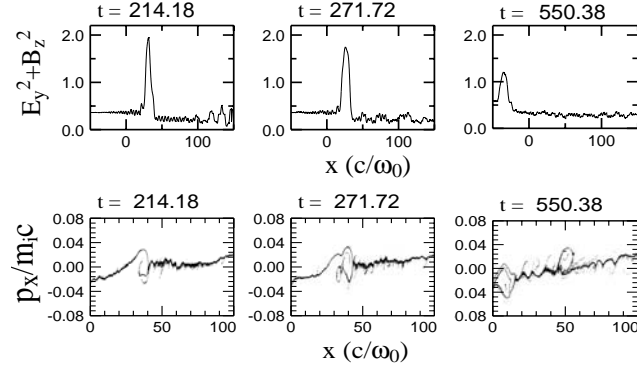


Figure 4.42: Energy density of EM field (top) and ion phase-space snapshots (bottom) for laser amplitude $a = 0.6$, [234].

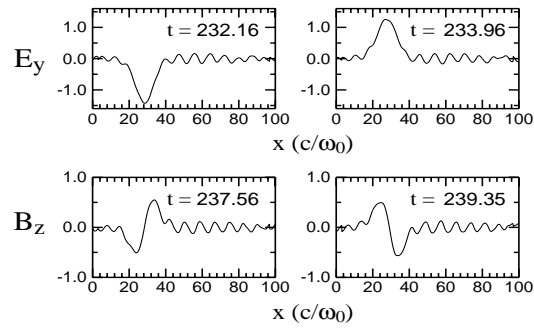


Figure 4.43: The snapshots for electronic field E_y and magnetic field B_z in the case of laser amplitude $a = 0.6$, [234].

aries gradually with time. As an inhomogeneous plasma is formed, the EM soliton will be then accelerated down the density profile [230]. We found that similar large relativistic EM solitons often form in the frontal region of the plasma and are accelerated backwards toward the front plasma-vacuum interface. As large amplitude EM soliton propagates into the boundary, as shown in Fig.4.42 (top), by large EM field and ES field inside the soliton the energy exchange between the soliton and ions continually takes place. Majority of ions are accelerated and trapped inside the soliton region. Along the soliton path, as shown in Fig.4.42 (bottom), several trapped ion-vortices (ion-holes) in the phase-space form and persist with time. The EM soliton gradually loses energy and its amplitude decreases. After the EM soliton arrives at the plasma-vacuum boundary, related ion acceleration and trapping is completed, also the formation of new ion-vortices stops. At later times, created ion-vortices blur and become hard to discern and eventually disappear due to energy loss and thermalization inside the bulk plasma. Finally, as shown in Fig.4.43, the soliton transverse electric field E_y is a half-cycle structure in space, while, the corresponding magnetic field B_z is an one-cycle structure. From Maxwell's equations, i.e., the Faraday law $B_z \sim \partial E_y / \partial x$, the x derivative of the Gaussian soliton profile E_y can lead to the B_z structure as shown in Fig.4.43. Moreover, the EM structure is periodic in time. [222, 232, 233] We also performed a run for inhomogeneous plasma by taking a linear density profile, $n = 0.35 - 1.05n_{cr}$ and laser amplitude $a = 0.6$, other simulation parameters are kept fixed. The same scenario as before emerges, i.e., generation of large amplitude EM soliton which travels down the gradient of the plasma density, however, this time leaving behind in the wake the chain of ion-vortices.

In conclusion, the T-SEAS instability induced by a linearly polarized laser in a sub-critical plasma which is overdense for standard SRS was studied by particle simulation. Its spectrum is initially well explained by a resonant three-wave parametric decay of the laser pump into the critical Stokes EM sideband and the trapped EAW, and it takes place whether the ion dynamics is taken into account or not in its initial stage (Sect. 12.5). However, when ion dynamics is considered, novel physical phenomena were observed: the excitation of large IAW, the generation of large EM soliton after the IAW front breaks up, and subsequent formation of the MeV range ion-vortices in ion phase-space. Ion-vortices were also found in simulations in nonuniform plasma. Also, it is found that the trapped EAW mode is similar to the KEEN waves.

Chapter 5

Ponderomotive Potential and Magnetization

High-intensity electromagnetic waves interacting with a plasma may cause a variety of ponderomotive effects, where the term ponderomotive usually refers to nonlinear slow timescale (low-frequency) phenomena induced by the fast timescale oscillating (high-frequency) fields. It appears as a generic multi-scale plasma paradigm, represented by two, nonlinearly interlinked, slow and fast timescale plasma dynamics. These ponderomotive effects play an important role in many physical- laboratory and fusion and astrophysical situations. In many treatments of ponderomotive effects, single-particle dynamics has been employed [254, 255]; that is, the effective force was taken the particle number density times the single particle force. This would mean that collective effects were neglected. Moreover, although the need for a more exact treatment was often mentioned, the only term taken into account in the ponderomotive force was the one involving the gradient of the time-averaged high-frequency electromagnetic radiation field energy density. Derivations of expressions for the ponderomotive force have used a variety of approaches, such as, fluid equations [256], kinetic approaches [257, 258, 259, 260], Lie transform technique [261] and phenomenological methods [262]. Typically, these derivations are all relatively complicated [263], and it is our aim to present a simple and rigorous Hamiltonian treatment of ponderomotive interactions in a Vlasov plasma following Škorić and ter Haar [264].

5.1 Hamiltonian formulation of ponderomotive interactions in a Vlasov plasma

A Hamiltonian formulation of ponderomotive interactions in a Vlasov plasma is presented. Transformation from the rest frame to the oscillation center frame (OCF) is achieved, and a Liouville equation is derived from the low-frequency OCF distribution function, the Hamiltonian in this equation includes the ponderomotive terms. The equation is solved in the adiabatic approximation, the corresponding charge and current densities evaluated, and the first-order nonadiabatic correction to the current density is derived.

Here, we shall consider a hot, collisionless, nonrelativistic electron plasma [264] and

neglect ion motions which serve as neutralizing background. In a Vlasov plasma the Liouville equation reduces to the Vlasov equation for the single electron distribution function $f(\mathbf{r}, \mathbf{v}, t)$ as

$$\frac{\partial f}{\partial t} + (\mathbf{v} \cdot \nabla)f - \frac{e}{m} \left(\mathbf{E} + (\mathbf{v} \times \mathbf{B}) \cdot \frac{\partial f}{\partial \mathbf{v}} \right) = 0, \quad (5.1)$$

where \mathbf{E} and \mathbf{B} are (self-consistent) electric and magnetic fields from the Maxwell equations ($c = 1$) and where $-e$ and m are the electron charge and mass, respectively. We shall restrict ourselves to the case where there are no external electric and magnetic fields. Consider now the situation where a (strong) high-frequency (transverse or longitudinal) electromagnetic wave, with electric and magnetic fields \mathbf{E}_H and \mathbf{B}_H , is excited in the plasma. We follow [261, 264], and introduce, instead of the rest-frame distribution function f , the so-called oscillation center frame (OCF) distribution function $F(\mathbf{r}, \mathbf{v}, t)$ where

$$\mathbf{u} = \mathbf{v} - \mathbf{v}_q, \quad (5.2)$$

with \mathbf{v}_q the linear electron quiver velocity in the high-frequency field, and

$$\frac{d\mathbf{v}_q}{dt} = -\frac{e}{m} \mathbf{E}_H. \quad (5.3)$$

The transformation from $f(\mathbf{r}, \mathbf{v}, t)$ to $F(\mathbf{r}, \mathbf{v}, t)$ reflects the fact that once the high-frequency transient effects have died out, the electrons respond linearly to a high-frequency field by relaxing toward the so-called the oscillating (Maxwell) distribution function; that is, to a distribution function f which is the initial (equilibrium) distribution function f_0 with the velocity argument shifted by the linear quiver velocity, thus

$$F = f_0(\mathbf{v} - \mathbf{v}_q). \quad (5.4)$$

Put mathematically, the transformation from $f \rightarrow F$, when made in Eq. (5.1) enables us to remove the lowest-order linear response, thus easing the perturbative calculation of higher-order nonlinear terms. It also turns out that the transformed Eq.(5.1) is suitable for compact Hamiltonian formalism. The equation for F is the (Hamiltonian) Liouville equation

$$\frac{\partial F}{\partial t} + [F, H] = 0, \quad (5.5)$$

where [...] is a Poisson bracket-in terms of \mathbf{r} and $\mathbf{p} = m\mathbf{u}$ and H is the OCF Hamiltonian.

$$H = \frac{1}{2}m(\mathbf{u} + \mathbf{v}_q)^2. \quad (5.6)$$

As standard, we split the various quantities into two, fast and slow timescales; i.e. a high frequency part and a low-frequency (time averaged, indicated by angular brackets $\langle \dots \rangle$), indicated, respectively, by the indices H and L . Equation (5.5) then reduces to the following pair of coupled equations:

$$\frac{\partial F_L}{\partial t} + [F_L, H_L] + \langle [F_H, H_H] \rangle = 0, \quad (5.7)$$

$$\frac{\partial F_H}{\partial t} + [F_H, H_L] + [F_L, H_H] = 0, \quad (5.8)$$

where we neglect terms corresponding to second and higher-order harmonics, an approximation as discussed elsewhere [263], - that is, concentrate on the high-frequency dynamics around the fundamental frequency Ω of the high-frequency wave. The slow timescale (L) and fast timescale (H) Hamiltonians are given by the equations

$$H_L = \frac{1}{2}(u^2 + \langle v_q^2 \rangle), H_H = m(\mathbf{u} \cdot \mathbf{v}_q). \quad (5.9)$$

The distribution functions F_H and F_L determine the moments, electron density n and current density \mathbf{j} .. in the rest frame, as follows:

$$\begin{aligned} \mathbf{n} &= \int f d^3 \mathbf{v} = \int F d^3 \mathbf{u}, \\ \mathbf{j} &= -e \int f \mathbf{v} d^3 \mathbf{v} = -en \mathbf{v}_q - \int \mathbf{u} F d^3 \mathbf{u}, \end{aligned} \quad (5.10)$$

or, split into low-frequency and high-frequency components

$$\mathbf{n}_L = \int F_L d^3 \mathbf{u}, \mathbf{n}_H = \int F_H d^3 \mathbf{u}, \quad (5.11)$$

$$\mathbf{j}_L = -e \langle n_H \mathbf{v}_q \rangle - \int \mathbf{u} F_L d^3 \mathbf{u}, \quad (5.12)$$

$$\mathbf{j}_H = -en_L \mathbf{v}_q - \int \mathbf{u} F_H d^3 \mathbf{u}.$$

We need, therefore to solve Eqs.(5.7) and (5.8), and to do this we shall use the perturbation treatment This has been done by other authors [257, 258, 259, 264], but we shall present a simpler albeit rigorous derivation [264] of the final results. We introduce a small parameter δ_T which characterizes the thermal dispersion and which is the ratio of the electron thermal velocity v_T to the phase velocity of the high-frequency waves [264, 265].

$$\delta_T = (v_T k_H / \omega) \ll 1, \quad (5.13)$$

where k_H is a typical high-frequency wavenumber. Assuming the validity of the inequality (5.13) we are the same time ensured of the absence of resonant kinetic high-frequency wave- electron effects. We now solve Eq. (5.8) for F_H in the linear approximation, keeping only terms of first order in δ_T . This leads to

$$\frac{\partial F_H}{\partial t} + [F_L, H_H] = 0, \quad (5.14)$$

or

$$F_H = \left[F_L, \int H_H dt \right] = -[F_L, m(\mathbf{u} \cdot \mathbf{r}_q)], \quad (5.15)$$

where the integration is on the high-frequency scale while $\mathbf{r}_q = \int \mathbf{v}_q dt$ is the linear quiver displacement. One can check by inspection that the term $[F_H, H_L]$ neglected in writing down (5.14) which gives nonlinear contribution, is small whenever $\overline{W} \ll 1$, where \overline{W} is the so-called plasma turbulence parameter $\overline{W} = v_q^2/v_T^2$. Substituting (5.15) into (5.7) we find [264]

$$\frac{\partial F_L}{\partial t} + [F_L, H_L] + \langle [H_H, [F_L, m(\mathbf{u} \cdot \mathbf{r}_q)]] \rangle = 0. \quad (5.16)$$

If the plasma is not very nonuniform so that typical wave-numbers corresponding to the spatial variation of F_L are much smaller than k_H and since, as can be verified a posteriori, the velocity gradient of F_L is sufficiently small, we can neglect all second derivatives of F_L . (We note that the terms involving $\partial^2 F_L / \partial u_i \partial u_j$ lead to a diffusion in velocity space [123]. More precisely, in the presence of a growing oscillation this effect could result in an increase of the time-averaged momentum and energy of nonresonant electrons. The so-called fake diffusion has been studied by some authors [261, 266, 267]. In such a case, the last term on the left-hand-side of (5.16) can be transformed as follows,

$$\begin{aligned} & \langle [H_H, [F_L, m(\mathbf{u} \cdot \mathbf{r}_q)]] \rangle = \\ & \left\langle \nabla(\mathbf{u} \cdot \mathbf{v}_q) \cdot \frac{\partial}{\partial \mathbf{u}} - (\mathbf{v}_q \cdot \nabla) \cdot (\mathbf{r}_q \cdot \nabla) - \nabla(\mathbf{u} \cdot \mathbf{r}_q) \cdot \frac{\partial}{\partial \mathbf{u}} F_L \right\rangle = \\ & \langle [\nabla F_L \cdot (\mathbf{r}_q \cdot \nabla) \mathbf{v}_q] \rangle - \left\langle \nabla(\mathbf{r}_q \cdot \nabla)(\mathbf{u} \cdot \mathbf{v}_q) \cdot \frac{\partial}{\partial \mathbf{u}} F_L \right\rangle \\ & - \langle (\mathbf{v}_q \cdot \nabla)(\mathbf{r}_q \cdot \nabla) + (\mathbf{r}_q \cdot \nabla)(\mathbf{v}_q \cdot \nabla) \rangle F_L \\ & + u_n \langle [(\mathbf{r}_q \cdot \nabla) \nabla_m v_{qn}] + [(\mathbf{v}_q \cdot \nabla) \nabla_m r_{qn}] \rangle \frac{\partial}{\partial u_m} F_L, \end{aligned} \quad (5.17)$$

where summation over repeated indices is implied. The last two terms on the right-hand-side of (5.17) are both time-averages of time derivatives and therefore vanish for slowly modulated waves, The first two terms on the right-hand-side of (5.17) can be combined into a single Poisson bracket so that we end up with the equation

$$\frac{\partial F_L}{\partial t} + [F_L, H_P] = 0, \quad (5.18)$$

where

$$H_P = H_L + \langle (\mathbf{r}_q \cdot \nabla) H_H \rangle, \quad (5.19)$$

is the effective -ponderomotive Hamiltonian, which, together with any low-frequency fields, determines the slow timescale dynamics of electrons in high-frequency waves. The approximation $H_P = H_L$ is the one mentioned in the introduction, while the extra term corresponds to what Cary and Kaufman [261] called, the ponderomotive Hamiltonian. We can rewrite Eq.(5.19) as follows,

$$H_P = \frac{1}{2}m[(\mathbf{u} - \mathbf{u}_0)^2 + \langle v_q^2 \rangle - u_0^2], \quad (5.20)$$

where we have introduced an ansatz for slow timescale induced drift velocity \mathbf{u}_0 , by the equation

$$\mathbf{u}_0 = -\langle (\mathbf{r}_q \cdot \nabla) \mathbf{v}_q \rangle \quad (5.21)$$

and Eq.(5.18) can be written in the form

$$\frac{\partial F_L}{\partial t} + [(\mathbf{u} - \mathbf{u}_0) \cdot \nabla F_L] + \nabla \left[-\frac{1}{2} \langle v_q^2 \rangle + (\mathbf{u} \cdot \mathbf{u}_0) \right] \cdot \frac{\partial F_L}{\partial \mathbf{u}} = 0, \quad (5.22)$$

a result also obtained via a different procedure[258]. We see that apart from the well-known gradient ponderomotive force $\nabla \frac{1}{2} \langle v_q^2 \rangle$ there is an additional term in the effective ponderomotive force which derives from the deformation of F_L due to the slow timescale flow induced by ponderomotive interactions (see Eq. (5.21)). In the case of a warm plasma when the phase velocity ω/k_L of the low-frequency motions is small compared with v_T ,

$$\omega/k_L \ll v_T, \quad (5.23)$$

we can look for a stationary solution of Eq.(5.18). In steady state this equation has the general adiabatic solution,

$$F_L = F_0(H_P), \quad (5.24)$$

where F_0 is an arbitrary distribution function. Before discussing this solution, a few remarks are appropriate. First, the rest frame distribution is obtained just by replacing \mathbf{u} with $\mathbf{u} - \mathbf{u}_0$. Second, if one wants to take into account the low-frequency charge separation field, one should simply replace H_P with $H_P - e\Phi$ in Eqs, (5.18) and (5.24), where Φ is the appropriate scalar potential. Third, in the absence of high-frequency waves, the solution (5.24) should reduce to the initial velocity distribution which we shall assume to be Maxwellian. Fourth, in the OCF, the solution for F_L is the initial distribution shifted by \mathbf{u}_0 as a result of nonlinear ponderomotive interactions. This lead to a linear, first order term that should affect the current density (5.12). Finally, we briefly examine the validity of adiabatic approximation. This approximation is also characteristics of most of earlier works [259], while Cary and Kaufman [261] also work essentially work in this approximation when obtaining their result for the low-frequency ponderomotive response. One might feel that as far as the nonadiabatic resonant type of correction to the high-frequency electron dynamics are concerned, the smallness of δ_T justifies the adiabatic procedure. However, the situation is different for the case of the slow timescale-low-frequency response. Condition (5.23) implies that a considerable number of electrons are in resonance with the low-frequency motion. It would therefore be useful to find the quantitative measure of such a nonadiabatic effect. To do this, we have assumed that $F_L = F_0 + \delta F$, where $|\delta F| \ll F_0$ and, substituting this expression into Eq. (5.18), linearizing and Fourier transforming and further assuming that F_0 is Maxwellian we find in the leading term of the Fourier transform $\delta j_L^{*,\omega}$ of the (nonadiabatic) resonant contribution to the nonlinear low-frequency current density, the expression

$$\delta j_L^{*\omega} = -i(\pi/2)^{1/2}(\Omega/kv_T)[n_L \mathbf{u}_0]_{\mathbf{k}, \Omega}^\perp, \quad (5.25)$$

where the superscript \perp indicates the component at the right angle to \mathbf{k} . We see that this correction gives a nonlinear Landau damping mechanism for high-frequency waves, which could be small as long as the condition (5.23) holds. Let us now return to Eq. (5.24). Assuming that F_0 is Maxwellian, and using the fact that $u_0^2 / \langle v_q^2 \rangle \sim \overline{W} \delta_T^2 \ll 1$ to neglect u_0^2 in H_p in the exponent, we get from Eqs. (5.11) and (5.12)

$$n_L = n_0 \exp(-\langle v_q^2 \rangle / 2v_T^2), \quad (5.26)$$

a well-known result for the electron density, modified because of ponderomotive interactions [268]. We now turn to the low-frequency ponderomotive current density \mathbf{j}_L . To evaluate $n_H \mathbf{v}_H$ we can use either (5.11) and (5.15) or the high-frequency equation of continuity. Either procedure gives us

$$n_H = -\nabla \cdot (n_L \mathbf{r}_q) \quad (5.27)$$

The second contribution to \mathbf{j}_L becomes $n_L \mathbf{u}_0$ if we use for F_L the shifted Maxwellian distribution. Using Eqs. (5.27) and (5.21) and the vanishing of the time average of expressions such as $(r_{qi}v_{qj} + v_{qi}r_{qj})$ (cf. discussion following Eq. (5.17)) we find

$$\mathbf{j}_L = e \langle (\nabla \cdot (n_L \mathbf{r}_q)) \mathbf{v}_q - en_L (\mathbf{v}_q \cdot \nabla) \mathbf{r}_q \rangle = \frac{1}{2} e [\nabla \times \langle (\mathbf{v}_q \times \mathbf{r}_q) \rangle], \quad (5.28)$$

which is important, hence less known result for the nonlinear ponderomotive electron current density. We note that this equation is consistent with the requirement of slow timescale quasineutrality $(\nabla \cdot \mathbf{j}_L) = 0$. The result given by (5.28) was obtained three decades ago in the search for a possible collisionless mechanism for the nonlinear excitation of quasistatic magnetic fields by Langmuir waves [257, 269]. However, it should be stressed that it is just a general manifestation of ponderomotive interactions as the more widely exploited density modification formula (5.26). Naturally, the basic generation equation for the low-frequency magnetic field $\delta \mathbf{B}$ due to the nonlinear current density (5.28) follows simply from the appropriate Maxwell equation in which we can neglect the displacement current and the ion contribution, therefore

$$\nabla^2 \delta \mathbf{B} = -(4\pi e/c)(\nabla \times \mathbf{j}_L),$$

$$\nabla^2 \delta \mathbf{B} = -(2\pi e/c)[\nabla \times (\nabla \times \langle (\mathbf{v}_q \times \mathbf{r}_q) \rangle)], \quad (5.29)$$

which for longitudinal \mathbf{E}_H simplifies to the formula

$$\delta \mathbf{B} = (2\pi e/c)n_L \langle (\mathbf{v}_q \times \mathbf{r}_q) \rangle. \quad (5.30)$$

If one goes beyond the adiabatic approximation, an integral term to the left-hand side of Eq. (5.29), would appear which represents the anomalous skin damping of the magnetic field, characteristic of the propagation of quasi-static (electro)-magnetic wave in a overdense Vlasov plasma $\Omega \ll \omega_{pe}$ so that the condition (5.23) is satisfied [271]. In conclusion, we note that above results indicate that slow-scale magnetic fields together with

well-known density modification are both expected as general features of ponderomotive effects in turbulent plasmas [272, 273, 274, 275].

5.2 The hydrodynamics of ponderomotive interactions in a collisionless plasma

Ponderomotive effects, that is, nonlinear low-frequency phenomena induced by high-intensity electromagnetic waves, have been the subject of many studies [254]. Ponderomotive interactions have been invoked to explain a number of important phenomena, both in laboratory, fusion, space and astrophysical plasmas. In particular, such as is a mechanism of nonlinear generation of ponderomotively driven large quasistatic magnetic fields in laser plasmas. As discussed above, it has been shown [257, 263] that in a collisionless plasma, magnetic fields can be excited by a ponderomotive solenoidal electron current \mathbf{j}_L , given by the expression

$$\mathbf{j}_L = -e \langle n\mathbf{v} \rangle = \frac{1}{2} e \nabla \times (n_L \langle \mathbf{v}_q \times \mathbf{r}_q \rangle),$$

where $-e, m$ and \mathbf{v} are, respectively, the electron charge, number density, and velocity, while the pointed brackets, as before, indicate time averaging over the period of high-frequency waves. The quantities \mathbf{v}_q and \mathbf{r}_q are, respectively, the electron linear quiver velocity and displacement in the high-frequency electromagnetic (transverse or longitudinal) field $(\mathbf{E}_H, \mathbf{B}_H)$, which satisfy the relations $d^2\mathbf{r}_q/dt^2 \equiv d\mathbf{v}_q/dt = -e\mathbf{E}_H/m$, where m is the nonrelativistic electron mass, and indices L and H denote, the high-frequency (fast timescale) and the low-frequency (slow timescale) parts of the relevant quantities, respectively. In earlier papers, e.g. in refs. [257, 263] (see above) the above equation for \mathbf{j}_L was obtained by using the adiabatic kinetic theory in a warm collisionless plasma assuming that mobile electrons are in equilibrium with the slow timescale motions. In that way the equation, as expected, is consistent with the requirement for the slow timescale quasineutrality, $(\nabla \cdot \mathbf{j}_L) = 0$. Later kinetic studies [258, 259, 270, 256, 269, 261] have examined nonlinear collisionless mechanism in more detail confirming the original result. Subsequent study using a Hamiltonian approach, given in a previous section, gave a simple formalism and physical insight into the mechanism [265, 272, 273, 274, 264, 261].

It has been often claimed that only a kinetic theory can derive the correct expression for \mathbf{j}_L in a collisionless plasma and that all attempts to use hydrodynamics without "a correction for the particle stress perturbed by ponderomotive terms" are doomed to failure [257, 258, 259]. This statement was further reinforced by the fact that most of earlier hydrodynamic attempts failed to obtain complete results [276, 277, 269, 278]. It is the purpose of the following to present a simple rigorous hydrodynamic derivation of the correct result, while showing the basic physical approximations involved [273, 274, 275, 279].

As usual, we split all physical quantities into their slow and fast timescale parts, the total slow timescale ponderomotive electron current density will consist of two terms, a fast timescale beat contribution and a slow timescale part:

$$\mathbf{j}_L = -e \langle n\mathbf{v} \rangle = -e(\langle n_H \mathbf{v}_H \rangle + n_L \mathbf{v}_L). \quad (5.31)$$

As we are interested only in the contributions to \mathbf{j}_L , which are quadratic in the high-frequency field amplitude, it is sufficient to evaluate the first "beat" term in (5.31) by solving the linear evolution for each, n_H and \mathbf{v}_H , or more precisely, by using the linearized equation of continuity for n_H and the equation of electron motion for \mathbf{v}_H , respectively. The thermal correction which is of the second-order in the dispersion parameter is neglected, cf. (13) in [264]. Thus, we simply have

$$-e \langle n_H \mathbf{v}_H \rangle = e \langle \nabla \cdot (n_L \mathbf{r}_q \mathbf{v}_q) \rangle \quad (5.32)$$

The slow timescale velocity in (5.31) is more difficult to evaluate, since as $n_L (\approx n_0)$ is the zero-order quantity, we have to calculate \mathbf{v}_L to the second order in the high-frequency field amplitude. We now introduce a hydrodynamic (fluid) description of the nonrelativistic electron motion:

$$\frac{\partial \mathbf{v}}{\partial t} + \mathbf{v} \times (\nabla \times \mathbf{v} - \frac{e}{mc} \mathbf{B}) + \frac{e}{m} \mathbf{E} + \nabla v^2 + \frac{1}{nm} \nabla p_e = 0 \quad (5.33)$$

where p_e is the electron pressure term, which we shall take into account in its standard, isotropic form. In that connection we should note an important result of the adiabatic kinetic theory (see above); the only effect on the collisionless ponderomotive interactions on the steady-state electron distribution is a shift by mean high- and low-frequency velocities; this means that if the electron distribution was initially Maxwellian, the electron pressure term remains isotropic [258, 264, 273].

We look for an expression for \mathbf{v}_L . Since $(\nabla \cdot \mathbf{j}_L) = 0$, together with (5.31) and (5.33) already defines the potential part of \mathbf{v}_L , it will be sufficient to determine the remaining solenoidal (transverse) component. Therefore, we take the **curl** of equation (5.33) to arrive at a general (Helmholtz) equation [in a nonuniform plasma $\nabla \times (\nabla p_e / nm)$ can give rise to a (non-ponderomotive) thermoelectric magnetization current proportional to $(\nabla n_L \times \nabla T)$ (e.g. see ref. [258, 259]):

$$\frac{\partial \omega}{\partial t} - \nabla \times (\mathbf{v} \times \omega) = \mathbf{0}, \quad (5.34)$$

describing the vortex dynamics of an electron fluid; the electron vorticity is defined by the equation $\omega = \nabla \times \mathbf{v} - e\mathbf{B}/mc$. As usual, splitting the physical quantities into low-frequency and high-frequency parts and neglecting second- (and higher- order) harmonics [257], we get from (5.34)

$$\frac{\partial \omega_H}{\partial t} - \nabla \times (\mathbf{v}_L \times \omega_H) - \nabla \times (\mathbf{v}_H \times \omega_L) = \mathbf{0}, \quad (5.35)$$

$$\frac{\partial \omega_L}{\partial t} - \nabla \times (\mathbf{v}_L \times \omega_L) - \nabla \times \langle \mathbf{v}_H \times \omega_H \rangle = \mathbf{0}; \quad (5.36)$$

if we assume that electrons are in a steady state as far as the slow time scale motion is concerned, we can drop the time derivative in (5.36). As the linear part ω_q of the high-frequency vorticity ω_H vanishes, we solve (5.35) for the nonlinear (third order in high-

frequency amplitude) part of ω_H . The zero value of ω_q follows directly from the equation of motion for \mathbf{v}_q , as

$$\frac{\partial}{\partial t} \nabla \times \mathbf{v}_q = -\frac{\nabla \times \mathbf{E}_H}{m} = \frac{e}{mc} \frac{\partial \mathbf{B}_H}{\partial t}.$$

From the above it follows that the introduction of the vorticity equation (5.34) - removes the lowest order linear response- which appears to be analogous to the transformation to the oscillating center frame in the kinetic approach (see above [264]). We can now solve (5.35) for the nonlinear ω_H , by using the linear high-frequency quantities for \mathbf{v}_q and ω_q , hence we have

$$\omega_H = \nabla \times (\mathbf{r}_q \times \omega_L). \quad (5.37)$$

Substituting (5.37) into (5.36) we readily get

$$\frac{\partial \omega_L}{\partial t} - \nabla \times [(\mathbf{v}_L \times \omega_L) + \langle \mathbf{v}_q \times \nabla \times (\mathbf{r}_q \times \omega_L) \rangle] = 0, \quad (5.38)$$

where in the steady state we can put the time derivative term equal to zero.

After some tedious manipulations (shown below), we find that the last term in the equation (5.38) can be transformed into

$$\nabla \times \langle \mathbf{v}_q \times \nabla \times (\mathbf{r}_q \times \omega_L) \rangle = \nabla \times [\omega_L \times \langle (\mathbf{v}_q \cdot \nabla) \mathbf{r}_q \rangle], \quad (5.39)$$

so that in the steady state equation (5.38) reduces to

$$\nabla \times [\omega_L \times (\mathbf{v}_L - \langle (\mathbf{v}_q \cdot \nabla) \mathbf{r}_q \rangle)] = 0, \quad (5.40)$$

which directly yields a trivial solution

$$\mathbf{v}_L = \langle (\mathbf{v}_q \cdot \nabla) \mathbf{r}_q \rangle, \quad (5.41)$$

which fully agrees with the kinetic result [257, 258, 259], contrary to some earlier statements. At this point, we stress that, indeed, equation (5.40) is the fourth order in the amplitude, which is necessary in order to derive the correct formulae for slow timescale-ponderomotive velocity term.

By combining equations (5.41) and (5.42) with (5.31) and (5.32) we readily get the required equation for the ponderomotive electron current

$$\mathbf{j}_L = e \langle \mathbf{v}_q (\nabla \cdot n_L \mathbf{r}_q) - n_L (\mathbf{v}_q \cdot \nabla) \mathbf{r}_q \rangle = \frac{1}{2} e \nabla \times (n_L \langle \mathbf{v}_q \times \mathbf{r}_q \rangle). \quad (5.42)$$

The basic equation for the generation of slow timescale magnetic fields by the ponderomotive magnetization current (5.42) follows simply from Ampère's law with the displacement current and the ion contribution neglected, as was pointed out earlier.

Let us briefly comment on some previous work on this subject. Some of hydrodynamic derivation in a cold electron fluid limit [276, 277, 278] typically recover only the first term in (5.36) and thus obtained $(\partial/\partial t)[\nabla \times \mathbf{v}_L - (e\mathbf{B}_L/mc)] = 0$. As was pointed out in Refs. [258, 261, 279] such result are applicable just for the short-time response, before electrons

have time to equilibrate with the slow timescale ponderomotive dynamics. Moreover, it was claimed that in most experimental situations in laser plasmas the actual scaling does not follow the cold plasma approximation, but it supports the steady state solution given by (5.42). Moreover, we note, the above result for the ponderomotive magnetization current is typically not recovered in the static and collisionless limit of many results on nonstationary ponderomotive interactions [280] (and references therein).

Derivation of equation (5.39),[279]

To prove Eq. (5.39) we shall use tensor notation involving the totally antisymmetric third rank unit tensor ϵ_{ijk} , which satisfies the relations

$$\epsilon_{ijk} = -\epsilon_{ikj} = -\epsilon_{jik},$$

and

$$\sum_k \epsilon_{ijk} \epsilon_{klm} = \delta_{li} \delta_{mj} - \delta_{mi} \delta_{lj},$$

where δ_{ij} is the Kronecker symbol.

We also use the fact that \mathbf{v}_q and \mathbf{r}_q are high-frequency quantities while ω_L is a low-frequency quantity, so that on averaging over the high-frequency motions we have relations like (compare the discussion in the above section)

$$\langle v_i \partial_j r_k \omega_l + r_i \partial_j v_k \omega_l \rangle = 0, \quad \langle r_i v_i \partial_j \omega_l \rangle = 0, \quad (5.43)$$

where v_i , ∂_i , r_i and ω_i denote, respectively, the components of \mathbf{v}_q , \mathbf{r}_q , ∇ and ω_L . We finally remind that from the definition of vorticity, $(\nabla \cdot \omega_L) = 0$.

We now write the i th component of the key vector expression in (5.39)

$$\begin{aligned} \left\langle \mathbf{v}_q \times \nabla \times (\mathbf{r}_q \times \omega_L) \right\rangle_i &= \sum_{\substack{j,k,l \\ m,p,s}} \langle \epsilon_{ijk} \epsilon_{klm} \epsilon_{mps} v_j \partial_l r_p \omega_s \rangle \\ &= \sum_{j,p,s} \langle \epsilon_{jps} v_j \partial_i r_p \omega_s + \epsilon_{ips} v_j \partial_j r_s \omega_p \rangle \\ &= \sum_{j,p,s} \langle \epsilon_{ips} \omega_p v_j \partial_j r_s + \epsilon_{ips} r_s v_j \partial_j \omega_p + \epsilon_{jps} v_j \partial_j r_p \omega_s \rangle \\ &= \omega_L \times \left\langle (\mathbf{v}_q \cdot \nabla) \mathbf{r}_q \right\rangle_i + \frac{1}{2} \left\langle \sum_{j,p,s} (\epsilon_{jps} (\partial_i (v_j r_p \omega_s) \right. \\ &\quad \left. + v_j r_p \partial_i \omega_s) + \epsilon_{ips} (r_s v_j \partial_j \omega_p + v_p r_j \partial_j \omega_s)) \right\rangle \\ &= \left\langle \mathbf{v}_q \times \nabla \times (\mathbf{r}_q \times \omega_L) \right\rangle_i + \frac{1}{2} \left\langle \nabla (\mathbf{v}_q \cdot \mathbf{r}_q \times \omega_L) \right\rangle_i \\ &\quad + \frac{1}{2} \sum_{j,p,s} \langle \epsilon_{jps} v_j r_p \partial_i \omega_s + \epsilon_{ips} (r_s v_j \partial_j \omega_p + v_p r_j \partial_j \omega_s) \rangle, \end{aligned}$$

where we have used (5.43) and the properties of ϵ_{ijk} . We now in the first sum, involving ϵ_{jps} , take into account that one out of j, p, s must necessarily equal i so that we can write

$$\sum_{j,p,s} \epsilon_{jps} r_p v_j \partial_i \omega_s = \sum_{p,s} \epsilon_{ips} (r_p v_i \partial_i \omega_s + r_s v_p \partial_i \omega_i + r_i v_s \partial_i \omega_p), \quad (5.44)$$

where we have indulged in some renaming of dummy indices. In the sums involving ϵ_{ips} we use the fact that j must for given p and s take on the values i, p , and s so that those sums can be written in the form

$$\begin{aligned} \sum_{j,p,s} \epsilon_{ips} (r_s v_j \partial_j \omega_p + v_p r_j \partial_j \omega_s) &= \sum_{p,s} \epsilon_{ips} (r_s v_i \partial_i \omega_p + r_i v_p \partial_i \omega_s + r_s v_p \partial_p \omega_p) \\ &+ r_p v_p \partial_p \omega_s + r_s v_s \partial_s \omega_p + r_s v_p \partial_s \omega_s). \end{aligned} \quad (5.45)$$

Combining (5.44) and (5.45) and using the properties of ϵ_{ips} we find for the expression

$$\begin{aligned} &\left\langle \sum_{p,s} \epsilon_{ips} [r_s v_p (\partial_i \omega_i + \partial_p \omega_p + \partial_s \omega_s) + r_p v_p \partial_p \omega_s + r_s v_s \partial_s \omega_p] \right\rangle \\ &= \langle \mathbf{v}_q \times \mathbf{r}_q (\nabla \cdot \omega_L)_i \rangle \end{aligned}$$

where we have used (5.43). Hence we finally get

$$\begin{aligned} \langle \mathbf{v}_q \times \nabla \times (\mathbf{r}_q \times \omega_L) \rangle &= \omega_L \times \langle (\mathbf{v}_q \cdot \nabla) \mathbf{r}_q \rangle + \frac{1}{2} \langle \nabla (\mathbf{v}_q \cdot \mathbf{r}_q \times \omega_L) \rangle \\ &+ \frac{1}{2} \langle \mathbf{v}_q \times \mathbf{r}_q (\nabla \cdot \omega_L) \rangle, \end{aligned}$$

from which (5.39) follows, if we use that $(\nabla \cdot \omega_L) = 0$.

5.3 Spontaneous generation of magnetostatic fields

In a collisionless plasma regime, large amplitude magnetostatic fields can be driven by the ponderomotive electron magnetization current. Accordingly, under an action of transverse pump field, generally two types of parametric instabilities: magneto-modulational instability and stimulated magnetostatic scattering instability were found [274, 275]. Parametric growth rates indicate possible importance in high-intensity laser plasma interaction studies.

Under the action of intense laser light (pump) various plasma oscillation modes can become coupled and can grow in time and space before getting saturated at large amplitudes and dissipated in a plasma. A linear parametric theory of laser light instabilities, including a decay, oscillating-two-stream (OTS), stimulated Brillouin (SBS), stimulated Raman (SRS) and stimulated Compton scattering and filamentation, is well developed [97, 281, 105].

In particular, much ongoing effort has been put into studies of scattering instabilities which have a potential to substantially reduce laser light absorption in a target. In this section, we wish to discuss a less known competing parametric processes due to excitation

of magnetostatic field instabilities. In a collisionless regime, the basic mechanism driving magnetostatic (slow timescale) fields has appeared to be due to the ponderomotive electron magnetization current, derived above (5.42), written in the form

$$\mathbf{j}_M = -\frac{ie\omega_{pe}^2}{16\pi m\omega_0^3}\nabla \times (\mathbf{E} \times \mathbf{E}^*), \quad (5.46)$$

where, \mathbf{E} is the complex amplitude of the high-frequency (ω_0) laser field.

The basic magnetostatic field generation equation is readily obtained from the Amperes law, following the procedure, indicated above (for details see Kono et al., [256]), written as

$$\nabla^2 \delta \mathbf{B} + \mathbf{S}_{kin} = \frac{ie\omega_{pe}^2}{4mc\omega_0^3}\nabla \times \nabla \times (\mathbf{E} \times \mathbf{E}^*), \quad (5.47)$$

with the displacement current neglected, and where \mathbf{S}_{kin} represents the skin (anomalous) damping term which characterizes propagation of a magnetostatic mode ($\omega \ll \omega_{pe}$) through a warm overcritical density plasma.

5.3.1 Coupled mode equations

We shall focus on a nonlinear state of a nonisothermal ($T_e \gg T_i$) collisionless plasma subjected to an action of a finite amplitude laser pump wave $\tilde{\mathbf{E}}(\omega_0, \mathbf{k}_0)$. We generalize the standard derivation of parametrically coupled modes [97, 281, 105], by taking into account, apart from the usual low-frequency density perturbation, the additional ponderomotive effect in the form of ponderomotively driven magnetostatic fluctuations. Leaving out details of the straightforward procedure (see Refs. [274, 275]) the basic set of coupled equations is written as

$$\frac{\partial^2 \tilde{\mathbf{E}}}{\partial t^2} + \omega_{pe}^2 \tilde{\mathbf{E}} + \mathbf{c}^2 \nabla \times (\nabla \times \tilde{\mathbf{E}}) - 3v_{Te}^2 \nabla (\nabla \cdot \tilde{\mathbf{E}}) = \frac{\delta n}{n_0} \omega_{pe}^2 \tilde{\mathbf{E}} + \frac{e}{mc} \frac{\partial \tilde{\mathbf{E}}}{\partial t} \times \delta \mathbf{B}, \quad (5.48)$$

$$\frac{\partial^2 \delta n}{\partial t^2} - \nabla^2 \delta n = \frac{1}{16\pi M} \nabla^2 |\tilde{\mathbf{E}}|^2, \quad (5.49)$$

$$\nabla^2 \delta \mathbf{B} = \frac{ie\omega_{pe}^2}{4mc\omega_0^3} \nabla \times \nabla \times (\mathbf{E} \times \mathbf{E}^*) - \mathbf{S}_{kin}, \quad (5.50)$$

where

$$\mathbf{S}_{kin} = -\frac{\omega_{pe}^2}{(2\pi)^{3/2} c^2 v_{Te}} \frac{\partial}{\partial t} \int \frac{\delta \mathbf{B}(\mathbf{r}')}{|\mathbf{r} - \mathbf{r}'|} d\mathbf{r}', \quad (5.51)$$

where $\tilde{\mathbf{E}}$ is the high-frequency laser field with a complex amplitude \mathbf{E} and δn and $\delta \mathbf{B}$ stand for the low-frequency density and magnetostatic field perturbation, respectively. An integral term (5.51) represents the anomalous skin effect (Landau damping). From equations (5.48) to (5.51) it appears that parametric excitation of magnetostatic fields ([274, 275]) coexists with standard type of laser-plasma instabilities, such as e.g. OTS and stimulated Brillouin and Raman scattering instabilities.

5.3.2 Instability analysis

Applying a linear parametric theory method, we investigate the instability growth rate against an excitation of magnetostatic fields $\delta\mathbf{B}(\Omega, \mathbf{q})$. One finds that generally taken, the parametric coupling involves a pump (t), a magnetostatic wave (m) and high-frequency side-bands. Depending on a nature of these side-bands, two types of magnetostatic instabilities were found by Škorić, [274, 275]

I MMI- magneto-modulational instability involving the Langmuir (l) side-bands;

II MSI- magnetostatic stimulated scattering instability which corresponds to a fully electromagnetic (t) instability.

In order to further illustrate, we put some typical values for calculated instability growth rates, which depend on the laser pump intensity v_0/c ($v_0 \equiv eE_0/m\omega_0$), the frequency mismatch $\Delta\omega = \omega_0 - \omega_{pe}$, and the electron temperature v_{Te} .

(i) Magneto-modulational instability (*MMI*). ($t \rightarrow l + m$)

This instability is of a purely growing type (4-wave) involving both resonant Langmuir sidebands. An interesting case is when $\mathbf{k}_0 \ll 2(\mathbf{k}_0 \perp \mathbf{q})$ with a dispersion relation

$$(i\xi - 1)(\Omega^2 - \Delta\omega_0^2) + \frac{1}{4} \frac{\omega_{pe}^2}{\omega_0} \frac{q^2}{q^2 + k_0^2} \Delta\omega_0 \left(\frac{v_0}{c}\right)^2 = 0, \quad (5.52)$$

where $\Delta\omega_0 = (c^2k_0^2 - 3v_{Te}^2q^2)/2\omega_0$, $\omega_0^2 = \omega_{pe}^2 + c^2k_0^2$, and the Landau damping term gives $\xi = (\pi/2)(\omega_{pe}^2\Omega/c^2v_{Te}q^3)$. In the case of weak damping, i.e. $\xi \ll 1$, one gets for a maximum growth rate

$$\gamma = \frac{\omega_{pe}^2}{8\omega_0} \left(\frac{v_0}{c}\right)^2, \quad (5.53)$$

for $q_{\max}^2 = \left[c^2k_0^2 + (\omega_{pe}^2/4)(\frac{v_0}{c})^2/3v_{Te}^2\right]$, which is a slow instability, of the order of weakly relativistic correction (relativistic mass increase).

For a nonzero damping, $\xi \sim \sigma(1)$, one normally expects an instability growth rate smaller than (5.53). In a dipole pump limit, above results agree with the other results, being similar to the magneto-modulational instability studied in detail for the Langmuir pump by Kono et al., [269, 256].

(ii) Stimulated magnetostatic scattering instability (*MSI*). ($t \rightarrow t' + m$)

This instability, proposed by Škorić [274, 275], looks particularly interesting, as a 3-wave process (resonant Stokes sideband) with a dispersion relation in the form

$$(\Omega + i\omega_*) (\Omega - \Delta\omega_0) - i\omega_* \frac{\omega_{pe}^2}{\omega_0} \left(\frac{v_0}{c}\right) \sin^2\theta = 0, \quad (5.54)$$

where $\omega_* = \Omega/\xi$, (ξ is given above) comes from the Landau damping term (\mathbf{S}_{kin}), $\Delta\omega_0 = c^2q(2k_0 \cos\theta - q)/2\omega_0$, and angle $\theta \angle (\mathbf{k}_0, \mathbf{q})$. Following (5.54), we get for a finite k_0 , a maximum growth rate $\gamma \equiv \text{Im}(\Omega)$

$$\gamma \simeq 0.3\omega_0 \left(\frac{v_{Te}}{c}\right)^{\frac{1}{2}} \left(\frac{v_0}{c}\right) \left(\frac{ck_0}{\omega_0}\right)^{\frac{3}{2}}, \quad (5.55)$$

for

$$\theta \sim 40^\circ, \text{ if } \frac{k_0 c}{\omega_0} \gg \frac{v_{Te}}{c} \left(\frac{\omega_0}{\omega_{pe}} \right)^2 \left(\frac{v_0}{c} \right)^2,$$

which can become pronounced in a high-intensity laser driven hot plasma regimes.

For the resonance regime, in a limit of dipole pump, both sidebands are driven resonant (4-wave), resulting in a growth rate lower than (5.55), given as

$$\gamma \simeq \frac{\omega_{pe}}{2\sqrt{2}} \frac{ck_0}{\omega_0} \frac{v_0}{c}, \quad (5.56)$$

for

$$\theta = \pi/2, \text{ if } 1 \ll (q/k_0)^2 < \left(1/\sqrt{2} \right) (\omega_{pe}/ck_0) (v_0/c).$$

Generally taken, MSI which maximizes for perturbations transverse to the pump field is pronounced at high (laser) intensities in low density hot plasmas; coexisting and possibly competing with electromagnetic stimulated scattering instabilities, such as, is SBS, SRS and Compton; as well as with the 4-wave filamentation type of instability. Magnetostatic field excitation, appears as a general feature of parametrically unstable warm plasmas. For a more complete and consistent description of electromagnetic parametric instabilities by laser light, inclusion of (weak) relativistic effects would be appropriate [282].

Bibliography

- [1] B.B. Kadomtsev: *Plasma Turbulence* (Academic Press, New York 1976).
- [2] V.E. Zakharov: Sov. Phys. JETP **35**, 980 (1972).
- [3] S.G. Thornhill, D. ter Haar: Phys. Rep. **43**, 43 (1978).
- [4] V.E. Zakharov, E.A. Kuznetsov: in *Nonlinear Science at the Dawn of the 21st Century*, ed. P.R. Christiansen, M.P. Sørensen, A. Scott (Springer New York 2001) pp. 3-42.
- [5] D. Ter Haar: in *Plasma Physics; Nonlinear Theory and Experiments*, H. Wilhelmsson, ed. (Plenum Press, New York 1977).
- [6] V.E. Zakharov, A.M. Rubenchik: Sov. Phys.–JETP **38**, 494 (1974).
- [7] A.A. Vedenov, L.I. Rudakov: Sov. Phys. Dokl. **9**, 1073 (1965).
- [8] A.A. Gailitis: Izv. Akad. Nauk Latv. SSR, Ser. Fiz. Tekh. Nauk **4**, 13 (1965).
- [9] N.S. Buchelnikova, E.P. Matochkin, Novosibirsk Nucl. Phys. Inst. Preprint 78-76 (1978).
- [10] T. A. Gorbushina, L.M. Degtyarev, R.Z. Sagdeev, V.D. Shapiro, V.I. Shevchenko: Preprint Inst. Appl. Math. Acad. So. USSR, No. 17 (1978).
- [11] M.V. Goldman: Rev. Mod. Phys. **56**, 709(1984).
- [12] S.V. Antipov, M.V. Nezhlin, E.N. Snezhkin, A.S. Trubnikov: Sov. Phys. JETP **49**, No. 5 (1979).
- [13] D.R. Nicholson, M.V. Goldman: Phys. Fluids **21**, 1766 (1978) .
- [14] L.I. Rudakov, V.N. Tsytovich: Phys. Repts. **40**, 1 (1978).
- [15] D. ter Haar: Phys. Scr. **T2B**, 522 (1982).
- [16] F.Kh. Khakimov, V N. Tsytovich: Sov. Phys. JETP **43**, 929 (1976).
- [17] V.N. Tsytovich: *Plasma Turbulence* (Plenum New York 1977).
- [18] M.M. Škorić, D. Ter Haar: Physica C **98**, 212 (1980).

- [19] E.A. Kuznetsov: (a) Sov. Phys. JETP **39**, 1003 (1974); (b) Sov. J. Plasma Phys. **2**, 178 (1976).
- [20] E.W. Laedke and K.H. Spatschek, Phys. Rev. Lett. **42**, 1534 (1979).
- [21] J. Gibbons, S.G. Thornhill, M.L. Wardrop, D. Ter Haar: J. Plasma Phys. **17**, 153 (1977).
- [22] A.V. Gaponov, M.A. Miller: Sov. Phys. JETP **7**, 168 (1958).
- [23] R.C. Davidson: *Methods in Non-Linear Plasma Theory* (Academic Press, New York 1972).
- [24] E.A. Kuznetsov, V.E. Zakharov, A.M. Rubenchik: Phys. Rep. **142**, 103 (1986).
- [25] C. Sulem, P.-L. Sulem: *The Nonlinear Schrödinger Equation: Self-Focusing and Wave Collapse* (Springer-Verlag New York 1999).
- [26] A.G. Litvak, G.M. Fraiman, A. D, Yunakovskii: JETP Lett. **19**, 13 (1974).
- [27] L.M. Degtyarev, V.E. Zakharov, L.I. Rudakov: Sov. Phys. JETP **41**, 57 (1975).
- [28] M. Watanabe, K. Nishikawa: J. Phys. Soc. Japan **41**, 1029 (1976).
- [29] A. A. Galeev, R.Z. Sagdeev, Yu.S. Sigov, V.D. Shapiro, V.I. Shevchenko: Sov. J. Plasma Phys. **1**, 5 (1975).
- [30] V.E. Zakharov: in *Handbook of Plasma Physics*, ed. A. A. Galeev, R. N. Sudan (North-Holland, Amsterdam 1983), Vol. 2.
- [31] V.V. Gorev, A.S. Kingsep, L.I. Rudakov: Radiophys. Quan. Electron. **19**, 486 (1976).
- [32] A.A. Galeev, R.Z. Sagdeev, V.D. Shapiro, V.I. Shevchenko: Sov. Phys. JETP **46**, 711 (1977).
- [33] M.V. Goldman, D.R. Nicholson, Phys. Rev. Lett. **41**, 406 (1978).
- [34] R.Z. Sagdeev: Rev. Mod. Phys. **51**, 1 (1979).
- [35] P.A. Robinson: Rev. Mod. Phys. **69**, 507 (1997).
- [36] Lj.R. Hadžievski, M.M. Škorić. A.M. Rubenchik, E.G. Shapiro, S.K. Turitsin: Phys. Rev. A **42** 3561 (1990).
- [37] M.A. Berezovskii, A.I. Dyachenko, A.M. Rubenchik: Sov. Phys.-JETP **61**, 701 (1985).
- [38] H.L. Rowland: Phys. Fluids **28**, 150 (1986).
- [39] M.V. Goldman, J.C. Weatherall, D.R. Nicholson: Phys. Fluids **24**, 668 (1981).

- [40] J.P. Sheerin, J.C. Weatherall, D.R. Nicholson, G.L. Payne, M.V. Goldman, P.J. Hansen: *J. Atmos. Terr. Phys.* **44**, 1043 (1982).
- [41] H.L. Pecseli, J. J. Rasmussen, K. Thomsen: *Phys. Lett. A* **99**, 175 (1983).
- [42] M.J. Giles: *Phys. Rev. Lett.* **47**, 1606 (1981).
- [43] V.V. Krasnosel'skikh, V.I. Sotnikov: *Sov. J. Plasma Phys.* **3**, 491 (1977).
- [44] B.A. Trubnikov S.K. Zhdanov: *Phys. Rep.* **155**, 137 (1987).
- [45] P.A. Jansenn, J. J. Rasmussen: *Phys. Fluids* **26**, 1297 (1983).
- [46] N.R. Pereira, R.N. Sudan, J.Denavit: *Phys. Fluids* **20**, 936 (1977).
- [47] P.A. Robinson, D.L. Newman, M. V. Goldman: *Phys. Rev. Lett.* **62**, 2132 (1989).
- [48] S. Lipatov: *JETP Lett.* **26**, 337 (1977).
- [49] V.E. Zakharov. E.A. Kuznetsov: *Sov. Phys. JETP* **64**, 773 (1986).
- [50] E.A. Kuznetsov, M.M. Škorić: *Phys. Lett. A* **129** 459 (1988) ; *Phys. Rev. A* **38**, 1422 (1988).
- [51] V. Vlasov, L. I. Piskunova, V. I. Talanov: in *Proceedings of the Third Workshop on Nonlinear and Turbulent Processes in Physics*, ed. V.M. Cheronoushenko (Naukova Dumka Kiev 1987) Vol.2 p.210.
- [52] V.M. Malkin: *JETP Lett.* **48**, 653 (1988).
- [53] M. Kono, M.M. Škorić, D. ter Haar: *J. Plasma Phys.* **26**, 123 (1981).
- [54] M. Kono, M.M. Škorić, D. ter Haar: *Phys. Lett. A* **78**, 140 (1980).
- [55] S.L. Musher, A.B. Rubenchik, B.I. Sturman: *Plasma Phys.* **20**, 1131 (1978).
- [56] S.L. Musher, A.M. Rubenchik, I.Ya. Shapiro: in *European Space Agency Report No. ESA SP-251* (1986) pp. 465-472.
- [57] V.N. Tsytovich: *Comm. Plasma Phys. Contr. Fusion* **4**, 81 (1978).
- [58] M. Porkolab, R.P.H. Chang: *Rev. Mod. Phys.* **50**, 745 (1972).
- [59] Lj.R. Hadžievski, M.M. Škorić: *Phys. Fluids B* **3** 2452 (1991) ; **5**, 1076 (1993).
- [60] Lj.R. Hadžievski, M.M. Škorić, M. Kono, T. Sato: *Phys. Lett. A* **248**, 247 (1998).
- [61] D.F. DuBois, A. Hansen, H.A. Rose, D. Russel: *Phys. Fluids B* **5**, 2616 (1993).
- [62] D.L. Newman, M.V. Goldman, R.E. Ergun: *Phys. Plasmas* **1**, 1691 (1994).
- [63] P.A. Robinson, A. Melatos, W. Rozmus: *J. Geophys. Res.* **101**, 21545 (1996).

- [64] A. Melatos, P.A. Robinson: Phys. Plasmas **3**, 1263 (1996).
- [65] P.A. Robinson, A. Melatos, W. Rozmus: Phys. Plasmas **3**, 133 (1996).
- [66] P.A. Robinson: Phys. Plasmas **3**, 192 (1996).
- [67] A. Melatos, W.E.P. Padden, P.A. Robinson: Phys. Plasmas **3**, 498 (1996).
- [68] S.I. Popel: Plasma Phys. Repts. **24**, 1022 (1998).
- [69] D. Jovanovic, J. Vranjes, J. Weiland: Phys. Rev. E **53**, 1051 (1996).
- [70] D.R. Shklyar, B. Kliem: J. Geophys. Res. A, Space Physics **111**, A06204 (2006).
- [71] G. Benford, J.C. Weatherall: Phys. Fluids B **4**, 4111 (1992).
- [72] A. Melatos, P.A. Robinson: Proc. Astron. Soc. Australia **10**, 283 (1993).
- [73] G. Thejappa, M.L. Goldstein, R.J. MacDowall, K. Papadopoulos, R.G. Stone: J. Geophys. Res. A **104**, 28279 (1999).
- [74] P.W. Schuck, J.W. Bonnell, P.M. Kintner, Jr.: IEEE Trans. Plasma Sci. **31**, 1125 (2003).
- [75] D. Jovanovic, P.K. Shukla, G. Morfil: Phys. Plasmas **14**, 082901 (2007).
- [76] J. Guckenheimer and P.Holmes: *Nonlinear Oscillations, Dynamical Systems, and Bifurcations of Vector Fields*,(Springer, New York 1983)
- [77] A.R. Bishop, M.G. Forest, D.W. Mc Laughlin and E.A. Overman II: Physica D **23**, 293 (1986)
- [78] O. Larrroche and D. Pesme: in *Nonlinear and Chaotic Phenomena in Plasmas, Solids and Fluids*, eds. W. Rozmus and I.A. Tuszinski (World Scientific 1991) p.308
- [79] R. Teman: *Infinite-Dimensional Dynamical Systems in Mechanics and Physics*, (Springer, New York 1988)
- [80] M. Tabor: *Nonintegrable Systems and Chaos*, (Springer, New York 1989) pp.278-360
- [81] D.J. Kaup, A. Rieman and A. Bers: Review of Modern Physics **51**, 275 (1979); *ibid.*, **51**, 915 (1979)
- [82] D.J. Kaup and A.B. Malomed: Phys. Lett. A **169**, 35 (1992); **183**, 283 (1993)
- [83] J.M. Wersinger, J.M. Finn and E. Ott: Phys. Fluids, **23**, 1142 (1980)
- [84] C. Meunier, M.N. Bussac and G. Laval: Physica D **4**, 262 (1980)
- [85] C.C. Chow, A. Bers and A.K. Ram: Phys. Rev. Lett. **68**, 3379 (1992)
- [86] A.M. Maluckov, *MSc thesis*, (University of Belgrade , 1997) (in Serbian, unpublished)

- [87] V. Fuchs and G. Beaudry: J. of Math. Phys. **16**, 616 (1975)
- [88] V. Fuchs: Phys. Fluids **19**, 1554 (1976)
- [89] C.J. Mc Kinstrie: Phys. Fluids **31**, 288 (1988)
- [90] V. Fuchs and G. Beaudry: J. of Math. Phys. **17**, 208 (1976)
- [91] R.W. Harvey and G. Schmidt: Phys Fluids **18**, 1395 (1975)
- [92] D. Pesme, G. Laval and R. Pellat: Phys. Rev. Lett. **31**, 203 (1973)
- [93] O. Larroche and D. Pesme: Phys. Fluids B **2**, 1751 (1980)
- [94] M.S. Jovanović and M.M. Škorić: Physica Scripta **54**, 200 (1996)
- [95] Z.X. Wang and D.R. Guo: *Special Functions*, (World Scientific 1989) pp.654-658
- [96] K.Mima, M.M. Škorić, S. Miyamoto, A. Maluckov and M.S. Jovanović: In *Laser Interaction and Related Plasma Phenomena*, vol.**14**, ed. G.H. Miley and E.M. Campbell (AIP Press 1997) pp. 177-182
- [97] W.J. Kruer: *The Physics of Laser Plasma Interactions*, (Addison-Wesley Publishing 1988)
- [98] M.M. Škorić and M.S. Jovanović: In *Laser Interaction and Related Plasma Phenomena*, ed. H. Hora, G. Miley (AIP Conf. Proc. **318**, 1994) pp. 380-389
- [99] M.I. Rabinovich and D.I. Trubeckov: *Vvedenie v teoriju kolebanij i voln*, (Nauka, 1984) (in Russian)
- [100] K. Nishikawa and C.S. Liu: In *Advances in Plasma Physics*, Vol **6**, ed. by A. Simon, W.B. Thompson (Wiley, New York 1976)
- [101] M.M. Škorić, M.S. Jovanović and M. R. Rajković: In *Dynamical Systems and Chaos*, edited by Y. Aizawa, S. Saito and K. Shiraiwa (World Scientific, Singapore, 1995), pp. 165-176
- [102] M.M. Škorić, M.S. Jovanović and M.R. Rajković: Phys. Rev. E **53**, 4056 (1996)
- [103] M.M. Škorić, M.S. Jovanović and M.R. Rajković: Europhys. Lett. **34**, 19 (1996)
- [104] M.M. Škorić, T. Sato, A. M. Maluckov and M.S. Jovanović, *Complexity in Laser Plasmas*, (general invited iecture); 24th ICPIG, Warsaw, Poland (1999), J. Tech. Physics (Poland), Special issue, **41** (2000) pp. 147-163
- [105] D. W. Forslund, J. M. Kindel and E. L. Lindman: Phys. Fluids **18**, 1002 (1975)
- [106] J. A. Heikkinen and S. J. Karttunen: Phys. Fluids **29**, 1291 (1986)
- [107] G. Bonnaud, D. Pesme and R. Pellat: Phys. Fluids B **2**, 1618 (1990)

- [108] T. Kolber, W. Rozmus and V. T. Tikhonchuk: *Phys. Fluids B* **5**, 138 (1993)
- [109] H. P. Drake and S. H. Batha: In *Nonlinear and Chaotic Phenomena in Plasmas, Solids and Fluids*, edited by W. Rozmus and J. A. Tuszynski (World Scientific, Singapore, 1991), p.345
- [110] W. L. Kruer: *Phys. Scr.* **T30**, 5 (1990)
- [111] F. Chen: *Phys. Scr.* **T30**, 14 (1990)
- [112] R. Bingham: *Phys. Scr.* **T30**, 24 (1990)
- [113] W. Rozmus: *Phys. Scr.* **T30**, 64 (1990)
- [114] M. C. Cross and P. Hohenberg: *Rev. Mod. Phys.* **65**, 851 (1993)
- [115] W.H. Press, B.P Flannery, S.A. Teukolsk and W.T. Vetterling: *Numerical Recipes*, (Cambridge University Press 1986)
- [116] M.M. Škorić, M.S. Jovanović, M.R. Rajković and M. Kono: In *Transport, Chaos and Plasma Physics 2*, ed. by S. Benkadda, F. Doveil and Y. Elskens (World Scientific, 1996) pp. 245-249
- [117] M.S. Jovanović and M.M. Škorić: In *Low Temperature and General Plasmas*, ed. by M. Milosavljević (NOVA Science, N.Y. 1996) pp. 291-300
- [118] P. Manneville: *Dissipative Structures and Weak Turbulence* (Academic, San Diego, 1990)
- [119] D. Stassinopoulos and P. Alstrøm: *Phys. Rev. A* **45**, 675 (1992)
- [120] R. Ramshankar and K. R. Sreenivasan: *Physica* **23D**, 246 (1986).
- [121] Aceves, H. Adachihara, C. Jones, J. C. Lerman, D. W. McLaughlin, J. V. Moloney and A. C. Newell: *Physica* **18D**, 85 (1986).
- [122] K. Kaneko: *Prog. Theory. Phys.* **74**, 1033 (1985)
- [123] R. Z. Sagdeev and A. Galeev: *Nonlinear Plasma Theory* (Benjamin, New York, 1969)
- [124] M.M. Škorić, T. Sato, A. Maluckov and M.S. Jovanović: *Phys. Rev.* **E60**, 7426 (1999)
- [125] M.M. Škorić, T. Sato, A. Maluckov and M.S. Jovanović: *J. Plasma and Fusion Res.***2**, 32 (1999)
- [126] M. N. Rosenbluth and C. S. Liu: *Phys. Rev. Lett.* **29**, 701 (1972)
- [127] T. W. Johnston, P. Bertrand, A. Ghizzo, M. Shoucri, E. Fijalkow and M. R. Feix: *Phys. Fluids B* **4**, 2523 (1992)

- [128] P. Grassberger and I. Procaccia: *Physica* **9D**, 189 (1983)
- [129] K. Fukunaga and R. R. Olsen: *IEEE Trans. Comput.* **20**, 176 (1971)
- [130] H. Akaike: *IEEE Trans. Autom. Control* **19**, 716 (1974)
- [131] J. Rissanen: *Automatika* **14**, 465 (1978)
- [132] K. M. Wong, Q. T. Zhang, J. P. Reilley and P. C. Yip: *IEEE Trans. Acoust. Speech Signal Process.* **38**, 11 (1990)
- [133] D. Ruelle: *Proc. R. Soc. London, Ser. A* **427**, 241 (1990)
- [134] A. Passamante, T. Heideger, and M. Gollub: *Phys. Rev. A* **39**, 3640 (1989)
- [135] L. Sirovich: *Q. Appl. Math* **45**, 561 (1987)
- [136] N. Aubry, R. Guyonnet and R. Lima: *J. Stat. Phys.* **64**, 683 (1991)
- [137] Rajković, J. Riznić and M. Ishii: *Nucl. Eng. Des.* **149**, 53 (1994)
- [138] H. Chate and P. Manneville: *Phys. Rev. Lett.* **58**, 112 (1987)
- [139] P. C. Hohenberg and B. I. Shraiman: *Physica* **37D**, 109 (1993)
- [140] Y. Pomeau: *Physica* **23D**, 3 (1986)
- [141] T. Sato and the Complexity Group: *Phys. Plasmas* **3**, 2135 (1996)
- [142] T. Sato and the Complexity Group: *Phys. Plasmas* **2**, 3609 (1996)
- [143] G. Nicolis and I. Prigogine :*Exploring Complexity* (Freeman, New York, 1989)
- [144] H. Rose: *Phys. Plasmas* **5**, 3886 (1998)
- [145] H. Rose: *Phys. Plasmas* **5**, 3876 (1998)
- [146] H. Rose: *Phys. Plasmas* **6**, 1294 (1999)
- [147] B. Coppi, R.D. Blanford and M.J. Rees, *MNRAS* **262**, 603 (1993)
- [148] S.J. Kartunnen, T.J. Pattinkagas, R.P. Saloma and S.K. Sipila: *Nucl. Fusion* **31**, 1079 (1991)
- [149] H. Takamaru, T. Sato, R. Horiuchi, K. Watanabe and Complexity Group: *J. Phys. Soc. Jpn* **66**, 3826 (1996)
- [150] C.K. Birdsall and A.B. Langdon: *Plasma Physics via Computer Simulations* (IoP Publishing, Bristol, 2005)
- [151] S. Miyamoto, K. Mima, M.M. Škorić and M.S. Jovanović: *J. Phys. Soc. Jpn* **67**, 3826 (1998)

- [152] C. Coverdale, C.B. Darrow et al.: Phys. Rev. Lett. **74**, 4569 (1995)
- [153] C.A. Coverdale, C.B. Darrow et al.: Plasma Phys. Rept. **22**, 617 (1996)
- [154] A. I. Akhiezer, R. V. Polovin, Soviet Phys. JETP **3**, 696-706 (1956).
- [155] P. Kaw and J. Dawson: Phys. Fluids **13**, 472 (1970)
- [156] C. Max and F. Perkins: Phys. Rev. Lett. **27**, 1342 (1971)
- [157] M. Tabak, J. Hammer, M. Glinsky, W. Kruer, S. Wilks, J. Woodworth, E. M. Campbell, M. Perry and R. Mason: Phys. Plasmas **1**, 1626 (1994)
- [158] S. Atzeni and J. Meyer-ter-Vehn: *The Physics of Inertial Fusion* (Clarendon Press, Oxford 2004)
- [159] P. Amendt, D. C. Eder and S. C. Wilks: Phys. Rev. Lett. **66**, 2589 (1991)
- [160] T. Tajima and J. Dawson: Phys. Rev. Lett. **43**, 267 (1979)
- [161] A. Modena, Z. Najmudin, A. E. Dangor, C. E. Clayton, K. A. Marsh, C. Joshi, V. Malka, C. B. Darrow, C. Danson, D. Neely and A. F. Walsh: Nature (London) **377**, 608 (1995)
- [162] G.A. Mourou, T. Tajima and S. V. Bulanov: Rev. Mod. Phys. **78**, 309 (2007)
- [163] G.A. Mourou, C.L. Labaune, M. Dunne, N. Naumova and V. T. Tikhonchuk: Plasma. Phys. Contr. Fus. **49**, B667 (2007)
- [164] A.V. Borovsky, A.L. Galkin, O.B. Shiryayev and T. Auguste: *Laser Physics at Relativistic Intensities* (Springer, Berlin 2003)
- [165] K. Mima and K. Nishikawa: in *Basic Plasma Physics II*, edited by A. A. Galeev and R. N. Sudan, (North-Holland, Amsterdam 1984), p. 451.
- [166] A. C-L. Chian, Plasma Phys. Control Fusion **41**, A437 (1999)
- [167] B. J. MacGowan, B. B. Afeyan, C. A. Back, R. L. Berger, G. Bonnaud, M. Casanova, B. I. Cohen, D. E. Desenne, D. F. DuBois, A. G. Dulieu, K. G. Estabrook, J. C. Fernandez, S. H. Glenzer, D. E. Hinkel, T. B. Kaiser, D. H. Kalantar, R. L. Kauffman, R. K. Kirkwood, W. L. Kruer, A. B. Langdon, B. F. Lasinski, D. S. Montgomery, J. D. Moody, D. H. Munro, L. V. Powers, H. A. Rose, C. Rousseaux, R. E. Turner, B. H. Wilde, S. C. Wilks and E. A. Williams: Phys. Plasmas **3**, 2029 (1996)
- [168] D. S. Montgomery, B. B. Afeyan, J. A. Cobble, J. C. Fernández, M. D. Wilke, S. H. Glenzer, R. K. Kirkwood, B. J. MacGowan, J. D. Moody, E. L. Lindman, D. H. Munro, B. H. Wilde, H. A. Rose, D. F. DuBois, B. Bezzerides and H. X. Vu, Phys. Plasmas **5**, 1973 (1998)
- [169] W. L. Kruer, B. B. Afeyan, A. E. Chou, R. K. Kirkwood, D. S. Montgomery, P. W. Rambo and S. C. Wilks, Phys. Scripta T**75**, 7 (1998)

- [170] R. L. Berger, C. H. Still, E. A. Williams and A. B. Langdon, *Phys. Plasmas* **5**, 4337 (1998)
- [171] W. L. Kruer, *Phys. Plasmas* **7**, 2270 (2000)
- [172] H. A. Rose, *Phys. Plasmas* **7**, 2571 (2000)
- [173] D. Mourenas, *Phys. Plasmas* **6**, 1258 (1999)
- [174] K. Estabrook and W. L. Kruer, *Phys. Fluids* **26**, 1892 (1983)
- [175] C. J. McKinstrie and R. Bingham, *Phys. Fluids B***4**, 2626 (1992)
- [176] Lj. Nikolić, PhD thesis, Graduate University for Advanced Studies, Japan (2002, unpublished), pp. 11-23
- [177] F. W. Sluijter and D. Montgomery: *Phys. Fluids* **8**, 551 (1965)
- [178] D. Montgomery and D. A. Tidman: *Phys. Fluids* **7**, 242 (1964)
- [179] C. E. Max, J. Arons and A. B. Langdon, *Phys. Rev. Lett.* **33**, 209 (1974)
- [180] S. Guérin, G. Laval, P. Mora, J.C. Adam, A. Héron and A. Bendib, *Phys. Plasmas* **2**, 2807 (1995).
- [181] C. J. McKinstrie and R. Bingham, *Phys. Fluids B***1**, 230 (1989)
- [182] A. S. Sakharov and V. I. Kirsanov, *Phys. Rev. E***49**, 3274 (1994)
- [183] B. Quesnel, P. Mora, J.C. Adam, A. Héron and G. Laval: *Phys. Plasmas* **4**, 3358 (1997)
- [184] B. Quesnel, P. Mora, J.C. Adam, A. Héron, S. Guérin and G. Laval: *Phys. Rev. Lett.* **78**, 2132 (1997)
- [185] H. C. Barr, P. Mason and D. M. Parr, *Phys. Plasmas* **7**, 2604 (2000)
- [186] Y. Omura and H. Matsumoto: KEMPO1 in *Computer Space Plasma Physics*, edited by H. Matsumoto and Y. Omura, (Terra Scientific Publishing Company, Tokyo 1993), p. 19.
- [187] P. Gibbon: *Short Pulse Laser Interactions with Matter* (Imperial College Press, London 2005)
- [188] V. A. Kozlov, A. G. Litvak and E. V. Suvorov: *Sov. Phys. JETP* **49**, 75 (1979)
- [189] K. V. Kotetishvili, P. Kaw and N. L. Tsintzadze: *Sov. J. Plasma Phys.* **9**, 468 (1983)
- [190] M. Y. Yu, P. K. Shukla and N. L. Tsintzadze: *Phys. Fluids* **25**, 1049 (1984)
- [191] S.V. Bulanov, I.N. Inovenkov, V.I. Kirsanov, N.M. Naumova and A.S. Sakharov: *Phys. Fluids B* **4**,1935 (1992)

- [192] H.H. Kuehl, C.Y. Zhang and T. Katsouleas: Phys. Rev. **E 47**, 1249 (1993)
- [193] P. K. Kaw, A. Sen, T. Katsouleas: Phys. Rev. Lett. **68**, 3172 (1992)
- [194] K. Mima, M. S. Jovanović, Y. Sentoku, Z. -M. Sheng, M. M. Škorić, T. Sato: Phys. Plasmas, **8**, 2349 (2001)
- [195] S. V. Bulanov, F. Califano, T. Zh. Esirkepov, K. Mima, N. M. Naumova, K. Nishihara, F. Pegoraro, Y. Sentoku, V. A. Vshivkov: Physica D, **152-153**, 682 (2001)
- [196] S. V. Bulanov, T. Zh. Esirkepov, N. M. Naumova, F. Pegoraro, V. A. Vshivkov: Phys. Rev. Lett. **82**, 3440 (1999)
- [197] D. Farina and S. V. Bulanov: Phys. Rev. Lett. **86**, 5289 (2001)
- [198] N. M. Naumova, S. V. Bulanov, T. Zh. Esirkepov, D. Farina, K. Nishihara, F. Pegoraro, H. Ruhl and A. S. Sakharov: Phys. Rev. Lett. **87**, 185004-1 (2001)
- [199] C. D. Decker, W. B. Mori, K. -C. Tzeng, T. Katsouleas: Phys. Plasmas **3**, 2047 (1996)
- [200] T. Zh. Esirkepov, F. F. Kamenets, S. V. Bulanov, N. M. Naumova: JETP Lett. **68**, 36 (1998)
- [201] Lj. Hadžievski, M.S. Jovanović, M. M. Škorić and K.Mima: Phys. Plasmas **9**, 2569 (2002)
- [202] J.D. Jackson: *Classical Electrodynamics* (Wiley, New York 1975) 2nd ed. p.222
- [203] C.J. McKinstrie and D.F. DuBois: Phys. Fluids **31**, 278 (1965)
- [204] A.S. Sakharov and V.I. Kirsanov: Plasma Physics Reports **21**, 596 (1995)
- [205] A. G. Litvak, A.M. Sergeev: JETP Lett. **27**, 517 (1978))
- [206] A. Mancic, Lj. Hadžievski and M. M. Škorić: Phys. Plasma **13**, 052309 (2006)
- [207] N. G. Vakhitov, A. A. Kolokolov: Izv. Vyssh. Uchebn. Zaved. Radiofizika **16**, 1020 (1973)
- [208] D. E. Pelinovsky, V. V. Afanasijev and Y. S. Kivshar: Phys. Rev. E **53**, 1940 (1996)
- [209] T. R. Taha, M. J. Ablowitz: J. Comput. Phys. **55**, 203 (1984)
- [210] Lj. Hadžievski, M. M. Škorić: Phys. of Fluids B, **3** 2452 (1991)
- [211] D. W. Forslund, J. M. Kindel and E. L. Lindman, Phys. of Fluids **18**, 1017 (1975)
- [212] K. Estabrook et al., Phys. of Fluids, **B 1**, 1282 (1989)
- [213] C. D. Decker, W. B. Mori and T. Katsouleas, Phys. Rev. **E50**, R3338 (1994)

- [214] W.B. Mori, C.D. Decker, D.E. Hinkel and T. Katsouleas: Phys. Rev. Lett **72**, 1482 (1994)
- [215] N.E. Andreev, L.M. Gorbunov, V.I. Kirsanov, A.A. Pogosova and R.R. Ramazashvili: Phys. Scr. **49**, 101 (1994)
- [216] Baiwen Li, S. Ishiguro, M. M. Škorić, Min Song and T. Sato: Phys. Plasmas **12**, 103103 (2005).
- [217] S. Hain and P. Mulser: Laser Part. Beams **15**, 541 (1997)
- [218] K.-C. Tzeng, W.B. Mori and C.D. Decker: Phys. Rev. Lett. **76**, 3332 (1996)
- [219] S. Wilks, W. Kruer, E.A. Williams, P. Amendt and C.D. Decker: Phys. Plasmas **2**, 274 (1995)
- [220] S. V. Bulanov, F. Califano, T. Tz. Esirkepov, K. Mima, et al., Plasma Fusion Res. **75**, 506 (1999)
- [221] Li Baiwen, S. Ishiguro, M. M. Škorić, H. Takamaru and T. Sato, Journal of Plasma and Fusion Research, Series Vol. **6** (2004).
- [222] Baiwen Li, S. Ishiguro, M.M. Škorić and T. Sato: Phys. Plasmas **13**, 042303 (2006)
- [223] Li Baiwen, S. Ishiguro and M.M. Škorić: Chinese Phys. **15**, 2046 (2006)
- [224] Hsing-Hen Chen and C. S. Liu, Phys. Rev. Lett. **37**, 693 (1976)
- [225] R. N. Sudan, Y. S. Dimant and O. B. Shiryayev, Phys. Plasmas **4(5)**, 1489 (1997)
- [226] S. Poornakala, A. Das, A. Sen and P.K. Kaw: Phys. Plasmas **9**, 1820 (2002)
- [227] A. V. Kochetov, V. A. Mironov, V. N. Bubukina *et al.*, Physica D **152-153**, 723 (2001);
- [228] T. Zh. Esirkepov, K. Nishihara, S. V. Bulanov *et al.*, Phys. Rev. Lett. **89**, 275002 (2003).
- [229] A. Pukhov and J. Meyer-ter-Vehn, Phys. Rev. Lett. **76**, 3975 (1996).
- [230] Y. Sentoku, T. Zh. Esirkepov, K. Mima, K. Nishihara, F. Califano, F. Pegoraro, H. Sakagami, Y. Kitagawa, N. M. Naumova, S. V. Bulanov: Phys. Rev. Lett. **83**, 3434 (1999)
- [231] M. Borghesi, S. Bulanov, D. H. Campbell, R. J. Clarke, T. Zh. Esirkepov, M. Galimberti, L. A. Gizzi, A. J. MacKinnon, N. M. Naumova, F. Pegoraro, H. Ruhl, A. Schiavi, and O. Willi: Phys. Rev. Lett. **88**, 135002 (2002)
- [232] M. M. Škorić, Lj. Nikolić, Li Baiwen and S. Ishiguro: in *Atoms, Solids and Plasmas in Super-Intense Laser Fields*, ed. D. Batani, Italian Physical Society (2003)

- [233] M. M. Škorić, Lj. Hadžievski, Li Baiwen and S. Ishiguro, in 31st EPS Conference on Plasma Phys. London, ECA Vol. **28G**, O-2.10 (2004)
- [234] Baiwen Li, S. Ishiguro, M.M. Škorić and T. Sato: Phys. Plasmas **14**, 032101 (2007)
- [235] J. C. Fernández *et al.*: Phys. Plasmas **7**, 3743 (2000)
- [236] H. X. Vu *et al.*, Phys. Rev. Lett. **86**, 4306 (2001)
- [237] D. S. Montgomery, R. J. Focia, H. A. Rose *et al.*, Phys. Rev. Lett. **87**, 155001 (2001)
- [238] D. S. Montgomery, J. A. Cobble, J. C. Fernandez, R. J. Focia, R. P. Johnson *et al.*, Phys. Plasmas **9**, 2311 (2002).
- [239] D. C. Montgomery: *Theory of Unmagnetized Plasma* (Gordon and Breach, New York 1971), p. 69.
- [240] J. P. Holloway and J. J. Dornig: Phys. Rev. A **44**, 3856 (1991)
- [241] H. A. Rose and D. A. Russell: Phys. Plasmas **8**, 4784 (2001)
- [242] Lj. Nikolić, M. M. Škorić, S. Ishiguro and T. Sato: Phys. Rev. E **66**, 036404 (2002)
- [243] Lj. Nikolić, S. Ishiguro and M.M. Škorić: in *Physics of Ionized Gases*, eds. Lj. Hadžievski, T. Grozdanov, AIP Conf. Series Vol **740**, 509-520 (2004)
- [244] Lj. Nikolić, S. Ishiguro and M.M. Škorić: Fusion Sci. and Tech. **43**, 359 (2003)
- [245] A. Ghizzo, T.W. Johnston, T. Rèveille, P. Bertrand and M. Albrecht-Marc: Phys. Rev. E **74**, 046407 (2006)
- [246] B. D. Fried and R. W. Gould, Phys. Fluids **4**, 139 (1961).
- [247] T. H. Stix: *The Theory of Plasma Waves* (McGraw-Hill, New York, 1962), p. 218
- [248] D. Farina and S. V. Bulanov: Plasma Phys. Controlled Fusion **47**, A73 (2005).
- [249] J. C. Adam, A. Héron, S. Guérin, G. Laval, P. Mora and B. Quesnel, Phys. Rev. Lett. **78**, 4765 (1997)
- [250] Z.-M. Sheng *et al.*: Phys. Rev. E **61**, 4362 (2000)
- [251] H. Schamel: Phys. Plasmas **7**, 4831 (2000)
- [252] F. Valentini, T. M. O’Neil and H. E. Dubin, Phys. Plasma **13**, 052303 (2006).
- [253] B. Afeyan, K. Won, V. Savchenko, T. W. Johnston, A. Ghizzo, and P. Bertrand, in *IFSA Proceedings, 2003*, edited by B. A. Hammel, D. D. Meyer-hofer. J. Meyer-ter-Vehn, and H. Azechi (ANS), Chap. V, pp. 213-217
- [254] H. Motz, C.J.H. Watson: Adv. Electron. Electron. Phys. **23**, 153 (1967).

- [255] F.F. Chen: *Introduction to Plasma Physics* (Plenum Press New York 1984).
- [256] M. Kono, M.M. Škorić, D. ter Haar: *J. Plasma Phys.* **26**, 123 (1981).
- [257] B. Bezzerides, D.F. DuBois, D.W. Forslund, E.L. Lindman: *Phys. Rev. Lett.* **38**, 495 (1977).
- [258] P. Mora, R. Pellat: *Phys. Fluids* **22**, 2408 (1979),
- [259] P. Mora, R. Pellat: *Phys. Fluids* **24**, 2219 (1981).
- [260] R. Pellat: in *Laser-Plasma Interaction*, ed. R. Balian, J. C. Adam (North-Holland 1982) pp.465-467.
- [261] J.R. Cary, A.N. Kaufman: *Phys. Fluids* **24**, 1238 (1981).
- [262] V.I. Karpman, A.G. Shagalov: *J. Plasma Phys.* **27**, 215 (1981).
- [263] B. Bezzerides, D.F. DuBois, D.W. Forslund: *Phys. Rev.* **A16**, 1678 (1977).
- [264] M.M. Škorić, D. ter Haar: *Phys. Fluids* **27**, 2375 (1984).
- [265] P. Mora: Thèse d'Etat, Université Paris-Sud, Orsay, France (1980).
- [266] R.E. Aamodt: Vella, *Phys. Rev. Lett.* **39**, 1273 (1977).
- [267] P. Mora, R. Pellat: *Phys. Lett.* **A 66**, 28 (1978).
- [268] S.G. Thornhill: D. Ter Haar, *Phys. Rep.* **43**, 43 (1981).
- [269] S.A. Bel'kov: V.N. Tsytovich, *Sov. Phys. JETP* **49**, 656 (1980).
- [270] M. Kono: M.M. Škorić, D. ter Haar, *Phys. Lett* **A 78**, 140 (1980).
- [271] S. Ishimaru: *Basic Principles of Plasma Physics* (Benjamin, Reading, MA 1973).
- [272] M.M. Škorić: Lj. Stokić, *Phys. Lett* **A 92**, 389 (1982).
- [273] M.M. Škorić: in *College on Radiation in Plasmas* (IAEA, ICTP- Trieste 1983).
- [274] M.M. Škorić: in *Next Twenty Years in Plasma Physics* (Wiley-Interscience 1985) pp. 292-302.
- [275] M.M. Škorić: *Laser and Particle Beams* **5**, 83 (1987).
- [276] T. Speziale, P.J. Catto: *Phys. Fluids* **21**, 2063 (1978).
- [277] W. Woo, K. Estabrook, J.S. DeGroot: *Phys. Rev. Lett.* **40**, 1094 (1978).
- [278] Y.M. Aliev, V.M. Bychenkov: *Sov. Phys.-JETP* **49**, 805 (1979).
- [279] M. Kono, M.M. Škorić, D. ter Haar: *Phys. Fluids* **30**, 270 (1987).

- [280] A. Zeidler, H. Schnabl, P. Mulser: Phys. Fluids **28**, 372 (1985).
- [281] J.F. Drake, P.K. Kaw, Y.C. Lee, G. Schmidt, C.S. Liu: Phys. Fluids **17**, 778 (1974).
- [282] P.K. Shukla, N.N. Rao, M.Y. Yu, N.L. Tsintsadze: Physics Reports **138**, 1 (1979) and references therein.